Journal of Experimental and Theoretical Physics, Vol. 92, No. 5, 2001, pp. 753–765.
From Zhurnal Éksperimental'noĭ i Teoreticheskoĭ Fiziki, Vol. 119, No. 5, 2001, pp. 867–880.
Original English Text Copyright © 2001 by Voĭtkiv, Grün.

NUCLEI, PARTICLES, AND THEIR INTERACTION

Induced Electron Capture in Field-Assisted Energetic Atomic Collisions[¶]

A. B. Voĭtkiv[a], * and N. Grün[b]

[a]*Physics Department, University of Freiburg, 79104 Freiburg, Germany*
**e-mail: voitkiv@uni-freiburg.de*

[b]*Institute for Theoretical Physics, University of Giessen, 35392, Giessen, Germany*

Received December 4, 2000

Abstract—We present model considerations for the process of the electron capture in energetic nonrelativstic collisions of light atomic particles in the presence of a relatively weak low-frequency external electromagnetic field. The field is treated as an elliptically polarized quantum single-mode field. Establishing validity of the dipole approximation to the electron transfer (where the total momentum of all emitted or absorbed photons can be well above the typical inneratomic momenta of an electron in the initial and final states) and neglecting the Doppler and aberration effects, we give a fully nonrelativistic treatment for the field-assisted collisions and show that the capture cross section is invariant with respect to the Galilean transformations. The model consideration suggests that the field can substantially influence the capture dynamics and considerably change the capture cross section compared to the field-free collisions. This is especially the case if the "resonance" conditions $n\omega \approx \pm v^2/2$ are satisfied, with $n\omega$ being the energy transferred to or absorbed from the electromagnetic field and v the collision velocity. © *2001 MAIK "Nauka/Interperiodica".*

1. INTRODUCTION

Electron transfer in nonrelativistic atomic collisions is one of the fundamental problems in atomic physics that has been studied in great detail (see, e.g., [1–3] and references therein). The inclusion of an electromagnetic field into atomic collisions introduces new degrees of freedom and can substantially influence the collision process under certain conditions. A good example of this influence is represented by the radiative electron capture process, where the interaction with the radiation field (with the QED photon vacuum field) dramatically changes the capture process at high collision velocities (see, e.g., [4, 5], and references therein). The present paper is an attempt at a preliminary analysis of the possibility to influence the electron transfer process in fast nonrelativistic collisions by an external monochromatic electromagnetic field. We consider nearly symmetrical collisions of light atomic particles, $Z_2 \sim Z_1 \sim 1$, one of which (Z_1) initially carries an electron in the ground state and the second is a bare nucleus. We assume that the collision velocity v is sufficiently high ($v \gg Z_{1,2}$), but not relativistic ($v \ll c$, where $c = 137$ a.u. is the speed of light). The electromagnetic field is treated as a quantized single-mode field that initially contains a definite number of photons. This field is assumed to be elliptically polarized in general and to have a frequency that is small compared to the minimal excitation energy of the electron bound in the ground state of the particles Z_1 or Z_2. The electric field strength F_0 is regarded to be small compared to a typical inner atomic field in the ground state,

$$F_{at} \sim \frac{Z_{1,2}}{a_0^2} = Z_{1,2}^3 \text{ a.u.}, \quad F_0 \ll F_{at}.$$

We also assume that there are no multiphoton resonances between the ground and excited states in particles 1 and 2. Using such a low-frequency electromagnetic field, we pursue two objects. First, a relatively weak low-frequency field allows us to avoid substantial depleting of the electron ground states in collision-free atomic systems. Second, as we see below, the coupling of the electron to a field in the charge exchange process is effectively stronger for lower frequencies.

Atomic units are used throughout the paper unless otherwise stated.

2. GENERAL CONSIDERATION

2.1. Preliminary Remarks

Since the collision velocity v is supposed to be sufficiently high, we can use the impact parameter approximation. We assume that the electron is initially in the

---

[¶] This article was submitted by the authors in English.

ground state of particle 1 moving along a straight-line trajectory

$$\mathbf{R}(t) = \mathbf{b} + \mathbf{v}t$$

in an inertial reference frame K. Particle 1 collides with particle 2, which rests at the origin in K. As the result of the collision in the presence of an electromagnetic field, the electron undergoes a transition into the ground state of particle 2 simultaneously with the induced emission or absorption of $m = 0, 1, 2, \ldots$ photons with the frequency ω.

To describe the system consisting of an electron subjected to the Coulomb interaction with two colliding Coulomb centers and the electromagnetic field, we take the Schrödinger equation

$$i\frac{\partial}{\partial t}|\Psi\rangle = (H_{\text{col}} + H_{\text{int}} + H_{\text{ph}})|\Psi\rangle, \tag{1}$$

where $|\Psi\rangle$ is the state vector of the system,

$$H_{\text{col}} = -\frac{\Delta}{2} + V_1(\mathbf{r} - \mathbf{R}(t)) + V_2(\mathbf{r}) \tag{2}$$

is the Hamiltonian of the electron in the fields of the two colliding centers, and

$$H_{\text{int}} = \frac{1}{c}\mathbf{A}\cdot\hat{\mathbf{p}} + \frac{A^2}{2c^2} \tag{3}$$

is the interaction of the electron with the electromagnetic field, with $\hat{\mathbf{p}}$ being the electron momentum operator.

In the Schrödinger picture, the vector potential $\mathbf{A}$ of the quantized electromagnetic field is given by (see, e.g., [6, 7])

$$\mathbf{A} = \lambda(\mathbf{e}a\exp(i\mathbf{k}\cdot\mathbf{r}) + \mathbf{e}^*a^\dagger\exp(-i\mathbf{k}\cdot\mathbf{r})), \tag{4}$$

where

$$\lambda = c\sqrt{\frac{2\pi}{\omega V}},$$

V is the quantization volume, $\mathbf{k}$ is the photon momentum, and a and $a^\dagger$ are the time-independent annihilation and creation operators, respectively. We assume that these operators are space-independent, i.e., that vector potential (4) corresponds to a plane wave.

The polarization vectors $\mathbf{e}$ and $\mathbf{e}^*$ are given by

$$\begin{aligned}\mathbf{e} &= \mathbf{e}_1\cos(\xi/2) + i\mathbf{e}_2\sin(\xi/2),\\ \mathbf{e}^* &= \mathbf{e}_1\cos(\xi/2) - i\mathbf{e}_2\sin(\xi/2),\end{aligned} \tag{5}$$

where $\mathbf{e}_1$ and $\mathbf{e}_2$ are the unit vectors that are perpendicular to the photon momentum $\mathbf{k}$ and to each other,

$$\mathbf{e}_{1,2}\cdot\mathbf{k} = 0, \quad \mathbf{e}_1\cdot\mathbf{e}_2 = 0.$$

The vectors $\mathbf{e}$ and $\mathbf{e}^*$ satisfy the relations

$$\begin{aligned}\mathbf{e}\cdot\mathbf{e}^* &= 1,\\ \mathbf{e}\cdot\mathbf{e} = \mathbf{e}^*\cdot\mathbf{e}^* &= \cos\xi.\end{aligned} \tag{6}$$

The angle ξ determines the degree of polarization; e.g., $\xi = 0$ and $\xi = \pi/2$ correspond to the linear and circular polarizations, respectively.

The term H_{ph} in Eq. (1) describes the free electromagnetic field. It can be written as (see the Appendix)

$$H_{\text{ph}} = \omega(N_a - N), \tag{7}$$

where

$$N_a = \frac{1}{2}(aa^\dagger + a^\dagger a)$$

and N is the initial number of photons in the electromagnetic field.

With the ansatz

$$|\Psi\rangle = \exp(-i\mathbf{k}\cdot\mathbf{r}(N_a - N))|\Psi_1\rangle, \tag{8}$$

the Schrödinger equation can be rewritten as

$$\begin{aligned}i\frac{\partial}{\partial t}|\Psi_1\rangle &= H_{\text{col}}|\Psi_1\rangle - \left(\mathbf{k}(N_a - N) - \frac{1}{c}\mathbf{A}_0\right)\cdot\hat{\mathbf{p}}|\Psi_1\rangle\\ &+ \left(\frac{k^2(N_a - N)^2}{2} + \omega(N_a - N) + \frac{A_0^2}{2c^2}\right)|\Psi_1\rangle,\end{aligned} \tag{9}$$

where

$$\mathbf{A}_0 = \lambda(\mathbf{e}a + \mathbf{e}^*a^\dagger) \tag{10}$$

is independent of the electron coordinates. Equation (9) can be simplified by noting two points. First, the term

$$\frac{k^2(N_a - N)^2}{2} = \omega(N_a - N)\frac{\omega(N_a - N)}{2c^2}$$

represents a relativistic correction to the term $\omega(N_a - N)$ and must be dropped within the accuracy of the nonrelativistic Schrödinger equation (see the Appendix). Second, a typical change of the electron momentum in the electron transfer process is approximately equal to $\mathbf{v}$, and the term $\mathbf{k}(N_a - N)\hat{\mathbf{p}}\,|\Psi_1\rangle$ can be roughly estimated as

$$\begin{aligned}\mathbf{k}(N_a - N)\hat{\mathbf{p}}|\Psi_1\rangle &\sim \mathbf{k}\cdot\mathbf{v}(N_a - N)|\Psi_1\rangle\\ &\sim \frac{v}{c}\omega(N_a - N)|\Psi_1\rangle.\end{aligned}$$

Thus, it is seen that the main effect of the term $\mathbf{k}(N_a - N)\hat{\mathbf{p}}|\Psi_1\rangle$ is related to the Doppler shift. For nonrelativistic collisions, one has

$$\mathbf{k}(N_a - N)\hat{\mathbf{p}}|\Psi_1\rangle \ll \omega(N_a - N)|\Psi_1\rangle$$

and the term $\mathbf{k}(N_a - N)\hat{\mathbf{p}}|\Psi_1\rangle$ can also be omitted.

The Schrödinger equation then becomes

$$i\frac{\partial}{\partial t}|\Psi_1\rangle = H_{\text{col}}|\Psi_1\rangle + \left(\frac{1}{c}\mathbf{A}_0\cdot\hat{\mathbf{p}} + \frac{A_0^2}{2c^2}\right)|\Psi_1\rangle + \omega(N_a - N)|\Psi_1\rangle. \tag{11}$$

This equation looks like the Schrödinger equation with the electromagnetic field taken in the dipole approximation. The remark about validity of the dipole approximation for the field-assisted electron transfer may now be in order. Although the momentum $k = \omega/c$ of one low-frequency photon is much less than a typical electron momentum in the ground state of the target ($p_1 \sim Z_1$) or of the projectile ($p_2 \sim Z_2$), the total momentum of all the emitted or absorbed photons can be well above $p_{1,2}$ (e.g., in the "resonance" case, see Section 3). We have analyzed the role of the photon momentum in the field-assisted electron transfer. The analysis shows that in general, the corrections to the capture cross section due to the photon momentum are of the order of v_e/c, where $v_e \sim v$ is a characteristic electron velocity in the process. Thus, with the electron assumed to be nonrelativistic in the capture process, the corrections to the capture cross section are of minor importance.

Now, with the validity of the dipole approximation for the electron transfer in nonrelativistic collisions being established, we can neglect the Doppler and aberration effects and give fully nonrelativistic treatment for the field-assisted electron transfer process where capture cross sections must be invariant under Galilean transformations [4].

Equation (11) can be further simplified. To this end, we consider the interaction term

$$\frac{1}{2c^2}A_0^2 = \frac{\lambda^2}{2c^2}((a^2 + a^{\dagger 2})\cos\xi + aa^\dagger + a^\dagger a)$$

in more detail. The quadratic terms a^2 and $a^{\dagger 2}$ can be removed from the Schrödinger equation by applying the so called "squeezed light" transformation (see, e.g., [8])

$$\begin{aligned} a &= b\cosh\chi + b^\dagger\sinh\chi, \\ a^\dagger &= b^\dagger\cosh\chi + b\sinh\chi, \end{aligned} \tag{12}$$

where

$$\tanh(2\chi) = -\frac{\lambda^2\cos\xi}{c^2\omega + \lambda^2}. \tag{13}$$

The corresponding Schrödinger equation for the electron interacting with "*b*-photons" is given by

$$i\frac{\partial}{\partial t}|\Psi_1\rangle = H_{\text{col}}|\Psi_1\rangle + \frac{\lambda}{c}(\mathbf{e}_b b + \mathbf{e}_b^* b^\dagger)\cdot\hat{\mathbf{p}} + \omega_{\text{eff}}N_b|\Psi_1\rangle, \tag{14}$$

where

$$N_b = \frac{1}{2}(b^\dagger b + bb^\dagger),$$

$$\omega_{\text{eff}} = \sqrt{(\omega + \lambda^2/c^2)^2 - (\lambda^4/c^4)\cos^2\xi}.$$

As follows from (13), the difference between "*a*-photons" and "*b*-photons" is determined by the factor

$$\frac{\lambda^2}{\omega c^2} = \frac{2\pi}{V\omega^2}.$$

Since the quantization volume V of a laser field is usually of a macroscopic dimension, we can assume that

$$\frac{2\pi}{V\omega^2} \longrightarrow 0$$

except for extremely low frequencies, which are not considered in this paper. Therefore, we have $\chi \approx 0$ and the difference becomes very small. Disregarding this difference and replacing "*b*-photons" with "*a*-photons" in Eq. (14), we finally arrive at the Schrödinger equation

$$i\frac{\partial}{\partial t}|\Psi_1\rangle = H_{\text{col}}|\Psi_1\rangle + \frac{\lambda}{c}(\mathbf{e}a + \mathbf{e}^*a^\dagger)\cdot\hat{\mathbf{p}} + \omega(a^\dagger a - N)|\Psi_1\rangle. \tag{15}$$

In Eq. (15), we have also neglected the difference between

$$N_a = 0.5(aa^\dagger + a^\dagger a) = a^\dagger a + 1/2$$

and

$$N_a' = a^\dagger a,$$

which is inessential for the electron transfer process.

2.2. Model One-Center Electron States Dressed by the Interaction with an Electromagnetic Field

We regard the charge transfer process as an electron transition, due to a collision with the second center, between the field-dressed electron states centered on the target and the projectile. We first consider the problem of an electron bound to center 1, which moves in the frame K with a constant velocity $\mathbf{v}$ and is subjected to the electromagnetic field. As shown in the previous subsection, the corresponding Schrödinger equation can be written as

$$i\frac{\partial}{\partial t}|\Phi_{i,0}\rangle = \left(H_{at,1} + \frac{\mathbf{A}_0}{c}\cdot\hat{\mathbf{p}} + \omega(a^\dagger a - N)\right)|\Phi_{i,0}\rangle, \quad (16)$$

where

$$H_{at,1} = -\frac{\Delta}{2} + V_1(\mathbf{r} - \mathbf{R}(t)) \quad (17)$$

is the Hamiltonian of the electron in the Coulomb field of the moving center.

The state vector $|\Phi_{i,0}\rangle$ of the system consisting of the electron bound to the moving center and of the electromagnetic field containing initially N photons with the frequency ω can be expanded as

$$|\Phi_{i,0}(t)\rangle = \sum_\alpha\sum_n \exp(-in\omega t)a_{\alpha,n}(t)\psi_\alpha(t)|N+n\rangle, \quad (18)$$

where the unknown time-dependent coefficients $a_{\alpha,n}$ must be determined. In (18), the summation runs over all the electron states $\{\psi_\alpha\}$ including the continuum and over the photon states with different numbers of additional photons ($n = 0, \pm1, \pm2, \ldots$). The states ψ_α of the electron in the field of binding center 1 moving along a straight-line trajectory

$$\mathbf{R}(t) = \mathbf{b} + \mathbf{v}t$$

are given by

$$\psi_\alpha(t) = \varphi_\alpha^{(1)}(\mathbf{r} - \mathbf{R}(t))\exp(-i\varepsilon_\alpha^{(1)}t) \times \exp(i\mathbf{v}\cdot\mathbf{r})\exp\left(-i\frac{v^2}{2}t\right), \quad (19)$$

where $\varphi_\alpha^{(1)}(\mathbf{r})$ is the atomic state (discrete or continuous) of the electron at center 1 with the energy $\varepsilon_\alpha^{(1)}$.

Inserting (18) in (16), we obtain the system of differential equations for the unknown coefficients $a_{\alpha,n}$

$$i\frac{da_{\alpha,n}}{dt} = \frac{1}{c}\sum_m\sum_\beta a_{\beta,m}\exp(i(n-m)\omega t) \times\langle N+n|\mathbf{A}_0|N+m\rangle\langle\psi_\alpha|\hat{\mathbf{p}}|\psi_\beta\rangle. \quad (20)$$

Taking into account that

$$\langle\psi_\alpha|\hat{\mathbf{p}}|\psi_\beta\rangle = \exp(i\omega_{\alpha\beta}t)(\mathbf{v}\delta_{\alpha\beta} + \langle\varphi_\alpha|\hat{\mathbf{p}}|\varphi_\beta\rangle), \quad (21)$$

where

$$\omega_{\alpha\beta} = \varepsilon_\alpha^{(1)} - \varepsilon_\beta^{(1)},$$

we obtain

$$\begin{aligned} i\frac{da_{\alpha,n}}{dt} &= \frac{\mathbf{v}}{c}\sum_m a_{\alpha,m}\exp(i(n-m)\omega t) \\ &\times\langle N+n|\mathbf{A}_0|N+m\rangle \\ &+ \frac{1}{c}\sum_m\sum_{\beta\neq\alpha} a_{\beta,m}\exp(i((n-m)\omega + \omega_{\alpha\beta})t) \\ &\times\langle N+n|\mathbf{A}_0|N+m\rangle\langle\varphi_\alpha|\hat{\mathbf{p}}|\varphi_\beta\rangle. \end{aligned} \quad (22)$$

The first and the second terms on the right-hand side of (22) correspond to different mechanisms of the dressing of the electron by the electromagnetic field. The double sum in (22) describes the part of the electron dressing that is accompanied by transitions of the electron into excited atomic states, including the atomic continuum. In our model treatment this part of the dressing will be neglected, which corresponds to taking into account the so called diagonal dressing of the electron by the electromagnetic field (see, e.g., [9]). For the electron initially occupying the state ψ_0, we then have

$$\begin{aligned} i\frac{da_{0,n}}{dt} &= \frac{\mathbf{v}}{c}\sum_m a_{0,m}\exp(i(n-m)\omega t)\langle N+n|\mathbf{A}_0|N+m\rangle, \\ a_{\alpha,n} &= 0, \quad \alpha\neq 0. \end{aligned} \quad (23)$$

Equations (23) together with the assumption that the coupling between the electron and the electromagnetic field is adiabatically switched on and off at $t \longrightarrow -\infty$ and $t \longrightarrow +\infty$, respectively, form the basis for our model of the system "bound electron + electromagnetic field."

The matrix elements $\langle N+n|\mathbf{A}_0|N+m\rangle$ are not equal to zero only for $m = n \pm 1$. We assume the initial number of photons N to be very large, $N \gg |n|$ and $N \gg |m|$, which corresponds to regarding the electromagnetic field as an inexhaustible source and sink of photons.

The matrix elements $\langle N+n|\mathbf{A}|N+n-1\rangle$ and $\langle N+n|\mathbf{A}|N+n+1\rangle$ can then be assumed to be n-independent and the system of equations (23) reduces to

$$i\frac{da_{0,n}}{dt} = \frac{\lambda\sqrt{N}}{c}(\mathbf{e}\cdot\mathbf{v}a_{0,n+1}\exp(-i\omega t) + \mathbf{e}^*\cdot\mathbf{v}a_{0,n-1}\exp(i\omega t)). \tag{24}$$

In order to solve (24), it is convenient to rewrite the scalar products $\mathbf{e}\cdot\mathbf{v}$ and $\mathbf{e}^*\cdot\mathbf{v}$ as

$$\begin{aligned}\mathbf{e}\cdot\mathbf{v} &= v_0\exp(i\phi),\\ \mathbf{e}^*\cdot\mathbf{v} &= v_0\exp(-i\phi),\end{aligned} \tag{25}$$

where v_0 and ϕ are given by

$$\begin{aligned}v_0 &= \sqrt{(\mathbf{v}\cdot\mathbf{e}_1\cos(\xi/2))^2 + (\mathbf{v}\cdot\mathbf{e}_2\sin(\xi/2))^2},\\ \phi &= \arctan\left(\frac{\mathbf{v}\cdot\mathbf{e}_2}{\mathbf{v}\cdot\mathbf{e}_1}\tan(\xi/2)\right).\end{aligned} \tag{26}$$

Using the ansatz

$$a_{0,n}(t) = f_n\exp(in(\omega t-\phi)), \tag{27}$$

where f_n are time-independent, and inserting (27) in (24), we obtain the simple relation

$$f_{n+1} + f_{n-1} = \frac{2n}{G}f_n, \tag{28}$$

where

$$G = -\frac{2\lambda v_0\sqrt{N}}{c\omega}. \tag{29}$$

The absolute value of G determines the effective strength of the electron-field coupling. Solutions of the recurrence relation (28) are the Bessel functions (see, e.g., [10]). Therefore,

$$a_{0,n} = C\zeta_n(G)\exp(in(\omega t-\phi)), \tag{30}$$

where ζ_n denotes the Bessel functions J_n, Y_n, $H_n^{(1)}$, $H_n^{(2)}$, or any linear combination thereof, and C is n-independent.

Taking Eqs. (30) and (18) into account, we rewrite the state vector as

$$|\Phi_{i,0}(t)\rangle = C\psi_0(t)\sum_n\zeta_n(G)\exp(-in\phi)|N+n\rangle. \tag{31}$$

In order to determine C and to find which of the Bessel functions corresponds to ζ_n, we note that, in the absence of the coupling between the electron and the electromagnetic field,

$$\mathbf{A}_0\cdot\mathbf{v} = 0,$$

the state vector has the form

$$|\Phi_{i,0}(t)\rangle = \psi_0(t)|N\rangle. \tag{32}$$

Therefore, in order to recover Eq. (32) from Eq. (31), one must set $C = 1$ and $\zeta_n(G) = J_n(G)$ in Eq. (31) with J_n being the Bessel function of the first kind. Then the initial state vector becomes

$$|\Phi_{i,0}(t)\rangle = \psi_0(t)\sum_n J_n(G)\exp(-in\phi)|N+n\rangle. \tag{33}$$

This state describes the moving electron bound in the ground state and dressed by the interaction with the electromagnetic field. Because the coupling to the field is switched off as $t \longrightarrow +\infty$, we have

$$|\Phi_{i,0}(t\longrightarrow+\infty)\rangle = \psi_0(t).$$

Within the adopted approximation, therefore, if no collision event occurs, the state vector of the "electron + electromagnetic field" system is finally the same as initially. Thus, the dressing given by (33) does not result in any electron transitions within the same center and can therefore be viewed, to some extent, as "hidden." It is the collision that can display the hidden dressing.

The final state vector $|\Phi_{f,m}\rangle$ describes the electron (finally) bound in the ground state $\varphi_0^{(2)}$ of particle 2 and the presence of $N+m$ photons. Within the approximation similar to that used to obtain the state vector $|\Phi(t)_{i,0}\rangle$, we obtain

$$|\Phi_{f,m}\rangle = \varphi_0^{(2)}\exp(-i(\varepsilon_0^{(2)}+m\omega)t)|N+m\rangle. \tag{34}$$

2.3. Transition Amplitudes and Cross Sections

Because the collision velocity is supposed to be sufficiently high, one can use perturbation theory in the Coulomb interaction to consider the charge exchange. It is known (see, e.g., [1–3] and references therein) that the boundary-corrected Born approximation must be employed in order to obtain reliable results for the nonradioactive charge exchange processes in energetic Coulomb collisions. However, in order to obtain just a preliminary insight into the field-assisted electron capture, we use a simpler approach that does not take the Coulomb-corrected boundary conditions into account and corresponds to the OBK approximation for the field-free collisions. It is known (see, e.g., [1]) that for external field-free collisions, the second-order terms (representing the Thomas double scattering mechanism) are of minor practical importance for the total 1s-1s capture cross sections. For example, in the

$$p + H(1s) \longrightarrow H(1s) + p$$

collisions, the second-order term dominates over the first-order one at $v \gtrsim 80$ a.u. At these velocities, however, the radiative electron capture dominates over the nonradiative one and in addition, the relativistic effects cannot be ignored in general. In the region of the collision velocities of interest in the present paper ($v \sim 10$ a.u.), the first-order term dominates in the 1*s*-1*s* cross sections. In this paper, we consider the 1s-1s capture and use the first-order approach,[1] which corresponds to the first-order OBK (OBK1) approximation for the field-free collisions (see, e.g., [12, 1]).

2.3.1. Prior form of the cross section of the field-assisted charge exchange. In the first order of perturbation theory in the prior form for the field-assisted electron capture accompanied by the emission or absorption of $|n|$ photons, the transition amplitude is given by

$$a^{(n)}_{\text{prior}} = -i\int_{-\infty}^{\infty} dt \langle \Phi_{f,n}|V_2(\mathbf{r})|\Phi_{i,0}\rangle, \tag{35}$$

where V_2 is the interaction of the electron with the second center and the initial and final state vectors are given by Eqs. (33) and (34), respectively.

After some straightforward but lengthy algebra, we rewrite the transition amplitude as

$$\begin{aligned} a^{(n)}_{\text{prior}} = {} & 2\pi i J_n(G)\int d^3q\chi_0^{(1)}(\mathbf{q}+\mathbf{v})(\varepsilon_0^{(2)} - 0.5q^2) \\ & \times(\chi_0^{(2)}(\mathbf{q}))^*\exp(i\mathbf{q}\cdot\mathbf{b}) \\ & \times\delta\left(\varepsilon_0^{(2)} + n\omega - \varepsilon_0^{(1)} + \frac{v^2}{2} + \mathbf{q}\cdot\mathbf{v}\right), \end{aligned} \tag{36}$$

where $\chi_0^{(1)}(\mathbf{q})$ and $\chi_0^{(2)}(\mathbf{q})$ are the Fourier transforms of the respective wavefunctions $\varphi_0^{(1)}(\mathbf{r})$ and $\varphi_0^{(2)}(\mathbf{r})$.

The cross section for the electron transfer accompanied by net emission ($n > 0$) or net absorption ($n < 0$) of $|n|$ photons is given by

$$\begin{aligned} \sigma^{(n)}_{\text{prior}} = {} & \int d^2\mathbf{b}\left|a^{(n)}_{\text{prior}}(\mathbf{b})\right|^2 = J_n^2(G)\frac{16\pi^4}{v} \\ & \times\int d^3q\left|\chi_0^{(1)}(\mathbf{q}+\mathbf{v})\right|^2(\varepsilon_0^{(2)} - 0.5q^2)^2 \\ & \times\left|\chi_0^{(2)}(\mathbf{q})\right|^2\delta\left(\varepsilon_0^{(2)} + n\omega - \varepsilon_0^{(1)} + \frac{v^2}{2} + \mathbf{q}\cdot\mathbf{v}\right). \end{aligned} \tag{37}$$

The charge exchange cross section is given by

$$\sigma_{\text{prior}} = \sum_n \sigma^{(n)}_{\text{prior}}. \tag{38}$$

In this equation, the different terms in the sum describe the electron transfer cross sections accompanied by the induced emission ($n > 0$) or absorption ($n < 0$) of different numbers of photons. The term with $n = 0$ corresponds to the capture where the net number of exchanged photons is zero.

2.3.2. Post form of the cross section of the field-assisted charge exchange. In the post form of the field-assisted electron capture accompanied by the emission or absorption of $|n|$ photons, the transition amplitude is represented by

$$a^{(n)}_{\text{post}} = -\int_{-\infty}^{\infty} dt \langle \Phi_{f,n}|V_1(\mathbf{r}-\mathbf{R}(t))|\Phi_{i,0}\rangle, \tag{39}$$

where V_1 is the interaction of the electron with the first center and the initial and final state vectors are again given by Eqs. (33) and (34), respectively.

In the post form, the cross sections for the electron transfer are given by

$$\begin{aligned} \sigma^{(n)}_{\text{post}} = {} & \int d^2\mathbf{b}\left|a^{(n)}_{\text{post}}(\mathbf{b})\right|^2 = J_n^2(G)\frac{16\pi^4}{v} \\ & \times\int d^3q\left|\chi_0^{(1)}(\mathbf{q}+\mathbf{v})\right|^2(\varepsilon_0^{(1)} - 0.5(\mathbf{q}+\mathbf{v})^2)^2 \\ & \times\left|\chi_0^{(2)}(\mathbf{q})\right|^2\delta\left(\varepsilon_0^{(2)} + n\omega - \varepsilon_0^{(1)} + \frac{v^2}{2} + \mathbf{q}\cdot\mathbf{v}\right) \end{aligned} \tag{40}$$

and

$$\sigma_{\text{post}} = \sum_n \sigma^{(n)}_{\text{post}}. \tag{41}$$

2.3.3. Galilean invariance of the charge exchange cross sections. One can give a slightly more general treatment for the field-assisted electron transfer by considering the process in an inertial reference frame *K'* where both particles 1 and 2 move with the respective velocities $\mathbf{v}_1$ and $\mathbf{v}_2$ along the trajectories

$$\mathbf{R}_1(t) = \mathbf{b}_1 + \mathbf{v}_1 t$$

---

[1] It is worthwhile to note the following. The dominance of the Thomas double scattering mechanism at asymptotically high collision velocities is directly related to the kinematics of the electron transfer in field-free collisions. However, it is not clear how an external field can influence the kinematics. In [11], for example, the radiative electron capture was considered as collision-stimulated transitions between one-center electron states dressed by the interaction with the radiation field, i.e., using an approach quite similar to that applied in the present paper. In [11], the Coulomb interaction with the other center was taken into account only in the first order. Nevertheless, this approach was shown to yield the correct velocity dependence for the radiative capture cross section $\sigma_{REC} \sim 1/v^5$ at asymptotically high velocities.

and

$$\mathbf{R}_2(t) = \mathbf{b}_2 + \mathbf{v}_2 t,$$

with

$$\mathbf{v} = \mathbf{v}_1 - \mathbf{v}_2$$

being the collision velocity. If one assumes that these trajectories are parallel lines, the collision impact parameter **b** is given simply by

$$\mathbf{b} = \mathbf{b}_1 - \mathbf{b}_2.$$

In the frame K', the initial state vector is described by Eq. (33) with the evident replacements $\mathbf{b} \longrightarrow \mathbf{b}_1$ and $\mathbf{v} \longrightarrow \mathbf{v}_1$ in the electron state, in the argument of the Bessel functions, and in the phase $\phi(=\phi_1)$. The final state vector is now represented by

$$|\Phi_{f,m}(t)\rangle = \psi_0^{(2)}(t)\exp(-im\omega t) \times \sum_{m'} J_{m'}(G_2)\exp(im'\phi_2)|N + m + m'\rangle, \tag{42}$$

where $\psi_0^{(2)}(t)$, ϕ_2, and G_2 are given by Eqs. (19), (26) and (29) with evident replacements. Because the electromagnetic field adiabatically switches off as $t \longrightarrow \infty$, the state vector (42) asymptotically reduces to

$$|\Phi_{f,m}(t)\rangle = \psi_0^{(2)}(t)\exp(-im\omega t)|N + m\rangle, \tag{43}$$

which describes the electron and the field with $N + m$ photons that are decoupled as $t \longrightarrow \infty$.

Using Graf's addition theorem for the Bessel functions (see [10, p. 363, no. 9.1.79]), one can show that this more general treatment yields cross sections that depend only on $\mathbf{v} = \mathbf{v}_1 - \mathbf{v}_2$ and are exactly equal to those given by Eqs. (37) and (38) or Eqs. (40) and (41).

The derivation briefly outlined above stresses the Galilean invariance of the cross sections.

3. RESULTS AND DISCUSSION

Analyzing the form of dressed state (33), transition amplitude (36), and cross sections (37) and (40), one can conclude that the effective strength of the coupling between the electron and the electromagnetic field occurring in the process of the electron transfer is determined by the factor $|G|$. The effective strength of this coupling is determined not only by the field parameters themselves but also by the change in the electron velocity. For high collision velocities, this coupling can therefore be strong even for relatively weak electromagnetic fields.

In what follows, we consider the electromagnetic field to be linearly polarized although similar conclusions can also be drawn for a more general case of the elliptical polarization. For a linearly polarized field, the coupling factor reduces to

$$|G| = \frac{|\mathbf{F}_0 \cdot \mathbf{v}|}{\omega^2},$$

where

$$\mathbf{F}_0 = \frac{\sqrt{2\pi\omega N}}{V}\mathbf{e}_1$$

is the electric component of the electromagnetic field.

3.1. Weak Coupling with the Electromagnetic Field

If the factor $|G|$ is much smaller than unity, the term with $n = 0$ dominates in the total charge exchange cross section. For $n \neq 0$, only the terms with $n \pm 1$ in (38) (or (41)) can reach noticeable values. In this case,

$$\sigma^{(0)} = J_0^2\left(\frac{\mathbf{F}_0 \cdot \mathbf{v}}{\omega^2}\right)\sigma_{OBK1} \approx \left(1 - \left(\frac{\mathbf{F}_0 \cdot \mathbf{v}}{2\omega^2}\right)^2\right)^2 \sigma_{OBK1} \approx \sigma_{OBK1}, \tag{44}$$

where

$$\sigma_{OBK1} = \frac{16\pi^4}{v}\int d^3q \left|\chi_0^{(1)}(\mathbf{q} + \mathbf{v})\right|^2 (\varepsilon_0^{(2)} - 0.5q^2)^2 \times \left|\chi_0^{(2)}(\mathbf{q})\right|^2 \delta\left(\varepsilon_0^{(2)} - \varepsilon_0^{(1)} + \frac{v^2}{2} + \mathbf{q} \cdot \mathbf{v}\right) \tag{45}$$

is the cross section of the nonradiative charge exchange obtained in the OBK1 approximation.

In accordance with (37), cross sections for the charge exchange accompanied by the emission and absorption of one photon are given by

$$\sigma^{(\pm 1)} \approx \left(\frac{\mathbf{F}_0 \cdot \mathbf{v}}{2\omega^2}\right)^2 \frac{16\pi^4}{v}\int d^3q \left|\chi_0^{(1)}(\mathbf{q} + \mathbf{v})\right|^2 \times (\varepsilon_0^{(2)} - 0.5q^2)^2 \left|\chi_0^{(2)}(\mathbf{q})\right|^2 \times \delta\left(\varepsilon_0^{(2)} - \varepsilon_0^{(1)} \pm \omega + \frac{v^2}{2} + \mathbf{q} \cdot \mathbf{v}\right). \tag{46}$$

Because ω is small, the terms $\pm\omega$ do not play an essential role in the integrands in Eq. (46) and can be dropped. Therefore, the processes accompanied by the emission and the absorption of one photon give practically identical contributions to the capture cross section and are related to the OBK1 cross section (45) by

$$\sigma^{(\pm 1)} \approx \left(\frac{\mathbf{F}_0 \cdot \mathbf{v}}{2\omega^2}\right)^2 \sigma_{OBK1}. \quad (47)$$

From (44) and (47), it follows that

$$\sigma^{(-1)} + \sigma^{(0)} + \sigma^{(+1)} \approx \sigma_{OBK1}, \quad (48)$$

i.e., that the total electron transfer is only very slightly influenced by the field in the case of a weak coupling.

We note that, for a weak coupling, the post form of the cross section (Eqs. (40) and (41)) yields results that are identical to (45) and (47).

3.2. Strong Coupling with the Electromagnetic Field

The ratio between the contributions of the charge transfer processes involving different numbers of emitted or absorbed photons to the total capture cross section becomes entirely different in the "intermediate" ($|\mathbf{F}_0 \cdot \mathbf{v}|/\omega^2 \gtrsim 1$) and, especially, in the strong-coupling ($|\mathbf{F}_0 \cdot \mathbf{v}|/\omega^2 \gg 1$) limits. For a strong coupling, $J_0(x) \ll 1$ for $x \gg 1$, and the charge transfer process without net emission or absorption of photons is therefore strongly suppressed compared to the weak coupling limit. The main contribution to the total charge exchange cross section is now due to the electron transfer accompanied by the absorption and emission of large numbers of photons. It follows from the properties of the Bessel function $J_n(x)$ [10, 13] that in order to obtain a noticeable contribution of the $|n|$-photon process, x must be at least of the order of $|n|$. Therefore, one can estimate that the maximum number of photons involved in the field-assisted charge exchange process is of the order of $|\mathbf{F}_0 \cdot \mathbf{v}|/\omega^2$.

"Resonance" conditions, the post-prior discrepancy, and the correspondence to different physical mechanisms of the charge exchange. The factors $|\chi_0^{(1)}(\mathbf{q} + \mathbf{v})|^2$ and $|\chi_0^{(2)}(\mathbf{q})|^2$ entering the integrands in (37) and (40) imply that at high velocities, each integrand (excluding the delta-function) has two peaks centered around $\mathbf{q} = -\mathbf{v}$ and $\mathbf{q} = 0$. Therefore, the integrals over the momentum transfer in (37) and (40) can be relatively large only if the argument of the delta-function can be equal to zero at $\mathbf{q} \approx -\mathbf{v}$ or $\mathbf{q} \approx 0$. This can occur if there is a considerable probability for many-photon processes where the numbers $|n|$ of the photons involved satisfy the "resonance" conditions given by

$$n\omega = \frac{v^2}{2} + \varepsilon_0^{(1)} - \varepsilon_0^{(2)} \approx \frac{v^2}{2} \quad (49)$$

for the emission and by

$$n\omega = -\frac{v^2}{2} + \varepsilon_0^{(1)} - \varepsilon_0^{(2)} \approx -\frac{v^2}{2} \quad (50)$$

for the absorption.

As in the radiative electron transfer, the resonance condition for the charge exchange stimulated by emission looks more transparent if we view the charge exchange in the rest frame of the projectile: the electron with the initial energy $\varepsilon_0^{(1)} + v^2/2$ undergoes a transition to the bound state of the projectile with the energy $\varepsilon_0^{(2)}$, transferring the energy difference to the electromagnetic field by means of photon emission. On the other hand, the resonance condition for the electron transfer accompanied by absorption looks more natural if we take the target frame as a reference frame: the electron with the initial energy $\varepsilon_0^{(1)}$ undergoes a transition to the bound state of the moving projectile, where its energy is equal to $\varepsilon_0^{(2)} + v^2/2$, absorbing the energy difference from the electromagnetic field. If the resonance conditions are satisfied, the collision kinematics for the electron transfer can be substantially improved in the same way as for the radiative electron capture, where only one high-energy photon with the frequency $\omega \approx v^2/2$ is spontaneously emitted.

Analyzing the strong coupling case, we encounter a difficulty related to the fact that the charge exchange cross sections obtained in the prior and post forms become drastically different. The integrands in (37) and (40) are strictly equal to each other only for $n = 0$ and approximately equal for low $|n|$. As $|n|$ increases, the difference between the integrands in (37) and (40) increases. This difference becomes especially large when the resonance conditions are satisfied. The latter case is of a particular interest, however, and the rest of this section is mainly devoted to the analysis of the resonance case.

In the integrand in (37) (excluding the delta-function), the ratio between the peaks at $\mathbf{q} \approx -\mathbf{v}$ and $\mathbf{q} \approx 0$ is proportional to v^4, which means that the peak at $\mathbf{q} \approx 0$ is negligible compared to the one at $\mathbf{q} \approx -\mathbf{v}$. This results in the conclusion that in accordance with (37), the electron capture is favored if it is accompanied by the emission of a large number of photons.

On the other hand, in the integrand in (40) (excluding the delta-function), the ratio of the peak at $\mathbf{q} \approx -\mathbf{v}$ to that at $\mathbf{q} \approx 0$ is proportional to v^{-4}, and the peak at $\mathbf{q} \approx -\mathbf{v}$ is therefore negligible compared to the one at $\mathbf{q} \approx 0$. This means that in accordance with (40), the electron capture is favored if it is accompanied by the absorption of a large number of photons.

As a first example, we now consider the capture cross sections for the

$$p + H(1s) \longrightarrow H(1s) + p$$

collisions assisted by the electromagnetic field with $F_0 = 2.15 \times 10^{-2}$ a.u. and $\omega = 0.117$ eV $= 4.3 \times 10^{-3}$ a.u. at the collision velocity $v = 10$ a.u. In this and all other examples, we assume that $\mathbf{F}_0$ is parallel (or antiparallel) to $\mathbf{v}$. Further, we take all the reported values of the cross sections to be multiplied by the factor 0.3, which is known to bring the OBK1 cross sections to a reasonable agreement with experimental data at intermediately high collision velocities. At the collision velocity $v = 10$ a.u., the cross section for the nonradiative capture in electromagnetic field-free collisions calculated in the OBK1 approximation (and multiplied by 0.3) is equal to $\sigma_{OBK1} = 1.14$ b.

Using the prior form of the cross sections, we obtain $\sigma^{(0)} = 6.2 \times 10^{-5}$ b, $\sum_{n=1}^{1000} \sigma_{\text{prior}}^{(n)} = 6.4 \times 10^{-2}$ b, $\sum_{n=1}^{10\,000} \sigma_{\text{prior}}^{(n)} = 38.24$ b, and $\sum_{n=1}^{12\,000} \sigma_{\text{prior}}^{(n)} = 367.3$ b for the collisions assisted by the electromagnetic field. Adding the higher-n terms does not noticeably change the prior cross section.[2] In accordance with the prior form, the main contribution comes from the terms with $10\,000 < n < 12\,000$ and the contribution from negative n is negligible.

Using the post form of the cross sections, we have

$$\sigma_0 = 6.2 \times 10^{-5} \text{ b}, \quad \sum_{n=-1}^{-10\,000} \sigma_{\text{post}}^{(n)} = 38.24 \text{ b},$$

$$\sum_{n=-1}^{-12\,000} \sigma_{\text{post}}^{(n)} = 367.3 \text{ b}$$

for the same collisions. In accordance with the post form, the main contribution is given by the terms with $-12\,000 < n < -10\,000$ and positive n contribute negligibly. Although the prior and the post forms yield the same transfer cross sections for symmetrical collisions, the physics that they describe is totally different. The prior form stresses the electron transfer due to emission (the induced multiphoton bremsstrahlung) and the post form supports the transfer process due to absorption (the multiphoton ionization).

As further examples, we consider the

$$p + \text{He}^{+} \longrightarrow \text{H} + \text{He}^{2+}$$

and

$$\text{He}^{2+} + \text{H} \longrightarrow \text{He}^{+} + \text{p}$$

collisions at $v = 10$ a.u. assisted by the electromagnetic field with the same parameters as in the first example. For the field-free collisions, one has $\sigma_{OBK1} = 27.5$ b for both colliding systems. For the field-assisted collisions, in accordance with the prior form, we obtain the respective cross section $\sigma_{\text{prior}} = 304$ b and $\sigma_{\text{prior}} = 9280$ b for the p–He^{+} and He^{2+}–H collisions. In both reactions, in the prior form, the terms with negative n (absorption) contribute negligibly. In accordance with the post form, we have $\sigma_{\text{post}} = 9280$ b and $\sigma_{\text{post}} = 304$ b for the p–He^{+} and He^{2+}–H collisions, respectively, and we find that the terms with positive n (emission) have a negligible impact on the cross section. Analyzing Eqs. (37) and (40), we conclude that the above correspondence between the prior and the post cross sections is a particular case of the relation

$$\sigma_{\text{post}}(Z_1, Z_2) = \sigma_{\text{prior}}(Z_2, Z_1), \tag{51}$$

which holds for the capture cross sections obtained in the prior and post forms.

Comparing the capture cross sections in the above three examples, we see that

$$\sigma_{\text{prior}} \propto Z_2^{\nu} \tag{52}$$

with $\nu \approx 5$, while the dependence of the cross section on Z_1 is relatively weak. On the other hand,

$$\sigma_{\text{post}} \propto Z_1^{\mu} \tag{53}$$

with $\mu \approx 5$ and the dependence of the cross section on Z_2 is relatively weak. Our calculations for other "target-projectile" pairs show similar dependences on Z_1 and Z_2 It is worthwhile to note that the dependence $\propto Z_1^5$ on the charge of the target nucleus is a signature of the photoeffect (see, e.g., [6]), while the dependence $\propto Z_2^5$ on the charge of the projectile is a signature of two closely related processes: the radiative recombination and the radiative electron capture [2].

In a rigorous theory, evidently, there must be no discrepancy between cross sections calculated in the prior and post forms. It is also clear that the large discrepancy between the prior and post forms in our case originates from the fact that the dressed states (33) and (34) do not exactly represent the system "electron in the field of a nucleus + field."[3] One way to deal with the difficulty

---

[2] Although the numbers of the emitted or absorbed photons are very large, simple estimates show that they are still much smaller than the huge number of photons available in the "coherence" volume $V_c \sim \lambda^3 = (2\pi c/\omega)^3$ of the field with $F_0 = 2.15 \times 10^{-2}$ a.u. and $\omega = 4.3 \times 10^{-3}$ a.u. Therefore, the assumption that the field is an inexhaustible source and sink of photons, which has been used in deriving Eq. (33), is not violated.

[3] The problem of the post–prior discrepancy is also known in the theory of the field-free electron transfer based on the eikonal approximation, where additional physical arguments are necessary in order to decide which form is more suitable (see, e.g., [1] and references therein).

is to try to remove the prior–post discrepancy by implementing exact solutions for the dressed states, which would yield identical results in both forms. However, this is very difficult to achieve and, in addition, one can then encounter the problem related to the overcomplete representation of the electron Hilbert space by two complete sets of states centered on the target and on the projectile. We choose another way instead. In what follows, we argue that one can still obtain physically reasonable results with the approximate dressed states (33) and (34) keeping in mind that with these states, the prior and post forms of the transition amplitude describe the electron transfer due to different physical processes. To analyze this, we first consider a collision-free system consisting of an atom that is initially in the ground state and a low-frequency relatively weak electromagnetic field. We are interested in ionization probability due to the interaction with the field and, in particular, in the probability of finally finding the electron in high-energy continuum states $\{\varphi_{\mathbf{p}}^{(1)}\}$.

For a high-energy continuum state, we can neglect its distortion due to the interaction with the target nucleus and write the state in the presence of the electromagnetic field as

$$\psi_{\mathbf{p}}^{(1)} \propto \exp(i\mathbf{p}\cdot\mathbf{r})\sum_n J_n\left(\frac{\mathbf{F}_0\cdot\mathbf{p}}{\omega^2}\right)|N+n\rangle. \tag{54}$$

For the amplitude of transitions from the ground state $\varphi_0^{(1)}$ to the high-energy state, we then have

$$a_{\mathbf{p},n}^{\text{ion}} \propto J_n\left(\frac{\mathbf{F}_0\cdot\mathbf{p}}{\omega^2}\right)\langle e^{i\mathbf{p}\cdot\mathbf{r}}|V_1|\varphi_0^{(1)}\rangle \times\delta\left(\frac{p^2}{2}-n\omega-\varepsilon_0^{(1)}\right). \tag{55}$$

For high $|\mathbf{p}|$, the magnitude $\left|a_{\mathbf{p},n}^{\text{ion}}\right|$ is very small. Still, in accordance with (55) and with the properties of the Bessel functions, we can expect the continuum states to be populated with a small but nonzero probability for all $|\mathbf{p}|$ up to

$$\frac{p_{\max}^2}{2} \approx n_{\max}\omega \approx \frac{F_0 p_{\max}}{\omega^2}\omega,$$

i.e., up to

$$p_{\max} \approx \frac{2F_0}{\omega}.$$

We now assume that the atom collides with a projectile having the velocity $-\mathbf{v}$. Because the ground state of the projectile can be represented by the continuum states of the target and the momentum of the ionized electron matches the momenta of the electron bound in the moving projectile, we see that if $p_{\max} \gtrsim v$, the atomic electron can finally be captured by the projectile as the result of ionization. It is now not difficult to see that using states (33) and (34) (or their counterparts in the rest frame of the target or in any other reference frame) and applying the post form with the interaction V_1 amounts to calculating the contribution to the electron transfer that is represented by the part of the target multiphoton ionization[4] where the final electron states in the continuum of the target match the ground state of the projectile. For $v \gg Z_2$, the high-energy continuum states with $\mathbf{p} \approx -\mathbf{v}$ can easily "cover" the ground state of any light projectile, independently of Z_2. Therefore, in applying the post form, we see that the capture cross section is almost independent of Z_2.

A similar analysis can also be performed for the contribution to the charge transfer described by the prior form of the transition amplitude. We consider a system consisting of a nucleus at rest (representing the projectile in its rest frame) and an incoming free electron moving in the presence of the electromagnetic field. The initial state of the electron with the momentum $\mathbf{q}$ is given by an expression similar to (54),

$$\psi_{\mathbf{q}}^{(2)} \propto \exp(i\mathbf{q}\cdot\mathbf{r})\sum_n J_n\left(\frac{\mathbf{F}_0\cdot\mathbf{q}}{\omega^2}\right)|N+n\rangle. \tag{56}$$

As a result of the collision with the nucleus, the electron can emit photons (the induced multiphoton bremsstrahlung) and undergo a transition to another state. One of the possible final states of the electron can be the ground state of the projectile, $\varphi_0^{(2)}$. The amplitude of this transition is given by

$$a_{\mathbf{q},n}^{br} \propto J_n\left(\frac{\mathbf{F}_0\cdot\mathbf{q}}{\omega^2}\right)\langle\varphi_0^{(2)}|V_2|e^{i\mathbf{q}\cdot\mathbf{r}}\rangle \times\delta\left(\frac{q^2}{2}-n\omega-\varepsilon_0^{(2)}\right). \tag{57}$$

Note that the state of the electron initially bound in the target moving with the velocity $\mathbf{v}$ in the rest frame of the projectile can be represented by a superposition of states given by Eq. (56). Taking that into account and comparing Eq. (57) with the transition amplitude in the prior form, Eqs. (35) and (36), we arrive at the following conclusion. Using states (33) and (34) (or their counterparts in any other reference frame) and applying the prior form with the interaction V_2 amounts to calculating the contribution to the electron transfer that is due to that part of the induced multiphoton bremsstrahlung of the electron, initially bound in the ground

---

[4] In the case under consideration, $F_0/\omega \gg 1$, we note that the ionization of an atom by a classical electromagnetic field with $F_0/\omega \gg 1$ can be viewed as a tunneling effect [14].

state of the target, where the final electron state is the ground state of the projectile.

The radiative electron capture that proceeds with a spontaneous emission of one high-energy photon is known to be weakly dependent on the charge of the target, Z_1, provided $Z_1 \ll v$, where v is the collision velocity [2]. According to our calculations, a similar situation is encountered in the case under consideration where the electron capture proceeds with the induced emission of a large amount of low-frequency photons.

Summarizing the above analysis, we can make the following important conclusions. First, for the field-assisted electron capture in the strong-coupling case, one can still use the approximate state vectors given by Eqs. (33) and (34) in order to describe the capture. Second, using these approximate states, one must keep in mind that the prior and post forms of the capture cross sections are drastically different in general. Third, this difference is related to the fact that in the adopted approximation for the dressed electron states, the prior and post forms describe the electron transfer due to different physical processes: the multiphoton ionization and the induced multiphoton bremsstrahlung. Fourth, the total cross section for the electron capture in the case of a strong coupling with the electromagnetic field can be evaluated as the sum of cross sections corresponding to different physical processes mentioned above,

$$\begin{aligned}\sigma_{\rm tot} &= \sum_{n<0}\sigma_{\rm post}^{(n)} + \sigma_0 + \sum_{n>0}\sigma_{\rm prior}^{(n)}\\ &\approx \sum_{n<0}\sigma_{\rm post}^{(n)} + \sum_{n>0}\sigma_{\rm prior}^{(n)},\end{aligned} \tag{58}$$

where $\sigma_{\rm prior}^{(n)}$ and $\sigma_{\rm post}^{(n)}$ are given by Eqs. (37) and (40), respectively, and describe the electron transfer due to the induced bremsstrahlung and photoionization, and

$$\sigma_0 = \sigma_{\rm prior}^{(0)} = \sigma_{\rm post}^{(0)} = J_0^2\left(\frac{|\mathbf{F}_0\cdot\mathbf{v}|}{\omega^2}\right)\sigma_{OBK1}$$

is negligible.

We have already mentioned that the problem of a large prior post discrepancy is also known in eikonal calculations for the field-free electron capture, where additional physical arguments must be used in order to decide which form should be applied. The same problem is encountered in first-order calculations for the electron capture in field-free collisions with multielectron targets. In the latter case, however, it is very difficult to decide which form should be given preference and sometimes one introduces the average transition amplitude

$$a_{if} = 0.5(a_{if}^{\rm prior} + a_{if}^{\rm post})$$

(see, e.g., [15]). This is different from the situation with the field-assisted collisions in the strong-coupling case, where one can argue that the post and prior forms correspond to different electron transfer channels that do not interfere and that the capture cross section must be evaluated in accordance with Eq. (58). One can add that because of the different dependences $\sigma_{\rm prior} \propto Z_2^5$ and $\sigma_{\rm post} \propto Z_1^5$, only one of these forms is of practical importance for calculations of the electron capture in asymmetric field-assisted collisions, where the ratio Z_2/Z_1 differs considerably from unity.

To conclude this discussion, we briefly compare our calculations for the electron transfer in collisions assisted by an external field to the radiative electron capture (REC) [11]. In the latter process, the resonance condition for the electron transfer $\omega_{sp} \sim v^2/2$ is satisfied due to a spontaneous emission of one high-energy photon and, naturally, the electron transfer with a photon absorption is not possible because there are no photons in the initial state of the free radiation field. In [11], the REC was considered as the collision-stimulated transitions between one-center electron states dressed by the interaction with the radiation field. It was found in [11] that the prior form of the REC cross section obtained within the approach that is obviously very similar to that employed here yields an excellent agreement with the well established results for the radiative capture cross section. However, the post form of the theory in [11] leads to REC cross sections that are smaller by many orders of magnitude. The reason is as follows. With the approximate one-center electron states dressed by the free radiation field as in [11], the prior and post forms are "responsible" (similarly to the present approach) for the electron transfer due to bremsstrahlung and photoionization, respectively. However, the coupling to the free radiation field, which can produce spontaneous bremsstranhlung, cannot result in photoionization.

4. CONCLUSIONS

The electron transfer process in fast collisions assisted by a relatively weak low-frequency electromagnetic field can represent an interesting example of an effectively strong coupling between the electron and the electromagnetic field. A key consequence of the strong electron-field coupling in the charge exchange collisions is the emission and absorption of a very large number of photons that can substantially improve the electron transfer kinematics under certain conditions.

The effect of a low-frequency electromagnetic field on the electron transfer process discussed in the present paper is closely related to some well-studied processes. We have already discussed the connection with the multiphoton ionization and the induced multiphoton bremsstrahlung. In addition, we now note the relation to a particular case of the induced bremsstrahlung–free electron–atom collisions in a laser field. Free electron-atom collisions assisted by the electromagnetic field were studied in some detail, mainly theoretically (see, e.g., [16] for a review). One of the conclusions of these studies that is relevant to the topic of the present paper is that the external electromagnetic field can substantially increase the magnitude of the scattering cross section if there are some quasi-stationary states that can be resonantly populated during the scattering via the stimulated emission or absorption of photons.

The present analysis suggests that the capture cross sections can be substantially influenced by the electromagnetic field. In addition, one can also expect the effect of the field to be reflected by noticeable changes in the spectra of high-energy photons that are spontaneously emitted during the radiative electron capture in field-assisted collisions.

ACKNOWLEDGMENTS

One of the authors (A. B. V.) acknowledges the support from the Deutsche Forschungsgemeinschaft (DFG) and the DFG Leibniz-Programm.

APPENDIX

To derive a suitable form of the nonrelativistic Schrödinger equation for the electron interacting with a quantized electromagnetic field, we start with the Dirac equation

$$\begin{aligned} i\frac{\partial}{\partial t}|\Psi\rangle &= c\boldsymbol{\alpha}\cdot\left(\hat{\mathbf{p}}-\frac{e}{c}\mathbf{A}\right)|\Psi\rangle + W|\Psi\rangle \\ &\quad + \beta m_e c^2|\Psi\rangle + \omega N_a|\Psi\rangle, \end{aligned} \tag{A.1}$$

where W describes the Coulomb interaction with the nuclei and $\boldsymbol{\alpha}$ and β are the Dirac matrices. Decomposing $|\Psi\rangle$ into major and minor components denoted by φ and χ respectively, we rewrite Eq. (A.1) as

$$\begin{aligned} \left(i\frac{\partial}{\partial t} - W - \omega N_a - m_e c^2\right)|\varphi\rangle &= c\boldsymbol{\sigma}\cdot\left(\hat{\mathbf{p}}-\frac{e}{c}\mathbf{A}\right)|\chi\rangle, \\ \left(i\frac{\partial}{\partial t} - W - \omega N_a + m_e c^2\right)|\chi\rangle &= c\boldsymbol{\sigma}\cdot\left(\hat{\mathbf{p}}-\frac{e}{c}\mathbf{A}\right)|\varphi\rangle, \end{aligned} \tag{A.2}$$

where $\boldsymbol{\sigma}$ are the Pauli spin matrices. A common way to derive the nonrelativistic equation from a relativistic one is to assume that all other energies in the system are much less than the electron rest energy $m_e c^2$. In our case, this assumption does not hold because, as simple estimates easily show, even for a very weak electromagnetic field occupying a macroscopic volume, its total energy is much larger than the electron rest energy. It is clear, however, that the relevant quantity is the amount of the electromagnetic energy that can be transferred between the electromagnetic field and the electron, rather than the total amount of the field energy. Making the ansatz

$$\begin{aligned} |\varphi\rangle &= \exp(-i(m_e c^2 + N\omega)t)|\varphi_1\rangle, \\ |\chi\rangle &= \exp(-i(m_e c^2 + N\omega)t)|\chi_1\rangle, \end{aligned} \tag{A.3}$$

where N is the initial number of photons in the quantum field, we remove the irrelevant part of the total field energy and obtain

$$\begin{aligned} \left(i\frac{\partial}{\partial t} - W - \omega(N_a - N)\right)|\varphi_1\rangle &= c\boldsymbol{\sigma}\cdot\left(\hat{\mathbf{p}}-\frac{e}{c}\mathbf{A}\right)|\chi_1\rangle, \\ \left(i\frac{\partial}{\partial t} - W - \omega(N_a - N) + 2m_e c^2\right)|\chi_1\rangle & \\ &= c\boldsymbol{\sigma}\cdot\left(\hat{\mathbf{p}}-\frac{e}{c}\mathbf{A}\right)|\varphi_1\rangle. \end{aligned} \tag{A.4}$$

Assuming that the energy transfer between the electromagnetic field and the electron is nonrelativistic,

$$\omega(N_a - N) \ll m_e c^2,$$

we can now approximate

$$|\chi_1\rangle = \frac{1}{2m_e c}\boldsymbol{\sigma}\cdot\left(\hat{\mathbf{p}}-\frac{e}{c}\mathbf{A}\right)|\varphi_1\rangle.$$

Inserting this expression into the first equation in (A.4) and neglecting the spin term, we obtain Schrödinger equation (1) for the major component.

REFERENCES

1. D. P. Dewangan and J. Eichler, Phys. Rep. **247**, 59 (1994).
2. J. Eichler and W. E. Meyerhof, *Relativistic Atomic Collisions* (Academic, San Diego, 1995).
3. S. K. Datta, N. Grün, and W. Scheid, Comments At. Mol. Phys. B **32**, 1 (1995).
4. R. Shakeshaft and L. Spruch, Rev. Mod. Phys. **51**, 369 (1979).
5. J. Eichler, Phys. Rep. **193**, 165 (1990).
6. W. Heitler, *The Quantum Theory of Radiation* (Clarendon Press, Oxford, 1954; Inostrannaya Literatura, 1956).
7. J. J. Sakurai, *Advanced Quantum Mechanics* (Addison-Wesley, Reading, 1967).

8. D.-S. Guo and T. Åberg, J. Phys. A **21**, 4577 (1988).
9. J. H. Eberly, J. Javanainen, and K. Rzazewski, Phys. Rep. **204**, 331 (1991).
10. M. Abramowitz and I. Stegun, *Handbook of Mathematical Functions* (Dover, New York, 1964; Nauka, Moscow, 1979).
11. A. B. Voitkiv and N. Grün, J. Phys. B **34**, 321 (2001).
12. M. R. C. McDowell and J. P. Coleman, *Introduction to the Theory of Ion–Atom Collisions* (North-Holland, Amsterdam, 1970).
13. *Tables of Higher Functions by Jahnke, Emde, and Lösch* Ed. by F. Lösch (Teubner, Stuttgart, 1960).
14. N. B. Delone and V. P. Krainov, *Multiphoton Processes in Atoms* (Springer-Verlag, Berlin, 2000).
15. D. Belkic and H. S. Taylor, Phys. Rev. A **35**, 1991 (1987).
16. F. Ehlotzky, A. Jaron, and J. Z. Kaminski, Phys. Rep. **297**, 63 (1998).
17. R. Loudon, *The Quantum Theory of Light* (Clarendon Press, Oxford, 1994).

Journal of Experimental and Theoretical Physics, Vol. 92, No. 5, 2001, pp. 766–770.
Translated from Zhurnal Éksperimental'noĭ i Teoreticheskoĭ Fiziki, Vol. 119, No. 5, 2001, pp. 881–885.
Original Russian Text Copyright © 2001 by Pravdin, Ivanov, Krasil'nikov, Mikhaĭlov, Sleptsov.

Analysis of Anisotropy of Cosmic Rays with the Energy of about 10^{17} eV by Yakutsk EAS Array Data

M. I. Pravdin*, A. A. Ivanov, A. D. Krasil'nikov, A. A. Mikhaĭlov, and I. E. Sleptsov

Institute of Cosmophysical Research and Aeronomy, Siberian Division, Russian Academy of Sciences,
pr. Lenina 31, Yakutsk, 677891 Russia
**e-mail: m.i.pravdin@ikfia.ysn.ru*

Received December 7, 2000

Abstract—A harmonic analysis of the directions of arrival of cosmic-ray particles with an energy of about 10^{17} eV in the vicinity of the registration threshold of the Yakutsk extensive air showers (EAS) array is given. A method for determining the contribution of inhomogeneous observation conditions and seasonal variations of the frequency of extensive air showers to the observed anisotropy is suggested. Taking into account these factors results in a considerable decrease of the amplitude characterizing the degree of anisotropy of cosmic-ray primaries. The amplitude of the first harmonic with respect to the right ascension is $(0.45 \pm 0.55)\%$, which shows that no probably significant anisotropy of the primary radiation is observed at 10^{17} eV. *© 2001 MAIK "Nauka/Interperiodica".*

1. INTRODUCTION

Determining the degree of anisotropy of the primary flux and its dependence on the energy E_0 is important for solving the problem of cosmic ray origin. At energies of 10^{17} eV or higher, the characteristics of the cosmic radiation are studied with the help of installations that register extensive air showers (EAS arrays) consisting of secondary particles generated when the primary particles with these energy enter the Earth's atmosphere. One of the main methods used to estimate the anisotropy on EAS arrays is the harmonic analysis of the distribution of the directions of the arrival of showers with respect to the right ascension [1]. In our previous work [2], we studied the data registered at the Yakutsk array [3] over the period 1982–1995 in the energy range of $3 \times 10^{16} < E_0 < 3 \times 10^{17}$ eV with respect to the right ascension and obtained a probably significant amplitude of the first harmonic $r_1 = (1.35 \pm 0.36)\%$ and the phase $\varphi_1 = 123° \pm 15°$. Earlier, in the study [4] performed on the Haverah Park EAS array in approximately the same range of energies, the value $r_1 = (1.7 \pm 0.4)\%$ was obtained; however, the phase $\varphi_1 = 218° \pm 14°$ is considerably different from the results obtained in [2]. It is seen from these data that the amplitude observed is small for this energy, and one must take into account the contribution of the equipment and the atmospheric conditions in order to estimate the true anisotropy of cosmic rays. In our previous work [2], we did not analyze the effect of seasonal changes of the atmospheric conditions.

In the process of the long-term operation of the EAS array, the registration of events is sometimes interrupted due to technical and technological reasons; in addition, the effective area of event registration can vary due to the temporal failure of certain detectors. This can result in an inhomogeneous sky survey at different time instants of both the solar and sidereal day. In addition, for the Yakutsk and similar arrays, the energy $E_0 \approx 10^{17}$ eV is the threshold one and atmospheric conditions, which have diurnal and seasonal variations, influence the frequency of the shower event registration. Since the direction survey conditions at different right ascensions depend on time (if the array is not on a pole), the inhomogeneity of the sky survey and variation of the atmospheric conditions can make a considerable contribution to measurements, which distorts the true anisotropy of the primary radiation. The degree of influence on the results of the analysis can be different in different experiments; it depends on a variety of factors, such as climatic conditions, the design of the trigger array (its effective area depends on temperature and pressure), criteria of event selection, possible systematic errors in determining the parameters and energy of showers under various atmospheric conditions, and the frequency of short-term switching off of the array at some moments of the day. For illustration purposes, Fig. 1 presents the calculation results of the dependence of the ratio of the first harmonic amplitude for the right ascension to the amplitude for sidereal time on the maximal zenith angle of the events at the latitude of the Yakutsk array. This dependence is an artifact arising due to observation conditions. It was assumed in the calculation that the showers registered are uniformly distributed over the sphere.

In order to investigate the anisotropy of cosmic rays by the data obtained on installations that do not measure the direction of arrival of individual events ($E_0 < 10^{14}$ eV), the distribution in sidereal time is analyzed. To take into account the influence of the variations caused by diurnal and seasonal cycles on the frequency of the events, the distribution of the same events in "antisidereal" time is analyzed using the method suggested in [5]. The same method can be also applied for the analysis of air showers when the direction of arrival is determined with poor accuracy or is not determined at all because of fluctuations of the time of arrival of different particles of the shower, which is the case in the vicinity of the registration threshold. At the same time, the data on the contribution of seasonal variations determined for antisidereal time can be used to estimate the degree of distortion of the anisotropy vector with respect to the right ascension. In this study, we use the analysis by sidereal time for the data obtained on the Yakutsk EAS array in the vicinity of $E = 10^{17}$ eV and compare the results with those obtained with respect to the right ascension for the same sample. In the process, we analyze how the factors mentioned above (inhomogeneous sky survey and atmospheric variations) affect the results obtained.

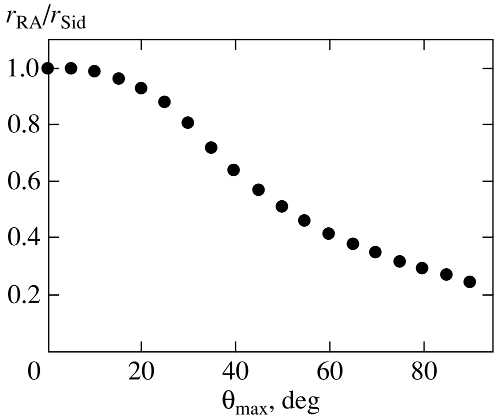

Fig. 1. Dependence of the ratio of the amplitude for the right ascension r_{RA} to the amplitude for sidereal time r_{Sid}, which is of artificial origin, on the maximal zenith angle θ_{max} for the events used in the analysis for the latitude of the Yakutsk EAS array. It was assumed in the calculation that the showers registered are uniformly distributed over the sphere.

2. SELECTION OF EVENTS

The Yakutsk EAS array selects a shower when an event is registered simultaneously by three neighboring stations forming a triangle. The selection scheme is based on two types of station configurations. The first one consists of stations located at the nodes of a triangular grid with a side of 500 m (Trigger-500); the other one is similar, but the side is 1000 m (Trigger-1000). In the first case, the registration threshold corresponds to showers with the energy of $(3–5) \times 10^{16}$ eV; in the second case, the energy is about 10^{18}. The data obtained is stored in primary storage devices, different at different periods of time. Until summer 1995, the data was stored in a working database after some preliminary processing. The data was stored in the database if the density of the shower particles on three stations exceeded a certain threshold. The selection criteria were slightly different at different periods of time. Since autumn 1982 until summer 1995, the threshold density was set to 0.8 m^{-2} (more than three particles per the entire area of the counters at the station). Beginning with summer 1995, the processing and storage are organized in such a way that all registered events can be used for the analysis.

In this paper, as well as in the previous one [2], we analyze the data obtained during the period from 1982 to 1995 in the range of energies from 3×10^{16} eV to 3×10^{17} eV with the azimuth angle $\theta < 60°$ that satisfied the uniform criteria, i.e., if three stations registered the event with a density more than 0.8 m^{-2}. For every year, the data obtained within the period November–May were analyzed. However, in contrast to [2], for each period the effective area of the array was used, which was determined by reliably operating observation stations. From the entire array of data, these criteria are satisfied by 135 566 events, which is 10% less than in [2]. The average energy of the showers selected is 1.6×10^{17} eV (the most frequently registered energy is 10^{17} eV); the average zenith angle is 24.2°. For this sample, the harmonic analysis of the distribution of events was performed with respect to solar, sidereal, and antisidereal time, as well as with respect to the right ascension.

3. TAKING INTO ACCOUNT INHOMOGENEITY OF THE SKY SURVEY

Most often, the array is switched off due to technical and technological reasons in the daytime; thus, these periods of time are inhomogeneously distributed across the day. The inhomogeneity of sky survey is also affected by variations of the effective area caused by temporary failure of certain observation stations. At the Yakutsk EAS array, a list of time moments at which registration was switched off and on is maintained, and information on stations actually operating at every instance of time is registered. Any change in the configuration of the trigger system is fixed as the beginning of a new period even if the array was not switched off. For showers registered in the vicinity of the threshold, the effective area is proportional to the number of triangles in the trigger-500 that actually register the events. In order to determine the degree of relative inhomogeneity of the sky survey over the whole period of observation, the total number of operating trigger triangles was counted for every minute of each day. The values obtained were normalized by the average value over all minutes. For the same periods with respect to solar time, similar distributions over minutes with respect to sidereal and antisidereal time can be easily obtained.

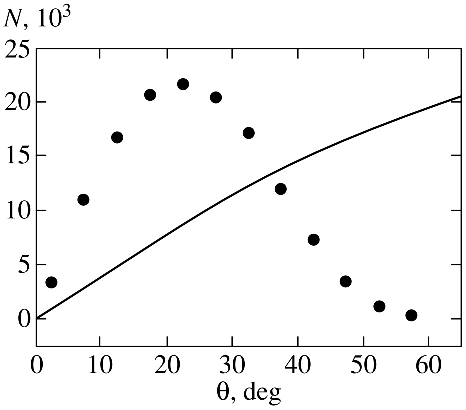

Fig. 2. Distribution of the showers in the sample under study over the zenith angle θ. The solid curve corresponds to the uniform distribution over the celestial sphere.

Inhomogeneity of the sky survey results in different observation conditions for different magnitudes of the right ascension, which depend on the distribution of the events over the zenith angle and the latitude of the array. In order to determine the sky observation conditions with respect to the right ascension, we determined the zenith–angular distribution of the showers. It is presented in Fig. 2. The contribution to the narrow interval of the RA from the part of the sky that is visible by the array at the fixed zenith angle θ at the fixed value of the sidereal time t_S is proportional to the number of events in the zenith–angular distribution of the showers multiplied by the value corresponding to t_S in the relative distribution of the sky survey with respect to the sidereal time. In order to obtain the complete distribution of the sky survey, these contributions were summed over all azimuth angles from 0 to 2π (assuming that they are distributed uniformly), as well as over all θ and t_S.

To take into account the inhomogeneity of the sky survey when determining the anisotropy vector parameters, the number of events in a certain minute-long interval or right ascension was normalized by the corresponding value in the relative distribution of the observation conditions.

The first two columns of Table 1 present the parameters of the vectors of the first harmonic characterizing the relative distributions of the observation conditions for different variables obtained for the operational periods of the array over the entire period of the sample analyzed. It is seen that the inhomogeneity is rather large, and the amplitude is 1.74% even for the right ascension. If the same distributions are considered for separate years, variations both in the amplitude and phase are observed. In different years, the number of trigger triangles was different; thus, we use individual corrections for every year in the subsequent analysis.

Table 1. Parameters of the first harmonic for various vectors (in total, 135566 events)

Vector	Sky survey conditions		Distribution of events			
			Without regard to survey		With regard to survey	
	r, %	φ, h	r, %	φ, h	r, %	φ, h
Solar	4.05	22.78	6.92 ± 0.39	22.75 ± 0.22	2.72 ± 0.39	22.48 ± 0.55
Sidereal	2.30	8.98	3.93 ± 0.39	9.00 ± 0.38	1.62 ± 0.39	10.40 ± 0.92
Antisidereal	2.15	13.34	3.50 ± 0.39	12.44 ± 0.43	1.41 ± 0.39	10.82 ± 1.06
RA	1.74	8.11	2.89 ± 0.39	9.35 ± 0.52	1.36 ± 0.39	10.97 ± 1.10
Sidereal–**VAR**			0.43 ± 0.55	8.51 ± 4.89	0.24 ± 0.55	11.96 ± 8.75
RA–**VAR**(RA)					0.45 ± 0.55	12.79 ± 4.67

Table 2. Variation of the parameters of the first harmonic for various vectors in different seasons

Months	Number of events	Solar vector			Sidereal vector		Vector with respect to right accension	
		r, %	φ, h	φ_S, h	r, %	φ, h	r, %	φ, h
11	14832	5.20	21.35	1.0	4.93	1.12	2.60	1.40
12–01	37605	1.78	1.18	7.9	2.00	8.17	1.12	6.08
02–03	40039	3.15	22.09	8.7	2.72	9.16	2.21	10.12
04–05	43090	3.07	22.66	13.3	3.02	13.03	2.83	12.74

4. RESULTS OF THE ANALYSIS

The amplitudes (r) in percent and phases (φ) in hours for the vectors of the first harmonic with respect to the solar, sidereal, and antisidereal time, and the right ascension are presented in Table 1 both with and without regard to the inhomogeneity of the sky survey. These data show that, first, the inhomogeneity of observation conditions is considerably different for different time intervals of the day ($\simeq 4\%$), and the amplitude of all variables substantially decreases when the inhomogeneity is taken into account. Second, even with regard to the inhomogeneity, a significant anisotropy with the amplitude $(2.72 \pm 0.39)\%$ with respect to the solar time remains, as well as a substantial influence of seasonal variations, which is seen from the amplitude of the antisidereal vector $(1.41 \pm 0.39)\%$.

We denote the vector that appears due to seasonal variations and contributes to the result observed with respect to the sidereal time by **VAR**. It is mirror symmetric to the antisidereal vector with respect to the solar one; i.e., it equals the antisidereal vector in absolute value and has the phase

$$2\varphi_{\mathrm{Sol}} - \varphi_{\mathrm{Anti}},$$

where φ_{Sol} is the phase of the solar vector and φ_{Anti} is the phase of the antisidereal vector. The next to last row in Table 1 shows an estimate of the anisotropy of the primary radiation after subtracting the vector **VAR**. The amplitude obtained is less than σ both with and without regard to the inhomogeneity of the sky survey. Figure 3 shows the anisotropy vectors obtained with regard to the influence of the inhomogeneity of the sky survey.

The contribution of seasonal variations to the summary vector with respect to the right ascension **VAR**(RA) can be estimated similarly to the calculation of the relative distribution of the sky survey with respect to the right ascension. The calculation is based on the same experimental distribution of the showers over the zenith angle, and the weight of the inhomogeneity with respect to sidereal time at the instance t_{S} is specified on the basis of the parameters obtained for the vector **VAR**. The last row of Table 1 shows the results for the right ascension obtained after subtracting the calculated atmospheric component. The amplitude is less than σ, as is the case in the analysis with respect to sidereal time.

In addition, we performed a similar analysis of the same sample for certain months of the year. The results are presented in Table 2, where the observed parameters are given with regard to the inhomogeneity of the sky survey. In the column φ_{S}, the phase in terms of the sidereal time is given for the solar vector, which corresponds to the solar phase at the middle of the season. It is seen from this table that both the phase of the sidereal vector and the one with respect to the right ascension for different seasons vary with variation of the solar vector direction in celestial coordinates. This fact confirms that the main contribution to the amplitude with respect to the right ascension is caused by seasonal variations of atmospheric origin. After all the relevant factors are taken into account, no statistically significant anisotropy of the primary radiation at the energy of 10^{17} eV is observed for the sample under study. In our previous work [2], we did not take into account the contribution of the atmospheric variations, which is responsible for the significant amplitude obtained.

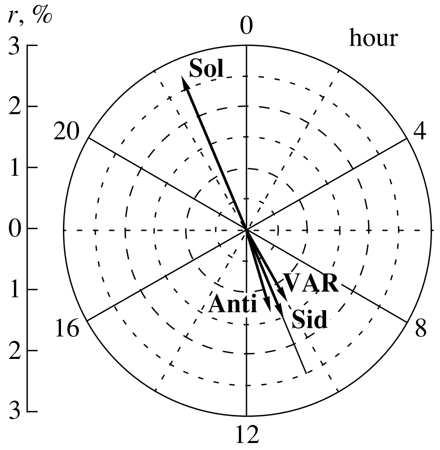

Fig. 3. Mutual location of the anisotropy vectors for various variables: **Sol** is the solar vector; **Sid** is the sidereal vector; **Anti** is the antisidereal vector; and **VAR** is the contribution of the atmospheric variations to **Sid**.

At the present time, we are revising the list of operational periods of the Yakutsk EAS array for recent years and are restoring all the data registered up to 1995 that were not written to the working database because of the selection criteria. This will enable us to continue the detailed analysis of the complete data array containing records of more than 10^6 events. The results can be used to estimate the anisotropy of the primary radiation with energy of about 10^{17} eV.

5. CONCLUSIONS

The results obtained in this study show that the inhomogeneity of the sky survey must be taken into account when analyzing data with the purpose of estimating the anisotropy of the primary radiation. The inhomogeneity arises due to short-term switching off of the array and variations of its effective area. In addition, seasonal variations of the frequency of events of atmospheric origin make a contribution to the vector observed with respect to the right ascension. This contribution can be estimated by the vector with respect to antisidereal time and the zenith–angular distribution of the showers. As a result, it is estimated that the amplitude of the first harmonic with respect to the right ascension with regard to the perturbing factors is $(0.45 \pm 0.55)\%$. Thus, the true anisotropy of the primary radiation at the energy 10^{17} eV is less than 1.25%

with a probability of 0.95, judging by the data obtained at the Yakutsk EAS array.

ACKNOWLEDGMENTS

This work was supported by the Russian Foundation for Basic Research, project nos. 98-02-17725 and 00-15-96787.

REFERENCES

1. J. Linsley, Phys. Rev. Lett. **34**, 1530 (1975).
2. A. A. Mikhaĭlov and M. I. Pravdin, Pis'ma Zh. Éksp. Teor. Fiz. **66**, 293 (1997) [JETP Lett. **66**, 305 (1997)].
3. V. P. Artamonov, B. N. Afanas'ev, A. V. Glushkov, *et al.*, Izv. Akad. Nauk, Ser. Fiz. **58**, 92 (1994).
4. R. N. Coy, J. Lloyd-Evans, M. Patel, *et al.*, in *Proceedings of the 17th International Cosmic Ray Conference, Paris, 1981*, Vol. 9, p. 183.
5. F. J. Farley and J. R. Storey, Proc. Phys. Soc. London, Sect. A **67**, 996 (1954).

Translated by A. Klimontovich

Journal of Experimental and Theoretical Physics, Vol. 92, No. 5, 2001, pp. 771–776.
Translated from Zhurnal Éksperimental’noĭ i Teoreticheskoĭ Fiziki, Vol. 119, No. 5, 2001, pp. 886–892.
Original Russian Text Copyright © 2001 by Semenova, Prokhorov.

ATOMS, SPECTRA, RADIATION

Raman Scattering of Light by 2*LO*-Phonons

L. E. Semenova* and K. A. Prokhorov
General Physics Institute, Russian Academy of Sciences, Moscow, 117942 Russia
**e-mail: semenov@sci.lebedev.ru*

Received November 17, 2000

Abstract—A theory of resonance Raman scattering of light by 2*LO*-phonons in semiconductor crystals is presented. Wannier excitons are considered as intermediate states. Analytic expressions are obtained that take into account contributions from different chains of intermediate states. The scattering cross section is shown to be weakly dependent on the wave vector imparted to the phonon system. The theoretical model permits the calculation of the scattering cross section for the energy of the exciting radiation photon below the level of exciton resonances. *© 2001 MAIK “Nauka/Interperiodica”.*

1. INTRODUCTION

The study of resonance Raman scattering near the edge of fundamental absorption of a crystal is of considerable interest because the scattering spectrum exhibits a number of specific features. One of these features is the alternating change in the scattering cross section with increasing number of phonons excited in a CdS crystal [1, 2]. In this case, the fourth-order lines dominate in the spectrum. This feature was explained in paper [1] within the framework of a theoretical model that considered excitons as intermediate states. The interaction of excitons with phonons was treated using the mechanism of the intraband Frölich electron–phonon interaction. According to this model, the microscopic mechanism of Raman scattering accompanied by emission of *n* phonons can be described by the following sequence of processes: (1) Absorption of a photon of exciting radiation accompanied by the transition of the electronic system to the excited state; (2) transition between excitonic states accompanied by emission of *n* phonons; (3) emission of a photon of scattered light and return of the electronic system to the ground state. An irregular nature of line intensities in Raman spectra is caused by different alternation of intermediate states of the *s* and *p* types. This follows from the expansion of the matrix element of the Frölich interaction in the phonon wave vector $\mathbf{q}_p$:

$$F_{\lambda'\lambda} \propto \langle\chi^{\lambda'}_{cv}|\hat{q}_p\mathbf{r}|\chi^{\lambda}_{cv}\rangle + \frac{i}{2q_p}\frac{m_e^* - m_h^*}{m_e^* + m_h^*} \times \langle\chi^{\lambda'}_{cv}|(\mathbf{q}_p\cdot\mathbf{r})^2|\chi^{\lambda}_{cv}\rangle + \ldots, \qquad (1)$$

where $\hat{q}_p$ is the unit vector in the direction of the phonon wave vector; m_e^* and m_h^* are the effective masses of an electron and a hole, respectively; $\chi^{\lambda}_{cv}(r)$ is the hydrogen wave function; and λ denotes a set of quantum numbers characterizing the relative electron–hole motion. The first nonvanishing term, which corresponds to the dipole approximation, describes transitions between the *s* and *p* excitonic states. Transitions between the *s* states correspond to the second (quadrupole) term in expansion (1). Because the dipole transition from the ground state is allowed only to the *s* excitonic state, the odd orders necessarily include the process of scattering of the same parity (*s*–*s* for 1*LO* and *s*–*p*–*s*–*s* for 3*LO)* into the chain of the intermediate states. Therefore, the scattering cross section for such processes contains a factor that, in the case of close values of the effective masses of an electron and a hole, leads to an irregular distribution of the intensities of multiphonon lines.

Multiphonon Raman scattering has been studied in papers [1, 3–5]. However, at present a theory of multiphonon scattering of light that takes into account excitonic effects is absent. In this paper, we propose a theoretical model of Raman scattering of light by 2*LO*-phonons for the energy of an incident photon lying near the exciton levels.

2. THEORY

2.1 Matrix Elements

The probability of two-photon Raman scattering of light is described in the fourth order of the perturbation theory by the expression [6]

$$W^{RS}_{2LO} = \frac{2\pi}{\hbar^2}\sum_f\left|\sum_{a,\,b,\,c}\frac{\langle f|\hat{H}_{ER}|c\rangle\langle c|\hat{H}_{EL}|b\rangle\langle b|\hat{H}_{EL}|a\rangle\langle a|\hat{H}_{ER}|i\rangle}{(E_c-\hbar\omega_S)(E_b+\hbar\omega_p-\hbar\omega_L)(E_a-\hbar\omega_L)}\right|^2\delta(\omega_L-\omega_S-2\omega_p), \qquad (2)$$

1063-7761/01/9205-0771$21.00 © 2001 MAIK “Nauka/Interperiodica”

where $|i\rangle$ and $|f\rangle$ are the initial and final states, respectively; $|a\rangle$, $|b\rangle$, and $|c\rangle$ are the intermediate virtual states; ω_L, ω_S, and ω_p are the frequencies of exciting radiation, scattered light, and lattice phonons, respectively; and $\hat{H}_{ER}$ and $\hat{H}_{EL}$ are Hamiltonians of the electron–photon and electron–phonon interactions. In the case of resonance Raman scattering, the frequencies of exciting radiation and scattered light are close to the energy gap, so that the process of scattering can be treated within the framework of a two-band model.

Considering Wannier excitons as the intermediate virtual states of an electron system, we will write the matrix element of transition from the ground state to an exciton state upon absorption of a photon in the dipole approximation [7]

$$\langle a|\hat{H}_{ER}|i\rangle = \frac{e}{mn_L}\sqrt{\frac{2\pi\hbar}{\omega_L}} \times N_L^{1/2}(2\pi)^{3/2}\hat{\varepsilon}_\alpha^L\pi_{cv}^\alpha\chi_{cv}^{\lambda_a *}(0)\delta(\mathbf{K}_a-\mathbf{q}_L), \tag{3}$$

where e and m are the charge and mass of an electron; $\hat{\varepsilon}_L$, $\mathbf{q}_L$, and N_L are polarization, the wave vector, and the density of exciting photons; n_L is the refractive index; $\mathbf{K}_a$ is the wave vector of an exciton; and π_{cv} is the interband matrix element of the electron momentum operator. Hereafter, the subscripts L and S correspond to exciting radiation and scattered light. One can see from expression (3) that the dipole transition is allowed only to the s excitonic state.

A matrix element of the intraband Frölich exciton–phonon interaction has the form [1, 8]

$$\langle b|\hat{H}_{EL}|a\rangle = \gamma_F V^{-1/2}(n_p+1)^{1/2}\delta(\mathbf{K}_b+\mathbf{q}_p-\mathbf{K}_a)P_{\lambda_b\lambda_a}(\mathbf{q}_p), \tag{4}$$

where

$$P_{\lambda_b\lambda_a}(\mathbf{q}_p) = \left\langle \chi_{cv}^{\lambda_b}\middle| iq_p^{-1}(\exp(-i\alpha_e\mathbf{q}_p\cdot\mathbf{r})-\exp(i\alpha_h\mathbf{q}_p\cdot\mathbf{r}))\middle|\chi_{cv}^{\lambda_a}\right\rangle, \tag{5}$$

$$\gamma_F = e\sqrt{2\pi\hbar\omega_p(\varepsilon_\infty^{-1}-\varepsilon_0^{-1})}. \tag{6}$$

Here, ε_∞ and ε_0 are the high-frequency and low-frequency dielectric constants; V is the crystal volume; and n_p is the number of phonons. The parameter $\alpha_{e(h)}$ is defined as $\alpha_{e(h)} = m_{h(e)}^*/(m_h^*+m_e^*)$.

By inserting matrix elements (3) and (4) into (2) and replacing sums over the phonon wave vectors by integrals, we obtain [1, 9]

$$W_{2LO}^{RS} = \frac{e^4N_L(n_p+1)^2}{2m^4n_L^2n_S^2\omega_L\omega_S}\int\left|\hat{\varepsilon}_\alpha^L\hat{\varepsilon}_\beta^S\gamma_F^2\pi_{cv}^\alpha\pi_{vc}^\beta\{\alpha(\mathbf{q}_p,\mathbf{q}_L-\mathbf{q}_S-\mathbf{q}_p)+\alpha(\mathbf{q}_L-\mathbf{q}_S-\mathbf{q}_p,\mathbf{q}_p)\}\right|^2\delta(\omega_L-\omega_S-2\omega_p)d\mathbf{q}_p, \tag{7}$$

where

$$\alpha(\mathbf{q},\mathbf{q}') = \sum_{\lambda_1,\lambda_2,\lambda_3}\frac{\chi_{cv}^{\lambda_3}(0)\left\langle\chi_{cv}^{\lambda_3}\middle|\frac{i}{q'}(\exp(-i\alpha_e\mathbf{q}'\cdot\mathbf{r})-\exp(i\alpha_h\mathbf{q}'\cdot\mathbf{r}))\middle|\chi_{cv}^{\lambda_2}\right\rangle}{(E_{\lambda_3}-\hbar\omega_S)\left(E_{\lambda_2}+\frac{\hbar^2q^2}{2M}+\hbar\omega_p-\hbar\omega_L\right)} \times\left\langle\chi_{cv}^{\lambda_2}\middle|\frac{i}{q}(\exp(-i\alpha_e\mathbf{q}\cdot\mathbf{r})-\exp(i\alpha_h\mathbf{q}\cdot\mathbf{r}))\middle|\chi_{cv}^{\lambda_1}\right\rangle\chi_{cv}^{\lambda_1 *}(0)(E_{\lambda_1}-\hbar\omega_L)^{-1}. \tag{8}$$

Here, $M = m_e^* + m_h^*$.

2.2 Green Function Method

In calculating $\alpha(\mathbf{q}, \mathbf{q}')$, the summation over all the intermediate excitonic states of the discrete and continuous spectra involves significant difficulties. If the exciting radiation frequency is lower than the excitonic resonance frequency ($E_{1S} > \hbar\omega_L$), this problem can be solved using the Green function method [10, 11]. In this case, the sum over all the intermediate s-excitonic states can be written as [11]

$$\sum_\lambda\frac{\chi_{cv}^\lambda(\mathbf{r})\chi_{cv}^{\lambda *}(0)}{E_\lambda-\hbar\omega} = \frac{\mu}{2\pi\hbar^2r}\Gamma(1-\kappa)W_{\kappa,1/2}\left(\frac{2r}{\kappa a}\right), \tag{9}$$

where μ is the reduced mass of an exciton ($\mu^{-1} = m_e^{*-1} + m_h^{*-1}$); $\Gamma(z)$ is the gamma function; $W_{\kappa,1/2}(z)$ is the Whittaker function; $\kappa = \sqrt{R/(E_g-\hbar\omega)}$; R and a are the exciton binding energy and its Bohr radius; and E_g is the energy gap. Using the Green method, we calculate the function

$$f_\lambda(\mathbf{q}) = \sum_{\lambda_3} \frac{\chi_{cv}^{\lambda_3}(0)\left\langle \chi_{cv}^{\lambda_3}\middle| iq^{-1}(\exp(-i\alpha_e\mathbf{q}\cdot\mathbf{r}) - \exp(i\alpha_h\mathbf{q}\cdot\mathbf{r}))\middle|\chi_{cv}^{\lambda}\right\rangle}{E_{\lambda_3} - \hbar\omega_S}. \tag{10}$$

Taking into account (9), expression (10) assumes the form

$$f_\lambda(\mathbf{q}) = i\frac{\mu}{2\pi q\hbar^2}\Gamma(1-\kappa_S)\int\chi_{cv}^{\lambda}(\mathbf{r})(\exp(-i\alpha_e\mathbf{q}\cdot\mathbf{r}) - \exp(i\alpha_h\mathbf{q}\cdot\mathbf{r}))W_{\kappa_S,1/2}\left(\frac{2r}{\kappa_S a}\right)\frac{d\mathbf{r}}{r}. \tag{11}$$

We will calculate the integral (11) by using the expansion of a plane wave in spherical functions [12]:

$$e^{i\mathbf{q}\cdot\mathbf{r}} = 4\pi\sum_{l=0}^{\infty}\sum_{m=-l}^{l} i^l j_l(qr)Y_{lm}(\vartheta_q,\varphi_q)Y_{lm}^*(\vartheta,\varphi), \tag{12}$$

where $j_l(z)$ is a spherical Bessel function and $Y_{lm}(\vartheta,\varphi)$ ($Y_{lm}(\vartheta_q,\varphi_q)$) is a spherical function of the polar angle and azimuth of direction of the vector $\mathbf{r}(\mathbf{q})$ with respect to a fixed coordinate system. Then, we will write the wave function of the relative electron–hole motion as $\chi_{cv}^{\lambda}(\mathbf{r}) = Y_{lm}(\vartheta,\varphi)R_\lambda(r)$ [12] and, taking into account the orthogonality of the spherical functions

$$\int_0^{2\pi}\int_0^{\pi} Y_{lm}^*(\vartheta,\varphi)Y_{l',m'}(\vartheta,\varphi)\sin\vartheta\, d\varphi\, d\vartheta = \delta_{ll'}\delta_{mm'}, \tag{13}$$

we will find the integral over angular variables

$$f_\lambda(\mathbf{q}) = i^{l+1}\frac{2\mu}{\hbar^2 q}\Gamma(1-\kappa_S)Y_{lm}(\vartheta_q,\varphi_q) \times\int_0^{\infty}W_{\kappa_S,1/2}\left(\frac{2r}{\kappa_S a}\right)R_\lambda(r)\{(-1)^l j_l(\alpha_e qr) - j_l(\alpha_h qr)\}r\,dr. \tag{14}$$

By inserting the radial functions

$$R_{nl}(\rho) = \frac{2}{\sqrt{a^3}n^{l+2}(2l+1)!}\sqrt{\frac{(n+l)!}{(n-l-1)!}}(2\rho)^l \times\exp\left(-\frac{\rho}{n}\right)F\left(-n+l+1, 2l+2, \frac{2\rho}{n}\right) \tag{15}$$

and

$$R_{kl}(\rho) = \frac{2k\exp(\pi/2k)\left|\Gamma(l+1-ik^{-1})\right|}{\sqrt{V}(2l+1)!}(2k\rho)^l \times\exp(-ik\rho)F\left(\frac{i}{k}+l+1, 2l+2, 2ik\rho\right) \tag{16}$$

for the discrete and continuous parts of the spectrum ($\rho = r/a$) [12], we obtain

$$f_\lambda(\mathbf{q}) = i^{l+1}\frac{2\mu}{\hbar^2 q}\Gamma(1-\kappa_S)\frac{Y_{lm}(\vartheta_q,\varphi_q)}{(2l+1)!}\sqrt{a}\begin{cases} C_n\{(-1)^l A_l(n,\alpha_e qa) - A_l(n,\alpha_h qa)\}, & \lambda = (nlm), \\ C_k\left\{(-1)^l A_l\left(\frac{i}{k},\alpha_e qa\right) - A_l\left(\frac{i}{k},\alpha_h qa\right)\right\}, & \lambda = (klm), \end{cases} \tag{17}$$

where

$$A_l(n,Q) = \int_0^{\infty}\exp\left(-\frac{\rho}{n}\right)F\left(-n+l+1, 2l+2, \frac{2\rho}{n}\right) \times W_{\kappa_S,1/2}\left(\frac{2\rho}{\kappa_S}\right)j_l(Q\rho)\rho^{l+1}d\rho, \tag{18}$$

$$C_n = \frac{2^{l+1}}{n^{l+2}}\sqrt{\frac{(n+l)!}{(n-l-1)!}}, \tag{19}$$

$$C_k = \sqrt{\frac{a^3}{V}}(2k)^{l+1}\exp\left(\frac{\pi}{2k}\right)\left|\Gamma\left(l+1-\frac{i}{k}\right)\right|. \tag{20}$$

We calculated integral (18) using the relation

$$j_l(z) = \frac{1}{z}\sum_{\nu=0}^{l}\frac{(l+\nu)!}{\nu!(l-\nu)!}\frac{1}{(2z)^\nu}\mathrm{Re}(i^{l+1-\nu}e^{-iz}) \tag{21}$$

for the Bessel function [13] and the integral representation of the Whittaker function [14],

$$W_{\kappa,1/2}(z) = \frac{ze^{-z/2}}{\Gamma(1-\kappa)}\int_0^{\infty}e^{-zt}\left(\frac{1+t}{t}\right)^{\kappa}dt. \tag{22}$$

By inserting expressions (21) and (22) into (18) and taking into account that the Laplace transform for a hypergeometric function has the form [14}

$$\int_0^{\infty}e^{-sp}F(a,c;k\rho)\rho^{b-1}\,d\rho = \frac{\Gamma(b)}{s^b}F\left(a,b;c;\frac{k}{s}\right), \tag{23}$$

we obtain

$$A_l(n,Q) = \frac{2\kappa_S^4}{Q^{l+1}\Gamma(1-\kappa_S)}I_l(Q,\kappa_S,n), \tag{24}$$

where

$$I_l(Q, \kappa_S, n) = \frac{1}{2^{l+2}\kappa_S^3}$$
$$\times \sum_{\nu=0}^{l} \frac{(l+\nu)!}{\nu!}(l+1-\nu)(\kappa_S Q)^{l-\nu} \operatorname{Re}\left\{ i^{l+1-\nu} \int_0^{\infty} \left(\frac{1+t}{t}\right)^{\kappa_S} \left[t + \frac{1}{2} + \frac{\kappa_S}{2n} + i\frac{\kappa_S Q}{2}\right]^{-l-2+\nu} \right. \tag{25}$$
$$\left. \times F\left(-n+l+1, l+2-\nu; 2l+2; \frac{\kappa_S n^{-1}}{t + \frac{1}{2} + \frac{\kappa_S}{2n} + i\frac{\kappa_S Q}{2}}\right) dt \right\}.$$

Thus, the function $f_\lambda(q)$ has the form

$$f_\lambda(\mathbf{q}) = \frac{\kappa_S^4}{R\sqrt{a}} \frac{Y_{lm}(\vartheta_q, \varphi_q)}{(2l+1)!} \begin{cases} \dfrac{2^{l+2}}{n^{l+2}} \sqrt{\dfrac{(n+l)!}{(n-l-1)!}} J_l(Q, \kappa_S, n), & \lambda = (nlm), \\ \sqrt{\dfrac{a^3}{V}} 2^{l+2} k^{l+1} \exp\left(\dfrac{\pi}{k}\right) \left|\Gamma\left(l+1-\dfrac{i}{k}\right)\right| J_l\left(Q, \kappa_S, \dfrac{i}{k}\right), & \lambda = (klm), \end{cases} \tag{26}$$

where

$$J_l(Q, \kappa_S, n) = \frac{i^{l+1}}{Q} \left\{ (-1)^l \frac{I_l(\alpha_e Q, \kappa_S, n)}{(\alpha_e Q)^{l+1}} - \frac{I_l(\alpha_h Q, \kappa_S, n)}{(\alpha_h Q)^{l+1}} \right\}. \tag{27}$$

2.3 Scattering Cross Section

Taking the results obtained above, we rewrite expression (8) in the form

$$\alpha(\mathbf{q}, \mathbf{q}') = \frac{4\kappa_S^4 \kappa_L^4}{\pi R^3 a} \sum_l P_l(\cos\gamma) \alpha_l(qa, q'a), \tag{28}$$

$$\alpha_l(Q, Q') = \frac{2^{2l}}{(2l+1)!(2l)!} \left\{ \sum_n \frac{(n+l)!}{(n-l-1)! n^{2l+4}} \frac{J_l(Q', \kappa_S, n) J_l(Q, \kappa_L, n)}{\eta(\omega_L, Q) - n^{-2}} \right.$$
$$\left. + \int \left| \frac{k}{1 - \exp(-2\pi/k)} \right| \prod_{s=1}^{l} (s^2 k^2 + 1) \frac{J_l(Q', \kappa_S, ik^{-1}) J_l(Q, \kappa_L, ik^{-1})}{\eta(\omega_L, Q) + k^2} dk \right\}, \tag{29}$$

where $\eta(\omega_L, Q) = R^{-1}(E_g + \hbar^2 Q^2/2Ma^2 + \hbar\omega_p - \hbar\omega_L)$, $Q = qa$, and $P_l((\mathbf{q}' \cdot \mathbf{q})/q'q)$ is the Legendre polynomial. One can see from (29) that $l = 0$ corresponds to a chain of intermediate states *s*-*s*–*s*, $l = 1$ corresponds to the chain *s*–*p*–*s*, etc.

The differential cross section for two-photon Raman scattering can be written in this case as

$$\frac{d\sigma}{d\Omega} = \frac{e^4 n_S \omega_S [n_p + 1]^2 V}{\pi^5 m^4 c^4 a^5 n_L \omega_L} \iint \left| C\kappa_S^4 \kappa_L^4 \sum_l P_l(\cos\gamma)[\alpha_l(Q, |\mathbf{Q}_{LS} - \mathbf{Q}|) + \alpha_l(|\mathbf{Q}_{LS} - \mathbf{Q}|, Q)] \right|^2 Q^2 dQ do, \tag{30}$$

where $C = \hat{\varepsilon}_\alpha^L \hat{\varepsilon}_\beta^S \pi_{cv}^\alpha \pi_{vc}^\beta \gamma_f^2 / R^3$; $do = \sin\vartheta d\vartheta d\varphi$; $\mathbf{Q}_{LS} = (\mathbf{q}_L - \mathbf{q}_S)a$ is the wave vector imparted to the phonon system; and γ is the angle between vectors $\mathbf{Q} = \mathbf{q}a$ and $\mathbf{Q}_{LS} - \mathbf{Q}$.

3. DISCUSSION

Consider the dependence of the scattering cross section on the magnitude of the wave vector $\mathbf{Q}_{LS}$ imparted to the phonon system. The photon wave vectors are small compared to the dimensions of the Brillouin zone. Thus, for backward Raman scattering by 2*LO* phonons in a CdS crystal, $Q_{LS} \approx 0.2$. To estimate the contributions from phonons with small wave vectors ($Q \ll 1$), we consider expression (18). Because the Bessel function of a small argument has the form [12]

$$j_l(z) \approx \frac{z^l}{(2l+1)!!}, \tag{31}$$

the quantities $A_l(n, Q)$ and $I_l(Q, \kappa_S, n)/Q^{l+1}$ depend on Q as Q^l for $Q \longrightarrow 0$. For $Q, Q' \ll 1$, this yields $\alpha_l(Q, Q') \propto (QQ')^{l-1}$ for $l \geq 1$ ($\alpha_0(Q, Q') \propto QQ'$). Therefore, in the limiting case $Q, Q' \longrightarrow 0$ only a chain of the intermediate states *s–p–s* makes a contribution to scattering because $\alpha_1(Q, Q') \longrightarrow$ const. In this case, the contribution of the region $Q \ll 1$ to the integral (30) will be small. Thus, phonons with $Q, Q' \gg Q_{LS}$ play a major role in scattering. This leads to a weak dependence of the scattering cross section on the wave vector imparted to the phonon system. This conclusion agrees well with the results of the study of multiphonon scattering performed in paper [1], where its was found experimentally that below the fundamental absorption edge the scattering cross section for even-order multiphonon processes is independent of the wave vector imparted to the phonon system. Therefore, we can assume in the calculation of the scattering cross section that two photons are created in the process of Raman scattering which have equal in magnitude and oppositely directed wave vectors, i.e.,

$$\alpha(\mathbf{q}_{LS} - \mathbf{q}, \mathbf{q}) \approx \alpha(\mathbf{q}, \mathbf{q}_{LS} - \mathbf{q}) \approx \alpha(\mathbf{q}, -\mathbf{q}). \tag{32}$$

Note that the region in which the approximation (31) is valid expands with distance from the resonance. This is distinctly demonstrated in Fig. 1, where the dependences $I_1(Q, \kappa_S, 2)/Q^2$ on Q are presented for $\kappa_S = 0.9$ and 0.2. This property follows from relation (18). Indeed, the integrand contains the function $\exp[-(\rho/\kappa_S)(1 + i\kappa_S Q)]$, which is expanded in a series in a small parameter $\kappa_S Q \ll 1$. Therefore, the dependence of the scattering cross section on $\mathbf{q}_L - \mathbf{q}_S$ becomes weaker with distance from the resonance.

It follows from expression (14) that in the case of close magnitudes of the effective masses of an electron and a hole, scattering is determined only by the states with odd l to which chains of the intermediate states *s–p–s*, *s–f–s*, etc. correspond. In addition, the contribution from the corresponding intermediate states decreases with increasing l. Therefore, for $m_e^* \approx m_h^*$, the scattering mechanism involving a chain of the intermediate states *s–p–s* makes the dominant contribution. However, if the effective masses of an electron and a hole are greatly different, one should also take into account the transitions between the *s* excitonic states (*s–s–s*). Figure 2 shows the dependences of relative contributions Λ_l to the scattering cross section on the effective masses of an electron and a hole for two chains of the intermediate states *s–s–s* (Λ_l) and *s–p–s* (Λ_0), where

$$\Lambda_l = \int |\alpha_l(Q, Q)|^2 Q^2 dQ. \tag{33}$$

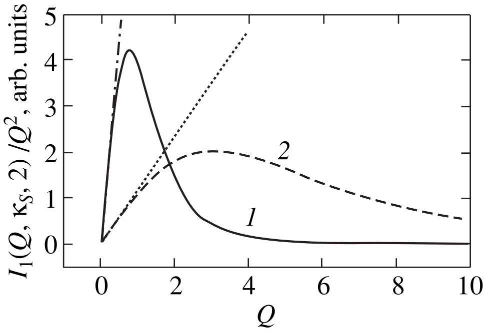

Fig. 1. Dependences of the function $I_1(Q, \kappa_S, 2)/Q^2$ on the phonon wave vector Q for $\kappa_S = 0.9$ (curve *1*) and 0.2 (curve *2*). The dashed and dot-and-dash curves describe corresponding approximate functions $f(\kappa_S, 2)Q$, where $I_1(Q, \kappa_S, n)/Q^2 \xrightarrow[Q \to 0]{} f(\kappa_S, n)Q$.

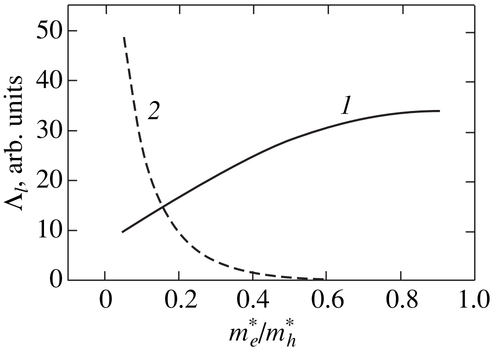

Fig. 2. Dependences of the relative contributions Λ_l of two chains of the intermediate states s–p–s (Λ_1, curve *1*) and *s–s–s* (Λ_0, curve *2*) to the scattering cross section on the ratio m_e^*/m_h^* of the effective masses of an electron and a hole.

One can see from this figure that for $m_e^*/m_h^* > 0.5$ the contribution from transitions between *s* excitonic states is negligibly small ($\Lambda_0 \ll \Lambda_1$); however, already for $m_e^*/m_h^* \approx 0.2$, the contributions Λ_1 and Λ_0 prove to be of the same order, whereas when the effective masses are substantially different ($m_e^*/m_h^* < 0.15$), the magnitude of Λ_0 exceeds that of Λ_1.

Using the theoretical model developed in this paper, we estimated the cross section for Raman scattering of light by 2*LO* phonons in a CdS crystal taking into account the contributions from two chains of intermediate states: *s–s–s* ($l = 0$) and *s–p–s* ($l = 1$). We performed calculations for the same geometry as for mul-

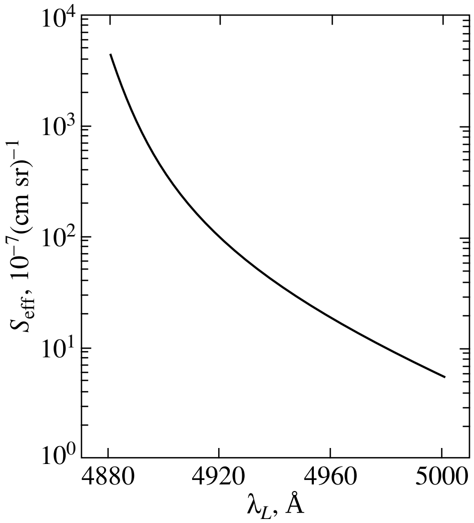

Fig. 3. Efficiency S_{eff} of Raman scattering of light by 2*LO* phonons in a CdS crystal as a function of the exciting radiation wavelength.

tiphonon scattering studied in paper [1]. In this case, the excitonic series *A*, *B*, and *C* contribute to scattering. We used in our calculations the following crystal parameters: the energy gaps E_{gA}, E_{gB} and E_{gC} are 2.579, 2.596, and 2.66 eV, respectively; the exciton binding energies R_A, R_B, and R_C are 0.03, 0.028, and 0.026 eV, respectively [15]; the oscillator strengths for the 1*S* excitonic are $4\pi f_A = 0.0125$, $4\pi f_B = 0.0075$, and $4\pi f_C = 0.005$ for excitonic series *A*, *B*, and *C*, respectively [16]; $\hbar\omega_p = 305$ cm^{-1}; $\varepsilon_0 = 9.3$; $\varepsilon_\infty = 5.2$ [17]; and $m_e^*/m_h^* = 0.2$ [8]. The efficiency of two-phonon Raman scattering $S_{\text{eff}} = V^{-1}d\sigma/d\Omega$ calculated with these parameters as a function of the exciting radiation wavelength is presented in Fig. 3.

CONCLUSIONS

The theoretical model of resonance Raman scattering of light by 2*LO* phonons was developed. The model allows one to calculate the cross section for two-photon Raman scattering when the exciting radiation frequency is lower than the exciton transition frequency. It is shown that below the fundamental absorption edge, the dependence of the scattering cross section on the wave vector $\mathbf{q}_L - \mathbf{q}_S$ imparted to the phonon system is weak and weakens with distance from the resonance. Analytic expressions are obtained which take into account contributions from different chains of the intermediate states. It is shown that when the effective masses of an electron and a hole are close, the scattering is mainly determined by a chain of the intermediate states *s*–*p*–*s*, but when m_e^* and m_h^* are substantially different, the transitions between *s* excitonic states should be also taken into account. The model was used to calculate the efficiency of Raman scattering by 2*LO* phonons in a CdS crystal at different excitation wavelengths.

ACKNOWLEDGMENTS

This work was supported by the Russian Foundation for Basic Research, project no. 98-02-17607.

REFERENCES

1. A. A. Klochikhin, S. A. Permogorov, and A. N. Reznitskiĭ, Zh. Éksp. Teor. Fiz. **71**, 2230 (1976) [Sov. Phys. JETP **44**, 1176 (1976)].
2. R. H. Callender, S. S. Sussman, M. Selders, *et al.*, Phys. Rev. B **7**, 3788 (1973).
3. A. K. Ganguly and J. L. Birman, Phys. Rev. **162**, 806 (1967).
4. A. A. Klochikhin, Ya. V. Morozenko, and S. A. Permogorov, Fiz. Tverd. Tela (Leningrad) **20**, 3557 (1978) [Sov. Phys. Solid State **20**, 2057 (1978)].
5. E. L. Ivchenko and M. M. Sobirov, Fiz. Tverd. Tela (Leningrad) **28**, 2023 (1986) [Sov. Phys. Solid State **28**, 1131 (1986)].
6. R. Loudon, *The Quantum Theory of Light* (Clarendon Press, Oxford, 1973; Mir, Moscow, 1976).
7. M. M. Denisov and V. P. Makarov, Phys. Status Solidi B **56**, 9 (1973).
8. R. M. Martin, Phys. Rev. B **4**, 3676 (1971).
9. J. M. Ziman, *Principles of the Theory of Solids* (Cambridge Univ. Press, London, 1964; Mir, Moscow, 1966).
10. L. Hostler, J. Math. Phys. **5**, 591 (1964).
11. G. D. Mahan, Phys. Rev. **170**, 825 (1968).
12. L. D. Landau and E. M. Lifshitz, *Course of Theoretical Physics*, Vol. 3: *Quantum Mechanics: Non-Relativistic Theory* (Nauka, Moscow, 1989, 4th ed.; Pergamon, New York, 1977, 3rd ed.).
13. G. N. Watson, *Treatise on the Theory of Bessel Functions* (Cambridge Univ. Press, Cambridge, 1945; Inostrannaya Literatura, Moscow, 1949).
14. *Heigher Transcendental Functions (Bateman Manuscript Project)*, Ed. by A. Erdelyi (McGraw-Hill, New York, 1953, 1953, 1955; Nauka, Moscow, 1965, 1966, 1967), Vols. 1–3.
15. F. Pradere, Thèse de doctorat d'état des-sciences physiques (Univ. de Paris Sud, 1973).
16. J. Jackel and H. Mahr, Phys. Rev. B **17**, 3387 (1978).
17. *Physical Quantities: a Handbook*, Ed. by I. S. Grigor'ev and E. Z. Meilikhov (Énergoizdat, Moscow, 1991).

Translated by M. Sapozhnikov

Journal of Experimental and Theoretical Physics, Vol. 92, No. 5, 2001, pp. 777–788.
Translated from Zhurnal Éksperimental'noĭ i Teoreticheskoĭ Fiziki, Vol. 119, No. 5, 2001, pp. 893–905.
Original Russian Text Copyright © 2001 by Mur, Popruzhenko, Popov.

ATOMS, SPECTRA, RADIATION

Energy and Momentum Spectra of Photoelectrons under Conditions of Ionization by Strong Laser Radiation (the Case of Elliptic Polarization)

V. D. Mur[a], S. V. Popruzhenko[a, *], and V. S. Popov[b]
[a] *Moscow State Institute of Engineering Physics, Moscow, 115409 Russia*
[b] *Institute of Theoretical and Experimental Physics, Moscow, 117218 Russia*
**e-mail: poprz@theor.mephi.ru*

Received December 7, 2000

Abstract—Analytical and numerical studies are made into the momentum distribution and energy spectra of photoelectrons emitted during nonlinear ionization of atoms and molecules by laser radiation with elliptic polarization. The dependence of these distributions on the ellipticity ξ of an electromagnetic wave is treated, as well as their evolution upon variation of the Keldysh parameter γ from the region of optical tunneling ($\gamma \ll 1$) to the region of $\gamma \gg 1$, in which the ionization is multiphoton. The quasiclassical approximation is used in the calculations, in particular, the imaginary-time method and the saddle-point method with expansion in the vicinity of the field ellipse. *© 2001 MAIK "Nauka/Interperiodica".*

1. INTRODUCTION

The analytical theory of multiphoton ionization of atoms and ions in the field of monochromatic laser radiation was developed in [1–4], where the cases of linear [1–3] and circular [2, 3] polarization were treated. The most general case of elliptic polarization of electromagnetic wave,

$$\mathbf{F}(t) = F\cos(\omega t)\mathbf{e}_x + \xi F\sin(\omega t)\mathbf{e}_y, \qquad (1)$$

was treated in [4, 5] (here, F is the maximum value of electric field and ξ is the ellipticity of radiation (previously denoted by ε [4]), $1 \le \xi \le 1$). Perelomov *et al.* [4] have derived analytical formulas for the probability of ionization and for the momentum photoelectron spectrum that are valid for all values of the Keldysh parameter γ, and have demonstrated that, at $0 < \xi^2 < 1$, the most probable momentum of outgoing electron $\mathbf{p}_{\max}$ is directed along the minor axis of the field ellipse (y axis in Eq. (1)). They have also noted that, at $\xi = 0$ (linear polarization of radiation), the momentum $\mathbf{p}_{\max}$ is directed along the electric field $\mathbf{F}$, and, at $\xi = \pm 1$ (circular polarization), the photoelectron distribution becomes isotropic in the $\mathbf{F}(t)$ plane. However, the formulas for momentum spectrum given in [4] are invalid in the narrow range of $\xi \longrightarrow \pm 1$, where the transition to circular polarization occurs. Goreslavskii and Popruzhenko [5] investigated (including numerical investigations) the polarization dependences (for all values of ξ) of the momentum, angular, and energy distribution of photoelectrons and of the ionization rate of atoms in the case of a low-frequency ($\gamma \ll 1$) laser field. Note that no comparison was previously made of the results of [4, 5].

It is the objective of this study to investigate the energy and momentum spectra of photoelectrons as functions of the ellipticity ξ for all values of the Keldysh parameter [1]

$$\gamma = \omega\kappa/F = (2K_0\epsilon)^{-1}. \qquad (2)$$

Here and in what follows, use is made of the atomic units $\hbar = m = e = 1$ (m is the electron mass), $K_0 = \kappa^2/2\omega$ is the parameter indicative of the number of quanta necessary for the process, $\epsilon = F/\kappa^3$ is the reduced electric field, I is the ionization potential of atomic state, and $\kappa = \sqrt{2I}$ is the momentum characteristic of that state. It is assumed that the conditions

$$K_0 \gg 1, \quad \epsilon \ll 1 \qquad (2')$$

are valid, which provide for the validity of the quasiclassical approximation for many-quantum processes. We will treat in detail the evolution of the energy photoelectron spectrum upon transition from the conditions of optical tunneling ($\gamma \ll 1$) to the antiadiabatic region of $\gamma \gg 1$, as well as to the transition region of $\gamma \sim 1$. We will demonstrate that (except for the narrow range of $1 - \xi^2 \lesssim \epsilon \ll 1$), the results of [4, 5] obtained using different methods virtually coincide.[1] Also treated is the variation of the momentum spectrum of electrons in the range of $1 - \xi^2 \sim \epsilon$, i.e., for close-to-circular polarization. Explicit analytical expressions (12), (14), and (18) are derived for the energy spectrum, which cover

---

[1] The statements, made in [5] (for example, pp. 1201 and 1206) to the effect that the formulas of [4] are valid only in a very limited range of values of ξ are based on misunderstanding and are essentially wrong. See Fig. 4 and the discussion of Eqs. (27) and (31) below, and Section 5 in [6].

1063-7761/01/9205-0777$21.00 © 2001 MAIK "Nauka/Interperiodica"

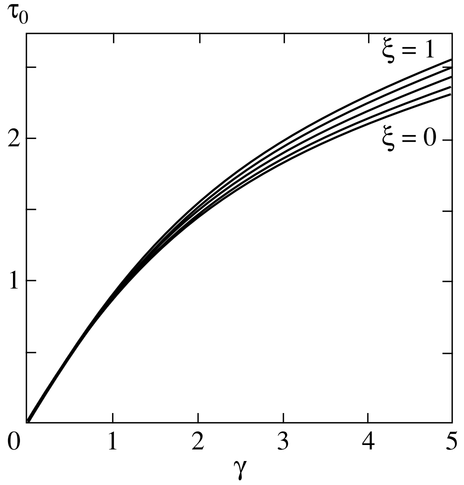

Fig. 1. The dimensionless "time" $\tau_0(\gamma, \xi)$ of subbarrier motion, found numerically from Eq. (5). The curves correspond (from the bottom upwards) to the values of ellipticity $\xi = 0, 0.5, 0.75, 0.9$, and 1.0.

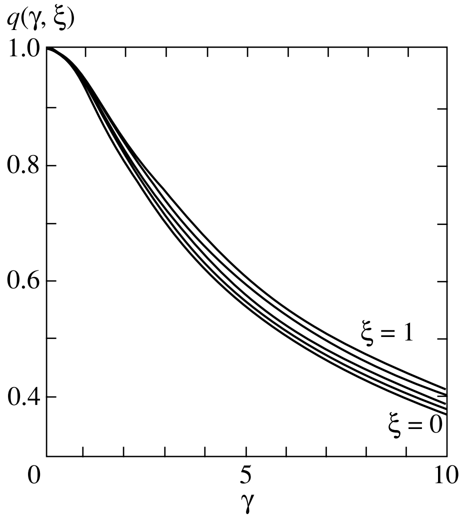

Fig. 2. The function $g(\gamma, \xi)$ which defines the exponential factor in expression (6) for the ionization probability. The curves correspond (from the bottom upwards) to the values of $\xi = 0, 0.5, 0.75, 0.9$, and 1.0.

the entire range of variation of the parameter γ and are characterized (as demonstrated by their comparison with the results of numerical calculations) by a fairly good accuracy. The momentum distribution of electrons is found in the case of circularly polarized field for arbitrary values of γ (see formula (33) below).

At present, the problem of detailed description of the momentum and energy spectra of photoelectrons under conditions of multiphoton ionization of atoms and molecules appears to be topical in at least two respects. First, a number of experiments were performed within the last decade, which involved measurements (to a high resolution) of the distribution of photoelectrons, including their distribution in an elliptically polarized field [7–10]. Much of the experimental results are associated with the transition region of the adiabaticity parameter ($\gamma \sim 1$), little investigated by analytical methods. In this study, we have derived simple analytical expressions fit to describe the energy spectra of photoionization in an elliptically polarized field for different values of γ. Second, the calculations of the structure of spectrum of direct photoionization are necessary during investigation of the processes associated with interaction, in the final state, between ionized electron and parent atom (ion) (such processes include the generation of higher harmonics of laser radiation [11, 12], multielectron noncascade ionization [13, 14], and rescattering of photoelectrons [15]).

2. QUASICLASSICAL APPROXIMATION

The rate of ionization of the atomic level in a laser field and the momentum spectrum of emitted electrons are defined by the probability of tunneling through a time-variable barrier, which may be conveniently calculated using the imaginary-time method [4, 16]. Subbarrier trajectories are introduced into the treatment, which formally satisfy the classical equations of motion but with imaginary time (which is reflective of the fact that such trajectories are not realized in classical mechanics). The exponential factor in the tunneling probability is defined by the so-called "extreme" subbarrier trajectory (which minimizes the imaginary part of the action function and defines the most probable tunneling path of a particle); in order to find the momentum spectrum and the preexponential factor, one needs to treat a beam of close-to-extreme trajectories. For details and necessary refinements, see [4, 16–18].

In the case of ionization of the s-level bound by a short-range potential (binding energy $I = \kappa^2/2$, the range of action of the forces $r_0 \ll 1/\kappa$) under the effect of the electric field of the wave as given by Eq. (1), the momentum spectrum of photoelectrons has the form

$$dw(\mathbf{p}) = |F(\mathbf{p})|^2 d^3 p,$$

$$|F(\mathbf{p})|^2 = A\exp\left[-\frac{1}{\omega}(c_x p_x^2 + c_z p_z^2)\right] \tag{3}$$

$$\times\left\{\exp\left[-\frac{c_y}{\omega}(p_y - p_{\max})^2\right] + \exp\left[-\frac{c_y}{\omega}(p_y + p_{\max})^2\right]\right\}.$$

The values of A, c_i, and $p_{\max}$ are defined by formulas (23)–(28) in [4]; these quantities are expressed in terms of the variable $s = s(\gamma, \xi)$, which satisfies the transcendental equation (20) in [4]. The formulas of the latter study are simplified considerably if we change over from s to a new variable τ_0,

$$\tau_0 = \operatorname{Arctanh}\sqrt{\frac{s^2 + \gamma^2}{1 + \gamma^2}},$$

$$s = \frac{\sqrt{\sinh^2\tau_0 - \gamma^2}}{\cosh\tau_0} = |\xi|\left(1 - \frac{\tanh\tau_0}{\tau_0}\right), \tag{4}$$

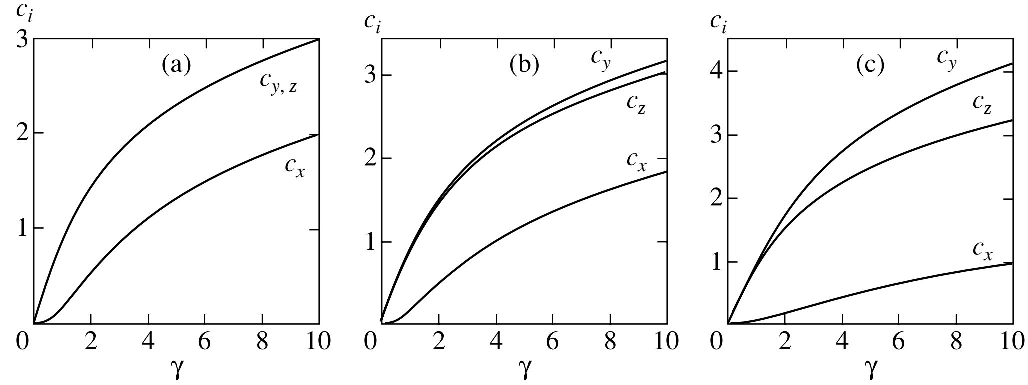

Fig. 3. The coefficients $c(\gamma, \xi)$ of Eq. (3) for momentum distribution as functions of the Keldysh parameter γ at ξ = (a) 0, (b) 0.5, and (c) 0.9.

which is found from the equation

$$\sinh^2\tau_0\left[1-\xi^2\left(\coth\tau_0-\frac{1}{\tau_0}\right)^2\right] = \gamma^2 \qquad (5)$$

and has a transparent physical meaning: $\tau_0 = -i\omega t_0$, where t_0 is the "initial moment" (purely imaginary), or the total "time" of the subbarrier motion of electron (Fig. 1). All quantities entering the formulas for the ionization probability are readily expressed in terms of τ_0,

$$A = C_\kappa^2\frac{\omega^2}{2\pi^2 F}P(\gamma,\xi)\exp\left\{-\frac{2}{3\epsilon}g(\gamma,\xi)\right\}, \qquad (6)$$

$$g(\gamma,\xi) = \frac{3}{2\gamma}$$
$$\times\left[\left(1+\frac{1+\xi^2}{2\gamma^2}\right)\tau_0-(1-\xi^2)\frac{\sinh 2\tau_0}{4\gamma^2}-\xi^2\frac{\sinh^2\tau_0}{\gamma^2\tau_0}\right], \qquad (7)$$

$$c_x = \tau_0-\sigma\tanh\tau_0, \quad c_y = \tau_0+\sigma\xi^2\frac{(\tau_0-\tanh\tau_0)^2}{\tau_0^2\tanh\tau_0},$$
$$c_z = \tau_0, \quad P(\gamma,\xi) = \frac{2\sigma\gamma}{\sinh 2\tau_0} \qquad (7')$$

(Figs. 2 and 3), and we used the notation

$$\sigma = \left(1-\xi^2+\xi^2\frac{\tanh\tau_0}{\tau_0}\right)^{-1}$$
$$= \begin{cases}1+(1-\tanh\tau_0/\tau_0)\xi^2+\ldots, & \xi = 0,\\ \tau_0/\tanh\tau_0, & \xi = 1.\end{cases}$$

Note that $c_y \geq c_z > c_x$ (the equality $c_y = c_z$ is observed only at $\xi = 0$, i.e., in the case of linear polarization, Fig. 3a). In so doing, the coefficients c_y and c_z are numerically close to each other except for the case of $|\xi| \approx 1$ (i.e., close-to-circular ellipticities).

In Eq. (6), C_κ is the asymptotic (at distances $r \gg 1/\kappa$ from the nucleus) coefficient of atomic wave function.[2] Thus, $C_\kappa^2 = 1$ in the case of the ground (1*s*) and 2*s*-states of hydrogen atom (the values of C_κ for other atoms and ions are given in [17]), and $C_\kappa^2 = 1/2$ for the level in the δ-potential.

Note that our normalization of the coefficients C_κ corresponds to that in [17, 24] and differs from that adopted in [2–5].

One can see in Fig. 2 that, as the ellipticity of light increases, the value of $g(\gamma, \xi)$increases monotonically, and the ionization probability decreases.[3] Even more considerable is the decrease in $g(\gamma, \xi)$ during transition from the adiabatic region of $\gamma \ll 1$ to the multiphoton region of $\gamma \gg 1$, which leads to a sharp (because $2/3\epsilon \gg 1$) increase in the ionization probability.

Therefore, the spectrum given by Eq. (3) is the sum of two anisotropic Gaussian distributions with the centers at the points $\pm p_{\max}$ on the *y* axis (the minor axis of the ellipse $\mathbf{F}(t)$). In so doing, the most probable momentum of outgoing electron is (see Appendix *A*)

$$p_{\max} = |\xi| p_F, \quad p_F = \frac{F}{\omega}\frac{\sinh\tau_0}{\tau_0} = \kappa\frac{\sinh\tau_0}{\gamma\tau_0}. \qquad (8)$$

The results of calculation of the energy spectrum of photoelectrons using the foregoing formulas will be

---

[2] These coefficients occur repeatedly in quantum mechanics and atomic physics and may be calculated by the Hartree–Fock method: see, for example, [19]. In addition, simple analytical approximations are available for these coefficients, which were derived by Hartree [20], as well as those derived using the quantum defect method [21–23] and from the expansion of effective radius [24]. For neutral atoms and singly charged positive ions, these approximations are characterized by a fairly high accuracy (in connection with this, see Table 2 in [6]). As is seen in Table 1 in [17], the numerical values of C_κ for the *s*-states are fairly close to unity.

[3] For a fixed amplitude of the field *F*. In so doing, the radiation intensity $J = (1 + \xi^2)cF^2/8\pi$ also varies, but not more than by a factor of two.

described below, but we will first treat two limiting cases for which explicit analytical expressions may be derived.

(a) $\gamma \ll 1$ (low-frequency laser radiation). Here,

$$\tau_0 = \gamma - \frac{1}{9}(1+k)\gamma^3 + \frac{13}{405}\left(1 + 2k + \frac{35}{26}k^2\right)\gamma^5 + \ldots, \tag{9}$$

$$\begin{gathered} g(\gamma, \xi) = 1 - \frac{1}{15}(1+k)\gamma^2 + O(\gamma^4), \\ P = 1 - \frac{1}{9}(2+5k)\gamma^2 + \ldots, \\ c_x = \frac{2}{3}k\gamma^3 + \ldots, \quad c_y = \gamma - \frac{1}{3}k\gamma^3 + \ldots, \\ c_z = \gamma - \frac{1}{9}(1+k)\gamma^3 + \ldots, \end{gathered} \tag{10}$$

$$p_F = \frac{F}{\omega}\left\{1 + \frac{1}{6}\gamma^2 + \left[\frac{1}{120} - \frac{1}{27}(1+k)\right]\gamma^4 + \ldots\right\}, \tag{11}$$

where $k = (1-\xi^2)/2$.[4] We perform integration with respect to d^3p (for details, see Appendix B) to derive, for the probability of n-photon ionization,

$$\begin{gathered} w_n = w_{n_0}a(\gamma(n-n_0)) \\ \times \exp\left\{-\frac{2}{3}(1-\xi^2)\gamma^3(n-n_0)\right\}, \\ w_{n_0} = \frac{2}{\sqrt{\pi}}\kappa^2 C_\kappa^2 \epsilon^{3/2}\gamma^2 \\ \times \exp\left\{-\frac{2}{3\epsilon}\left[1 - \frac{1}{10}\left(1 - \frac{\xi^2}{3}\right)\gamma^2\right]\right\}, \end{gathered} \tag{12}$$

where

$$n > n_0 = \frac{F^2}{4\omega^3}[1 + 3\xi^2 + O(\gamma^2)]$$

and the function

$$a(x) = e^{-x}I_0(x) = \begin{cases} 1 - x + \dfrac{3}{4}x^2 + \ldots, & x \longrightarrow 0, \\ \dfrac{1}{\sqrt{2\pi x}}\left[1 + \dfrac{1}{8x} + \ldots\right], & x \longrightarrow \infty, \end{cases} \tag{13}$$

is introduced, where $I_0(x)$ is the modified Bessel function.

In the case of $n < n_0$,

$$\begin{gathered} w_n \propto \exp\left\{-\xi^2\frac{F\kappa}{\omega^2}\left(1 - \sqrt{\frac{n-\nu}{n_0-\nu}}\right)^2\right\}, \\ \nu = \frac{F^2}{4\omega^3}(1+\xi^2), \end{gathered} \tag{14}$$

where ν is the photoionization threshold. We will use the notation $\xi_1 = \omega/\sqrt{F\kappa} = \gamma\sqrt{\epsilon}$ ($\xi_1 \ll 1$). If the ellipticity $\xi \gg \xi_1$, distribution (14) is "pressed against" $n = n_0$ and makes a negligibly small contribution (of the order of $\sqrt{\epsilon}$) to the total probability (or to the rate of level ionization) W. We integrate Eq. (12) with respect to n from $n = n_0$ to infinity to derive

$$\begin{gathered} W = \sqrt{\frac{3\epsilon}{\pi(1-\xi^2)}}\kappa^2 C_\kappa^2 \epsilon \\ \times \exp\left\{-\frac{2}{3\epsilon}\left[1 - \frac{1}{10}\left(1 - \frac{\xi^2}{3}\right)\gamma^2\right]\right\}, \end{gathered} \tag{15}$$

which is in complete agreement with the adiabatic approximation in view of the correction proportional to γ^2 in the exponent [3, 4]. The main contribution to Eq. (15) is made by the region of $n - n_0 \gtrsim \gamma^{-1} \gg 1$, in which

$$\begin{gathered} w_n \approx \text{const}\frac{1}{\sqrt{n-n_0}} \\ \times \exp\left\{-\frac{2}{3}(1-\xi^2)\gamma^3(n-n_0)\right\}. \end{gathered} \tag{12'}$$

(b) In the opposite case of $\gamma \gg 1$, Eq. (5) takes the form

$$\sqrt{[1 - \xi^2(1-\tau_0^{-1})^2]}e^{\tau_0} = 2\gamma, \tag{5'}$$

whence

$$\tau_0(\gamma, \xi) = \begin{cases} \ln(2\gamma/\sqrt{1-\xi^2}), & 1 - \xi^2 \gg 1/\ln(2\gamma), \\ \ln(\gamma\sqrt{2\ln\gamma}), & \xi = \pm 1. \end{cases} \tag{16}$$

We will restrict ourselves to logarithmic approximation and assume that $\tau_0 \gg 1$; then, $\sigma = \tau_0\delta$,

$$\begin{gathered} g(\gamma, \xi) = \frac{3}{2\gamma}\left[\tau_0 - \frac{1}{2} - \frac{\xi^2\delta}{2\tau_0(1+\xi^2\delta)}\right], \\ c_x = \tau_0(1-\delta), \quad c_y = \tau_0(1+\xi^2\delta), \\ c_z = \tau_0, \quad P = \gamma^{-1}(1+\xi^2\delta), \end{gathered} \tag{17}$$

where $\delta = 1/[(1-\xi^2)\tau_0 + \xi^2] \le 1$. In particular, at $\xi \longrightarrow 0$,

---

[4] Note that, for $\gamma \lesssim 10$, the momentum $p_{\max}$ is almost proportional to the ellipticity of light ξ (see Fig. 2 in [4]).

$$c_x = \tau_0 - 1 - \left(1 - \frac{1}{\tau_0}\right)\xi^2 + O(\xi^4), \quad c_y = \tau_0 + \frac{\xi^2}{\tau_0} + \ldots,$$

$$\tau_0 = \ln(2\gamma) + \frac{1}{2}\xi^2 + \ldots,$$

and, at $\xi \longrightarrow \pm 1$,

$$c_x = 2\tau_0^2 k + O(k^2), \quad c_y = 2\tau_0 - 2\tau_0^2 k + \ldots,$$

where k has the same value as in Eqs. (9)–(11). After simple computations (see Eq. (B.7)), we derive Gaussian distribution for the probability of n-photon ionization,

$$w_n = w_{\max}\exp\left\{-\frac{(n-n_0)^2}{2(\Delta n)^2}\right\}, \quad \Delta n = \mu\sqrt{n_0}, \tag{18}$$

where $w_{\max} = w_{n_0}$,

$$\mu = \frac{\sqrt{\xi^2[(1-\xi^2)\tau_0 + \xi^2]}}{(1-\xi^2)\tau_0^2 + 2\xi^2\tau_0},$$

$$n_0 = K_0\left(1 + \frac{\xi^2}{(1-\xi^2)\tau_0^2 + 2\xi^2\tau_0}\right)$$

(see also [25]). On observing that $K_0 = I/\omega \gg 1$,

$$\mu = \begin{cases} \tau_0^{-3/2}\{\xi^2/[1-(1-3\tau_0^{-1})\xi^2]\}^{1/2}, & 1-\xi^2 \gg 1/\tau_0, \\ \dfrac{1}{2\tau_0}\left[1 - \dfrac{1}{8}\tau_0^2(1-\xi^2)^2\right], & \xi \longrightarrow 1 \end{cases}$$

and $\tau_0 \gtrsim \ln(2\gamma) \gg 1$, we see that the distribution given by Eq. (18) is always much narrower than the Poisson distribution with $\langle n\rangle = n_0$ (for which, apparently, $\mu = 1$).

Unlike that given by Eq. (18), the distribution given by Eqs. (12) and (14) is asymmetric relative to the value of $n = n_0$ that corresponds to the maximum probability of ionization. In view of formula (21) (see the text below), Eq. (12) yields ($\gamma \ll 1$)

$$n_0 \sim K_0\gamma^{-2} \gg 1,$$
$$\frac{\langle n\rangle - n_0}{n_0} \sim \frac{\Delta n}{\langle n\rangle} \sim \frac{\epsilon}{1-\xi^2}, \tag{19}$$

where $\langle n\rangle$ and Δn denote the average number of absorbed photons and its dispersion. This estimate is valid for $1 - \xi^2 \gg \epsilon$; in the case of circular polarization [6],

$$\frac{\Delta n}{\langle n\rangle} \sim \begin{cases} \omega/\sqrt{F\kappa} = \gamma\sqrt{\epsilon}, & \gamma \ll 1, \\ (\sqrt{K_0}\ln\gamma)^{-1}, & \gamma \gg 1. \end{cases}$$

Finally, it follows from Eq. (18) that, at $\gamma \gg 1$,

$$\langle n\rangle \approx n_0, \quad \frac{\Delta n}{\langle n\rangle} \sim \mu\sqrt{\frac{\omega}{I}} \sim \frac{1}{\sqrt{K_0}} \times \begin{cases} \tau_0^{-3/2}\sqrt{\xi^2/(1-\xi^2)}, & \xi < 1, \\ \tau_0^{-1}, & \xi \longrightarrow 1. \end{cases} \tag{20}$$

Therefore, the distribution with respect to n is always relatively narrow (in units of average $\langle n\rangle$).

In the general case (any values of γ and ξ), the photoionization threshold ν and the most probable number n_0 of absorbed photons are [4]

$$\nu = \frac{F^2}{4\omega^3}(1 + \xi^2 + 2\gamma^2),$$
$$n_0 = \nu\left[1 + \frac{2\xi^2}{1+\xi^2+2\gamma^2}\left(\frac{\sinh\tau_0}{\tau_0}\right)^2\right], \tag{21}$$

where $\tau_0(\gamma, \xi)$ is determined from Eq. (5). Hence,

$$\frac{n_0 - \nu}{\nu} \approx \begin{cases} 2\xi^2/(1+\xi^2), & \gamma \longrightarrow 0, \\ \xi^2/[(1-\xi^2)\tau_0^2 + 2\xi^2\tau_0], & \gamma \longrightarrow \infty. \end{cases} \tag{22}$$

Therefore, $n_0 - \nu \gg 1$ if $\gamma \ll \exp[\sqrt{K_0\xi^2/(1-\xi^2)}\,]$, which is almost always valid except for the case of linear polarization $\xi = 0$ (when $n_0 - \nu \sim 1$ if $\gamma \gg 1$ [1]). Thus, with $\xi \neq 0$, the distribution of w_n covers many values of n, even if $\gamma \gg 1$: this enables one, in calculating the ionization rate W, to replace the summation with respect to n by integration.

For the photoelectron energy distribution, we have derived asymptotic formulas (12), (14), and (18), which are valid for low and high values of γ, respectively. In the case of arbitrary values of γ, this distribution may be represented in the form of a single integral (see Eqs. (B.3) and (B.4) in Appendix B).

3. MOMENTUM SPECTRUM IN THE TUNNEL LIMIT

As was already mentioned above, the distribution given by Eq. (3) is invalid in the narrow ellipticity range of $1 - \xi^2 \leq \epsilon \ll 1$. In the case when the tunnel mode of ionization is realized ($\gamma \ll 1$), analytical expressions for momentum distributions have been obtained [5], which are valid in this narrow range as well and provide for direct limiting transition to the case of circular polarization.

We will follow Goreslavskii and Popruzhenko [5] and treat the ionization as a quantum transition from the bound state of Ψ_0 with the ionization potential I to the state of continuum with the asymptotic momentum **p**, which is approximated by the nonrelativistic Volkov wave function,

$$\Psi_{\mathbf{p}} = \exp\left\{i\mathbf{p}\cdot\mathbf{r} - i\int_{-\infty}^{t} E_{\mathbf{p}}(t')dt'\right\}, \qquad (23)$$

where $E_{\mathbf{p}}(t) = [\mathbf{p} + \mathbf{A}(t)/c]^2/2$ is the time-dependent kinetic energy of electron in the laser field with the vector potential

$$\mathbf{A}(t) = -c\int^{t}\mathbf{F}(t')dt',$$

and the field $\mathbf{F}(t)$ is described by expression (1). The momentum spectrum is described by formula (3), where, at this point,

$$\begin{aligned} F(\mathbf{p}) &= i\frac{\sqrt{\omega}}{(2\pi)^2}\Psi_0(\mathbf{p})\left(I + \frac{p^2}{2}\right) \\ &\times \int_0^{2\pi/\omega} dt \exp\left\{iIt + i\int_{-\infty}^{t} E_{\mathbf{p}}(t')dt'\right\}. \end{aligned} \qquad (24)$$

Under conditions of $K_0 \gg 1$ and $F^2/\omega^3 \gg 1$, the time integral in the amplitude equation (24) is calculated by the saddle-point method. In the tunnel limit, the equation for the saddle point $t_s(\mathbf{p}) = t_0(\mathbf{p}) + it_1(\mathbf{p})$ is simplified, which enables one to write the ionization rate in the form

$$\begin{aligned} dW(\mathbf{p}) &= \frac{\omega}{4\pi^2 F} \\ &\times \sum_{\alpha} \exp\left\{-\frac{4\sqrt{2}}{3}\frac{[I + E_{\mathbf{p}}(t_{0\alpha})]^{3/2}}{F(t_{0\alpha})}\right\}d^3p, \end{aligned} \qquad (25)$$

where the sum is computed over all saddle points or solutions of Eq. (14) in [5] (in the case of linear polarization, two such solutions exist, and, as the value of ξ approaches unity, one solution remains). When conditions (2') are valid, the value of $dW(\mathbf{p})$ is defined by the exponent, and the main contribution to Eq. (25) is made by the region of momentum space with the least value of $[I + E_{\mathbf{p}}(t_0)]^{3/2}/F(t_0)$. The preexponential factor in Eq. (25) corresponds to the case of ionization from the ground state in the potential of zero range of action (δ-potential).

Expression (25) describes implicitly the momentum spectrum of photoelectrons and is valid for any values of ξ. In order to derive explicit expressions, one must take into account the fact that, with the preassigned direction of the electron momentum, the distribution given by Eq. (25) reaches its maximum provided

$$\mathbf{p} = \mathbf{P}_F(t_0) = -\frac{1}{c}\mathbf{A}(t_0). \qquad (26)$$

As the parameter t_0 varies within the optical period, the vector $\mathbf{P}_F(t_0)$ describes in the momentum space an ellipse which will be referred to as field ellipse,[5] and in which the distribution given by Eq. (25) reaches a local maximum. By virtue of the condition $1/\epsilon \gg 1$, the ionization probability decreases rapidly with deviation from the field ellipse; the characteristic value of such deviation is $\Delta p \sim \sqrt{\epsilon}\, p_F \ll p_F$. Therefore, in Eq. (25) one can change over to the explicit dependence on momentum [5],

$$\begin{aligned} dW &= A\exp\left[-\frac{\gamma^2}{6I\epsilon}(1-\xi^2)p_x^2\right] \\ &\times \left\{\exp\left[-\frac{E(\mathbf{p},\xi)}{\epsilon I}\right] + \exp\left[-\frac{E(\mathbf{p},-\xi)}{\epsilon I}\right]\right\}d^3p, \end{aligned} \qquad (27)$$

where A is obtained from Eq. (6) at $\gamma \ll 1$; the following notation is used:

$$\begin{aligned} E(\mathbf{p},\xi) &= \frac{1}{2}\lambda\left(\sqrt{p_y^2 + \xi^2 p_x^2} - \xi p_F\right)^2 + \frac{1}{2}p_z^2, \\ \lambda &= \frac{\xi^4 p_x^2 + p_y^2}{\xi^2 p_x^2 + p_y^2}. \end{aligned} \qquad (28)$$

In deriving Eq. (27) from (25), the ellipticity ξ was taken to be arbitrary. In using Eq. (28), one can readily see that the distribution given by Eq. (27) provides for the limiting transition to the known cases of linear and circular polarization [2, 3].

We will treat the correlation between formulas (3) and (27) which describe one and the same momentum spectrum. Except for the narrow region of "high values" of ellipticity ($1 - \xi^2 \le \epsilon$), the quantity $\xi^2 p_x^2$ in Eq. (28) is small compared with p_y^2 either because of the smallness of ξ (at $\xi < \sqrt{\epsilon}$) or because of the marked elongation of distribution along the minor axis y of polarization ellipse (1) at $1 - \epsilon > \xi > \sqrt{\epsilon}$ [4–6]. In view of the foregoing, expression (27) is simplified and coincides completely with Eq. (3)[6] in the case when the latter formula is written for the *s*-level in a short-range potential. However, unlike Eq. (3), formula (27) is valid at $\xi \longrightarrow 1$ as well and describes the isotropization of distribution over the azimuth angle ϕ, which occurs during transition to the circular field.

Figure 4 gives the momentum distribution of photoelectrons $|F(p_x, p_y, p_z = 0)|^2$, calculated from Eqs. (3) and (27) for different values of the degree of polarization. In a field that is close to linearly polarized ($\xi \lesssim \gamma\sqrt{\epsilon}$), the distribution is a peak with a maximum at

---

[5] It lies in the polarization plane and differs from Eq. (1) by the factor $1/\omega$ and by a phase shift through $\pi/2$.

[6] If a transition to the $\gamma \ll 1$ limit is made in Eq. (3).

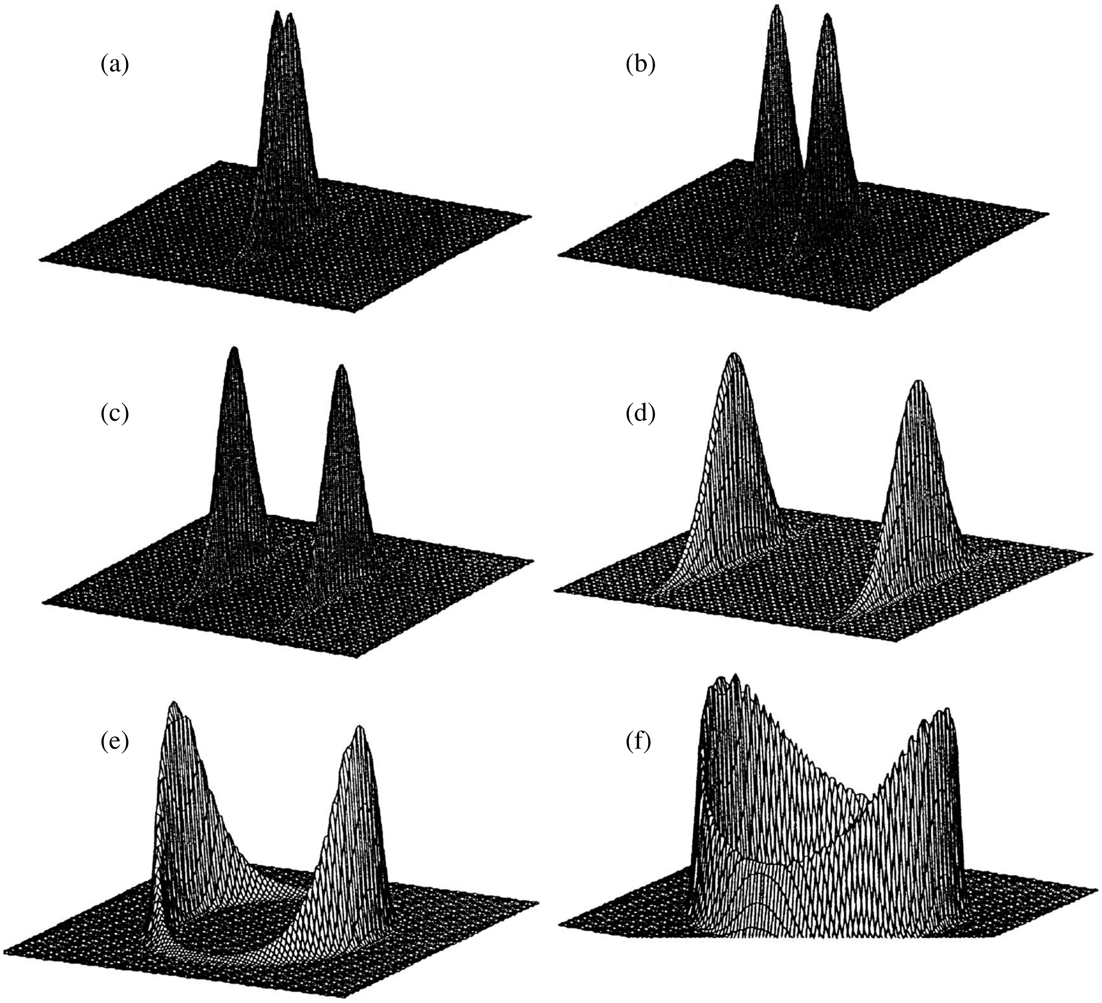

Fig. 4. The momentum distribution of photoelectrons calculated by Eqs. (3) (graphs a–d) and (27) (graphs e and f) for the case of ionization of Ne^{3+} ions ($I \approx 97$ eV) by the field of a titanium–sapphire laser ($\hbar\omega = 1.58$ eV) with the intensity of 2×10^{16} W/cm^2 [26]; in this case, $\epsilon = 0.04$ and $\gamma = 0.2$. The horizontal plane coincides with the plane $p_z = 0$ in the momentum space. The ionization probability is plotted on the vertical axis in arbitrary units. The series of graphs demonstrates the evolution of distribution upon variation of ellipticity ξ = (a) 0.05, (b) 0.25, (c) 0.50, (d, e) 0.8, (f) 0.95.

$\mathbf{p} = 0$ elongated along the major axis of polarization ellipse. A two-peak structure is formed in the $\gamma\sqrt{\epsilon} < \xi < \sqrt{\epsilon}$ range (Fig. 4a), which becomes clearly defined at $\xi > \sqrt{\epsilon}$ and survives up to values of $|\xi| \approx 1 - \epsilon$ (Figs. 4b–4d). In this ellipticity range, the position of maxima in the momentum distribution is defined by formula (8) (for the width of the maxima, see [5, 6]). As the field polarization approaches circular, the distribution becomes isotropic in the azimuth plane, as is well seen in Figs. 4e and 4f. Formula (27) must be used here to describe the distribution.

Therefore, in the tunnel ($\gamma \ll 1$) limit, the combination of expressions (3) and (27) provides for an adequate description of momentum spectrum of photoelectrons in the entire range of variation of the field ellipticity $-1 \le \xi \le 1$.

4. ENERGY SPECTRUM

The evolution of the photoelectron energy spectrum in an elliptically polarized field was previously treated only in the tunnel limit [5]. The expressions derived in Section 2 describe energy spectra in the regions of low and high values of the adiabaticity parameter γ (see formulas (12) and (14) and (18), respectively). In order to assess the accuracy of these asymptotic formulas, as well as to construct an integral pattern of evolution of energy spectrum during transition from the tunnel to multiphoton mode of ionization, we will give the results of numerical calculation of the spectrum, based on direct integration of momentum distribution.

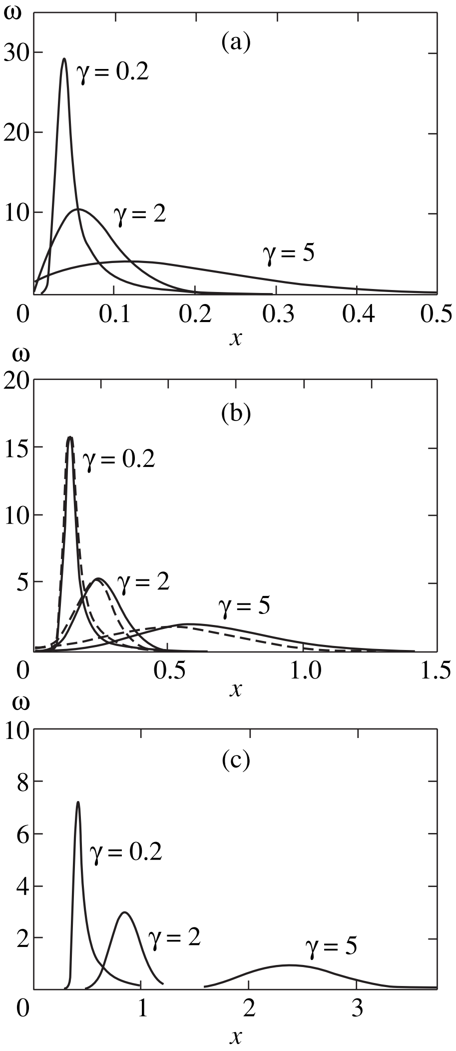

Fig. 5. The energy spectrum of photoelectrons obtained by numerical integration of Eq. (3) for the case of ionization of Ne^{3+} ions by the field of a titanium-sapphire laser with the intensity of 3.2×10^{13} W/cm^2 ($\gamma = 5.0$), 2×10^{14} W/cm^2 ($\gamma = 2.0$), and 2×10^{16} W/cm^2 ($\gamma = 0.2$). [26]; in this case, $\epsilon = 0.04$ and $\gamma = 0.2$. The series of graphs demonstrates the evolution of distribution $w(x) = dW/dx$ ($x = E/E_0$ is the dimensionless electron energy) upon variation of ellipticity ξ = (a) 0.25, (b) 0.5, (c) 0.9. Dashed curves in (b) correspond to the results of calculations based on the asymptotic formulas (12) and (14) for $\gamma = 0.2$ and (18) for $\gamma = 2.0$ and 5.0.

Figure 5 gives photoelectron spectra calculated by formula (B.3); the integration over the variable u in Eq. (B.4) was performed numerically. Because the typical number of above-the-threshold peaks in the important region of the spectrum is large, only their envelope is given in the graphs. The ionization probability is given as a function of dimensionless energy $x = E/E_0$, where $E = p^2/2 = \hbar\omega(n - \nu)$ is the final energy of electron, and the quantity $E_0 = F^2/\omega^2$ is equal to the mean vibrational energy of electron in the field given by Eq. (1) within the factor $(1 + \xi^2)/4$.

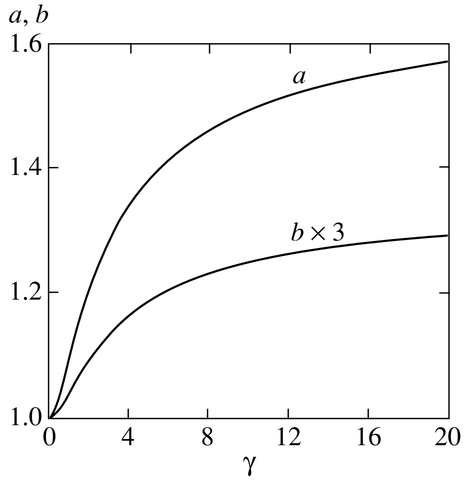

Fig. 6. The values of a and b as functions of γ (see (B.5) and (B.6)).

The presented series of graphs demonstrates the following regularities found in Section 2 as a result of analysis of asymptotic expressions (12), (14), and (18).

(1) For all values of γ, the position of a maximum is defined to a good accuracy by the condition

$$E_{\max} = \frac{1}{2}\xi^2 p_F^2, \tag{29}$$

which immediately follows from Eq. (8).

(2) For all values of ξ, the shape of spectrum varies from an asymmetric narrow peak at $\gamma \ll 1$ to a relatively wide and symmetric (Gaussian) one at $\gamma \gg 1$.

Figure 5b ($\xi = 0.5$) shows further (by broken lines) the spectra calculated by approximate analytical formulas (12), (14), and (18). A comparison of the curves with the results of numerical calculation reveals that these asymptotic formulas describe the spectrum to a high accuracy for all values of the adiabaticity parameter, including the intermediate ones ($\gamma \sim 1$). In particular, one can see that, even at $\gamma = 2$, the shape of the spectrum differs little from Gaussian (see Eq. (18)). An agreement between analytical approximations and the results of numerical calculations is observed for other values of ellipticity ξ as well.

5. CONCLUSION

The results obtained by us pertain to the ionization of systems bound by short-range forces. As is demonstrated in [3, 18], in the low-frequency limit, the effect of the long-range Coulomb potential of atomic core on the ionization probability may be taken into account using the methods of the quasiclassical perturbation theory and reduces to the emergence of a great (in magnitude) preexponential factor in the expression for the ionization rate (for details, see, for example, [17]). Because the shape of spectra and their dependence on the ellipticity ξ and the Keldysh parameter γ are largely defined by the exponential factors, the results obtained by us may be used also to describe the ionization of real atoms.

Finally, note the following fact. Although the distribution given by Eq. (3) ceases to be valid in the $-1 - \xi^2 \le \epsilon \ll 1$ range close to $\xi = \pm 1$, it may be readily rewritten in a form that permits limiting transition to circular polarization. Indeed, expression (3) may be written in different forms which are asymptotically equivalent to one another in the $\epsilon = F/\kappa^3 \longrightarrow 0$ limit. At $\xi = \pm 1$, zero mode arises, which is associated with the symmetry of escape of photoelectrons in the plane of light polarization. In this case, it is natural to change over from Cartesian components of momentum to cylindrical ones: $p_\perp = \sqrt{p_x^2 + p_y^2}$, p_z, and $\varphi = \arctan(p_x/p_y)$. We assume that $\gamma \ll 1$ and $\xi^2(1 - \xi^2) \gg \epsilon$ to derive

$$p_{\max} = |\xi|\frac{F}{\omega}, \quad \Delta p_x \sim \sqrt{\frac{\epsilon}{(1-\xi^2)}}\frac{F}{\omega},$$
$$\Delta p_{y,z} \sim \sqrt{\frac{F}{\kappa}} \sim \gamma\sqrt{\epsilon}\frac{F}{\omega}. \tag{30}$$

Therefore, $p_{\max} \gg \Delta p_x \gg \Delta p_y = \Delta p_z$, and the momentum distribution given by Eq. (3) takes the form

$$dW(\mathbf{p}) \propto \exp\left\{-\frac{\kappa}{F}\left[\left(p_\perp - |\xi|\frac{F}{\omega}\right)^2 + p_z^2\right]\right.$$
$$\left. - \frac{(1-\xi^2)}{3\epsilon}\sin^2\varphi\right\}. \tag{31}$$

At $1 - \xi^2 \le \epsilon$, this distribution starts spreading over the azimuth angle φ (as is well seen in Figs. 4e and 4f) and, at $\xi = \pm 1$, changes directly to the known distribution for circular polarization [26, 27]. It is possible to demonstrate [5] that formula (31) follows from (27) as well.

As to the total probability (or ionization rate) $W = \sum_n w_n$, the relevant formulas derived in [2, 3] (valid for any values of γ) in the tunnel limit of $\gamma \ll 1$ coincide with the expressions given in [5], provided the inaccuracies in the latter expressions, which were referred to in Section 5 of [6], are corrected.

Therefore, the "inconsistency" between the results of [4] and [5], referred to in [5], is fully eliminated (note that the calculations in [4, 5] were performed for different calibrations of the electromagnetic field).

ACKNOWLEDGMENTS

We are grateful to S.P. Goreslavskii for numerous fruitful discussions, to S.G. Pozdnyakov for assistance in performing numerical calculations, and to N.S. Libova and M.N. Markina for assistance in preparing the manuscript.

This study was supported in part by the Russian Foundation for Basic Research (project nos. 98-02-17007, 00-02-16534, and 00-02-17078). One of the authors (S.N. Popruzhenko) is grateful to the International Association for Assistance to Cooperation with Scientists from New Independent States of the former Soviet Union for financial support (INTAS, project no. 99-450).

APPENDIX A

The following is a simple derivation of formula (8), based on the imaginary time method. The extreme subbarrier trajectory of electron in the field given by Eq. (1) has the form

$$x(t) = \frac{F}{\omega^2}(\cosh\tau_0 - \cosh\tau),$$
$$y(t) = -i\xi\frac{F}{\omega^2}\left(\sinh\tau - \frac{\sinh\tau_0}{\tau_0}\tau\right), \quad z = 0, \tag{A.1}$$

where $\tau = -i\omega t$ varies from $\tau_0 = \tau_0(\gamma, \xi)$ (the initial moment of subbarrier motion) to $\tau = 0$ at the moment of electron exit from under the barrier. Hence,

$$p_x(0) = p_z(0) = 0,$$
$$p_y(0) = -i\omega\frac{dy}{d\tau} = \frac{\xi F}{\omega}\left(\frac{\sinh\tau_0}{\tau_0} - 1\right). \tag{A.2}$$

After exiting from under the barrier, the electron moves in the classical trajectory; therefore,

$$p_x(t) = p_x(0) + F\int_0^t \cos\omega t' dt',$$
$$p_y(t) = p_y(0) + \xi F\int_0^t \sin\omega t' dt'. \tag{A.3}$$

These integrals assume a unique meaning if one takes into account the switching off of the external field at $t \longrightarrow +\infty$,

$$J_1 = \lim_{\alpha \to +0}\int_0^\infty e^{-\alpha t}\cos\omega t dt = \frac{\alpha}{\omega^2 + \alpha^2} \longrightarrow 0,$$
$$J_2 = \lim_{\alpha \to +0}\int_0^\infty e^{-\alpha t}\sin\omega t dt = \frac{\omega}{\omega^2 + \alpha^2} \longrightarrow \frac{1}{\omega}. \tag{A.4}$$

The results of integration in (A.3) do not depend on the concrete form of switching off the external field; it is only required that this switching off should be sufficiently slow ($\alpha \ll \omega$), which may be illustrated using the following example. We replace the cut-off factor $\exp(-\alpha t)$ in (A.4) by the Gaussian factor $\exp[-(\alpha t)^2]$ to derive

$$J_1 = \frac{\sqrt{\pi}}{2\alpha}\exp\left(-\frac{\omega^2}{4\alpha}\right) \longrightarrow 0, \quad J_2 = \frac{1}{\alpha}w\left(\frac{\omega}{2\alpha}\right) \longrightarrow \frac{1}{\omega}. \tag{A.4'}$$

Here,

$$w(x) = e^{-x^2}\int_0^x e^{y^2}dy = x_1F_1\left(1, \frac{3}{2}; -x^2\right) = \begin{cases} x - \frac{2}{3}x^2 + \frac{4}{15}x^3 - \dots, & x \longrightarrow 0, \\ \frac{1}{2x} + \frac{1}{4x^3} + O(x^{-5}), & x \longrightarrow \infty \end{cases} \tag{A.5}$$

is the so-called Doson function [28]. Analogously, with the Lorentz form of cut-off $[1 + (\alpha t)^2]^{-1}$, we have $J_1 \sim \exp(-\omega/\alpha)$ and $J_2 = \omega^{-1}[1 + O(\alpha^2/\omega^2)]$. For an arbitrary smooth (analytical) function of switching off of the field, the momentum difference $p_x(\infty) - p_x(0)$ is exponentially small.

We find, from (A.2)–(A.4),

$$p_x(\infty) = p_z(\infty) = 0, \quad p_y(\infty) = p_y(0) + \frac{\xi F}{\omega} = \frac{\xi F}{\omega}\frac{\sinh\tau_0}{\tau_0} \equiv p_{\max}, \tag{A.6}$$

which coincides with Eq. (8). In the case of $0 < |\xi| < 1$, the momentum $\mathbf{p}_{\max}$ is directed on the y axis, i.e., along the minor axis of the field ellipse [4].

Note that, in the subbarrier motion, the coordinate $x(t)$ is real, and the coordinate $y(t)$ is purely imaginary. Accordingly, the velocity component $v_x(t) = dx/dt$ is purely imaginary, and the component $v_y(t)$ is real. Because at $t > 0$, the motion is classically allowed, the electron momentum at the exit from under the barrier may be directed only along the y axis. The situation is analogous in the case of ionization by constant electric and magnetic fields of arbitrary direction [24, 29], when the subbarrier trajectory is non-one-dimensional due to the effect of the Lorentz force. Therefore, in multidimensional problems of quantum mechanics, the turning point is not, generally speaking, the arrest point of a classical particle.

Note that the foregoing inference is valid only for short laser pulses, when $\alpha/\omega \ll 1$. For long pulses, the variation of the time average (drift) electron momentum under the effect of the gradient force is significant [30]. In order to calculate the distribution of outgoing electrons by the final kinetic energies, one must treat their motion in a spatially nonuniform field in the region of laser focus and take into account the effect of ponderomotive acceleration. In simple models, this can be done analytically [31], and for realistic field profiles, numerically [32].

APPENDIX B

The probability of n-photon ionization of the atomic s-level is determined as a result of integration of the distribution given by Eq. (3) with the δ-function expressing the law of conservation of energy in the case of multiphoton ionization by periodic field [1, 4],

$$w_n = \int\delta\left(\frac{p^2 - p_n^2}{2}\right)|F(\mathbf{p})|^2 d^3p, \quad p_n = \sqrt{2\omega(n-\nu)}. \tag{B.1}$$

We assume that

$$p_x = p_n\sqrt{1-u^2}\sin\varphi, \quad p_y = p_n u, \quad p_z = p_n\sqrt{1-u^2}\cos\varphi \tag{B.2}$$

($-1 \le u \le 1$) and perform integration over the azimuth angle φ to derive

$$w_n = 2\pi A p_n J, \tag{B.3}$$

where

$$J = \int_{-1}^{1} du \exp\{-2(n-\nu)[c_x(1-u^2) + c_y(u - \xi q)^2]\} \times a(c(1-u^2)). \tag{B.4}$$

Here, $q = p_F/p_n$, $c = (n - \nu)(c_z - c_x)$, the coefficients c_i are given in (7'), the function $a(x)$ is defined in (13), and the quantities A and p_F have the same values as in formulas (6) and (8).

Therefore, the calculation of the probabilities w_n that preassign the energy spectrum is reduced to a single integral, which generally speaking, is not calculated analytically. Below, we will treat three limiting cases in which further simplifications are possible.

1. For $\gamma \ll 1$, we take into account expansions (9)–(11) to find

$$J = \int_{-1}^{+1} du \exp\{-(n-\nu)\gamma[b_1(1-u^2) + b_2(u - \xi q)^2]\} \times a((n-\nu)\gamma b_3(1-u^2)), \tag{B.5}$$

where

$$b_1 = 2(1-\xi^2)\gamma^2/3, \quad b_2 = 2-(1-\xi^2)\gamma^2/3, \quad b_3 = 1-[1-(7/9)\xi^2]\gamma^2/2. \tag{B.6}$$

Because $b_1 \ll b_2$, the exponent in Eq. (B.5) has a maximum of width $\delta u/u_0 = \xi_1/\xi$ with $u = u_0 = |\xi|q + O(\gamma^2)$, where $\xi_1 = \omega/\sqrt{F\kappa} = \gamma\sqrt{\epsilon} \ll 1$. On eliminating the small region of values of ellipticity $0 \le \xi \le \xi_1$, we can assume that $\delta u \ll 1$. If $|\xi|q < 1$, i.e., $p_n > p_F$, the point u_0 lies in the path of integration. We factor the slowly varying function given by Eq. (13) outside the integral sign and take into account the equality $(n-\nu)(1-u_0^2) = n - n_0$ to arrive at the distribution given by (12). On the contrary, with $|\xi|q > 1$, the integrand in Eq. (B.5) has a maximum at the boundary of the integration region ($u = 1$ or $u = -1$), which produces the distribution given by (14).

2. In the opposite limiting case of $\gamma \gg 1$, in view of (17), we have

$$c_1 = (n-\nu)\frac{2(1-\xi^2)\tau_0^2}{(1-\xi^2)\tau_0+\xi^2},$$
$$c_2 = (n-\nu)\frac{2[(1-\xi^2)\tau_0^2+2\xi^2\tau_0]}{(1-\xi^2)\tau_0+\xi^2}, \tag{B.7}$$
$$c_3 = (n-\nu)\frac{\xi^2\tau_0}{(1-\xi^2)\tau_0+\xi^2}.$$

Outside the narrow interval of $1 \ge |\xi| > 1-(\tau_0\sqrt{n_0-\nu})^{-1}$, the coefficient $c_1 \gg 1$, and the integral given by Eq. (B.4) is formed on the edge of the integration region, so that, at $\tau_0 \gg 1$,

$$w_n \propto \exp\left\{-2\tau_0\left[\frac{(1-\xi^2)\tau_0+2\xi^2}{(1-\xi^2)\tau_0+\xi^2}\right] \times (\sqrt{n-\nu}-\sqrt{n_0-\nu})^2\right\}, \tag{B.8}$$

whence immediately follows distribution (18).

3. Finally, in the case of linear polarization,

$$c_x = \tau_0 - \tanh\tau_0, \quad c_y = 2\tau_0, \quad c_z = (n-\nu)\tanh\tau_0, \quad \tau_0 = \operatorname{arcsinh}\gamma. \tag{B.9}$$

In view of the value of the integral

$$\int_0^1 \exp(-2cu^2) \times a(c(1-u^2))du = w(\sqrt{2c})/\sqrt{2c}, \quad c > 0 \tag{B.10}$$

(the function $w(x)$ was defined in (A.5)), we derive from Eqs. (B.4) and (B.5) the expressions for probabilities w_n, which were earlier derived for this case ($\xi = 0$) previously in [2, 3].

REFERENCES

1. L. V. Keldysh, Zh. Éksp. Teor. Fiz. **47**, 1945 (1964) [Sov. Phys. JETP **20**, 1307 (1964)].
2. A. I. Nikishov and V. I. Ritus, Zh. Éksp. Teor. Fiz. **50**, 255 (1966) [Sov. Phys. JETP **23**, 168 (1966)].
3. A. M. Perelomov, V. S. Popov, and M. V. Terent'ev, Zh. Éksp. Teor. Fiz. **50**, 1393 (1966) [Sov. Phys. JETP **23**, 924 (1966)].
4. A. M. Perelomov, V. S. Popov, and M. V. Terent'ev, Zh. Éksp. Teor. Fiz. **51**, 309 (1966) [Sov. Phys. JETP **24**, 207 (1967)].
5. S. P. Goreslavskiĭ and S. V. Popruzhenko, Zh. Éksp. Teor. Fiz. **110**, 1200 (1996) [JETP **83**, 661 (1996)].
6. V. S. Popov, Zh. Éksp. Teor. Fiz. **118**, 56 (2000) [JETP **91**, 48 (2000)].
7. M. Bashkansky, P. H. Bucksbaum, and D. W. Shumaher, Phys. Rev. Lett. **59**, 274 (1987); **60**, 2458 (1988).
8. L. D. van Woerkom, P. Hansch, and M. A. Walker, in *Proceedings of the 7th International Conference on Multiphoton Processes, 1996*, Ed. by P. Lombropoulos and H. Walther (Institute of Physics Publ., Bristol, 1996); Inst. Phys. Conf. Ser. **154**, 78 (1997).
9. G. G. Paulus, F. Zacher, H. Walther, *et al.*, Phys. Rev. Lett. **80**, 484 (1998).
10. G. G. Paulus, F. Grasbon, A. Dreischuh, *et al.*, Phys. Rev. Lett. **84**, 3791 (2000).
11. E. A. Nersesov and D. F. Zaretsky, Laser Phys. **3**, 1105 (1993).
12. W. Becker, A. Lohr, M. Kleber, and M. Lewenstain, Phys. Rev. A **56**, 645 (1997).
13. M. Yu. Kuchiev, J. Phys. B **28**, 5093 (1995).
14. A. Becker and F. H. M. Faisal, in *Proceedings of the 7th International Conference on Multiphoton Processes, 1996*, Ed. by P. Lombropoulos and H. Walther (Institute of Physics Publ., Bristol, 1997); Inst. Phys. Conf. Ser. **154**, 118 (1997).
15. A. Lohr, M. Kleber, R. Kopold, and W. Becker, Phys. Rev. A **55**, R4003 (1997).
16. V. S. Popov, V. P. Kuznetsov, and A. M. Perelomov, Zh. Éksp. Teor. Fiz. **53**, 331 (1967) [Sov. Phys. JETP **26**, 222 (1968)].
17. V. S. Popov, B. M. Karnakov, and V. D. Mur, Zh. Éksp. Teor. Fiz. **113**, 1579 (1998) [JETP **86**, 860 (1998)].
18. A. I. Baz', Ya. B. Zel'dovich, and A. M. Perelomov, *Scattering, Reactions and Decays in Nonrelativistic Quantum Mechanics* (Nauka, Moscow, 1971, 2nd ed.; Israel Program for Scientific Translations, Jerusalem, 1966).
19. A. A. Radtsig and B. M. Smirnov, *Reference Data on Atoms, Molecules, and Ions* (Énergoatomizdat, Moscow, 1986; Springer-Verlag, Berlin, 1985).
20. D. R. Hartree, Proc. Cambridge Philos. Soc. **24**, 89 (1927).

21. M. J. Seaton, Mon. Not. R. Astron. Soc. **118**, 504 (1958); Rep. Prog. Phys. **46**, 167 (1983).
22. D. R. Bates and A. Damgaard, Philos. Trans. R. Soc. London **242**, 101 (1949).
23. L. P. Rapoport, B. A. Zon, and N. L. Manakov, *Theory of Multiphoton Processes in Atoms* (Atomizdat, Moscow, 1978).
24. V. D. Mur, B. M. Karnakov, and V. S. Popov, Zh. Éksp. Teor. Fiz. **115**, 521 (1999) [JETP **88**, 286 (1999)]; Dokl. Akad. Nauk **365**, 329 (1999) [Dokl. Phys. **44**, 156 (1999)].
25. V. S. Popov, Pis'ma Zh. Éksp. Teor. Fiz. **70**, 493 (1999) [JETP Lett. **70**, 502 (1999)]; Laser Phys. **10**, 1033 (2000).
26. P. Dietrich, N. H. Burnett, M. Ivanov, and P. B. Corkum, Phys. Rev. A **50**, R3585 (1994).
27. V. P. Krainov, J. Opt. Soc. Am. B **14**, 425 (1997).
28. *Handbook of Mathematical; Functions*, Ed. by M. Abramowitz and I. A. Stegun (Dover, New York, 1965).
29. L. P. Kotova, A. M. Perelomov, and V. S. Popov, Zh. Éksp. Teor. Fiz. **54**, 1151 (1968) [Sov. Phys. JETP **27**, 616 (1968)].
30. A. V. Gaponov and M. A. Miller, Zh. Éksp. Teor. Fiz. **34**, 242 (1958) [Sov. Phys. JETP **7**, 168 (1958)].
31. S. P. Goreslavskiĭ, N. B. Narozhnyĭ, and V. P. Yakovlev, Pis'ma Zh. Éksp. Teor. Fiz. **46**, 173 (1987) [JETP Lett. **46**, 219 (1987)]; S. P. Goreslavskii, N. B. Narozhny, and V. P. Yakovlev, J. Opt. Soc. Am. B **6**, 1572 (1989).
32. J. H. Eberly, J. Javanainen, and K. Rzazewsky, Phys. Rep. **204**, 331 (1991).

Translated by H. Bronstein

Journal of Experimental and Theoretical Physics, Vol. 92, No. 5, 2001, pp. 789–794.
Translated from Zhurnal Éksperimental'noĭ i Teoreticheskoĭ Fiziki, Vol. 119, No. 5, 2001, pp. 906–912.
Original Russian Text Copyright © 2001 by Knyr, Nasyrov, Popov.

ATOMS, SPECTRA, RADIATION

Application of the *J* Matrix Method for Describing the (*e*, 3*e*) Reaction in the Helium Atom

V. A. Knyr[a, *], V. V. Nasyrov[a, **], and Yu. V. Popov[b, *]**
[a]*Khabarovsk State Technical University, Khabarovsk, 680035 Russia*
[b]*Skobel'tsyn Research Institute of Nuclear Physics, Moscow State University, Vorob'evy gory, Moscow, 119899 Russia*
**e-mail: knyr@fizika.khstu.ru*
***e-mail: nasyrov@fizika.khstu.ru*
****e-mail: popov@srdlan.npi.msu.su*

Received December 13, 2000

Abstract—The nondemocratic decay model is used to calculate the differential cross sections for a series of (*e*, 3*e*) experiments employing the *J* matrix method. The results of computations are compared with the experimental data as well as with the theoretical results obtained by other authors. © *2001 MAIK "Nauka/Interperiodica".*

1. INTRODUCTION

The structure of quantum systems with more than two particles and the reactions between them, which are referred to in the scientific literature as "few body problems in physics," drew the attention of scientists even at the dawn of the creation of quantum mechanics. The powerful impetus received by this field during the last two decades is due to a significant improvement in the technical basis for the so-called coincidental experiments in which the largest number of parameters (energies, angles, polarization, etc.) of the fragments of the decay reactions are triggered by a particle impinging on a many-particle system (nucleus, atom, molecule, thin film). The matrix elements for describing such reactions include many-particle wave functions with different asymptotic forms of the channels, and hence the problem of their correct approximate computation assumes prime importance. It was observed that the larger the number of decay fragments, the more accurate the approximate algorithms required for solving the many-particle Schrödinger equation.

At present, the most widely used is the close-coupling formalism, in which a many-particle wave function is expanded in some "convenient" basis to transform the initial Schrödinger equation into an infinite system of coupled linear algebraic equations for the coefficients of such an expansion. Thus, the problem is reduced to the selection of the initial basis which can best reflect the physics of the process under consideration, and to the creation of an optimal and economical computational algorithm.

The differential cross sections of elastic and quasielastic scatterings of electrons by atoms reproduce the experimental data quite satisfactorily, even on the absolute scale. The calculations of the process of single ionization of an atom by an electron (called the (*e*, 2*e*) reaction) and photoionization are currently made by using a modification of the close-coupling method, which was developed by Bray *et al*. [1, 2] as a computer program called the convergent close-coupling (CCC) method. An analogous computer program was developed independently at the Khabarovsk State Technical University by the authors for the case of single ionization of a helium atom by electron impact [3]. The high energy of the incident and scattered electrons (of the order of 5–8 keV in the experiments conducted by the Orsay group [4]) allowed the authors to make a number of simplifying assumptions, including the description of a fast electron by a plane wave and the use of the one-photon exchange approximation (confining to the first Born term).

The results of our computations [3] show that for large values of the transferred momenta $Q > 1$ at. unit and energies of the emitted electron $E_1 > 20$ eV, its angular distribution in the reaction He(*e*, 2*e*)He^+ is in good agreement with the experiment if the He^+ ion is in the ground state. However, the difference between the theoretical results and the experimental data is found to increase uniformly in the region of the inverse peak upon a decrease in the values of Q and E_1. It was observed [5] that all theoretical results obtained for this kinematic region, including the simplest models of the wave functions for the initial as well as final states, lead to nearly identical results which do not match the experimental data.

A similar regularity is observed if the He^+ ion is in the excited state: a higher value of the multiplying factor is required with decreasing Q and E_1. However, the contribution of the two-photon exchange (second Born term) becomes significant in this case [6], although this problem has not been investigated comprehensively.

A series of (e, 3e) experiments on helium atoms [7] conducted recently by the Orsay group revealed even greater disparities between the theoretical and experimental results. In this series, the incident and the scattered electrons again have high energies of the order of 5 keV, while the two slow emitted electrons have low energies (not exceeding 10 eV). The emission angle of one of the electrons was fixed while the fivefold differential cross section was treated as a function of the angle at which the other electron was emitted. The small value (0.24 at. units) of the transferred momentum Q might indicate the closeness of the experimental situation to the optical limit and the dominance of the contribution from the dipole transition. However, the results of measurements do not confirm this assumption on the whole. This prompted us to carry out computations for the series of (e, 3e) experiments using the CCC modification based on the J matrix method, which was found to be highly effective in the analysis of (e, 2e) processes [3].

2. THEORY

In this work, the J-matrix method was used for computations of the He(e, 3e)He^{++} reaction, for which a large body of experimental data is available on the measurement of the angular distribution of the electrons emitted from the helium atom [7]. The kinematic conditions under which these experiments were carried out (the incident and scattered electron energy $E_i \approx E_s \approx$ 5–8 keV, while the energies E_1 and E_2 of the electrons emitted by the helium atom are of the order of a few electron-volts) made it possible to confine the analysis to the first Born approximation (exchange of a virtual photon between the incident electron and the atom) and to use the nondemocratic decay model, whose principal assumption stipulates the existence of an intermediate pseudostate for the He$^+$ ion with an energy equal to the energy of one of the electrons knocked out in the (e, 3e) reaction. This allows us to present the amplitude of the (e, 3e) process in the form of the sum

$$f^{(e,3e)} = \sum_{\mu} f_{\mu}^{(e,2e)} f_{\mu}^{(e,e)},$$

where $f_{\mu}^{(e,2e)}$ is the amplitude of the (e, 2e) reaction and $f_{\mu}^{(e,e)}$ is the amplitude of the second electron emission as a result of shaking—the subscript μ labels the pseudostates of the He$^+$ ion which can be conveniently characterized by the quantum numbers (n, l, m). In a more elaborate form of the notation, we can write

$$f^{(e,3e)} = -\frac{2}{\mathbf{Q}^2}\sum_{nlm}\langle\psi^{-}_{nlm}(\mathbf{p}_1)|\exp(i\mathbf{Q}\cdot\mathbf{r}_1) + \exp(i\mathbf{Q}\cdot\mathbf{r}_2) - 2|\phi_0\rangle\langle\Phi^{-}_{C}(\mathbf{p}_2)|\Phi_{nlm}\rangle. \quad (1)$$

Here, $\psi^{-}_{nlm}(\mathbf{p}_1; \mathbf{r}_1, \mathbf{r}_2)$ is the wave function of the final state in the (e, 2e) process in which, however, the pseudostate is considered instead of the wave function of the real ion-core, $\Phi^{-}_{C}(\mathbf{p}_2)$ is the Coulomb function of the electron scattered in the field of the He^{++} ion, $\mathbf{Q} = \mathbf{p}_i - \mathbf{p}_s$ is the momentum transferred to the system, Φ_{nlm} is the wave function of the pseudostate of the He$^+$ ion, and ϕ_0 is the wave function of the helium atom.

For numerical computations, it is convenient to determine the total orbital angular momentum L of two electrons and its projection M in the wave function $\psi^{-}_{nlm}(\mathbf{p}_1; \mathbf{r}_1, \mathbf{r}_2)$ of the final state. In this case, the wave function of the final state of the He$^+$ ion and of the knocked-out electron can be presented in the form of the expansion

$$|\psi^{-}_{nlm}(\mathbf{p}_1)\rangle = \frac{1}{\sqrt{p_1}}\sum_{\lambda\mu} a^{L}_{\nu'\Gamma'\Gamma}(E) \times C^{LM}_{lm\lambda\mu} Y_{\lambda\mu}(\hat{\mathbf{p}}_1)|(n'l')(\nu'\lambda') : LM\rangle, \quad (2)$$

where $Y_{\lambda\mu}(\hat{\mathbf{p}}_1)$ is a spherical function, nlm are the quantum numbers of the He$^+$ ion in the final state, $\lambda\mu$ are the quantum numbers of the knocked-out electron, $\Gamma' \equiv (n'l'\lambda')$ is the index of the reaction channel, $E = p_1^2/2 + \varepsilon_{nl}$ is the total energy, $\varepsilon_{n'l'}$ is the energy of the pseudostate, and the basis vectors $|(\nu\lambda)(nl) : LM\rangle$ have the following form in the coordinate representation:

$$\langle\mathbf{r}_1, \mathbf{r}_2|(nl)(\nu\lambda) : LM\rangle = \begin{cases} \dfrac{1}{r_1 r_2}\mathcal{P}[\chi_{nl}(r_2)\chi_{\nu\lambda}(r_1)\mathcal{Y}_{l\lambda LM}(\hat{\mathbf{r}}_2, \hat{\mathbf{r}}_1)], & n \le N_l, \\ \dfrac{1}{r_1 r_2}\mathcal{P}[\chi_{nl}(r_2)\phi_{\nu\lambda}(\xi_\lambda r_1)\mathcal{Y}_{l\lambda LM}(\hat{\mathbf{r}}_2, \hat{\mathbf{r}}_1)], & n > N_l, \end{cases} \quad (3)$$

where $\mathcal{P}$ is the symmetrization operator, $\chi_{nl}(r)$ are the radial wave functions of the pseudostates, and

$$\mathcal{Y}_{l\lambda LM}(\hat{\mathbf{r}}_2, \hat{\mathbf{r}}_1) = \sum_{m\mu}\langle lm\lambda\mu|LM\rangle Y_{lm}(\hat{\mathbf{r}}_2)Y_{\lambda\mu}(\hat{\mathbf{r}}_1).$$

The wave function of the ground state of the He atom is also sought in the form of an expansion in the basic set (3):

$$|\phi_0\rangle = \sum_{\lambda l}\sum_{n=0}^{N_l}\sum_{\nu=0}^{N_\lambda} a^{(0)}_{n\nu l\lambda}|(nl)(\nu\lambda) : 00\rangle. \quad (4)$$

The wave functions $\chi_{nl}(r)$ are defined by the method of pseudostates in which it is assumed that one of the electrons may be in a pseudostate characterized by the wave function

$$\Phi_{nlm}(\mathbf{r}) = \frac{1}{r}\chi_{nl}(r)Y_{lm}(\hat{\mathbf{r}}), \quad (5)$$

while the other electron is in a state which may pertain to a discrete or a continuous spectrum. The number of pseudostates is assumed to be finite, and hence the wave functions $\chi_{nl}(r)$ are sought in the form of an expansion in basis functions:

$$\chi_{nl}(r) = \sum_{n'=0}^{N_l} D^l_{nn'}\phi_{n'l}(\xi_l r), \tag{6}$$

where ξ_l is the basis parameter. It is convenient to solve problems with Coulomb interaction using the Laguerre basis:

$$\begin{aligned}\phi_{nl}(x) &= \sqrt{\frac{n!}{(n+2l+1)!}}\\ &\times x^{l+1}\exp\left(-\frac{x}{2}\right)L_n^{2l+1}(x),\end{aligned} \tag{7}$$

where $L_n^{\alpha}(x)$ are the associated Laguerre polynomials. The quantity N_l defines the accuracy of calculations of wave functions [8]. This parameter can be selected independently for each partial wave.

The expansion coefficients $a^L_{\nu'\Gamma'\Gamma}(E)$ are the solutions of the infinite set of algebraic equations

$$\begin{aligned}&\sum_{M\Gamma'}\sum_{\nu'=0}^{\infty} a^L_{\nu'\Gamma'\Gamma}(E)\langle(n'l')(\nu'\lambda') : LM\\ &\times|H-E|(n''l'')(\nu''\lambda'') : LM\rangle = 0,\end{aligned} \tag{8}$$

where H is the Hamiltonian of the two-electron target, which can be presented without taking into account the spin–orbit interaction in the form

$$H = -\frac{1}{2}\Delta_1 - \frac{1}{2}\Delta_2 - \frac{Z}{r_1} - \frac{Z}{r_2} + \frac{1}{r_{12}}. \tag{9}$$

The system of equations (8) is solved approximately with the help of the *J*-matrix method [9]. The application of the main approximation of the *J*-matrix formalism to this problem involves the disregard of the matrix elements of the residual interaction $V = r_1^{-1} - r_{12}^{-1}$ under the condition $\nu' > N_{\lambda'}$ and (or) $\nu'' > N_{\lambda''}$.

Consequently, the system of equations (8) splits into two parts, viz., the internal part ($\nu'' \le N_{\lambda''}$) and the external part ($\nu'' > N_{\lambda''}$). For $\nu'' \le N_{\lambda''}$, the infinite system of equations can be analytically solved exactly, and its solutions are essentially the exact Coulomb functions of the ejected electron in the chosen discrete representation, multiplied by the wave functions of the pseudostates of the ion-core. For $\nu'' \le N_{\lambda''}$, the system of equations (8) is solved by the method of diagonalization. By matching the internal and external solutions, we can determine the parameters of the continuous spectrum of a two-electron atomic system. In order to determine the wave function $\phi_0(\mathbf{r}_1, \mathbf{r}_2)$ of the ground state, it is sufficient to diagonalize the matrix of Hamiltonian (9) in basis (3).

The application of the above-mentioned theoretical model for computations of the (*e*, 2*e*) reactions in a helium atom gave quite satisfactory results [3]. The amplitude of the (*e*, 2*e*) process can be obtained by using the functions (2) and (4), which are symmetric relative to the transposition of coordinates $\mathbf{r}_1$ and $\mathbf{r}_2$:

$$\begin{aligned}f^{(e,2e)}_{nlm} &= -\frac{4}{Q^2}\langle\psi^-_{nlm}|\exp(i\mathbf{Q}\cdot\mathbf{r}_1) - 1|\phi_0\rangle\\ &= -\frac{4}{Q^2}\sum_{L\lambda} J^{\Gamma}_L(Q)C^{L0}_{lm\lambda,-m}Y^*_{\lambda,-m}(\hat{\mathbf{p}}_1),\end{aligned} \tag{10}$$

where

$$J^{\Gamma}_L(Q) = \sum_{\nu'\Gamma'}(a^*)^L_{\nu'\Gamma'\Gamma}D^{L0}_{\nu'\Gamma'}(Q), \tag{11}$$

$$\begin{aligned}D^{LM}_{\nu\Gamma}(Q) &= \langle(n'l')(\nu'\lambda') : LM\\ &\times\|1 - i^L\sqrt{4\pi}j_L(Qr)Y_L(\hat{\mathbf{r}})\|\psi_0\rangle,\end{aligned} \tag{12}$$

$C^{L0}_{lm\lambda,-m}$ is the Glebsch–Gordan coefficient and j_L is a spherical function.

The amplitude $f^{(e,e)}_{nlm}$ is computed in an analogous manner.

Using the expression for the amplitude $f^{(e,3e)}$ and taking into account the normalization of the wave function (2), we can easily obtain the differential cross section $\sigma^{(5)}$ of the (*e*, 3*e*) reaction in the form

$$\sigma^{(5)} \equiv \frac{d^5\sigma}{d\Omega_s dE_1 d\Omega_1 dE_2 d\Omega_2} = \frac{p_s}{p_i p_2}\left|f^{(e,3e)}\right|^2. \tag{13}$$

3. DISCUSSION OF RESULTS

The close-coupling method applied to (*e*, 3*e*) reactions has a significant drawback: the strong repulsion of the electrons ejected from the target upon a decrease in the angle between them and the closeness of their energies cannot be explained by taking into account the finite number of pseudostates. In order to take into account the electron–electron repulsion, the wave function of the final state can be multiplied [10] by the so-called Gamow factor introduced in [11]:

$$\varphi(|\mathbf{p}_1 - \mathbf{p}_2|) = \exp\left(-\frac{\pi}{|\mathbf{p}_1 - \mathbf{p}_2|}\right)\Gamma\left(1 - \frac{1}{|\mathbf{p}_1 - \mathbf{p}_2|}\right).$$

The Gamow factor is a part of the approximate three-particle function of the final state having a regular three-particle asymptotic form. However, such a multiplication results in the loss of orthogonality of the two-electron continuum functions and, consequently, the

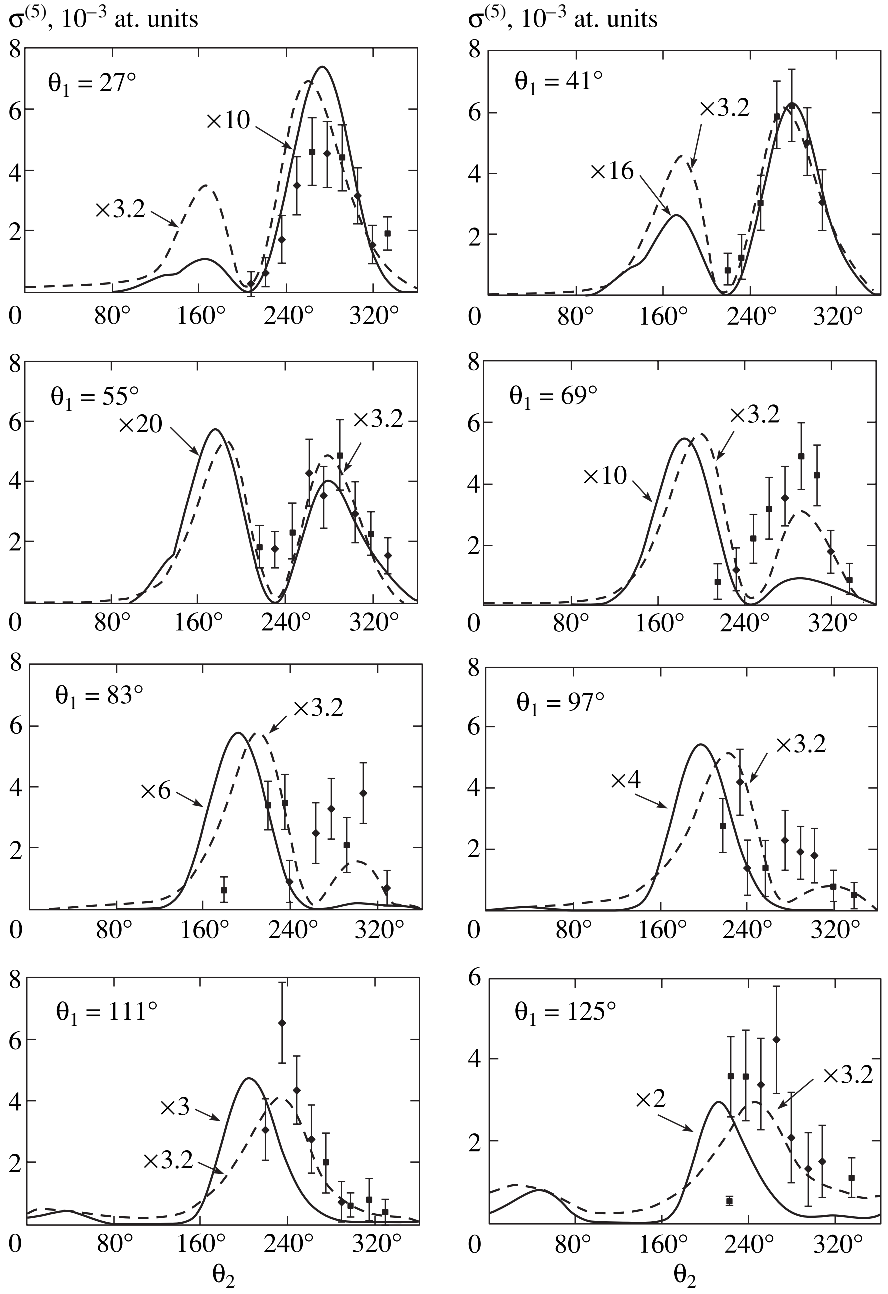

Fig. 1. Differential cross sections $\sigma^{(5)} = d^5\sigma/d\Omega_s dE_1 d\Omega_1 dE_2 d\Omega_2$ of the $(e, 3e)$ reaction in a helium atom for the projectile electron energy $E_i = 5599$ eV. The angle of the scattered electron $\theta_s = 0.45°$, and transferred momentum $Q = 0.24$ at. units. The emitted electron energies are $E_1 = E_2 = 10$ eV. The solid curves correspond to our calculations, and the dashed curves to the calculations made in [7]. The experimental results are borrowed from [7].

absolute value of the differential cross section $\sigma^{(5)}$ decreases sharply. In order to restore the correct absolute value, we normalize the result to the differential cross section $\sigma^{(4)}$:

$$\sigma^{(4)} = \int_0^{\pi} \sigma^{(5)} d\theta_2.$$

Thus, the differential cross section $\sigma_G^{(5)}$ is calculated by using the following expression:

$$\sigma_G^{(5)} = \frac{\sigma^{(5)}|\varphi(|\mathbf{p}_1 - \mathbf{p}_2|)|^2}{\int_0^{\pi} \sigma^{(5)}|\varphi(|\mathbf{p}_1 - \mathbf{p}_2|)|^2 d\theta_2} \sigma^{(4)}.$$

It should be observed that such a normalization is quite appropriate in the present case since a considerable part

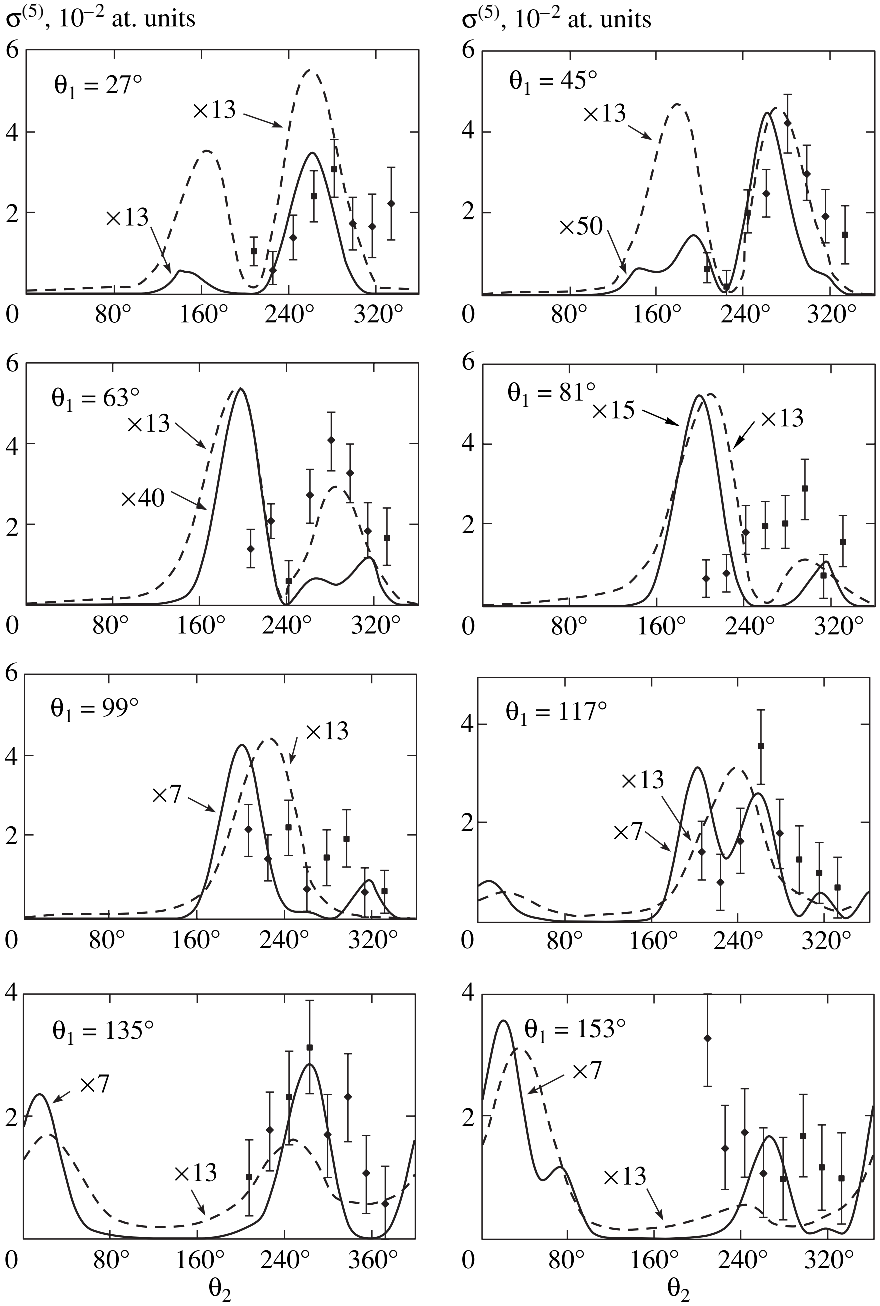

Fig. 2. Differential cross sections $\sigma^{(5)} = d^5\sigma/d\Omega_s dE_1 d\Omega_1 dE_2 d\Omega_2$ of the $(e, 3e)$ reaction in a helium atom for the projectile electron energy $E_i = 5599$ eV. The angle of the scattered electron $\theta_s = 0.45°$, and transferred momentum $Q = 0.24$ at. units. The emitted electron energies are $E_1 = E_2 = 4$ eV. The solid curves correspond to our calculations, and the dashed curves to the calculations made in [7]. The experimental results are borrowed from [7].

of interactions of the knocked-out electrons in the final state are taken into account during computation of the amplitude $f_{nlm}^{(e, 2e)}$ using the *J*-matrix approach.

The results of computations are shown in Figs. 1 and 2. The differential cross sections of the He$(e, 3e)$He^{++} process are shown in the graphs (in atomic units) as functions of the plane emission angle of one of the helium electrons measured from the direction of the beam of incident fast electrons ($E_i = 5599$ eV), the plane angle of the second electron being fixed and indicated in the upper left corner of the graphs. The energies of the electrons are 10 eV (Fig. 1) and 4 eV (Fig. 2), respectively. In all the figures, $\theta_Q = 319°$. The solid curve corresponds to the results of our calculations, and the dashed one, to the calculations made by Kheifets [7] using the CCC technique. The experimental results are borrowed from the same work.

The results of our calculations show a close coincidence (except for the multiplication factor) of the angular distribution of the emitted electrons with the calculations made by Kheifets et al. on a powerful multiprocessor computer. The same physical model of nondemocratic decay was used in both cases. However, it should be remarked that in a number of cases, both calculations displayed a significant discrepancy with the experimental results in magnitude and in the angle of emission of the electron. These departures from the results of independent qualitative computations clearly indicate the manifestation of new physical effects even in a simple atom like helium.

First, it is apparent that the nondemocratic decay model, which stems from experiments involving the emission of high-energy (of the order of 300–500 eV) electrons [12], is less suitable for the physics of low-energy processes with emission energies of 5–20 eV. This conclusion is confirmed, among other things, by the recent series of (*e*, 3*e*) experiments carried out by the Ulrich group in Germany [13]. Thus, a basically new model for taking correlation into account is required for calculating the differential cross sections of an (*e*, 3*e*) reaction in the kinematic region of close and low electron emission energies.

Second, neither of the trial wave functions of the helium atom ground state used in these calculations brings us any closer to a formal solution of the Schrödinger equation [14]. Nevertheless, these trial functions are convenient for numerical computations. For example, it was observed that the simple trial functions for helium, which were used successfully in calculations of elastic, quasielastic, and even (*e*, 2*e*) reactions, are utterly inadequate for describing the differential cross-sections of (*e*, 3*e*) processes, and more cumbersome multiconfigurational Hartree–Fock or Hylleraas polynomial functions are required for this purpose. However, both the theory and the latest experimental data point towards the possibility of asymptotic quantization of the angle between the electron radius vectors which was postulated by Heisenberg as early as in 1920s. In turn, this considerably changes the form of the atomic wave function at middle distances of electrons from the nucleus, which make the main contribution to the integral of the matrix element used in computations.

Finally, the effect of the intermediate multielectron continuum on the results of calculations cannot be reproduced completely even by a large but finite number of pseudostates in the case of a system with Coulomb potentials.

Thus, more and more serious "ideological" and computational problems are encountered when the close-coupling method is used in the investigations of multielectron ionization processes. New ideas and computational algorithms are needed even for a simple atom like helium.

ACKNOWLEDGMENTS

The authors are deeply indebted to A. Lahmam-Bennani for providing the results of his experimental investigations.

This work was financed under the program "Basic Research in High School Science and Humanities: Russian Universities" (project no. 01.01.58) of the Ministry of Education of the Russian Federation, the special Federal research program "Quantum and Wave Processes" of the Ministry of Industry and Science of the Russian Federation (contract no. 108–39(00)–P), and partly under the special Federal program "Integration" (project no. A0028).

REFERENCES

1. I. Bray, Phys. Rev. A **49**, 1066 (1994).
2. D. V. Fursa and I. Bray, J. Phys. B **30**, 5895 (1997).
3. V. A. Knyr, V. V. Nasyrov, Yu. V. Popov, and L. Ya. Stotland, Zh. Éksp. Teor. Fiz. **109**, 361 (1996) [JETP **82**, 190 (1996)].
4. C. Dupre, A. Lahmam-Bennani, A. Duguet, *et al.*, J. Phys. B **25**, 259 (1992).
5. Yu. V. Popov, V. A. Knyr, V. V. Nasyrov, and A. Lahmam-Bennani, Few-Body Syst., Suppl. **10**, 235 (1999).
6. P. J. Marchalant, C. T. Whelan, and H. R. J. Walters, J. Phys. B **31**, 1141 (1998).
7. A. Kheifets, I. Bray, A. Lahmam-Bennani, *et al.*, J. Phys. B **32**, 5047 (1999).
8. Yu. F. Smirnov, L. Ya. Stotland, and A. M. Shirokov, Izv. Akad. Nauk SSSR, Ser. Fiz. **54**, 897 (1990).
9. H. A. Yamani and L. Fishman, J. Math. Phys. **16**, 410 (1975).
10. M. Grin, C. Dal Cappello, R. El. Mkhanter, and J. Rasch, J. Phys. B **33**, 131 (2000).
11. M. Brauner, J. S. Briggs, and H. Klar, J. Phys. B **22**, 2265 (1989).
12. R. L. Brown, Phys. Rev. A **1**, 586 (1970).
13. A. Dorn, R. Moshammer, C. D. Schröder, *et al.*, J. Phys. IV **9**, Pr6-89 (1999).
14. Yu. V. Popov and L. U. Ancarani, Phys. Rev. A **62**, 042702 (2000).

Translated by Ram Wadhwa

Journal of Experimental and Theoretical Physics, Vol. 92, No. 5, 2001, pp. 795–810.
Translated from Zhurnal Éksperimental'noĭ i Teoreticheskoĭ Fiziki, Vol. 119, No. 5, 2001, pp. 913–930.
Original Russian Text Copyright © 2001 by P. N. Brusov, P. P. Brusov.

SOLIDS
Electronic Properties

Collective Properties of Superconductors with Nontrivial Pairing

P. N. Brusov[a], * and P. P. Brusov[b]
[a]*Cornell University, Ithaca, NY 14853, USA*
[b]*Rostov State University, pr. Stachki 194, Rostov-on-Don, 344104 Russia*
**e-mail: pnb@ccmr.cornell.edu*

Received March 17, 2000

Abstract—Three- and two-dimensional models of *p*- and *d*-pairing are constructed for superconductors and superfluid quantum liquids using the functional integration formalism. In these models, the collective excitation spectra are calculated for superconductors with nontrivial pairing (such as high-temperature superconductors (HTSC) and heavy-fermion superconductors (HFSC)) for *p*- and *d*-pairing. Both three- and two- dimensional systems are considered. Some of recent ideas concerning the realization of the mixture of different states in HTSC are considered. In particular, the mixture of states $d_{x^2-y^2} + id_{xy}$ is analyzed. The obtained results of calculations of collective excitation spectra in superconductors with nontrivial pairing may be used for determining the type of pairing and the order parameter in HTSC and HFSC and also for interpreting the experimental results on ultrasound and microwave absorption in these system. *© 2001 MAIK “Nauka/Interperiodica”.*

1. INTRODUCTION

Until recently, the study of collective excitations in superconductors with nontrivial pairing was rather exotic for several reasons. First, nontrivial pairing was not established reliably even for an individual superconductor in spite of the existence of certain evidence [1] concerning the nontrivial type of pairing in some superconductors (high-temperature superconductors (HTSC) and heavy-fermion superconductors (HFSC)). Second, no sound proof was obtained for the existence of collective excitations in superconductors. The situation has changed radically during recent years and especially during the last year so that the study of collective excitations in superconductors with nontrivial pairing has become a reality. In the light of recent experiments [1], this subject becomes quite vital. Above all, the so-called amplitude mode (with a frequency of the order of 2Δ) associated with order parameter amplitude oscillations was experimentally observed for the first time a few years ago in films of traditional (low-temperature) superconductors [1]. It should be noted that only the first of the two collective modes existing in superconductors and associated with phase and amplitude oscillations in the complex order parameter (zero sound) had been observed experimentally before that. Besides, the type of pairing has been established for many superconductors during the last year (see, for example, [2]): *s*-pairing takes place in traditional (low-temperature superconductors and in HTSC with electron-type conductivity; *d*-pairing is observed in HTSC with hole-type conductivity, organic superconductors, and some HFSC (UPd_2Al_3, $CePd_2Si_3$, $CeIn_3$, $CeNi_2Ge_2$, etc.), while *p*-pairing was detected in pure ^{3}He, ^{3}He in aerogel, Sr_2RuO_4 (HTSC), and UPt_3 (HFSC).

2. MODELS OF *p*- AND *d*-PAIRING FOR SUPERCONDUCTORS

The method of continual integrations as applied to a nonrelativistic Fermi system at a temperature *T* necessitates integration over the space of anticommuting functions $\chi(\mathbf{x}, \tau)$, $\chi(\mathbf{x}, \tau)$ with the Fourier expansion

$$\chi_s(x) = \frac{1}{\sqrt{\beta V}}\sum_p a_s(p)\exp[i(\omega\tau + \mathbf{k}\cdot\mathbf{x})], \qquad (1)$$

where $p = (\mathbf{k}, \omega)$, $\omega = (2n + 1)\pi T$ being the Fermi frequencies; $x = (\mathbf{x}, \tau)$, $\beta = 1/T$; V is the system volume; and T is the temperature.

Let us consider the functional of action for an interacting Fermi system:

$$S = \int_0^\beta d\tau^3 x\sum_s \bar{\chi}_s(\mathbf{x}, \tau)\partial_\tau\chi_s(\mathbf{x}, \tau) - \int_0^\beta \mathcal{H}(\tau)d\tau, \qquad (2)$$

which corresponds to the Hamiltonian

$$\begin{aligned}\mathcal{H}(\tau) = {}& \int d^3x\sum_s \frac{1}{2m}\nabla\bar{\chi}_s(\mathrm{x}, \tau)\nabla\chi_s(\mathbf{x}, \tau)\\ &- (\lambda + s\mu_0 H)\bar{\chi}_s(\mathbf{x}, \tau)\chi_s(\mathbf{x}, \tau) + \frac{1}{2}\int d^3x d^3y U(\mathbf{x} - \mathbf{y}) \qquad (3)\\ &\times\sum_{ss'}\bar{\chi}_s(\mathbf{x}, \tau)\bar{\chi}_{s'}(\mathbf{y}, \tau)\chi_{s'}(\mathbf{y}, \tau)\chi_s(\mathbf{x}, \tau).\end{aligned}$$

1063-7761/01/9205-0795$21.00 © 2001 MAIK “Nauka/Interperiodica”

Here, H is the magnetic field, λ is the chemical potential, μ is the magnetic moment of a particle, U is the pair interaction potential, and s and s' are the spin indices, each of which assumes the value "+" or "–".

Let us first integrate over fast fields χ_1, for which $|k - k_F| > k_0$ or $|\omega| < \omega_0$ in expansion (1), and then over slow Fermi fields, $\chi_0 = \chi - \chi_1$ (here, k_0 and ω_0 are the parameters specifying the layer width at the Fermi surface, which are determined from the order of magnitude and do not affect the physical results). After integrating over fast fields, we consider the terms describing noninteracting quasiparticles at the Fermi surface, which are defined by the quadratic form S_2, and their pair interaction corresponding to the fourth-degree form S_4. Form S_2 can be written as

$$S_2 \approx \sum_{s,\,p} \frac{1}{Z}[i\omega - c_F(k - k_F) + s\mu H] a_s^+(p) a_s(p). \quad (4)$$

Here, Z is the normalization constant and c_F is the velocity of a particle on the Fermi surface. Form S_4 is different for different types of pairing, and hence, the cases of p- and d-pairing will be considered separately.

2.1. p-Pairing

In the case of the triplet pairing, form S_4 can be written as

$$\begin{aligned} S_4 = {} & \frac{1}{\beta V} \sum_{p_1 + p_2 = p_3 + p_4} t_0(p_1, p_2, p_3, p_4) a_+^+(p_1) \\ & \times a_-^+(p_2) a_-(p_4) a_+(p_3) \\ & - \frac{1}{2\beta V} \sum_{p_1 + p_2 = p_3 + p_4} t_1(p_1, p_2, p_3, p_4) \\ & \times [2a_+^+(p_1) a_-^+(p_2) a_-(p_4) a_+(p_3) \\ & + a_+^+(p_1) a_+^+(p_2) a_+(p_4) a_+(p_3) \\ & + a_-^+(p_1) a_-^+(p_2) a_-(p_4) a_-(p_3)]. \end{aligned}$$

Here, $p = (\mathbf{k}, \omega)$ is the 4-momentum, $t_0(p_i)$ and $t_1(p_i)$ are the symmetric and antisymmetric scattering amplitudes for transpositions $p_1 \longleftrightarrow p_2$, $p_3 \longleftrightarrow p_4$, the superscript on a, a^+ correspond to the values of s, s' (±). In the vicinity of the Fermi sphere, we can put $\omega_i = 0$, $\mathbf{k}_i = \mathbf{n}_i k_F$ ($i = 1, 2, 3, 4$). Amplitudes t_0, t_1 must be functions of only two invariants, say, $(\mathbf{n}_1, \mathbf{n}_2)$ and $(\mathbf{n}_1 - \mathbf{n}_2, \mathbf{n}_3 - \mathbf{n}_4)$, the function t_0 being even and t_1 being odd in the second invariant. Consequently, we can write

$$t_0 = f((\mathbf{n}_1, \mathbf{n}_2), (\mathbf{n}_1 - \mathbf{n}_2, \mathbf{n}_3 - \mathbf{n}_4)),$$

$$t_1 = (\mathbf{n}_1 - \mathbf{n}_2, \mathbf{n}_3 - \mathbf{n}_4) g((\mathbf{n}_1, \mathbf{n}_2), (\mathbf{n}_1 - \mathbf{n}_2, \mathbf{n}_3 - \mathbf{n}_4)),$$

functions f and g being even in the second argument. Functions f and g can be easily evaluated in the gas model; for high-density systems, they must be determined from experiment. We consider the model with $f = 0$, $g = \text{const} < 0$ as a model of the BCS type (weak coupling approximation) for superconductors and superfluid quantum liquids with pairing in the p-state.

The most economical way of describing collective excitations is the transition from the initial Fermi fields to Bose fields describing Cooper pairs of quasiparticles. Such a transition can be carried out by inserting, say, a Gaussian integral of $\exp(c^+Ac)$ over a Bose field c, where A is a certain operator, into the integral over slow Fermi fields. After a translation of the Bose field by the quadratic form of the Fermi fields annihilating form S_4, the integral over the Fermi fields becomes a Gaussian integral and is equal to the determinant of operator $\hat{M}(c^+, c)$.

Having integrated over slow Fermi fields, we arrive at the functional of hydrodynamic action in the form

$$\begin{aligned} S_{\text{eff}} = {} & \frac{1}{g} \sum_{p,\,i,\,a} c_{ia}^+(p) c_{ia}(p) \\ & + \frac{1}{2} \ln\det \frac{M(c_{ia}, c_{ia}^+)}{M(c_{ia}^{(0)}, c_{ia}^{(0)+})}, \end{aligned} \quad (5)$$

where $c_{ia}^{(0)}$ are the condensate values of the Bose fields c_{ia} and $M(c_{ia}, c_{ia}^+)$ is a 4 × 4 matrix depending on the Bose fields and quasifermionic parameters, whose elements are given by

$$\begin{aligned} M_{11} &= \frac{1}{Z}[i\omega + \xi - \mu(\mathbf{H} \cdot \boldsymbol{\sigma})] \delta_{p_1 p_2}, \\ M_{22} &= \frac{1}{Z}[-i\omega + \xi + \mu(\mathbf{H} \cdot \boldsymbol{\sigma})] \delta_{p_1 p_2}, \\ M_{12} &= \frac{1}{\beta V}(n_{1i} - n_{2i}) c_{ia}(p_1 + p_2) \sigma_a, \\ M_{21} &= -\frac{1}{\beta V}(n_{1i} - n_{2i}) c_{ia}^+(p_1 + p_2) \sigma_a. \end{aligned} \quad (6)$$

Here, σ_a ($a = 1, 2, 3$) are the Pauli spin matrices, $\sigma = (\sigma_1, \sigma_2, \sigma_3)$. The hydrodynamic action functional contains the entire information on the physical properties of the model system and determines, among other things, the spectrum of its collective excitations [3].

2.2. d-Pairing

In the case of singlet pairing, S_4 has the form

$$\begin{aligned} S_4 = {} & -\frac{1}{\beta V} \sum_{p_1 + p_2 = p_3 + p_4} t(p_1, p_2, p_3, p_4) \\ & \times a_+^+(p_1) a_-^+(p_2) a_-(p_4) a_+(p_3). \end{aligned} \quad (7)$$

The first version of the *d*-pairing model for superconductors, which was obtained by the method of functional integration, was proposed by us earlier [4] in 1994, when the first attempts were made to seriously consider the idea of *d*-pairing in HTSC. We will present below a modified self-consistent model of superconductors with *d*-pairing [5], which will be subsequently used to analyze the spectrum of collective modes in HTSC and HFSC.

In the case of *d*-pairing, we have

$$t(p_1, p_2, p_3, p_4) = V(\hat{k}, \hat{k}') = \sum_{m=-2}^{2} g_m Y_{2m}(\hat{k}) Y^*_{2m}(\hat{k}'). \tag{8}$$

Here,

$$k_1 = k + q/2, \quad k_2 = -k + q/2,$$

$$k_3 = k' + q/2, \quad k_4 = -k' + q/2,$$

and $Y_{2m}(\hat{k})$ are spherical harmonics with $l = 2$. We consider the spherically symmetric case which requires only one coupling constant g. In order to take into account the lattice symmetry, additional coupling constants must be introduced (up to five in the general case, since five is the number of spherical harmonics with $l = 2$). However, this number decreases to two in the case of cubic symmetry and to three in the case of hexagonal symmetry: $g_{|m|}$ ($m = 0, \pm 1, \pm 2$).

It was mentioned above that the number of degrees of freedom for the order parameter in the case of singlet *d*-pairing is equal to ten; i.e., we must have five complex canonical variables. It is natural to chose for canonical variables the following combinations of initial variables:

$$c_1 = c_{11} + c_{22}, \quad c_2 = c_{11} - c_{22}, \quad c_3 = c_{12} + c_{21},$$

$$c_4 = c_{13} + c_{31}, \quad c_5 = c_{23} + c_{32}.$$

In the canonical variables c_j ($j = 1, 2, 3, 4, 5$), the effective functional of action has the form

$$S_{\text{eff}} = \frac{1}{2g}\sum_{p,\,j} c_j^+(p) c_j(p)(1 + 2\delta_{j1}) + \frac{1}{2}\ln\det\frac{M(c_j^+, c_j)}{M(c_j^{+(0)}, c_j^{(0)})}, \tag{9}$$

where

$$M_{11} = \frac{1}{Z}[i\omega + \xi - \mu(\mathbf{H}\cdot\boldsymbol{\sigma})]\delta_{p_1p_2},$$

$$M_{22} = \frac{1}{Z}[-i\omega + \xi + \mu(\mathbf{H}\cdot\boldsymbol{\sigma})]\delta_{p_1p_2},$$

$$M_{12} = M^*_{21} = \frac{1}{\beta V}\left(\frac{15}{32\pi}\right)^{1/2} \times [c_1(1 - 3\cos^2\theta) + c_2\sin^2\theta\cos^2\varphi + c_3\sin^2\theta\sin 2\varphi + c_4\sin 2\theta\cos\varphi + c_5\sin 2\theta\sin\varphi]. \tag{10}$$

Here, δ_{j1} is the Kronecker delta symbol and $\delta_{p_1p_2}$ is the delta function.

3. COLLECTIVE PROPERTIES OF SUPERCONDUCTORS WITH NONTRIVIAL PAIRING

3.1. p-Pairing

The first results on *p*-pairing were obtained by us earlier [3] for *A*-, *B*-, A_1-, 2*D*- and polar phases associated with superfluid ^{3}He in which the first three phases were discovered experimentally. We considered additional superconducting phases that may be formed in HTSC or HFSC.

The results are presented below. It should be recalled that the spectrum of collective modes in each superconducting phase consists of 18 modes including high-frequency and Goldstone modes (Δ is the gap in the Fermi spectrum, Δ_0 is the amplitude of the gap in the Fermi spectrum for an anisotropic gap, and $k_{\parallel}$ is the momentum component of collective excitation, which is parallel to the orbital anisotropy axis $\mathbf{l}$; here and below, the number of collective modes is given in parentheses).

A phase:

$$E = \Delta_0(T)(1.96 - 0.31i) \ (3),$$

$$E = \Delta_0(T)(1.17 - 0.13i) \ (6),$$

$$E^2 = c_F^2 k^2/3 \ (3),$$

$$E^2 = c_F^2 k_{\parallel}^2 \ (6).$$

B phase:

$$E^2 = 12\Delta^2/5 \ (5), \quad E^2 = 8\Delta^2/5 \ (5),$$

$$E^2 = 4\Delta^2 \ (4), \quad E^2 = c_F^2 k^2/3 \ (1),$$

$$E^2 = c_F^2 k^2/5 \ (1), \quad E^2 = c_F^2 k^2/5 \ (2).$$

2*D* phase:

$$E = 0 \ (6); \quad E = \Delta_0(T)(1.96 - 0.31i) \ (2),$$

$$E = \Delta_0(T)(1.17 - 0.13i) \ (4),$$

$$E = 2\mu H \ (2), \quad E_0^2 = \Delta_0^2(T)(1.96 - 0.31i)^2 + 4\mu^2 H^2 \ (2),$$

$$E^2 = \Delta_0^2(T)(0.518)^2 + 4\mu^2 H^2 \ (1),$$

$$E^2 = \Delta_0^2(T)(0.495)^2 + 4\mu^2 H^2 \ (1).$$

A_1 phase:

$$E = \Delta_0(T)(1.96 - 0.31i) \ (1),$$

$$E = \Delta_0(T)(1.17 - 0.13i) \ (2),$$

$$E = 2\mu H \ (8), \quad E = 0 \ (1).$$

Here, as before, H is the magnetic field. Six other modes have an imaginary spectrum (this is due to the instability of the A_1 phase to small perturbations).

In the polar phase, $c_{ia} = \delta_{i3}\delta_{a3}$, we obtain the following set of equations for the collective mode spectrum:

$$\int_0^1 dx(1-x^2)\left[\left(1-\frac{4\Delta^2}{q^2}\right)J-1\right] = 0 \quad (6),$$

$$\int_0^1 dx(1-x^2)(J-2) = 0 \quad (6),$$

$$\int_0^1 dx x^2\left(1+\frac{4\Delta^2}{q^2}\right)J = 0 \quad (3),$$

$$\int_0^1 dx x^2 J = 0 \quad (3).$$

Here,

$$J = \frac{1}{\sqrt{1+4\Delta^2/q^2}}\ln\frac{1+\sqrt{1+4\Delta^2/q^2}}{1-\sqrt{1+4\Delta^2/q^2}},$$

$$x = \cos\theta, \quad q^2 = \omega^2 + c_F^2(\mathbf{k}\cdot\mathbf{n}).$$

Quantity J depends on the gap in the Fermi spectrum, which in the general case is a function of angular variables θ and φ. Putting $\kappa = 0$ and solving these equations numerically, we obtained the roots $E = \Delta_0(T)(1.20 - 1.75i)$ for the second equation and $E = 0$ for the third equation. The roots for the first and fourth equations could not be determined.

Thus, for the polar phase, we obtained six strongly attenuating modes with energy (frequency) $E = \Delta_0(T)(1.20 - 1.75i)$ and three Goldstone modes. The presence of strongly attenuating modes is associated with the fact that in contrast to axial and planar phases, where the gap vanishes only at poles and where collective modes attenuate moderately and can be observed as resonances in experiments on ultrasound absorption, the gap in the polar phase vanishes along the equator.

For the three phases

$$\frac{1}{\sqrt{2}}\begin{pmatrix} 1 & 0 & 0 \\ 0 & -1 & 0 \\ 0 & 0 & 0 \end{pmatrix}, \quad \frac{1}{\sqrt{2}}\begin{pmatrix} 0 & 1 & 0 \\ 1 & 0 & 0 \\ 0 & 0 & 0 \end{pmatrix}$$

and

$$\frac{1}{\sqrt{2}}\begin{pmatrix} 0 & -1 & 0 \\ 1 & 0 & 0 \\ 0 & 0 & 0 \end{pmatrix},$$

the spectrum is identical and can be determined from the following set of equations:

$$\int_0^1 dx(1-x^2)\left(1+\frac{4\Delta^2}{q^2}\right)J = 0 \quad (2),$$

$$\int_0^1 dx(1-x^2)\left(1+\frac{6\Delta^2}{q^2}\right)J = 0 \quad (3),$$

$$\int_0^1 dx(1-x^2)\left(1+\frac{8\Delta^2}{q^2}\right)J = 0 \quad (1),$$

$$\int_0^1 dx(2-x^2)\left(1+\frac{4\Delta^2}{q^2}\right)(J-1) = 0 \quad (1),$$

$$\int_0^1 2dx x^2\left(1+\frac{6\Delta^2}{q^2}\right)(J-1) = 0 \quad (2),$$

$$\int_0^1 dx(1-x^2)\left(1-\frac{2\Delta^2}{q^2}\right)J = 0 \quad (2),$$

$$\int_0^1 dx(1-x^2)J = 0 \quad (3),$$

$$\int_0^1 dx(1-x^2)\left(1-\frac{4\Delta^2}{q^2}\right)J = 0 \quad (1),$$

$$\int_0^1 dx x^2\left[\left(1-\frac{2\Delta^2}{q^2}\right)J-1\right] = 0 \quad (2),$$

$$\int_0^1 dx x^2(J-1) = 0 \quad (1).$$

The numerical solution of these equations leads to the following spectrum of high-frequency modes (for $\kappa = 0$):

$$E = \Delta_0(T)(1.83 - 0.06i) \quad (1),$$

$$E = \Delta_0(T)(1.58 - 0.04i) \quad (2),$$

$$E = \Delta_0(T)(1.33 - 0.10i) \quad (1),$$

$$E = \Delta_0(T)(1.33 - 0.08i) \quad (2),$$

$$E = \Delta_0(T)(1.28 - 0.04i) \quad (2),$$

$$E = \Delta_0(T)(1.09 - 0.22i) \quad (3),$$

$$E = \Delta_0(T)(0.71 - 0.05i) \quad (3),$$

$$E = \Delta_0(T)(0.33 - 0.34i) \quad (1),$$

$$E = \Delta_0(T)(0.23 - 0.71i) \quad (2).$$

The last two modes have imaginary components of the same order of magnitude as the real components. This means that they strongly attenuate and cannot be treated as resonances.

For the phase $\begin{pmatrix} 1 & 1 & 0 \\ i & i & 0 \\ 0 & 0 & 0 \end{pmatrix}$, we obtain the following set of equations for the collective excitation spectrum:

$$\int_0^1 dx\, x^2\left(1 + \frac{2\Delta^2}{q^2}\right)(J-1) = 0 \quad (6),$$

$$\int_0^1 dx(1-x^2)\left(1 + \frac{2\Delta^2}{q^2}\right)J = 0 \quad (4),$$

$$\int_0^1 dx(1-x^2)\left(1 + \frac{\Delta^2}{q^2}\right)J = 0 \quad (4),$$

$$\int_0^1 dx(1-x^2)\left(1 + \frac{3\Delta^2}{q^2}\right)J = 0 \quad (4).$$

The numerical solution of these equations leads to the following spectrum of high-frequency modes (for $\kappa = 0$):

$$E = \Delta_0(T)(0.66 - 0.02i), \quad E = \Delta_0(T)(0.64 - 0.02i),$$

$$E = \Delta_0(T)(0.46 - 0.04i), \quad E = \Delta_0(T)(0.36 - 0.04i).$$

For the phase $\frac{1}{\sqrt{6}}\begin{pmatrix} -1 & 0 & 0 \\ 0 & -1 & 0 \\ 0 & 0 & 2 \end{pmatrix}$, we obtained the following two equations for the spectrum:

$$\int_0^1 dx\left[\left(1 + \frac{n\Delta^2}{q^2} + \frac{m\Delta^2}{q^2}\frac{1-x^2}{3}\right)J(1-x^2) - \frac{4}{3} + \frac{16}{9\sqrt{3}}\arctan\sqrt{3}\right] = 0,$$

$$\int_0^1 dx\left[\left(1 + \frac{n\Delta^2}{q^2} + \frac{m\Delta^2}{q^2}\frac{2}{3}[A + (2A-1)x^2]\right)J(1-x^2) - \frac{4}{3} + \frac{16}{9\sqrt{3}}\arctan\sqrt{3}\right]$$
$$\times \int_0^1 dx\left[2\left(1 + \frac{n\Delta^2}{q^2} + \frac{mA\Delta^2}{q^2}\frac{2x^2}{3}\right)Jx^2 + \frac{2}{3} - \frac{8}{9\sqrt{3}}\arctan\sqrt{3}\right]$$
$$-2\left[\int_0^1 dx J\frac{\Delta^2}{q^2}\frac{2}{3}(1-x^2)x^2\right]^2 = 0.$$

The first of these equations leads to an equation describing the modes corresponding to variables $u_{11} - u_{22}$, $u_{12} + u_{21}$, where $u_{ij} + v_{ij}i = c_{ij}$ are the Bose fields from Eq. (5) for $n = 4$ and $m = 1$; to variables $u_{12} - u_{21}$ for $n = 4$, $m = 0$; to variables $v_{11} - v_{22}$, $v_{12} + v_{21}$ for $n = 0$, $m = -1$; and to variables $v_{12} - v_{21}$ for $n = 0$, $m = 0$. The second equation describes the modes corresponding to variables $u_{11} + u_{22}$, u_{33} for $A = 1$, $n = 4$, $m = 1$; to variables $v_{11} + v_{22}$, v_{33} for $A = 1$, $n = 0$, $m = -1$; to variables (u_{23}, u_{32}), (u_{13}, u_{31}) for $A = 0$, $n = 4$, $m = 1$; and to variables (v_{23}, v_{32}), (v_{13}, v_{31}) for $A = 0$, $n = 0$, $m = -1$.

For the phase $\begin{pmatrix} 0 & 0 & 0 \\ 0 & 0 & 0 \\ 1 & 1 & 0 \end{pmatrix}$, we have the following equation for the spectrum:

$$\int_0^1 dx\int_0^{2\pi} d\varphi(A - x^2)(1 \pm A\sin\varphi) \times \left[\left(1 + \frac{n\Delta^2}{q^2}\right)J + A - 1\right] = 0.$$

It describes the modes corresponding to variable u_{31}, u_{32}, v_{33} for $A = 0$, $n = 0$; to variables u_{33}, v_{31}, v_{32} for $A = 0$, $n = 4$; to variables $u_{11} \pm u_{21}$, $u_{12} \pm u_{22}$, $v_{13} \pm v_{23}$ for $A = 1$, $n = 0$; and to variables $v_{11} \pm v_{21}$, $v_{12} \pm v_{22}$, $u_{13} \pm u_{23}$ for $A = 1$, $n = 4$.

For the phase $\begin{pmatrix} 0 & 0 & 1 \\ 0 & 0 & 1 \\ 0 & 0 & 0 \end{pmatrix}$, we obtained the following two equations for the spectrum:

$$\int_0^1 dx\int_0^{2\pi} d\varphi x^2\left[\left(1 + \frac{n\Delta^2}{q^2}\right)J - 1\right] = 0,$$

$$\int_0^1 dx \int_0^{2\pi} d\varphi (1-x^2)(1\pm\sin\varphi)\left(1+\frac{n\Delta^2}{q^2}\right)J = 0.$$

The first equation describes the modes corresponding to variables u_{31}, u_{32}, v_{33} for $n = 0$ and to variables u_{33}, v_{31}, v_{32} for $n = 4$. The second equation describes the modes corresponding to variables $u_{11} \pm u_{21}$, $u_{12} \pm u_{22}$, $v_{13} \pm v_{23}$ for $n = 0$ and to variables $v_{11} \pm v_{21}$, $v_{12} \pm v_{22}$, $u_{13} \pm u_{23}$ for $n = 4$.

For the two phases

$$\frac{1}{\sqrt{2}}\begin{pmatrix} 0 & 0 & 1 \\ 0 & 0 & 0 \\ \pm 1 & 0 & 0 \end{pmatrix} \text{ and } \frac{1}{\sqrt{2}}\begin{pmatrix} 0 & 0 & 0 \\ 0 & 0 & 1 \\ 0 & \pm 1 & 0 \end{pmatrix},$$

the spectra are identical and can be determined from two equations, the first of which,

$$\int_0^1 dx \int_0^{\pi/2} d\varphi \left[\left(1+\frac{2\Delta^2}{q^2} + \frac{2\Delta_0^2}{q^2}[A(1-x^2)\cos^2\varphi + Bx^2]\right)J(1-x^2)\cos^2\varphi + \frac{1}{2}[(1-x^2)\cos^2\varphi - x^2]\ln(1-(1-x^2)\cos^2\varphi)\right]$$

$$\times \int_0^1 dx \int_0^{\pi/2} d\varphi \left[\left(1+\frac{2\Delta^2}{q^2} + \frac{2\Delta_0^2}{q^2}[B(1-x^2)\cos^2\varphi + Ax^2]\right)Jx^2 - \frac{1}{2}[(1-x^2)\cos^2\varphi - x^2]\ln(1-(1-x^2)\cos^2\varphi)\right]$$

$$-\left[\int_0^1 dx \int_0^{\pi/2} d\varphi \frac{4\Delta_0^2}{q^2}x^2(1-x^2)\cos^2\varphi J\right]^2 = 0,$$

leads to an equation describing the modes corresponding to variables v_{11}, v_{33} for $A = 1$, $B = 0$; to variables u_{11}, u_{33} for $A = -1$, $B = 0$; to variables v_{13}, v_{31} for $A = 0$, $B = 1$; and to variables u_{13}, u_{31} for $A = 0$, $B = -1$. The second equation,

$$\int_0^1 dx \int_0^{\pi/2} d\varphi \left\{\left(1+\frac{2\Delta^2}{q^2}N + \frac{2\Delta_0^2}{q^2}x^2P\right)\right.$$

$$\times J\{(1-x^2)[(z-y)\cos^2\varphi + y] + x^2(1-z-y)\}$$

$$+ [(1-x^2)\cos^2\varphi - x^2](2z+y-1)$$

$$\left. + \frac{1}{2}[3(1-x^2)\sin^2\varphi - 1]y\ln[1-(1-x^2)\cos^2\varphi]\right\} = 0,$$

describes the mode corresponding to variable u_{22} for $y = 1$, $z = 0$ and $N = 0$, $P = 0$; to variable v_{22} for $N = 2$, $P = 0$; to variable u_{21} for $N = 0$, $P = 1$; to variable v_{21} for $N = 2$, $P = -1$; to variable u_{23} for $N = 1$, $P = -1$; to variable v_{23} for $N = 1$, $P = 1$; to variable u_{12} for $y = 0$, $z = 1$ and $N = 0$, $P = 0$; to variable v_{12} for $N = 2$, $P = 0$; to variable u_{32} for $y = 0$, $z = 0$ and $N = 0$, $P = 0$; and to variable v_{32} for $N = 2$, $P = 0$.

For phase $\begin{pmatrix} 0 & 0 & 1 \\ 0 & 0 & 0 \\ 1 & 0 & 0 \end{pmatrix}$, we obtain from the second equation the high-frequency modes

$$E = \Delta_0(T)(1.80 - 0.09i), \quad E = \Delta_0(T)(0.55 - 0.80i),$$

the last of which has the imaginary component of the same order of magnitude as the real component. This means that it attenuates strongly and cannot be treated as a resonance.

Tewordt [6] analyzed the collective mode spectrum for the order parameter in Sr_2RuO_4 under the assumption that p-pairing takes place in this system. He considered two possible superconducting phases with the order parameters

$$\hat{d} = \Delta_0\hat{z}(k_x + ik_y), \quad \hat{d} = \frac{\Delta_0}{2}\hat{z}(k_x + k_y).$$

It should be noted that the first phase is an analogue of the A-phase of superfluid ^{3}He. Tewordt [6] determined the mode $E = 2\Delta_0$ for this phase and the mode $E = \sqrt{3}\Delta_0$ for the second phase. Both modes are coupled with charge density fluctuations, but this coupling is weak in view of the smallness of the quantity $dN(E)/dE$, which is a measure of the electron–hole asymmetry on the Fermi surface. Comparing the results obtained by Tewordt ($E = 2\Delta_0$) with our results, we note that the value of frequency $E = \Delta_0(T)(1.96 - 0.31i)$ obtained by us for high-frequency modes in the phase which is an analogue of the A-phase of superfluid ^{3}He is more accurate. This is due to the fact that Tewordt did not calculate the imaginary components of collective mode frequencies whose presence renormalizes the real energy components by virtue of dispersion relations.

We also considered the second superconducting phase $\begin{pmatrix} 0 & 0 & 1 \\ 0 & 0 & 1 \\ 0 & 0 & 0 \end{pmatrix}$ studied by Tewordt. The equations for the mode spectrum of this phase are given above (however, the solution of these equations have not been obtained).

Considering the pairing amplitude different in the *xy* plane and in a plane perpendicular to it, Tewordt obtained a number of quasi-Goldstone modes with frequencies $\omega^2 = \Delta_0^2 \ln(T_c/T_{cj})$, where $T_{cj} < T_c$ is the superconducting transition temperature corresponding to pairing in the *xy* plane. Since both pairing amplitudes are assumed to be equal in our analysis, we obtained pure Goldstone modes ($T_c = T_{cj}$ and, hence, $\omega = 0$) instead of quasi-Goldstone modes. It should be noted, however, that the number of superconducting phases in the case of *p*-pairing considered by us is much larger than those analyzed by Tewordt.

3.2. *d*-Pairing

3.2.1. Collective Excitations in HTSC with *d*-Pairing

Let us consider the superconducting states $d_{x^2-y^2}$, d_{xy}, d_{xz}, d_{yz}, and $d_{3z^2-r^2}$ emerging in the symmetry classification of HTSC (Table 1).

Let us calculate the collective mode spectrum for the given five states. In the first approximation, the collection excitation spectrum is determined by the quadratic component of the effective action S_{eff} obtained by the translation $c_j(p) \longrightarrow c_j(p) + c_j^0(p)$ in formula (9) for S_{eff}. Here, $c_j^0(p) = \sqrt{\beta V}\, c\delta_{p0} c_j^0$ are the condensate values of canonical Bose fields and the values of c_j^0 for the cases listed in Table 1 are as follows:

$$1)\ c_1^0 = -2, \quad 2)\ c_2^0 = 2, \quad 3)\ c_4^0 = 2,$$

$$4)\ c_5^0 = 2, \quad 5)\ c_3^0 = 2,$$

the remaining components $c_j(p)$ being equal to zero.

The spectrum can be determined from the equation $\det Q = 0$, where Q is the matrix of the quadratic form. For each superconducting phase, we determined five high-frequency modes (Table 2) and five Goldstone (quasi-Goldstone) modes whose energies are equal to zero or small ($\le 0.1\Delta_0$).

We calculated the spectrum of collective modes for the five superconducting phases of HTSC, namely, for $d_{x^2-y^2}$, $d_{3z^2-r^2}$, d_{xy}, d_{xz}, and d_{yz}, using the model of *d*-pairing constructed by us using the functional integration method and considering the case of spherical symmetry that needs only the coupling constant *g*. The inclusion of the lattice symmetry requires the introduction of additional coupling constants (up to five in the general case).

Table 1

No.	Phase	Order parameter	Gap in Fermi spectrum
1	$d_{3z^2-r^2}$	$\begin{pmatrix} -1 & 0 & 0 \\ 0 & -1 & 0 \\ 0 & 0 & 2 \end{pmatrix}$	$\Delta_0\lvert 3\cos^2\theta - 1\rvert$
2	$d_{x^2-y^2}$	$\begin{pmatrix} 1 & 0 & 0 \\ 0 & -1 & 0 \\ 0 & 0 & 0 \end{pmatrix}$	$\Delta_0\sin^2\theta\lvert\cos 2\varphi\rvert$
3	d_{xy}	$\begin{pmatrix} 0 & 1 & 0 \\ 1 & 0 & 0 \\ 0 & 0 & 0 \end{pmatrix}$	$\Delta_0\sin^2\theta\lvert\sin 2\varphi\rvert$
4	d_{xz}	$\begin{pmatrix} 0 & 0 & 1 \\ 0 & 0 & 0 \\ 1 & 0 & 0 \end{pmatrix}$	$\Delta_0\lvert\sin 2\theta\cos\varphi\rvert$
5	d_{yz}	$\begin{pmatrix} 0 & 0 & 0 \\ 0 & 0 & 1 \\ 0 & 1 & 0 \end{pmatrix}$	$\Delta_0\lvert\sin 2\theta\sin\varphi\rvert$

For each of the five phases, we determined five high-frequency modes in each phase with frequencies lying between Δ_0 and $2\Delta_0$ as well as five Goldstone (quasi-Goldstone) modes with frequencies smaller than $0.1\Delta_0$.

It should be noted that the frequencies (energies) of all collective modes are complex-valued. This is a consequence of *d*-pairing or, in other words, a consequence of gap vanishing in chosen directions. In this case, Bose excitations decay into fermions, which leads to the attenuation of collective modes. The value of the imaginary frequency (energy) component $\operatorname{Im} E_i$ amounts to 25 to 80%. Some of these modes attenuate moderately and may be treated as resonances, while others attenuate more strongly, which complicates their observation. The inclusion of the Coulomb interaction converts the zero sound mode into a plasma mode.

The obtained spectra of collective modes in HTSC may be used for interpreting ultrasonic experiments and the experiments on microwave absorption in HTSC as well as for identifying the type of pairing and the order parameter in HTSC.

Table 2

$d_{3z^2-r^2}$	$d_{x^2-y^2}$, d_{xy}	d_{xz}, d_{yz}
$E_1 = \Delta_0(2.0 - 1.65i)$	$E_1 = \Delta_0(1.88 - 0.79i)$	$E_1 = \Delta_0(1.76 - 1.1i)$
$E_{2,3} = \Delta_0(1.85 - 0.69i)$	$E_2 = \Delta_0(1.66 - 0.50i)$	$E_2 = \Delta_0(1.70 - 0.48i)$
$E_{4,5} = \Delta_0(1.64 - 0.50i)$	$E_3 = \Delta_0(1.14 - 0.68i)$	$E_3 = \Delta_0(1.14 - 0.68i)$
	$E_4 = \Delta_0(1.13 - 0.71i)$	$E_4 = \Delta_0(1.13 - 0.73i)$
	$E_5 = \Delta_0(1.10 - 0.65i)$	$E_5 = \Delta_0(1.04 - 0.83i)$

3.2.2. Collective Excitations in Heavy-Fermion Superconductors with d-Pairing

In heavy-fermion superconductors (HFSC), as in HTSC, the order parameter and the type of pairing have been established only for some compounds. The traditional BCS pairing contradicts the nonexponential temperature dependence of most thermodynamic quantities such as specific heat. The complex phase diagram of HFSC also points to a nontrivial pairing in these systems. Examples of HFSC with *p*-pairing as well as *d*-pairing are known. The case of *p*-pairing was considered above. Here, we will apply the functional integration method for an analysis of the *d*-pairing in HFSC in analogy with the procedure used by us for all the superconducting states emerging in the symmetry classification of HTSC. We will calculate the complete spectrum of collective excitations for all superconducting states emerging in the symmetry classification of HFSC. Let us consider three superconducting states including $d\gamma$ and Y_{2-1}. Collective excitations in the two latter phases were studied earlier by Hiroshima and Namaizawa [7] using the method of kinetic equation. At the end of the section, we will compare our results for two of the three phases with the results obtained in [7].

In each superconducting phase of HFSC, there exist 10 collective modes. We established that five of them are high-frequency modes; i.e., they have frequencies of the order of the gap width in the Fermi spectrum. At the same time, the remaining five modes are Goldstone (or quasi-Goldstone) modes with frequencies (energies) vanishing (small) for zero pulses.

Thus, we will again consider the three-dimensional model of *d*-pairing in superconductors. It should be recalled that the model is described by the hydrodynamic action functional obtained by successive functional integration over fast and then slow Fermi fields. The hydrodynamic action functional determines all properties of the system under investigation (HFSC in the given case), including the collective excitation spectrum.

3.2.2.1. Calculation of Collective Mode Spectrum

We consider the following superconducting states emerging in the symmetry classification of HFSC:

(1) $d\gamma$ phase $\begin{pmatrix} e^{4\pi i/3} & 0 & 0 \\ 0 & e^{2\pi i/3} & 0 \\ 0 & 0 & 1 \end{pmatrix}$ with the gap $\Delta(T) = \Delta_0(T)(e^{4\pi i/3}k_x^2 + e^{4\pi i/3}k_y^2 + k_z^2)$;

(2) Y_{2-1} phase $\begin{pmatrix} 0 & 0 & 1 \\ 0 & 0 & -i \\ 1 & -i & 0 \end{pmatrix}$ with the gap $\Delta(T) = \Delta_0(T)\sin 2\theta e^{-i\varphi}$;

(3) phase $\begin{pmatrix} 1 & i & 0 \\ i & -1 & 0 \\ 0 & 0 & 0 \end{pmatrix}$ with a gap proportional to $\sin^2\theta$.

Let us calculate the collective mode spectrum for these three states in analogy with Subsection 3.2.1. The values of c_j^0 for the cases considered here are

$$1)\ c_1^0 = -1, \quad c_2^0 = -i\sqrt{3};$$

$$2)\ c_4^0 = 2, \quad c_5^0 = 2i;$$

$$3)\ c_2^0 = 2, \quad c_3^0 = 2i,$$

while the remaining components of c_j^0 are equal to zero.

In order to obtain the quadratic component of the effective action S_{eff}, we present the second term in expression (9) in the form

$$\frac{1}{2}\ln\det(1 + Cu),$$

$$G^{-1} = M(c^{0+}, c^0), \tag{9'}$$

$$u = \frac{1}{\sqrt{\beta V}}\begin{pmatrix} 0 & [cY^*] \\ [cY^*] & 0 \end{pmatrix}.$$

Here,

$$[cY^*] = c_1(1-3\cos^2\theta) + c_2\sin^2\theta\cos 2\varphi$$
$$+ c_3\sin^2\theta\sin 2\varphi + c_4\sin 2\theta\cos\varphi + c_5\sin 2\theta\sin\varphi.$$

We expand expression (9') into a power series in new Bose fields c_j and retain the terms up to the second order in c_j. The second-order term is given by

$$-\frac{1}{4}\sum_{p_1,\,p_2,\,p_3,\,p_4}\mathrm{Tr}(G_{p_1p_2}u_{p_2p_3}G_{p_3p_4}u_{p_4p_1}).$$

(the first-order term vanishes as a result of minimization). After calculations, we obtain the quadratic form determining the collective excitation spectrum.

EQUATION FOR THE GAP

Let us consider the first term in expression (9) for S_{eff}. Constant g describing the interaction of quasifermions must be eliminated using the equation for the gap. In order to derive this equation, we must calculate S_{eff} in the Ginzburg–Landau region (for $T \sim T_c$), where the wave function of Cooper pairs (order parameter) is (modulo) small:

$$S_{\mathrm{eff}} = \frac{1}{2g}\sum_{p,\,j}|c_j(p)|^2(1+2\delta_{j1}) + \frac{1}{2}\mathrm{Tr}\ln(1+Gu).$$

Expanding the second term into a power series in Gu, we obtain

$$-\sum_{n=1}^{\infty}\frac{1}{4n}\mathrm{Tr}(Gu)^{2n}.$$

Carrying out summation and substituting

$$u_{p_1p_2} = \frac{\alpha}{\sqrt{\beta V}}\begin{pmatrix} 0 & [cY^*] \\ [cY^*] & 0 \end{pmatrix}$$

and

$$G = \frac{Z\sigma_3\delta_{p_1p_2}}{i\omega-\xi},$$

we obtain

$$S_{\mathrm{eff}} = \frac{A}{2g}\beta V c^2 + \frac{1}{2}\ln\left(1+\frac{\alpha^2c^2Z^2[c^0Y^*][c^{+0}Y]}{\omega^2+\xi^2}\right).$$

Here, $\alpha = \sqrt{15/35\pi}$, σ_3 is the Pauli matrix, and the following substitution has been made: $c_j^0(p) = \sqrt{\beta V}\,c\delta_{p0}c_j^0$. Constant c can be determined from the equation $\delta S_{\mathrm{eff}}/\delta c = 0$, which leads to the following equation for the gap:

$$\frac{A}{g} + \frac{1}{\beta V}\sum_p\frac{\alpha^2Z^2[c^0Y^*][c^{+0}Y]}{\omega^2+\xi^2+\alpha^2Z^2[c^0Y^*][c^{+0}Y]} = 0.$$

Here, $A = 6$ for the first phase and $A = 8$ for the second and third phases. For different superconducting phases, we obtain the following equations:

$$1)\ \frac{1}{g} + \frac{\alpha^2Z^2}{6\beta V}$$
$$\times\sum_p\frac{(1-3\cos^2\theta)^2+3\sin^4\theta\cos^4 2\varphi}{\omega^2+\xi^2+\frac{\Delta_0^2}{4}[(1-3\cos^2\theta)^2+3\sin^4\theta\cos^2 2\varphi]} = 0,$$

$$2)\ \frac{1}{g} + \frac{\alpha^2Z^2}{2\beta V}\sum_p\frac{\sin^2 2\theta}{\omega^2+\xi^2+\Delta_0^2\sin^2 2\theta} = 0,$$

$$3)\ \frac{1}{g} + \frac{\alpha^2Z^2}{2\beta V}\sum_p\frac{\sin^4 2\theta}{\omega^2+\xi^2+\Delta_0^2\sin^4 2\theta} = 0,$$

where $\Delta_0 = 2cZ\alpha$. Eliminating the term $1/g$ using the equation for the gap, we arrive at the following expression for the quadratic component of S_{eff}:

$$\begin{aligned} S_{\mathrm{eff}} = {} & -\frac{\alpha^2Z^2}{2A\beta V}\sum_p\frac{[c^0Y^*][c^{+0}Y]}{\omega^2+\xi^2+\alpha^2Z^2[c^0Y^*][c^{+0}Y]} \\ & \times\sum_j(1+2\delta_{j1})c_j^+(p)c_j(p) \\ & + \frac{Z^2}{4\beta V}\sum_{p_1+p_2=p}\frac{1}{M_1M_2}\{(i\omega_1+\xi_1)(i\omega_2+\xi_2) \\ & \times([c^+(p)Y(p_2)][c(p)Y^*(p_1)] \\ & + [c^+(p)Y(p_1)][c(p)Y^*(p_2)]) \\ & - \Delta^2[c^+(p)Y(-p_1)][c^*(-p)Y(-p_2)] \\ & - \Delta^{+2}[c(p)Y^*(-p_1)][c(-p)Y^*(-p_2)]\}. \end{aligned} \tag{11}$$

This is the general quadratic form for all three superconducting states of HFSC. Only parameter A and the gap structure (through $[c^0Y^*][c^{+0}Y]$ and M_i) are different for different superconducting states. Note that $\Delta = \Delta^+$ (or $c^0 = c^{0+}$) for all three superconducting states.

The coefficients of the quadratic form are proportional to the sums of the products of Green's functions for quasifermions. At low temperatures ($T_c - T \sim T_c$), we can pass from summation to integration in accordance with the rule

$$\frac{1}{\beta V}\sum_{p} \longrightarrow \frac{1}{(2\pi)^4}\frac{k_F^2}{c_F}\int d\omega d\xi d\Omega. \tag{12}$$

The integrals will be evaluated using Feynman's identity:

$$\begin{aligned}&[(\omega_1^2+\xi_1^2+\Delta^2)(\omega_2^2+\xi_2^2+\Delta^2)]^{-1}\\ &= \int d\alpha[\alpha(\omega_1^2+\xi_1^2+\Delta^2)+(1-\alpha)(\omega_2^2+\xi_2^2+\Delta^2)]^{-2}.\end{aligned} \tag{13}$$

With the help of this identity, the integrals with respect to variables ω and ξ and then with respect to parameter α and angular variables can be easily evaluated.

After evaluating all integrals (except those over angular variables), we equate the determinant of the quadratic form to zero and arrive at the following set of equations determining the complete spectrum of collective modes in HFSC with *d*-pairing (index *i* labels the branches of collective modes pertaining to the same phase):

1) $k = 1, \quad i = 1$

$$\int_0^1 dx\int_0^{2\pi} d\varphi\left\{\frac{\sqrt{\omega^2+4f_1}}{\omega}\ln F_1 g_1 + (g_1-2f_1)\ln f_1\right\} = 0,$$

$$\int_0^1 dx\int_0^{2\pi} d\varphi\left\{\frac{\omega}{\sqrt{\omega^2+4f_1}}\ln F_1 g_1 + (g_1-2f_1)\ln f_1\right\} = 0,$$

$k = 1, \quad i = 2, 3, 4, 5$

$$\int_0^1 dx\int_0^{2\pi} d\varphi\left\{\frac{\sqrt{\omega^2+4f_1}}{\omega}\ln F_1 g_i + \left(g_i-\frac{2}{3}f_i\right)\ln f_1\right\} = 0,$$

$$\int_0^1 dx\int_0^{2\pi} d\varphi\left\{\frac{\omega}{\sqrt{\omega^2+4f_1}}\ln F_1 g_i + \left(g_i-\frac{2}{3}f_1\right)\ln f_i\right\} = 0, \tag{14}$$

2) $k = 2, 3, \quad i = 1$

$$\int_0^1 dx\int_0^{2\pi} d\varphi\left\{\frac{\sqrt{\omega^2+4f_k}}{\omega}\ln F_k g_1 + \left(g_1-\frac{3}{2}f_1\right)\ln f_k\right\} = 0,$$

$$\int_0^1 dx\int_0^{2\pi} d\varphi\left\{\frac{\omega}{\sqrt{\omega^2+4f_k}}\ln F_k g_1 + \left(g_1-\frac{3}{2}f_i\right)\ln f_1\right\} = 0,$$

$k = 2, \quad i = 2, 3, 4, 5$

$$\int_0^1 dx\int_0^{2\pi} d\varphi\left\{\frac{\sqrt{\omega^2+4f_2}}{\omega}\ln F_2 g_i + \left(g_i-\frac{1}{2}g_2\right)\ln f_2\right\} = 0,$$

$$\int_0^1 dx\int_0^{2\pi} d\varphi\left\{\frac{\omega}{\sqrt{\omega^2+4f_2}}\ln F_k g_i + \left(g_i-\frac{3}{2}g_2\right)\ln f_2\right\} = 0.$$

Here,

$$\ln\frac{\sqrt{\omega^2+4f_k}+\omega}{\sqrt{\omega^2+4f_k}-\omega} \equiv F_k,$$

$$g_1 = (1-3x^2)^2, \quad g_2 = (1-x^2)^2\cos^2 2\varphi,$$

$$g_3 = g = 4(1-x^2)x^2\cos^2\varphi,$$

$$g_4 = 4(1-x^2)x^2\sin^2\varphi,$$

$$g_5 = (1-x^2)^2\sin^2\varphi,$$

$$f_1 = \frac{1}{4}[(1-3x^2)^2+3(1-x^2)^2\cos^2 2\varphi],$$

$$f_2 = 4(1-x^2)x^2, \quad f_3 = (1-x^2)^2,$$

$$\cos\theta = x, \quad \omega = \omega/\Delta_0.$$

3.2.2.2. Results: Collective Mode Spectra in HFSC

Solving Eqs. (14) numerically, we determine the spectra of collective modes of the three phases under investigation. For each phase, we obtain 10 collective modes, five of which (derived from the second equations) are high-frequency modes; i.e., their frequencies are of the order of the gap width in the Fermi spectrum. At the same time, the remaining five modes (obtained from the first equations) are Goldstone (or quasi-Goldstone) modes with frequencies (energies) vanishing for zero momenta.

Table 3 presents the results for high-frequency modes (E_i is the energy (frequency) of the *i*th branch) It should be noted that in the $d\gamma$ state, the last three modes are quasi-degenerate. The spectra of the second (Y_{2-1}) and third (containing a gap proportional to $\sin^2\theta$) states are found to be identical. In both phases, three high-frequency modes are determined, two of which are doubly degenerate.

Thus, we have calculated the collective mode spectrum for three superconducting phases of HFSC, namely, for phases $d\gamma$ and Y_{2-1} and the phase with a gap proportional to $\sin^2\theta$, using the model of *d*-pairing constructed by us with the help of the functional integration method [4, 5] and considering the case of spherical symmetry in which only one coupling constant *g* is used. The inclusion of the lattice symmetry necessitates the introduction of additional coupling constants (up to five in the general case: five is the number of spherical harmonics with $l = 2$). However, this number is reduced to two in the case of cubic symmetry and to three in the case of hexagonal symmetry: $g_{|m|}(m = 0, \pm1, \pm2)$.

For each of the three phases, we have determined five high-frequency modes in each phase (from the second equations in (14)) with frequencies belonging to the interval $(1.19–1.93)\Delta_0$. The first equations give five Goldstone (quasi-Goldstone) modes (with frequencies smaller than $0.1\Delta_0$).

Note that the frequencies (energies) of all collective modes are complex-valued and their imaginary components ($\mathrm{Im}E_i$) describe the attenuation of collective modes associated with the decomposition of Cooper pairs into original fermions. The value of the imaginary component of frequency amounts from 20 to 50% of the real components $\mathrm{Re}E_i$. This means that collective modes attenuate in the case of d-pairing more strongly than in most cases of p-pairing, for which the imaginary components of the frequency (energy) amount to 8–15% of $\mathrm{Re}E_i$. This is due to the difference in the topology of zeros of the gap in the Fermi spectrum, which are points in the case of p-pairing (in most phases) and a combination of points and lines for d-pairing. It should be noted that a similar situation is sometimes encountered in the case of p-pairing (e.g., in the polar phase of superfluid ^{3}He, the attenuation of collective modes is stronger than in other phases (A, $2D$, etc.) just due to the presence of zero lines).

The attenuation of collective modes was not calculated by Hiroshima and Namaizawa [7]. This is a drawback of the kinetic equation method as compared to the functional integration method. Using the kinetic equation method, one can calculate only the real components $\mathrm{Re}E_i$ of collective mode frequencies. The inclusion of collective mode attenuation ($\mathrm{Im}E_i$) leads to a shift in $\mathrm{Re}E_i$ since, by virtue of the dispersion relations, the presence of the imaginary component of collective mode frequencies results in the renormalization of their real components $\mathrm{Re}E_i$.

Thus, we can compare only the real components of collective mode frequencies. We obtained five high-frequency modes in each phase. In the $d\gamma$ phase, the frequencies lie in the interval $(1.19–1.66)\Delta_0$. Hiroshima and Namaizawa [7] obtained five modes with frequencies belonging to the interval $(0.9–1.87)\Delta_0$ and two lower-lying modes with frequencies $E = 0.32\Delta_0$. The frequencies obtained by us for the Y_{2-1} phase belong to the interval $(1.59–1.93)\Delta_0$, while the frequencies corresponding to high-frequency modes from [7] lie in the interval $(1.22–1.57)\Delta_0$. In both works, Goldstone and low-lying modes were obtained.

It should be noted that the spectrum of the third mode was calculated by us for the first time and was found to be identical to the spectrum of the Y_{2-1} phase.

Some of the modes we obtained attenuate moderately and may be regarded as resonances, while others attenuate more strongly, which makes observing them difficult. The inclusion of the Coulomb interaction transforms the zero sound mode into a plasma mode.

Table 3

$d\gamma$ phase	Y_{2-1} and $\sin^2\theta$ phases
$E_1 = \Delta_0(T)(1.45 - 0.48i)$	$E_{1,2} = \mathrm{D}_0(T)(1.93 - 0.41i)$
$E_2 = \Delta_0(T)(1.66 - 0.50i)$	$E_3 = \Delta_0(T)(1.62 - 0.75i)$
$E_3 = \Delta_0(T)(1.24 - 0.64i)$	$E_{4,5} = \mathrm{D}_0(T)(1.59 - 0.83i)$
$E_4 = \Delta_0(T)(1.21 - 0.60i)$	
$E_5 = \Delta_0(T)(1.19 - 0.60i)$	

The obtained collective mode spectra in HFSC may be used for interpreting the results of ultrasonic experiments and in experiments on microwave absorption in HFSC as well as for identifying the type of pairing and the order parameter in these superconductors.

At the present time, the experiments on microwave absorption in HFSC (at frequencies of the order of 20 GHz) are being carried out at the Northwest University (Evanston, USA). Their aim is to determine the type of pairing and the order parameter in HFSC [1].

3.2.3. How to Distinguish between a Mixture of Two d-States and a Pure d-State

Recent experiments [8] and theoretical investigations [9, 10] indicate that, apparently, a mixture of d-states is realized in HTSC. We calculated for the first time the collective excitation spectrum in the mixed $d_{x^2-y^2} + id_{xy}$ state of HTSC [11] using our earlier constructed model [4, 5] based on the functional integration method.

We proved [11] that in spite of the fact that the spectra in both phases $d_{x^2-y^2}$ and d_{xy} are identical, the spectrum in the mixed $d_{x^2-y^2} + id_{xy}$ state differs completely from the spectra of the pure states. Consequently, an analysis of the collective mode spectrum in experiments on ultrasound and microwave absorption makes it possible to distinguish between a mixture of states and pure states.

Most scientists believe [1] that d-pairing ($d_{x^2-y^2}$ state) is realized in oxides. At the same time, various hypotheses concerning the extended s-pairing, the mixture of s and d states, and various d states are being intensely discussed even now [12]. One of the reasons behind such a situation is that it is unclear whether the gap exactly vanishes in a certain preferred direction in the momentum space (as in the case of the $d_{x^2-y^2}$ state) or it is anisotropic and does not exactly vanish (except, probably, at some points on the Fermi surface). The available experimental results [1] (on tunneling and other effects) do not provide an unambiguous answer to the above question, although it is of fundamental importance. On the other hand, some experimental results [8] can be explained [9] under the assumption that a mixture of states of the type $d_{x^2-y^2} + id_{xy}$ is realized in HTSC. Annett *et al.* [10] considered the possibility of realizing a mixture of various d states in HTSC and arrived at the conclusion that the $d_{x^2-y^2} + id_{xy}$ state is preferred. We propose a method for distinguishing between a mixture of states and pure states.

For this purpose, we calculated the spectrum of collective excitations in the mixed $d_{x^2-y^2} + id_{xy}$ state of HTSC. A comparison of this spectrum with the spectrum of pure d states of HTSC shows that they differ significantly and this difference may be used for determining the symmetry of the order parameter in HTSC.

We will use the model of d-pairing described by Eqs. (9) and (10) and consider the mixed $d_{x^2-y^2} + id_{xy}$ state of HTSC. The order parameter in this state has the form

$$\begin{pmatrix} 1 & 0 & 0 \\ 0 & -1 & 0 \\ 0 & 0 & 0 \end{pmatrix} + i\begin{pmatrix} 0 & 1 & 0 \\ 1 & 0 & 0 \\ 0 & 0 & 0 \end{pmatrix} \qquad (15)$$

and the gap is given by

$$\Delta(T) = \Delta_0(T)\sin^2\theta.$$

The equation for the gap can be written in the form

$$\frac{1}{g} + \frac{\alpha^2 Z^2}{2\beta V}\sum_p \frac{\sin^4\theta}{\omega^2 + \xi^2 + \Delta_0^2\sin^4\theta} = 0, \qquad (16)$$

where

$$\Delta_0 = 2cZ\alpha, \quad \alpha = \sqrt{15/32\pi}.$$

In the first approximation, the collective excitation spectrum is determined by the quadratic part of the effective action S_{eff} obtained through the translation $c_j(p) \longrightarrow c_j(p) + c_j^0(p)$ in S_{eff}. Here, $c_j^0(p) = \sqrt{\beta V}c\delta_{p0}c_j^0$ are the condensate values of canonical Bose fields, and the values of c_j^0 for the cases under investigation are

$$c_2^0 = 2, \quad c_3^0 = 2i,$$

while the remaining values of c_j^0 are equal to zero.

Eliminating the term $1/g$ with the help of the equation for the gap, we arrive at expression (11) for the quadratic component of S_{eff} for $A = 4$. The coefficients of the quadratic form are proportional to the sums of the products of Green's functions for quasifermions. At low temperatures ($T_c - T \sim T_c$), we can go over from summation to integration in accordance with the rule (12). We will evaluate the obtained integrals using Feynman's identity (13). With the help of this identity, we can easily evaluate the integrals with respect to variables ω and ξ and then with respect to parameter α and angular variables.

After evaluating these integrals (except the integrals over angular variables) and equating the determinant of the quadratic form to zero, we arrive at the following set of equations determining the complete spectrum of collective modes in the mixed $d_{x^2-y^2} + id_{xy}$ state (index i labels the branches of collective modes belonging to the same phase):

$$i = 1$$

$$\int_0^1 dx \int_0^{2\pi} d\varphi \left\{ \frac{\sqrt{\omega^2 + 4f}}{\omega} \ln F g_1 + \left(g_1 - \frac{3}{2}f_1\right)\ln f \right\} = 0,$$

$$\int_0^1 dx \int_0^{2\pi} d\varphi \left\{ \frac{\omega}{\sqrt{\omega^2 + 4f}} \ln F g_1 + \left(g_1 - \frac{3}{2}f_1\right)\ln f \right\} = 0,$$

$$i = 2, 3, 4 \qquad (17)$$

$$\int_0^1 dx \int_0^{2\pi} d\varphi \left\{ \frac{\sqrt{\omega^2 + 4f}}{\omega} \ln F g_i + \left(g_i - \frac{1}{2}g\right)\ln f \right\} = 0,$$

$$\int_0^1 dx \int_0^{2\pi} d\varphi \left\{ \frac{\omega}{\sqrt{\omega^2 + 4f}} \ln F g_i + \left(g_i - \frac{1}{2}g\right)\ln f \right\} = 0.$$

Here

$$\ln\frac{\sqrt{\omega^2 + 4f} + \omega}{\sqrt{\omega^2 + 4f} - \omega} \equiv \ln F, \quad g_1 = (1 - 3x^2)^2,$$

$$g_2 = (1 - x^2)^2\cos^2 2\varphi,$$

$$g_3 = g = 4(1 - x^2)x^2\cos^2\varphi,$$

$$g_4 = 4(1 - x^2)x^2\sin^2\varphi, \quad g_5 = (1 - x^2)^2\sin^2\varphi, \qquad (18)$$

$$f_1 = \frac{1}{4}[(1 - 3x^2)^2 + 3(1 - x^2)^2\cos^2 2\varphi],$$

$$f = (1 - x^2)^2$$

and the following substitutions have been used: $\cos\theta = x$, $\omega = \omega/\Delta_0$.

Having solved these equations, we obtain the following results for the collective mode spectrum in the $d_{x^2-y^2} + id_{xy}$ state. Ten collective modes are obtained, five of which (derived from the second equations) are high-frequency modes; i.e., their frequencies are of the order of the gap in the Fermi spectrum. At the same time, the remaining five modes are Goldstone (or quasi-Goldstone) modes with frequencies (energies) vanishing for zero momenta (of the order of $(0.03–0.08)\Delta_0(T)$).

We present the results for high-frequency modes (E_i is the energy of the ith branch):

$$\begin{aligned} E_{1,2} &= \Delta_0(T)(1.93 - 0.41i), \\ E_3 &= \Delta_0(T)(1.62 - 0.75i), \\ E_{4,5} &= \Delta_0(T)(1.59 - 0.83i). \end{aligned} \tag{19}$$

We can compare the results with the spectrum of pure $d_{x^2-y^2}$ and d_{xy} states obtained by us earlier [13]:

$$\begin{aligned} E_1 &= \Delta_0(T)(1.88 - 0.79i), \\ E_2 &= \Delta_0(T)(1.66 - 0.50i), \\ E_3 &= \Delta_0(T)(1.40 - 0.68i), \\ E_4 &= \Delta_0(T)(1.13 - 0.71i), \\ E_5 &= \Delta_0(T)(1.10 - 0.65i). \end{aligned} \tag{20}$$

In spite of the fact that the spectra in both phases $d_{x^2-y^2}$ and d_{xy} are identical, the spectrum in the mixed $d_{x^2-y^2} + id_{xy}$ state absolutely differs from the spectra of the pure states. In the latter states, all modes are nondegenerate, while in the mixed state, two high-frequency modes are doubly degenerate. The energies of high-frequency modes lie in the interval $(1.1\text{–}1.88)\Delta_0(T)$, while in the mixed state, they belong to the interval $(1.59\text{–}1.93)\Delta_0(T)$; i.e., collective modes have higher frequencies in the mixed state.

It should be noted that the attenuation of collective modes in the pure states is stronger than in the mixed state ($\mathrm{Im}E_i$ varies from 30 to 65% in the pure state and from 20 to 50% in the mixed state). This can be explained taking into account the fact that in pure states, the gap vanishes on the lines of the Fermi surface, while it vanishes only at two points (poles) in the mixed state.

The strong difference in the collective excitation spectra for pure d states and the mixed state makes it possible to verify the symmetry of the superconducting state in experiments on ultrasound and microwave absorption, in which collective modes are excited. Although rather high frequencies (of the order of tens gigahertz) might be required for such experiments, there are no limitations of fundamental nature on the frequencies of ultrasound (microwaves): since the frequencies of collective modes are proportional to the gap amplitude $\Delta_0(T)$ vanishing at T_c, any frequency may, in principle, be used as the temperature approaches T_c.

Thus, we are in a position to answer the following two fundamental questions:

(1) does the gap disappear along certain preferred lines?

(2) do we have a pure d state or a mixture of d states in HTSC?

Balatsky *et al.* [12] analyzed the mixture of two d-states and s- and d-states: $d_{x^2-y^2} + id_{xy}$ and $d_{x^2-y^2} + is$. In the case when the mixture of two d states is realized, they studied the situation when the d_{xy} state is induced by an external magnetic field (in accordance with the assumptions used by Laughlin [9] for explaining the results of Krishana's experiments [8]). They proved in this case the existence of an orbital magnetization mode corresponding to the oscillations of the relative phase φ between two components about the equilibrium value $\varphi = \pm\pi/2$. This mode is similar to the clapping mode in ^{3}He–A; the exact value of frequency for this mode was obtained in [3]. However, if the d_{xy} state is induced by an external magnetic field, the frequency of this mode is proportional to the external field, $\omega \approx B\Delta_0$ (B is the magnetic induction).

We did not consider the reason behind the formation of the impurity d_{xy} state, which may be numerous (the generation of the d_{xy} state near the magnetic impurity, the presence of vortex texture, etc.). In particular, we did not introduce the external magnetic field and, hence, did not study the field dependence of collective mode frequencies. At the same time, it should be noted that Balatsky *et al.* [12] studied a single specific mode in a mixture of states, while we considered the complete spectrum of collective modes.

4. TWO-DIMENSIONAL *p*- AND *d*-WAVE SUPERCONDUCTIVITY

4.1. Two-Dimensional Models of p- and d-Pairing in Superconductors

Two-dimensional (2D) models of superconductivity, including 2D models of d-pairing in HTSC are important for several reasons. Above all, CuO_2 planes are the common structural factor in virtually all the HTSC discovered so far. It is generally accepted that the entire physics of this phenomenon is associated just with these planes.

The existence of superfluidity in ^{3}He films was proved even 20 years ago [3] and was subsequently observed experimentally [14].

The 2D superconductivity has its own specific features due to the fact that, in accordance with Bogoliubov's ($1/k^2$) theorem, the condensate exists only at $T = 0$. However, superconductivity associated with a certain behavior of Bose-field correlators is also possible for $T \neq 0$: if these correlators decrease at large distances according to a power law and not exponentially, this indicates the existence of superconductivity in the system. In this case, the superconducting transition temperature T_c is the point of transition from an exponential decrease of Bose-field correlators to a power dependence. Alternative approaches associated with the introduction of the initial condensate generating the superfluid density of carriers of the order of their total density are also possible.

4.1.1. *p*-Pairing

In order to describe the 2D model of *p*-pairing, we consider the 3D model [3] with the following modification made for the 2D case.

a. The orbital angular momentum **l** (|**l**| = 1) must be perpendicular to the plane and may have only two components along the z axis: ±1. Since the *p*-pairing is a triplet process, the total spin of a pair is equal to unity, and hence there are $3 \times 2 \times 2 = 12$ degrees of freedom in the case of two-dimensional *p*-pairing. Consequently, the superconducting state in this case may be described by an arbitrary complex 2×3 matrix $c_{ia}(p)$ with the same number of degrees of freedom ($2 \times 3 \times 2 = 12$). This number is equal to the number of collective modes in each phase. It should be recalled that in the 3D case, this number is 18.

b. In this case **x** is a 2D vector, and the two-dimensional "volume" $S = L^2$ (instead of $V = L^3$ in the 3D case).

4.1.1.2. Collective Mode Spectrum

We present here the results (some of which were obtained earlier [3]) for the collective mode spectrum in various superconducting states of 2D superconductor with *p*-pairing (as before, the number of collective modes is given in parentheses):

a phase $\begin{pmatrix} 1 & 0 & 0 \\ i & 0 & 0 \end{pmatrix}$:

$$E^2 = c_F^2k^2/2 \ (3), \quad E^2 = 2\Delta^2 + c_F^2k^2/2 \ (6),$$

$$E^2 = 4\Delta^2 + (0.5 - 0.433i)c_F^2k^2/2 \ (3),$$

b phase $\begin{pmatrix} 1 & 0 & 0 \\ 0 & 1 & 0 \end{pmatrix}$:

$$E^2 = c_F^2k^2/2 \ (2), \quad E^2 = 3c_F^2k^2/4 \ (1),$$

$$E^2 = c_F^2k^2/4 \ (1), \quad E^2 = 2\Delta^2 \ (4),$$

$$E^2 = 4\Delta^2 + (0.15 + 0.22i)c_F^2k^2/2 \ (3),$$

$$E^2 = 4\Delta^2 + (0.85 - 0.22i)c_F^2k^2/2 \ (1),$$

$$E^2 = 4\Delta^2 + (0.5 - 0.43i)c_F^2k^2/2 \ (2),$$

phase $\begin{pmatrix} 0 & 0 & 1 \\ 0 & 0 & i \end{pmatrix}$:

$$E^2 = 0 \ (3), \quad E^2 = 2\Delta^2 \ (6), \quad E^2 = 4\Delta^2 \ (3),$$

phase $\begin{pmatrix} 0 & \pm 1 & 0 \\ 1 & 0 & 0 \end{pmatrix}$:

$$E^2 = 0 \ (4), \quad E^2 = 2\Delta^2 \ (4), \quad E^2 = 4\Delta^2 \ (4),$$

phase $\begin{pmatrix} 1 & 0 & 0 \\ 0 & -1 & 0 \end{pmatrix}$:

$$E^2 = 0 \ (4), \quad E^2 = 2\Delta^2 \ (4), \quad E^2 = 4\Delta^2 \ (4).$$

4.1.2. *d*-Pairing

It was mentioned above that CuO_2 planes are the common structural factor of almost all discovered HTSC, and it is generally accepted that the entire physics of superconductivity is associated just with these planes. Considering that *d*-pairing is apparently realized in most HTSC, an analysis of the 2D model of *d*-pairing is of considerable interest. There also exists additional arguments in favor of the study of such models. For example, it was proved for a 2D antiferromagnet that only the *d*-channel ensures attraction between fermions; *d*-pairing also emerges in the symmetry classification of HTSC [10, 15].

Thus, we consider the 2D model of *d*-pairing in CuO_2 planes, which was constructed by us earlier [4, 5] using the functional integration method. As in the 3D case, the model is described by the hydrodynamic action functional obtained by successive functional integration over fast and then slow Fermi fields. As in the 3D model the hydrodynamic action functional determines all the properties of the system under investigation (in the given case, CuO_2 planes), including the collective excitation spectrum.

In order to describe the 2D model of *d*-pairing in CuO_2 planes, we consider the 3D model used by us earlier. The basic differences observed in the 2D case are as follows.

a. The orbital angular momentum **l** (|**l**| = 2) must be perpendicular to the CuO_2 plane and may have only two components along the z axis: ±2. Since *d*-pairing is a singlet process, the total spin of a pair is equal to zero and, hence, there are $1 \times 2 \times 2 = 4$ degrees of freedom in the case of the 2D *d*-pairing. Consequently, the superconducting state in this case can be described by a complex symmetric traceless 2×2 matrix $c_{ia}(p)$ which possesses the same number of degrees of freedom ($2 \times 2 \times 2 - 2 - 2 = 4$). This number is equal to the number of collective modes in each phase. It should be recalled that in the 3D case, this number is equal to 10.

b. The pairing potential is given by the formula

$$t = V(\hat{k}, \hat{k}') = \sum_{m = -2, 2} g_m Y_{2m}(\hat{k}) Y^*_{2m}(\hat{k}'). \qquad (21)$$

In the case of circular symmetry, $g_2 = g_{-2} = g$, and we have only one coupling constant g, while less symmetric cases require the existence of both constants (g_2 and g_{-2}). We will consider the case of circular symmetry.

c. Vector **x** is two-dimensional, and the area $S = L^2$ (instead of $V = L^3$ in the 3D case). In view of these differences, we will describe our Fermi system by anticommuting functions $\chi_s(\mathbf{x}, \tau)$, $\bar{\chi}_s(\mathbf{x}, \tau)$ defined in "volume" $S = L^2$ and antiperiodic in time τ with period $\beta = T^{-1}$ (T is the temperature).

After the functional integration with respect to slow and fast Fermi fields, we obtain the effective functional of action, which formally has the same form (5) as in the 3D case.

In the 2D case, the number of degrees of freedom of the order parameter for d-pairing is equal to four. In other words, we have two complex canonical variables. It can easily be seen from the nondiagonal elements of matrix M that for canonical variables, we can choose

$$c_1 = c_{11} - c_{22}, \quad c_2 = c_{12} + c_{21}.$$

For conjugate variables, we have

$$\overset{+}{c}_1 = \overset{+}{c}_{11} - \overset{+}{c}_{22}, \quad \overset{+}{c}_2 = \overset{+}{c}_{12} + \overset{+}{c}_{21}.$$

In the canonical variables, S_{eff} has the form

$$S_{\text{eff}} = \frac{1}{2g}\sum_{p,\,j} \overset{+}{c}_j(p)c_j(p) + \frac{1}{2}\ln\det\frac{M(\overset{+}{c}_j, c_j)}{M(\overset{+}{c}{}_j^{(0)}, c_j^{(0)})}, \tag{22}$$

where

$$M_{11} = \frac{1}{Z}[i\omega - \xi + \mu(\mathbf{H}\cdot\boldsymbol{\sigma})]\delta_{p_1p_2},$$

$$M_{22} = \frac{1}{Z}[-i\omega + \xi + \mu(\mathbf{H}\cdot\boldsymbol{\sigma})]\delta_{p_1p_2},$$

$$M_{12} = \overset{+}{M}_{21} = \frac{\sigma_0\alpha}{\sqrt{\beta}}(c_1\cos 2\varphi + c_2\sin 2\varphi).$$

Functional S_{eff} determines all properties of 2D superconductors (CuO_2 planes and others). In particular, it determines the collective mode spectrum.

4.2. Collective Excitations in CuO_2 Planes of HTSC

Two superconducting states with the order parameters proportional to $\begin{pmatrix} 1 & 0 \\ 0 & -1 \end{pmatrix}$ and $\begin{pmatrix} 0 & 1 \\ 1 & 0 \end{pmatrix}$ are formed in the symmetry classification of CuO_2 planes. In the first phase, the gap is proportional to

$$Y_{22} + Y_{2-2} \propto \sin^2\theta|\cos 2\varphi| \propto |\cos 2\varphi|,$$

while in the second phase it is proportional to

$$-i(Y_{22} - Y_{2-2}) \propto \sin^2\theta|\sin 2\varphi| \propto |\sin 2\varphi|.$$

In the 2D case, we put $\theta = \pi/2$ and $\sin\theta = 1$.

Let us calculate the collective mode spectrum for the two given states. In the first approximation, the collective excitation spectrum is determined by the quadratic part of the effective action S_{eff} obtained by the translation $c_j(p) \longrightarrow c_j(p) + c_j^0(p)$ in S_{eff}. Here, $c_j^0(p)$ are condensate values of canonical Bose fields $c_j(p)$.

The quadratic component of the effective action S_{eff} is defined by formula (11) for $A = 4$. In this case, $\Delta = \Delta_0|\cos 2\varphi|$ for phase $\begin{pmatrix} 1 & 0 \\ 0 & -1 \end{pmatrix}$ and $\Delta = \Delta_0|\sin 2\varphi|$ for phase $\begin{pmatrix} 0 & 1 \\ 1 & 0 \end{pmatrix}$, $\Delta_0 = 2\alpha cZ$, $\alpha = \sqrt{15/32\pi}$, and $M_i = \omega_i^2 + \xi_i^2 + \Delta^2$.

The first term in the expression for S_{eff} contains the coupling constant g which must be eliminated using the equation for the gap, which has the following forms for the first and second phases, respectively:

$$\frac{1}{g} + \frac{\alpha^2Z^2}{\beta S}\sum_p \frac{\cos^2 2\varphi}{\omega^2 + \xi^2 + \Delta_0^2\cos^2 2\varphi} = 0,$$

$$\frac{1}{g} + \frac{\alpha^2Z^2}{\beta S}\sum_p \frac{\sin^2 2\varphi}{\omega^2 + \xi^2 + \Delta_0^2\sin^2 2\varphi} = 0.$$

Here, $\Delta_0^2 = 4a^2c^2Z^2$. At low temperatures, we can go over from summation to integration using the following rule:

$$\frac{1}{\beta S}\sum_p \longrightarrow \frac{1}{(2\pi)^3}\frac{k_F}{c_F}\int d\omega d\xi d\varphi.$$

Here, as before, k_F is the Fermi momentum of a quasifermion and c_F is the velocity on the Fermi surface. After integrating with respect to ω and ξ with the help of the Feynman procedure, we arrive at the following equations for the collective mode spectrum, obtained from the condition $\det Q = 0$, where Q is the matrix of the quadratic part of functional S_{eff}:

$$\begin{gathered}\int_0^1 \frac{dx}{\sqrt{1-x^2}}\left\{\frac{\sqrt{\omega^2 + 4g_k}}{\omega}\ln Gg_1 - (g_k - g_i)\ln g_k\right\} = 0,\\ \int_0^1 \frac{dx}{\sqrt{1-x^2}}\left\{\frac{\omega}{\sqrt{\omega^2 + 4g_k}}\ln Gg_1 - (g_k - g_i)\ln g_k\right\} = 0.\end{gathered} \tag{23}$$

Here, $G \equiv (\sqrt{\omega^2 + 4g_k} + \omega)/(\sqrt{\omega^2 + 4g_k} - \omega)$, k denotes the phase and i labels the modes, $g_1 = x^2$, $g_2 = 1 - x^2$, $x = \cos 2\varphi$, and $\omega = \omega/\Delta_0$. Consequently, for each fixed k, we have four equations leading to four frequencies of collective modes.

4.3. Discussion of Results

The spectra in both phases are found to be identical. We obtained two high-frequency modes in each phase (from the second equation in (23)) with the following frequencies:

$$E_1 = \Delta_0(1.42 - 0.65i),$$
$$E_2 = \Delta_0(1.74 - 0.41i).$$

Note that the frequencies of both modes are complex-valued. This is a consequence of *d*-pairing or, in other words, the consequence of gap vanishing in the chosen directions. In this case, Bose excitations decay into fermions, which leads to collective mode attenuation. The value of the imaginary component of the frequency amounts to 23% of its real component for the second mode and to 46% for the first mode. For this reason, both modes may be regarded as resonances. The second mode is defined better than the first mode.

The first equation in system (23) gives two Goldstone (quasi-Goldstone) modes with (frequencies smaller than $0.1\Delta_0$).

REFERENCES

1. P. N. Brusov, *Mechanisms of HTSC* (Rostov State University Publ., Rostov, 1999), Vols. 1, 2.
2. *Proceedings of International Conference on Low Temperature Physics LT-22, Helsinki, Finland, 1999;* Physica B **284–288** (2000).
3. P. N. Brusov and V. N. Popov, *Superfluidity and Collective Properties of Quantum Liquids* (Nauka, Moscow, 1988).
4. P. N. Brusov and N. P. Brusova, Physica B (Amsterdam) **194–196**, 1479 (1994).
5. P. N. Brusov and N. P. Brusova, J. Low Temp. Phys. **103**, 251 (1996).
6. L. Tewordt, Phys. Rev. Lett. **83**, 1007 (1999).
7. D. S. Hiroshima and H. Namaizawa, J. Low Temp. Phys. **73**, 137 (1988).
8. K. Krishana, N. P. Ong, Q. Li, *et al.*, Science **277**, 83 (1997).
9. R. B. Laughlin, Phys. Rev. Lett. **80**, 5188 (1998).
10. J. F. Annett, N. D. Goldenfeld, and A. J. Leggett, in *Physical Properties of High Temperature Superconductors V*, Ed. by D. M. Ginsberg (World Scientific, Singapore, 1996).
11. P. N. Brusov and P. P. Brusov, Physica B **281–282**, 949 (2000).
12. A. V. Balatsky, P. Kumar, and J. R. Schrieffer, Phys. Rev. Lett. **84**, 4445 (2000).
13. P. N. Brusov, N. P. Brusova, and P. P. Brusov, J. Low Temp. Phys. **108**, 143 (1997).
14. A. Sachrajda, R. F. Harris-Lowe, and J. Harrison, Phys. Rev. Lett. **55**, 1602 (1985).
15. M. Sigrist and T. M. Rice, Z. Phys. B **68**, 9 (1987).

Translated by N. Wadhwa

Journal of Experimental and Theoretical Physics, Vol. 92, No. 5, 2001, pp. 811–815.
From Zhurnal Éksperimental'noĭ i Teoreticheskoĭ Fiziki, Vol. 119, No. 5, 2001, pp. 931–936.
Original English Text Copyright © 2001 by Shevchenko, Kolesnichenko.

SOLIDS
Electronic Properties

Conductance of the Elliptically Shaped Quantum Wire¶

S. N. Shevchenko* and Yu. A. Kolesnichenko

Verkin Institute for Low Temperature Physics and Engineering, National Academy of Sciences of Ukraine,
Kharkov, 61164 Ukraine
**e-mail: sshevchenko@ilt.kharkov.ua*

Received 25 October, 2000

Abstract—The conductance of a ballistic elliptically shaped quantum wire is investigated theoretically. It is shown that the effect of the curvature results in a strongly oscillating dependence of the conductance on the applied bias. © *2001 MAIK "Nauka/Interperiodica".*

1. INTRODUCTION

Recent advances in semiconductor physics and technology enabled the fabrication and investigation of nanostructure devices possessing important properties, such as small size, reduced dimensionality, relatively small density of charge carriers, and hence, large mean free path (which means that particles exist in the ballistic regime and the scattering processes can therefore be neglected), and large Fermi wavelength λ_F. One of the mesoscopic systems of particular interest is the quantum wire in which particles are constrained to move along a one-dimensional curve due to quantization of the transverse modes.[1] One of the numerous important problems pertaining to the quantum wire is to determine the influence of the reduced dimensionality upon the system properties.

Jensen and Koppe [1] and da Costa [2] emphasized that a low-dimensional system, in general, has some knowledge of the surrounding three-dimensional Cartesian space: the effective potential arises from the mesoscopic confinement process, which constrains particles to move in a domain of a reduced dimensionality. Namely, it was shown that a particle moving in a one- or two-dimensional domain is affected by an attractive effective potential [2]; this result was first obtained in [3] and later in [4]. This idea was widely studied by several other authors (see [5–12] and, for example, [13] about the experimental realization of such systems).

It was also shown in [14] that the torsion of the twisted waveguide affects the wave propagation in the waveguide independently of the nature of the wave. In particular, the torsion of the waveguide results in the rotation of the polarization of light in a twisted optical fiber [15]. In [16], the authors prove that in a waveguide, be it quantum or electromagnetic one, bound states exist. Several papers have been devoted to the relation of the quantum waveguide theory to the classical theory of acoustic and electromagnetic waveguides in [6].

The effect of the curvature on quantum properties of electrons on a two-dimensional surface, in a quantum waveguide, or in a quantum wire can be observed by investigating kinetic and thermodynamic characteristics of quantum systems [8–12]. In this paper, we propose to use measurements of the conductance G of a quantum wire for this purpose; we show that the reflection of electrons from regions with a variable curvature results in a nonmonotonic dependence of the conductance on the applied bias.

In [4], the Schrödinger equation on the elliptically shaped ring was solved numerically in order to obtain the eigenvalue spectrum of a particle confined to the ring. The authors studied a quantum mechanical system confined to a narrow ring by the rectangular well potential. They showed that in the limit as the ring width γ tends to zero, the behavior of the system is similar to the straight line motion with the effective potential

$$V_{\mathrm{eff}} = -\frac{\hbar^2}{8mR^2}, \tag{1}$$

where R is the radius of curvature. Later [9], the electron energy spectrum in an elliptical quantum ring was considered in connection with the persistent current; the authors have concluded that the effective potentials V_{eff} are different for different confining potentials even in the limit as γ tends to zero. This conclusion is in contradiction with the results of some other papers [2, 6]. We address this problem in the present paper; we investigate the derivation of the one-dimensional Schrödinger equation in order to understand more deeply how the particle motion along the curve C is affected by the confining potential. We demonstrate the consistency with the previous results in [2]: the effective potential is universal for different confining potentials and depends only on the curvature (see Eq. (1)).

¶ This article was submitted by the authors in English.

[1] We study here only the one-channel wire with only the lowest subband occupied.

1063-7761/01/9205-0811$21.00 © 2001 MAIK "Nauka/Interperiodica"

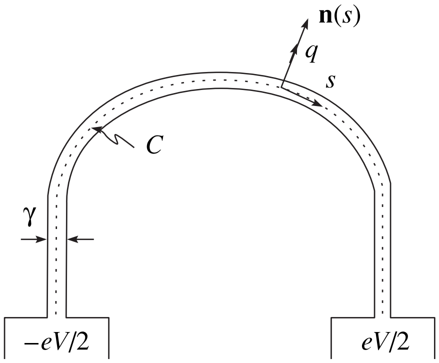

Fig. 1. Elliptically shaped quantum wire.

In Section 2, we derive a one-dimensional Schrödinger equation starting from the two-dimensional Schrödinger equation describing a nonrelativistic electron that moves in a plane[2] and is subjected to the confining potential V_γ. In Section 3, we apply these results to theoretically study the conductance of the quantum wire that consists of two linear parts and one elliptically shaped part between them; the wire is connected to two conducting reservoirs at different voltages (see Fig. 1). In Section 4, we discuss the influence of the curvature on the conductance.

2. SCHRÖDINGER EQUATION

In this section, we follow the approach proposed in [2]. We consider the electron with the effective mass m moving in a quantum wire along a curve C that is constructed by a prior confinement potential V_γ. For simplicity, we start with the two-dimensional motion. We introduce the orthonormal coordinate system[3] (s, q), where s is the arc length parameter and q is the coordinate along the normal $\mathbf{n} = \mathbf{n}(s)$ to the reference curve C. The curve C is then described by a vector valued function $\mathbf{r}(s)$ of the arc length s. In a vicinity of C, the position is therefore described by

$$\mathbf{R}(s, q) = \mathbf{r}(s) + q\mathbf{n}(s). \tag{2}$$

To obtain a meaningful result, the particle wave function must be "uniformly compressed" into a curve, thereby avoiding tangential forces [2, 4, 9]. We thus consider V_γ to depend only on the q coordinate that describes the displacement from the reference curve C; this means that points with the same q coordinate but different s coordinates (which describe the position on C) have the same potential. This potential involves a small parameter γ such that the potential increases sharply for every small displacement in the normal direction; γ is the characteristic width of the potential well V_γ. The simplest examples of these potentials are the rectangular well potential and the parabolic-trough potential (we note that the real potential would likely be a combination of both, however). The small parameter in the problem is therefore $\gamma/R \ll 1$ [5].

The motion of the electron obeys the time-independent Schrödinger equation

$$-\frac{\hbar^2}{2m}\Delta_{s,q}\psi + V_\gamma(q)\psi = \varepsilon\psi, \tag{3}$$

where the Laplacian is

$$\Delta_{s,q} = \frac{1}{h}\frac{\partial}{\partial s}\frac{1}{h}\frac{\partial}{\partial s} + \frac{1}{h}\frac{\partial}{\partial q}h\frac{\partial}{\partial q}, \tag{4}$$

with

$$h = 1 - k(s)q \tag{5}$$

being the Lamé coefficient (corresponding to the longitudinal coordinate s) that depends on the curvature $k = k(s)$ in accordance with the Frenet equation.

To eliminate the first-order derivative with respect to q from Eq. (3),[4] we introduce the new wave function $\tilde{\psi}$ by

$$\tilde{\psi}(s, q) = \sqrt{h}\psi(s, q). \tag{6}$$

This is the wave function introduced in [2] and normalized so that

$$\int ds\,dq|\tilde{\psi}(s, q)|^2 = 1. \tag{7}$$

The Schrödinger equation (3) then becomes

$$\begin{gathered}-\frac{\hbar^2}{2m}\left(\frac{\partial}{\partial s}\frac{1}{h^2}\frac{\partial}{\partial s} + \frac{\partial^2}{\partial q^2}\right)\tilde{\psi} \\ + V_{\text{eff}}(s, q)\tilde{\psi} + V_\gamma(q)\tilde{\psi} = \varepsilon\tilde{\psi},\end{gathered} \tag{8}$$

where

$$\begin{gathered}V_{\text{eff}}(s, q) = -\frac{\hbar^2}{2m} \\ \times\left(h^{-2}\frac{k^2}{4} + \frac{q}{2}h^{-2}\frac{d^2k}{ds^2} + \frac{5q^2}{4}h^{-4}\left(\frac{dk}{ds}\right)^2\right),\end{gathered} \tag{9}$$

which is in agreement with [5, 8].

One must be careful with Eq. (8) in order to avoid mistakes found in the literature [7, 9]. First, we cannot decompose this equation, which contains terms that are

---

[2] We consider only flat curves and we refer the reader interested in the effect of the torsion to [7].

[3] The advantages of establishing the (s, q) coordinate system from the very beginning are that it allows the most general analysis and that (because of the diagonal structure of the metric tensor) we can decompose the dynamical equation of motion into two equations in the zero-order approximation in the width of the quantum wire.

[4] We do this to eliminate terms of the form $f(q)\partial/\partial q$ that were called "dangerous terms" in [1]. We cannot use $f(q) = f(0)$ because $f(q)\partial/\partial q \approx [f(0) + q\,df(0)/dq]\partial/\partial q$: although $q \sim \gamma$, we have $\partial/\partial q \sim \gamma^{-1}$ and the second term in the brackets is therefore $\sim\gamma^0$, and this is the order of terms in which we are interested below.

functions of both s and q, into two equations introducing $\tilde{\psi}(s, q) = \chi_n(q)\chi_t(s)$ as in [7], where the authors obtained Eq. (31) for $\chi_t(s)$ with coefficients depending on the q variable. To understand another mistake [9], we consider Eq. (8) within the perturbation theory in the small parameter γ (which is small compared to R) (see also [6]). We expand h^{-2} and V_{eff} in series in $q \lesssim \gamma$ and explicitly write the zeroth term as

$$h^{-2} = 1 + \sum_{l=1}^{\infty} f_l(s)q^l,$$

$$V_{\text{eff}}(s, q) = -\frac{\hbar^2}{2m}\left(\frac{k^2(s)}{4} + \sum_{l=1}^{\infty} y_l(s)q^l\right).$$

Equation (8) can then be rewritten as

$$(\hat{H}_0 + \hat{V})\tilde{\psi} = \varepsilon\tilde{\psi}, \tag{10}$$

where

$$\hat{H}_0 = -\frac{\hbar^2}{2m}\left(\frac{\partial^2}{\partial s^2} + \frac{\partial^2}{\partial q^2}\right) - \frac{\hbar^2}{2m}\frac{k^2(s)}{4} + V_\gamma(q), \tag{11}$$

$$\hat{V} = \frac{\hbar^2}{2m}\sum_{l=1}^{\infty} q^l\left(-\frac{\partial}{\partial s}f_l(s)\frac{\partial}{\partial s} + y_l(s)\right). \tag{12}$$

We note that $\hat{V}$ is a second order differential operator in s. The solution of Eq. (10) is

$$\tilde{\psi} = \tilde{\psi}^{(0)} + \sum_{l=1}^{\infty} \tilde{\psi}^{(l)},$$

where $\tilde{\psi}^{(l)} \sim \gamma^l$ and $\tilde{\psi}^{(0)}$ corresponds to the zeroth-order problem, $\hat{H}_0\tilde{\psi}^{(0)} = \varepsilon\tilde{\psi}^{(0)}$. This equation can be decomposed by separating the wave function as $\tilde{\psi}(s, q) = \eta(q)\chi(s)$,

$$-\frac{\hbar^2}{2m}\frac{d^2}{dq^2}\eta + V_\gamma(q)\eta = E_t\eta \tag{13}$$

and

$$-\frac{\hbar^2}{2m}\frac{d^2}{ds^2}\chi + V_{\text{eff}}(s)\chi = E_l\chi, \tag{14}$$

where $V_{\text{eff}}(s)$ is given by Eq. (1), $\varepsilon = E_t + E_l$, and $R = k(s)^{-1}$ is the curvature radius (in the next section, we omit the subscript "l", identifying the energy E with its longitudinal component E_l). Equation (13) describes the confinement of the electron to a γ-neighborhood of the curve C and Eq. (14) describes the motion along the s coordinate (along C). In fact, Eq. (14) is a conventional one-dimensional Schrödinger equation for the electron moving in the s-dependent potential $V_{\text{eff}}(s)$; the latter relates the geometry and the dynamical equation. The origin of this potential is in the wavelike properties of the particles; V_{eff} is essential for the values of R/λ_F that are not large. We emphasize that the effective potential in Eq. (1) in the zeroth-order approximation in γ/R is independent of the "one-dimensionalization" method, i.e., of the choice of $V_\gamma(q)$ (compare this conclusion with the one derived in [9])

We also note that if we started from the three-dimensional equation of motion, we would obtain an additional effective potential that vanishes in the planar situation [2].

3. CONDUCTANCE

The conductance G of quantum contacts can be related to the transmission probability $T(E)$ by Landauer's formula [17]. At zero temperature and finite voltages V, it takes the form

$$G = \frac{G_0}{2}\left[T\left(E_F + \frac{eV}{2}\right) + T\left(E_F - \frac{eV}{2}\right)\right], \tag{15}$$

where $G_0 = 2e^2/h$ and E_F is the Fermi energy. The two terms in this equation correspond to two electronic beams moving in opposite directions with different bias energies. We are interested in the transmission probability $T(E)$ for the electron energy E.

In this section, we consider the curve C to consist of three ideally connected parts (see Fig. 1): (i) linear ($s < 0$), (ii) elliptical ($0 < s < l$, where l is half of the ellipse perimeter), and (iii) one more linear domain ($s > l$). We consider wave functions in regions (i) and (iii) to be the respective plane waves $\psi_1 = e^{ik_1 s} + re^{-ik_1 s}$ and $\psi_3 = te^{ik_1 s}$, where $k_1 = \sqrt{2mE/\hbar^2}$ is the wave vector and t and r are the transmission and reflection coefficients; the transmission probability is given by $T = |t|^2$. We have $\psi_2 \equiv \chi$, where χ is the solution of Eq. (14) with the effective potential given by Eq. (1). The curvature can be written most simply in the elliptical coordinate ν [18] defined by its Lamé coefficient

$$H = \frac{ds}{d\nu} = a\sqrt{1 - e^2\cos^2\nu}, \tag{16}$$

where e is the eccentricity of the ellipse and a is the length of its major semiaxis; we use $\nu(s = 0) = 0$. The effective (geometrical) potential in Eq. (1) can then be written as

$$V_{\text{eff}}(s) = -\frac{\hbar^2}{8ma^2}\frac{1 - e^2}{(1 - e^2\cos^2\nu)^3}, \tag{17}$$

which is in agreement with [4].

We introduce the new wave function

$$\xi(\nu(s)) = \chi(s)/\sqrt{H}, \tag{18}$$

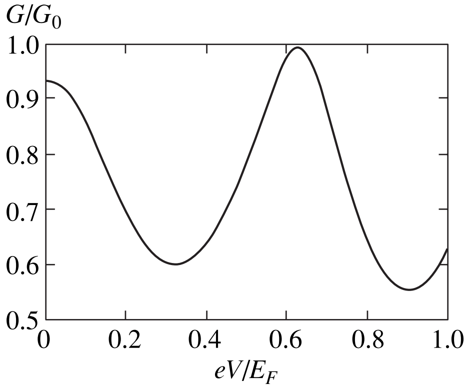

Fig. 2. Conductance as a function of the bias $G = G(eV)$ at $e = 0.99$, $a = 10\lambda_F$ (at the same value of a but with $e = 0$, the amplitude $\Delta G/G_0$ is on the order of 10^{-5}).

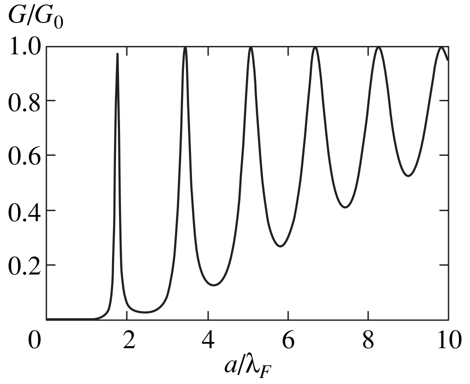

Fig. 3. Conductance as a function of the length of the major semiaxis $G = G(a)$ at $e = 0.99$, $V = 0$.

for which the equation takes the form (see Eqs. (14) and (16)–(18))

$$\frac{d^2}{d\nu^2}\xi + \left[\frac{2ma^2}{\hbar^2}Eg(\nu) + U(\nu)\right]\xi = 0, \qquad (19)$$

$$U(\nu) = \frac{5}{4}\frac{1-e^2}{g^2} - \frac{1-e^2/2}{g} - \frac{e^4}{16}\frac{\sin^2 2\nu}{g^2}, \qquad (20)$$

where $g = H^2/a^2 = 1 - e^2\cos^2\nu$. Equation (19) is the Hill equation with π-periodic coefficients; the fundamental system of its solutions is [19]

$$\xi_\pm = e^{\pm i\mu\nu}y(\pm\nu), \qquad (21)$$

where $y(\nu)$ is a π-periodic function and μ is the characteristic exponent. We then have (see Eqs. (18) and (21))

$$\chi = C_1 e^{i\mu\nu}\tilde{y}(\nu) + C_2 e^{-i\mu\nu}\tilde{y}(-\nu), \qquad (22)$$

where $\tilde{y}(\nu) \equiv \sqrt{H}y(\nu)$.

With the known wave functions, we are now interested in $T = |t|^2$, which describes the transmission over the potential well (see Eq. (17)). We use the continuity conditions for the wave function and its derivative, which gives a system of four equations that is similar to the one given in [20]; the result is

$$T = \left[1 + \frac{1}{4}\left(\kappa - \frac{1}{\kappa}\right)^2\sin^2\pi\mu\right]^{-1}, \qquad (23)$$

where we denoted

$$\kappa = -\frac{i}{ak_1\sqrt{1-e^2}}\left(\frac{\xi'_+}{\xi_+}\right)_{\nu=0}. \qquad (24)$$

(To obtain Eq. (23), we assumed that μ and κ are real, which is straightforward to proof.)

4. RESULTS AND DISCUSSION

To understand how the conductivity G depends on the bias eV and the geometry, we must find the solution of Hill equation (19). We did this numerically and also within the perturbation theory for an ellipse that is close to the circle (i.e., $e^2 \ll 1$); we found that the two solutions are in good agreement for $e < 1/2$. In the zeroth-order approximation in e^2 (i.e., for $e = 0$, the case of a circular arc), we have $\mu_0 = ak_2$ and $\kappa_0 = k_2/k_1$, where $k_2 = \sqrt{2mE/\hbar^2 + 1/4a^2}$ (see also [12]). This implies that oscillations in the $G(V)$ dependence can be observed if $a \gtrsim \lambda_F$ and the amplitude of these oscillations is sufficiently small.

The first-order approximation of the perturbation theory (for $a > \lambda_F$) yields

$$\mu \approx \mu_0 + e^2\mu_1, \quad \kappa \approx \kappa_0 + e^2\kappa_1, \qquad (25)$$

where

$$\mu_1 = -\frac{ak_1^2}{4k_2} \equiv \frac{\mu_0}{4\kappa_0}, \qquad (26)$$

$$\kappa_1 = \frac{k_1}{4k_2((ak_2)^2 - 1)}. \qquad (27)$$

We have solved Hill equation (19) numerically. The characteristic exponent μ is defined via the solution of Eq. (19) with the initial conditions $\xi_1(0) = 1$ and $\xi'_1(0) = 0$, and μ is then the solution of the equation $\xi_1(\pi) = \cos\pi\mu$ (see [19]). It is more difficult to find ξ_+ (see Eq. (21)), which can be formulated as the boundary value problem for Eq. (19) with the boundary conditions $\xi_2(0) = 0$ and $\xi_2(\pi) = \sin\pi\mu$ (where $\xi_2(\nu) = \mathrm{Im}\,\xi_+(\nu)$). Introducing $\xi_3(\nu) = \xi_2(\nu)/\xi'_2(0)$, we have the initial condition problem for $\xi_3(\nu)$ (with $\xi_3(0) = 0$, and $\xi'_3(0) = 1$), whose solution allows us to define κ, $(\xi'_+/\xi_+)_{\nu=0} = \xi'_2(0) = \sin\pi\mu/\xi_3(\pi)$. The results of the described procedure are numerically plotted in Figs. 2 and 3 for a sufficiently elongated ellipse with $e = 0.99$

(with $a/b = 7$, where a and b are the respective lengths of its major and minor semiaxes). We note about Fig. 3 that under the restriction $R \gg \gamma$, we must not let a go to zero; namely, we may suppose $R \gg \gamma$ for $a/\lambda_F \sim 10$ but may not for $a/\lambda_F \lesssim 1$ [for e close to unity]. We also note that Eq. (15) is, strictly speaking, correct for eV small compared with E_F and describes $G(V)$ dependence for $eV \sim E_F$ qualitatively. We conclude that e close to unity significantly increases oscillations in comparison to the case of $e = 0$; the amplitude of oscillations in $G = G(V)$ is defined by the value of a/λ_F.

In summary, we have rederived the quantum-mechanical effective potential induced by the curvature of the one-dimensional quantum wire. We have shown that for any confining potential V_γ depending only on the displacement q from the reference curve C, this effective potential is universal: it does not depend on the choice of V_γ and is given by Eq. (1). We have studied the effect of the curvature on the conductance of an ideal elliptically shaped quantum wire in the zeroth-order approximation in the width of the wire. It has been shown, in particular, that due to the effect of the curvature, the dependence of the conductance $G(V)$ on the applied bias changes drastically. Thus, the effect of the curvature can be observed by measuring the conductance of the quantum wire. On the other hand, one can change the characteristics of the quantum wire, such as the conductance, setting its size, shape, or applied bias.

ACKNOWLEDGMENTS

One of the authors (S.N.S.) would like to thank Prof. I.D. Vagner for his warm hospitality during his stay at the Grenoble High Magnetic Field Laboratory (France), where a part of this work was done. We also thank Prof. A.M. Kosevich for critical discussion of the manuscript.

REFERENCES

1. H. Jensen and H. Koppe, Ann. Phys. (N. Y.) **63**, 586 (1971).
2. R. C. T. da Costa, Phys. Rev. A **23**, 1982 (1981).
3. J. Marcus, J. Chem. Phys. **45**, 4493 (1966).
4. E. Switkes, E. L. Russell, and J. L. Skinner, J. Chem. Phys. **67**, 3061 (1977).
5. P. Exner and P. Šeba, J. Math. Phys. **30**, 2574 (1989).
6. P. Duclos and P. Exner, Rev. Math. Phys. **7**, 73 (1995).
7. I. J. Clark and A. J. Bracken, J. Phys. A **29**, 339 (1996).
8. I. J. Clark and A. J. Bracken, J. Phys. A **29**, 4527 (1996).
9. L. I. Magarill, D. A. Romanov, and A. V. Chaplik, Zh. Éksp. Teor. Fiz. **110**, 669 (1996) [JETP **83**, 361 (1996)].
10. L. I. Magarill and A. V. Chaplik, Pis'ma Zh. Éksp. Teor. Fiz. **68**, 136 (1998) [JETP Lett. **68**, 148 (1998)].
11. L. I. Magarill, D. A. Romanov, and A. V. Chaplik, Usp. Fiz. Nauk **170**, 325 (2000).
12. A. Namiranian, M. R. H. Khajehpour, Yu. A. Kolesnichenko, and S. N. Shevchenko, Physica E (Amsterdam) (2001) (in press).
13. V. Ya. Prinz, V. A. Seleznev, V. A. Samoylov, and A. K. Gutakovsky, Microelectron. Eng. **30**, 439 (1996).
14. M. Kugler and S. Shtrikman, Phys. Rev. D **37**, 934 (1988).
15. R. Y. Chiao and Y. S. Wu, Phys. Rev. Lett. **57**, 933 (1986); A. Tomita and R. Y. Chiao, Phys. Rev. Lett. **57**, 937 (1986).
16. J. Goldstone and R. L. Jaffe, Phys. Rev. B **45**, 14100 (1992).
17. R. Landauer, IBM J. Res. Dev. **1**, 233 (1957).
18. E. T. Whittaker and G. N. Watson, *A Course of Modern Analysis* (Cambridge Univ. Press, Cambridge, 1927).
19. E. Kamke, *Differentialgleichungen; Lösungsmethoden und Lösungen* (Geest and Portig, Leipzig, 1959; Nauka, Moscow, 1976).
20. L. D. Landau and E. M. Lifshitz, *Course of Theoretical Physics*, Vol. 3: *Quantum Mechanics: Non-Relativistic Theory* (Nauka, Moscow, 1963; Pergamon, New York, 1965).

Journal of Experimental and Theoretical Physics, Vol. 92, No. 5, 2001, pp. 816–819.
Translated from Zhurnal Éksperimental'noĭ i Teoreticheskoĭ Fiziki, Vol. 119, No. 5, 2001, pp. 937–941.
Original Russian Text Copyright © 2001 by Meilikhov, Raquet, Rakoto.

SOLIDS
Electronic Properties

Magnetoresistance of a Ferromagnetic Metal Nanocomposite with Nonspherical Granules

E. Z. Meilikhov[a], *, B. Raquet[b], and H. Rakoto[b]
[a]*Kurchatov Institute, Russian Scientific Centre, Moscow, 123182 Russia*
**e-mail: meilikhov@imp.kiae.ru*
[b]*Laboratoire de Physique de la Matiere Condensee de Toulouse, 31077 Toulouse, France*

Received October 31, 2000

Abstract—It is experimentally established that the magnetoresistance of a $Fe_x(SiO_2)_{1-x}$ nanocomposite ($x \approx 0.6$) in a strong magnetic field is described by a logarithmic function of the field strength. This field dependence is inconsistent with the well-known theory of the giant magnetoresistance in ferromagnetic nanocomposites. A model is developed according to which the unusual behavior of the magnetoresistance is explained by nonsphericity of the material grains, exhibiting a broad variety of shapes. The experimental results agree with conclusions and predictions of the proposed model. *© 2001 MAIK "Nauka/Interperiodica".*

1. INTRODUCTION

This study is devoted to the giant magnetoresistance (GMR) of a $Fe_x(SiO_2)_{1-x}$ nanocomposite with $x \approx 0.6$, which corresponds to the metal side of the metal–insulator percolation transition in this system. The material represents essentially a dispersion of ferromagnetic metal granules in a dielectric matrix. Our experiments showed that the electric resistance of such composites in a sufficiently strong magnetic field varies as a logarithmic function of the field strength. This field dependence is inconsistent with that predicted by the known theory of the GMR in ferromagnetic nanocomposites [1, 2]. We believe that the discrepancy is related to the fact that the traditional theory was developed for a system composed of spherical metal granules, whereas real nanocomposites usually consist of nonspherical particles. Moreover, the degree of nonsphericity of these particles may change as the granule shape varies from strongly elongated (prolate) to significantly oblate.

Below we will describe the GMR of a system composed of such granules within the framework of a simple model, which relates the unusual quasilogarithmic dependence of the magnetoresistance on the field strength to the scatter of shapes of the nonspherical granules of the nanocomposite.

2. EXPERIMENTAL RESULTS

We have studied thin $Fe_x(SiO_2)_{1-x}$ ($x \approx 0.6$) films with a thickness of 0.4 μm. The samples were prepared by the ion sputter deposition in vacuum using a mosaic target composed of Fe and SiO_2 pellets. The iron volume fraction in the deposit was checked by the electron-probe X-ray microanalysis. The size of Fe granules in the films varied from 2 to 20 nm.

The relative magnetoresistance $\Delta R/R$ of a sample (R is the electric resistance of the film at a given temperature and the zero field strength, ΔR is the change in the resistance upon application of a field with the induction B) was studied in a temperature range from 4.2 to 300 K using "long" (~0.1 s) magnetic field pulses with B up to 20 T.

Figure 1 shows the experimental plots of magnetoresistance versus induction measured at various temperatures. In Fig. 2, the high-field branches of these plots are constructed as functions of the logarithm of the "effective" induction B/T. As is seen, the sample resistance in the region of high fields is described by a logarithmic function of the field strength.

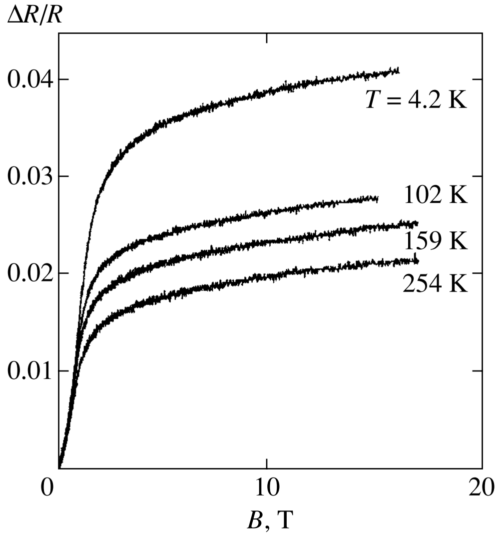

Fig. 1. The plots of magnetoresistance versus magnetic induction for a $Fe_x(SiO_2)_{1-x}$ nanocomposite ($x \approx 0.6$) at various temperatures.

3. MAGNETORESISTANCE OF A NANOCOMPOSITE WITH NONSPHERICAL METAL GRANULES

The electric conductivity of granulated metals (nanocomposites) and the GMR of ferromagnetic metals are determined by the electron tunneling between granules [1, 2]. However, in a real system containing granules of various dimensions, the maximum contribution is due to the granules having a size close to a certain "optimum" value [3, 4].

For a nanocomposite consisting of spherical granules, the optimum size is determined by interplay between the increased concentration (inherent in real systems) of small-size particles and their reduced degree of ionization (caused by the Coulomb effects). The optimum granule size is given by the formula [3]

$$a_{\mathrm{opt}}(T) \approx a_0\left(\frac{x}{4\pi}\right)^{1/2}\frac{\lambda}{a_0}\left(\frac{T}{T_0}\right)^{-5/9}, \tag{1}$$

where $kT_0 \approx (e^2/\varepsilon a_0)(a_0/\lambda)^{3/2}x^{-1/2}[1 - (x/x_c)^{1/3}]$, a_0 is the average granule size, λ is the electron wavelength in the insulator phase, ε is the dielectric constant, x is the bulk content of the metal phase, and x_c is the percolation threshold. The conductance $G(T)$ of a given system is determined by the "optimum cluster"—a cluster composed of granules possessing the optimum size $a_{\mathrm{opt}}(T)$, rearranging in accordance with the temperature T.

A change in the resistance of the system exposed to a magnetic field with the induction B is due to the magnetic-field-dependent probability of the tunneling transitions between spontaneously magnetized single-domain (because of small size) granules. The relative magnetoresistance $\Delta R(B, T)/R = [G(0, T) - G(B, T)]/G(0, T)$ can be expressed as [4]

$$\frac{\Delta R(B, T)}{R} = P^2\langle\cos\gamma\rangle^2, \tag{2}$$

where P is the electron spin polarization in a ferromagnetic granule and γ is the angle between the external magnetic field and the magnetic moment of each granule. The averaging is performed over granules constituting the optimum cluster. Thus, determination of the magnetoresistance reduces to calculating the $\langle\cos\gamma\rangle$ value averaged over the optimum cluster.

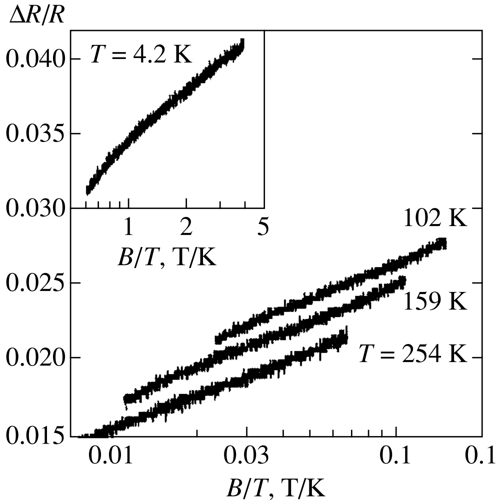

Fig. 2. The plots of high-field magnetoresistance versus effective magnetic induction (on a logarithmic scale) for a $Fe_x(SiO_2)_{1-x}$ nanocomposite ($x \approx 0.6$) at various temperatures.

In the general case, however, the granules in a real system are nonspherical. This implies that not all values of the angles γ_1 are equiprobable and, hence, the time-averaged value of $\overline{\cos\gamma_1}$ for a nonspherical granule is determined by its anisotropy (magnetic and geometric) and the external magnetic field [5]. For an ellipsoidal granule possessing a large (compared to the Bohr magneton) magnetic moment, this time-averaged value can be calculated as

$$\overline{\cos\gamma_1} = \int\exp\left(-\frac{W_A + W_B}{kT}\right) \times \cos\gamma_1 d\Omega\Big/\int\exp\left(-\frac{W_A + W_B}{kT}\right)d\Omega, \tag{3}$$

where $d\Omega = \sin\gamma_1 d\gamma_1 d\phi$ is the solid angle; ϕ is the azimuthal angle of the magnetic moment of a granule ($\cos\phi = [\cos\theta - \cos\gamma_1\cos\beta]/\sin\gamma_1\sin\beta$), θ and β being the angles between the large axis of the granule and the directions of the magnetic moment and the external magnetic field, respectively; $W_A = (1/2)VI_s^2\sin^2\theta$ is the magnetic anisotropy energy not depending explicitly on the magnetic field strength; $W_B = -I_sVB\cos\gamma_1$ is the Zeeman energy depending only on the γ_1 value; and I_s is the saturation magnetization of the granule material. In a sufficiently strong magnetic field, $|W_B| \gg W_A$ and the above expression simplifies to

$$\overline{\cos\gamma_1} = \coth h - 1/h \equiv L(h), \tag{4}$$

where $h = I_sVB/kT$. This relationship corresponds to the well-known Langevin model.

If the optimum cluster were composed of spherical granules possessing the optimum size a_{opt}, the volume V in formula (4) would be the same for all granules: $V = V_{\mathrm{opt}} = (4\pi/3)a_{\mathrm{opt}}^3(T) \propto T^{-5/3}$. In that case, $\langle\cos\gamma\rangle = \overline{\cos\gamma_1} = L(h_{\mathrm{opt}})$, where $h_{\mathrm{opt}} = I_sBV_{\mathrm{opt}}/kT \propto T^{-8/3}$. Evidently, the temperature dependence of the magnetic moment (proportional to $\langle\cos\gamma\rangle$) of the optimum cluster even in this idealized case is not described by the Langevin model, according to which $h \propto 1/T$.

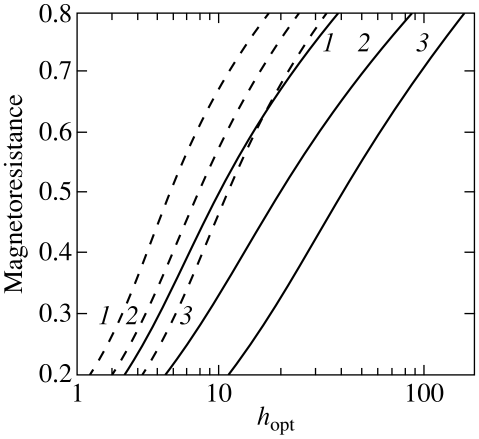

Fig. 3. The plots of magnetoresistance versus magnetic field strength for a model granulated ferromagnetic metal composite with nonspherical granules of elongated (solid curves, $x_0 = 0$) and oblate (dashed curves, $x_0 = 1$) shapes calculated using various distribution functions $f_z(z)$: (*1*) linearly increasing; (*2*) homogeneous (constant); (*3*) linearly decreasing.

In a system composed of nonspherical (ellipsoidal) granules, the situation is even more complicated. Here, the optimum granule size is determined by two factors [3]: (i) the concentration of charged granules depends on their capacitance C (for spherical granules, the latter quantity coincides with the sphere radius) and (ii) the average (tunneling) distance between granules possessing the same C depends on their concentration. Granules shaped as the ellipsoid of revolution possess two characteristic dimensions—a and b, representing the lengths of the long and short axes of the ellipsoid, respectively. Which of the two dimensions is more essential for the problem under consideration? As is known, the capacitance of an ellipsoidal granule with a large a value is weakly dependent on the smaller (transverse) size b. For such an elongated ellipsoid of revolution,

$$C = \frac{(a^2-b^2)^{1/2}}{\operatorname{arccosh}(a/b)} \approx \frac{a}{\ln(2a/b)},$$

whereas for the oblate ellipsoid,

$$C = \frac{(a^2-b^2)^{1/2}}{\arccos(a/b)},$$

which implies that $2/\pi < C/a < 1$ [6]. Therefore, the only significant dimension of ellipsoidal granules is the greater axis length: all granules with the a value close to a_{opt} are optimum. Thus, the optimal cluster is composed of granules with the volumes falling within the interval $V_{\min} < V < V_{\text{opt}}$, where $V_{\text{opt}} = (4\pi/3)a_{\text{opt}}^3$, $V_{\min} = (b_{\min}/a_{\text{opt}})^2 V_{\text{opt}}$ (for elongated ellipsoids) or $V_{\min} = (b_{\min}/a_{\text{opt}})V_{\text{opt}}$ (for oblate ellipsoids), and $b_{\min}/a_{\text{opt}}$ is the minimum (for a given nanocomposite) value of the ratio of characteristic dimensions describing maximum nonsphericity (elongation or flatness) of the granules. For $b_{\min}/a_{\text{opt}} \sim 0.1$, the optimum cluster may include granules with the volumes differing up to approximately 100 times (!). In this case, naturally, $\langle\cos\gamma\rangle \neq \overline{\cos\gamma_1}$ and the averaging have to be performed over all granules of the optimum cluster.

Let $f_b(b)$ be the function of distribution of the short axis length in a system composed of nonspherical (ellipsoidal) granules and x_0 be the volume fraction of such elongated granules. In this case,

$$\langle\cos\gamma\rangle = \int\limits_{b=b_{\min}}^{b=a_{\text{opt}}} \left\{(1-x_0)L\left(\frac{ab^2}{a_{\text{opt}}^3}h_{\text{opt}}\right) + x_0 L\left(\frac{a^2 b}{a_{\text{opt}}^3}h_{\text{opt}}\right)\right\} f_b(b)\,db = F(h_{\text{opt}}),$$

$$F(h_{\text{opt}}) = \int\limits_{z_{\min}}^{1} [(1-x_0)L(h_{\text{opt}}z^2) + x_0 L(h_{\text{opt}}z)]\, f_z(z)\,dz, \qquad (5)$$

where $f_z(z)$ is a function describing distribution of the granules with respect to the parameter $z \equiv b/a_{\text{opt}}$ ($0 < x < 1$, $z_{\min} = b_{\min}/a_{\text{opt}}$).

The function $f_z(z)$ entering into Eqs. (5) most probably depends on the method of nanocomposite synthesis. This is equally valid for the relative fractions of prolate and oblate granules described by the parameter x_0. In principle, these characteristics can be obtained by electron-microscopic investigation of each particular system. However, the results of calculations presented below show that, qualitatively, a relationship between the resistance and the magnetic field strength depends neither on selecting the distribution function $f_z(z)$ nor on the parameters $z_{\min}$ ($z_{\min} \ll 1$) and x_0. For this reason, we will consider a simple approximation offered by a system containing only elongated granules ($x_0 = 0$) possessing a homogeneous distribution function ($f_z(z) = \text{const}$). This means that elongated ellipsoidal granules of any shape, from spherical ($z = 1$) to needle-like ($z = 0$), are equiprobable in the system. The calculations were conducted for the case of $z_{\min} = 0.1$.

The magnetoresistance of this model system calculated using Eqs. (5) is presented in Fig. 3 (solid curve *2*). As is seen, the sample resistance variation in a broad range of the magnetic field strength ($5 < h_{\text{opt}} < 50$) is described by a logarithmic function. The results of our calculations show that the character of the magnetoresistance behavior is qualitatively the same for various $f_z(z)$ functions and x_0 values, which affect only the range of the magnetic field strength where the plots are quasilogarithmic.

The characteristic effective field strength in the range where the magnetoresistance exhibits a quasilogarithmic behavior is $h_{\text{opt}} \sim 20$ (see Fig. 3, solid curve *2* for the homogeneous distribution function $f_z(z)$). Comparing this value to the effective induction $B/T \approx 3 \times 10^{-2}$ T/K, corresponding to the experimental logarithmic field dependence of the sample resistance in the temperature interval $T \sim 100$–250 K (Fig. 2), we can estimate the optimal granule size $2a_{\text{opt}} \sim 20$ nm (for the saturation magnetization of Fe granules assumed to be equal to that of bulk iron, $I_s \approx 0.2$ T). This estimate agrees with the data of electron-microscopic investigation of the nanocomposites studied.[1]

Let us consider the temperature variation of the magnetoresistance in the region of the quasilogarithmic field dependence. Within the framework of the model employed, the only reason for the temperature effect is a change in the long axis length of granules in the optimum cluster: according to formula (1), $a_{\text{opt}}(T) \propto T^{-5/9}$. This implies that the magnetoresistance depends only on the combination of parameters determining the characteristic field: $h_{\text{opt}} \propto B/T^{8/3}$. In other words, the model predicts a parametric dependence of the magnetoresistance of the type $\Delta R/R = \Delta R(B/T^{8/3})/R$, whereby any $\Delta R/R$ value plotted as the function of $B/T^{8/3}$ must fit to the single master curve. Represented in the corresponding format (see Fig. 4), the experimental data confirm this conclusion.

We have demonstrated that the model of nanocomposite with nonspherical granules of variable shape suggests a quasilogarithmic behavior of the magnetoresistance in sufficiently strong magnetic fields. This is obviously related to the large scatter of the volumes of granules entering into the optimum cluster. The magnetoresistance saturates together with the magnetization of this cluster; however, as the field strength increases, more and more small-size granules contribute to the magnetization. This gradual involvement of new granules leads to a slow (close to logarithmic) saturation of the magnetization and, hence, of the magnetoresistance.

Thus, the proposed model of nonspherical granules provides for a qualitatively correct description of experimental data on the magnetoresistance of a granulated ferromagnetic metal nanocomposite $\text{Fe}_x(\text{SiO}_2)_{1-x}$ in strong magnetic fields.

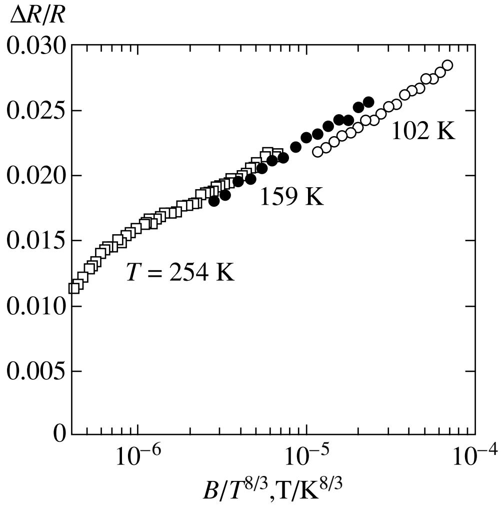

Fig. 4. The parametric plots of high-field magnetoresistance of a $\text{Fe}_x(\text{SiO}_2)_{1-x}$ nanocomposite ($x \approx 0.6$).

ACKNOWLEDGMENTS

This study was supported by the Russian Foundation for Basic Research (project nos. 99-02-16955 and 00-02-17191) and by the joint Russian–French PICS-RFBR Program (grant no. 98-02-22037).

REFERENCES

1. J. S. Helman and B. Abeles, Phys. Rev. Lett. **37**, 1429 (1976).
2. J. Inoue and S. Maekawa, Phys. Rev. B **53**, R11927 (1996).
3. E. Z. Meilikhov, Zh. Éksp. Teor. Fiz. **115**, 1484 (1999) [JETP **88**, 819 (1999)].
4. E. Z. Meilikhov, Pis'ma Zh. Éksp. Teor. Fiz. **69**, 579 (1999) [JETP Lett. **69**, 623 (1999)].
5. E. Z. Meilikhov, Zh. Éksp. Teor. Fiz. **116**, 2182 (1999) [JETP **89**, 1184 (1999)].
6. L. D. Landau and E. M. Lifshitz, *Course of Theoretical Physics*, Vol. 8: *Electrodynamics of Continuous Media* (Fizmatgiz, Moscow, 1959; Pergamon, New York, 1984).

Translated by P. Pozdeev

---

[1] According to formula (1), $a_{\text{opt}}(T) \propto T^{-1/2}$ and, hence, the optimum granule size at $T = 4.2$ K is $2a_{\text{opt}}(4.2\text{ K}) \sim 100$ nm. However, no such large granules were observed in real systems. This discrepancy indicates that the simple model is inapplicable at very low temperatures.

Journal of Experimental and Theoretical Physics, Vol. 92, No. 5, 2001, pp. 820–829.
Translated from Zhurnal Éksperimental'noĭ i Teoreticheskoĭ Fiziki, Vol. 119, No. 5, 2001, pp. 942–953.
Original Russian Text Copyright © 2001 by Zaĭtsev, Terekhina.

SOLIDS
Electronic Properties

On the Theory of Ferromagnetism of Hexagonal Diborides

R. O. Zaĭtsev[a], * and N. V. Terekhina[b], **

[a]Kurchatov Institute, Russian Research Center, pl. akademika Kurchatova 1, Moscow, 123182 Russia
*e-mail: zaitsev@mbslab.kiae.ru
[b]State Scientific Center "NIITeplopribor," Moscow, 129085 Russia
**e-mail: tnv–tnv@yahoo.com

Received November 13, 2000

Abstract—The electronic structure and the magnetic properties of the MnB_2 and CrB_2 compounds with hexagonal AlB_2-type lattices were studied. The problem was treated in terms of the generalized Hubbard model with an infinite electron-electron repulsion energy in the same atom. Equations for spin magnetic susceptibility were derived and used to determine the conditions of ferromagnetic instability and construct the phase diagram of the existence of ferromagnetic ordering. © *2001 MAIK "Nauka/Interperiodica".*

1. INTRODUCTION

The experimental studies of MeB_2 metal diborides showed magnetic susceptibility to increase in the series of 3*d* transition metals (Me = Ti, V, and Cr) [1]. The susceptibility of CrB_2 is an order of magnitude higher than that of all paramagnetic Group IV–VI metal diborides.

As iron, cobalt, and nickel diborides cannot be synthesized, MnB_2 is the only ferromagnetic diboride with a low transition temperature (approximately 143–157 K) and a low saturation magnetic moment of about 0.19–0.25 μB.

The electrical and magnetic properties of layered transition metal diborides with AlB_2-type structures are characterized by the presence of strongly split off $(2xy, x^2 - y^2)$ *d* states. These states are collectivized through boron ions, which are in degenerate p_x, p_y states.

The electronic state of the CrB_2 and MnB_2 complexes is close to half-filled for both Cr^+ and Mn^{2+} cations ($3d^5$) and B^- anions ($2s^22p^2$).

Generally, the condition of electrical neutrality written in terms of the mean occupation numbers of *d* (n_d) and *p* (n_p) electrons for the compounds under study (MnB_2 and CrB_2) has the form

$$\begin{aligned} n_d + 2n_p &= 8 \quad \text{for} \quad CrB_2, \\ n_d + 2n_p &= 9 \quad \text{for} \quad MnB_2, \end{aligned} \tag{1}$$

where n_d and n_p are the numbers of *d* and *p* electrons per cell, see Fig. 1.

According to the band calculations performed for CrB_2 [1], the charge of chromium cations equals 0.7, which, according to (1), corresponds to $n_d = 5.3$, $n_p = 1.35$. It follows that, generally, $5 < n_d < 6$, the $(3z^2 - r^2)$ two-electron chromium shell is incompletely occupied, and $1 < n_p < 3/2$.

In spite of the absence of calculations on MnB_2, it is natural to assume that the charge of Mn cations also does not exceed one.[1] Using the electrical neutrality condition, we as previously obtain $1 < n_p < 3/2$ and $6 < n_d < 7$.

Because of hexagonal symmetry of CrB_2, the chromium cation should have a completely occupied (xz, yz) shell and an incompletely occupied two-electron $(3z^2 - r^2)$ shell.

The four-electron $(2xy, x^2 - y^2)$ shell of the manganese cation in MnB_2 only begins to be occupied, whereas all the other shells are completely occupied.

In this work, the problem of ferromagnetism of MnB_2 is studied on the assumption of a strong interaction between electrons of the same atom. The corresponding matrix elements, which are also called the Hubbard energy, for chromium, manganese, and boron (14, 15, and 8 eV, respectively) exceed the energy of electron transfer to neighboring atoms and are hereafter considered infinite.

We will show that, when the lower Hubbard electronic subband is filled (for manganese *e* electrons), an increase in the number of electrons causes an increase in the total number of one-particle spin states, which corresponds to a paramagnetic (positive) correction to magnetic susceptibility.

However, if filling of the upper Hubbard subband occurs [for the $(3z^2 - r^2)$ chromium electrons], an increase

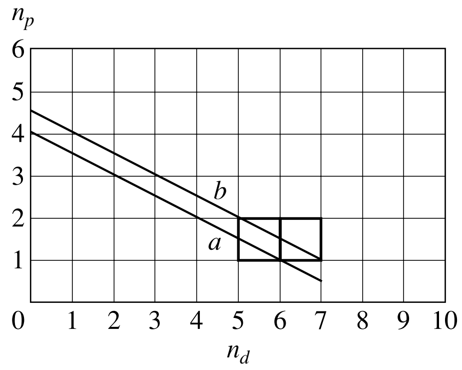

Fig. 1. Electrical neutrality lines in (n_d, n_p) coordinates: (*a*) $n_d + 2n_p = 8$ for CrB_2 and (*b*) $n_d + 2n_p = 9$ for MnB_2.

---

[1] As the electronegativities of Cr (1.6) and Mn (1.5) differ insignificantly, this assumption conforms to the Pauling electrical neutrality principle.

in the number of electrons results in an increase in the number of two-particle states with zero spin, which gives an antiferromagnetic contribution to magnetic susceptibility.

The corresponding Born scattering amplitudes calculated on the Fermi surface have opposite signs, and the spin part of magnetic susceptibility is infinite for MnB_2 at $T = 0$, whereas CrB_2 remains paramagnetic at all temperatures.

Magnetic susceptibility calculations are performed by differentiating the equation of state written at the level of the zero-loop approximation (Hubbard I approximation) and the one-loop approximation for manganese d electrons.

2. THE ELECTRONIC STRUCTURE AT ZERO MAGNETIC FIELD

The spectrum of elementary excitations is found using the generalized Hubbard–Emery model [2, 3], which takes into account various electron jump integrals between boron anions nearest to each other $t^{(p)}$ and between nearest neighbor boron anions and manganese cations t,

$$\begin{aligned}\hat{H} &= -\sum_{\mathbf{r},\mathbf{r}'}\hat{p}^{+}_{\nu,\sigma}(\mathbf{r})\hat{p}_{\nu',\sigma}(\mathbf{r}')t^{(p)}_{\nu,\nu'}(\mathbf{r},\mathbf{r}')\\ &\quad-\sum_{\mathbf{r},\mathbf{r}'}\{\hat{d}^{+}_{\lambda,\sigma}(\mathbf{r})\hat{p}_{\nu,\sigma}(\mathbf{r}')t_{\sigma,\nu}(\mathbf{r},\mathbf{r}')+\mathrm{H.c.}\}\\ &\quad+\sum_{\mathbf{r}}\varepsilon_p\hat{p}^{+}_{\nu,\sigma}(\mathbf{r})\hat{p}_{\nu,\sigma}(\mathbf{r})+\sum_{\mathbf{r}}\varepsilon_d\hat{d}^{+}_{\lambda,\sigma}(\mathbf{r})\hat{d}_{\lambda,\sigma}(\mathbf{r}).\end{aligned}\tag{2}$$

Here, $\hat{d}^{+}_{\lambda,\sigma}(\mathbf{r})$, $\hat{p}^{+}_{\nu,\sigma}(\mathbf{r})$ and $\hat{d}_{\lambda,\sigma}(\mathbf{r})$, $\hat{p}_{\nu,\sigma}(\mathbf{r})$ are the operators of creation and annihilation of d and p electrons, respectively.

In chromium, the $3z^2$ $(2xy, x^2 - y^2)$– r^2 shell is occupied, and the λ index therefore has only one value. In MnB_2, indices λ take on two values corresponding to two degenerate $(2xy, x^2 - y^2)$ states of cations. In both compounds, indices ν take on two values corresponding to two degenerate (x, y) boron states.

In AlB_2-type lattices, the distance between the nearest metal cations is two times larger than the distance between the nearest boron anions, which, in turn, equals the metal–boron–metal distance. For this reason, cation–cation electron jumps will not be taken into account (e.g., see monograph [1]).

If the axes are selected as shown in Fig. 2, it is easy to calculate all four matrix elements of the jump operator.

For MnB_2 (and CrB_2), we use the simplest model corresponding to the arrangement of energy levels at the Γ point instead of exact nondegenerate six (or five) branches.

For MnB_2, we have two doubly degenerate hybrid and one doubly degenerate nonhybrid subband of p electrons,

$$\begin{gathered}\xi^{\pm}_{\mathbf{p}} = \frac{v}{2}\pm\frac{1}{2}\sqrt{(r+v)^2+4g_p^2f_pg_e^2f_e|t_{\mathbf{p}}|^2}-\mu,\\ \mu = -\frac{\varepsilon_p+\varepsilon_e}{2},\quad \xi_{\mathbf{p}} = -v\tau_{\mathbf{p}}+\frac{r}{2}-\mu,\\ r = \varepsilon_p-\varepsilon_e,\quad v = g_p^2f_p.\end{gathered}\tag{3}$$

Electron jumps between transition element cations are not taken into account, because the distance between the nearest cations (3.02 Å) noticeably exceeds the minimum anion–cation distance (2.31 Å), which, in turn, exceeds the distance between boron anions (1.74 Å).

It can be shown that the presence of a narrow logarithmic singularity in the density of states for the factor

$$\tau_{\mathbf{p}} = \frac{2}{9}\left[\frac{3}{2}+\cos\alpha+\cos\beta+\cos(\alpha+\beta)\right]$$

insignificantly changes the phase diagram in its separate points. In the remaining broad region of energy, variable $\tau_{\mathbf{p}}$ changes, the corresponding density of states is almost constant, and, physically, the calculations given below are performed for the plane band model.

The dependence on transverse momentum p_z is inherent in the definition of excitation energy, which contains $x\cos^2(p_z/2)$ factors, and the final equation for the density of states has the form

$$\rho(\varepsilon) = \frac{2}{\pi}\int_0^1 dx\int_0^{\pi/2}d\alpha\,\delta(\varepsilon-x\cos^2\alpha) = \frac{2}{\pi}\sqrt{\frac{1-\varepsilon}{\varepsilon}}.\tag{4}$$

It follows that, at low energies, the density of states corresponds to one-dimensional motion, because $\rho \approx 1/\sqrt{\varepsilon}$. At high energies, the density of states corresponds to a three-dimensional isotropic spectrum: $\rho \approx \sqrt{1-\varepsilon}$.

Motion over boron layers is purely two-dimensional in character. The corresponding density of states has a narrow van Hove peak.

3. EQUATIONS OF STATE

Let us define the $A^{\lambda}(\mathbf{p})$normal coordinates used to express the diagonal elements of the one-particle virtual Green function,

$$\begin{aligned}A^{\lambda}(\mathbf{p}) &= \frac{1}{2}\\ &\times\left[1+\mathrm{sgn}\lambda\frac{r+v}{\sqrt{(r+v)^2+4f_pf_eg^2\cos^2(p_z/2)W_{\mathbf{p}}}}\right].\end{aligned}\tag{5}$$

The equations of state written in these coordinates in the $n_{p,\,e} < 1$ region have the form

$$n_p = 2f_p \times \left\{ \sum_{\mathbf{p}} \left[n_F(\xi(\mathbf{p})) + \sum_{p_z,\,\lambda = \pm} A^{\lambda}(\mathbf{p}, p_z) n_F(\xi^{\lambda}(\mathbf{p}, p_z)) \right] \right\}, \tag{6}$$

$$n_e = 4f_e \left\{ \sum_{p_z,\,\mathbf{p},\,\lambda = \pm} A^{(-\lambda)}(\mathbf{p}, p_z) n_F(\xi^{\lambda}(\mathbf{p}, p_z)) \right\}. \tag{7}$$

Here, $f_{e,\,p} = 1 - 3n_{e,\,p}/4$.

As has been mentioned, the most interesting region is that where the charge of Mn cations does not exceed one. According to electrical neutrality equation (1), we should then consider the region $1 < n_p < 2$, $6 < n_d < 7$ or $0 < n_e < 1$, where $n_e = n_d - 6$.

Accordingly, let us write the equations of state for the region $0 < n_e < 1$ or $1 < n_p < 2$:

$$n_p = 1 + 2g_p^2 f_p \times \left\{ \sum_{\mathbf{p}} \left[n_F(\xi(\mathbf{p})) + \sum_{p_z,\,\lambda = \pm} A^{\lambda}(\mathbf{p}, p_z) n_F(\xi^{\lambda}(\mathbf{p}, p_z)) \right] \right\}, \tag{8}$$

$$n_e = 4f_e \left\{ \sum_{p_z,\,\mathbf{p},\,\lambda = \pm} A^{\lambda}(\mathbf{p}, p_z) n_F(\xi^{\lambda}(\mathbf{p}, p_z)) \right\}, \tag{9}$$

where $f_p = (2 + n_p)/12$, and the excitation energy and normal coordinates depend on the $g_p^2 f_p$ product, where $g_p^2 = 3/2$ is the sum of the squares of the genealogical coefficients

$$A^{\lambda}(\mathbf{p}) = \frac{1}{2} \times \left[1 + \operatorname{sgn}\lambda \frac{r + v}{\sqrt{(r + v)^2 + 4g_p^2 f_p f_d \cos^2(p_z/2) W_{\mathbf{p}}}} \right], \tag{10}$$

$$W_{\mathbf{p}} = 2t^2 \frac{3}{4} \sqrt{3 + 2S_{\mathbf{p}}},$$

$$S_{\mathbf{p}} = \cos p_x + \cos\left(\frac{p_x}{2} + \frac{\sqrt{3}p_y}{2}\right) + \cos\left(\frac{p_x}{2} - \frac{\sqrt{3}p_y}{2}\right), \tag{11}$$

$$v = f_p g_p^2 |t_p| \frac{3}{2}.$$

$$\xi^{\lambda}(\mathbf{p}, p_z) = \frac{v}{2} + \operatorname{sgn}\lambda \sqrt{\left(\frac{r + v}{2}\right)^2 + g_p^2 f_p f_d \cos^2\left(\frac{p_z}{2}\right) W_{\mathbf{p}}} - \mu, \tag{12}$$

$$\xi(\mathbf{p}) = -g_p^2 f_p t_p \frac{\sqrt{3 + 2S(\mathbf{p})}}{2} + \varepsilon_p.$$

For CrB_2, we must consider filling of the same $p_{x,\,y}$ shell of boron electrons. Using the notation $n_z = n_d - 4$ for the number of electrons in the open $(3z^2 - r^2)$ chromium shell, we can write for the $1 < n_z < 2$ region of interest:

$$n = z = 1 + 2f_z \times \left\{ \sum_{p_z,\,\mathbf{p},\,\lambda = \pm} A^{(-\lambda)}(\mathbf{p}, p_z) n_F(\xi^{\lambda}(\mathbf{p}, p_z)) \right\}, \tag{13}$$

$$n_p = 1 + 2g_p^2 f_p \times \left\{ \sum_{\mathbf{p}} \left[n_F(\xi(\mathbf{p})) + \sum_{p_z,\,\lambda = \pm} A^{\lambda}(\mathbf{p}, p_z) n_F(\xi^{\lambda}(\mathbf{p}, p_z)) \right] \right\}, \tag{14}$$

where f_e is everywhere replaced by $f_z = n_z/2$.

4. FERROMAGNETIC INSTABILITY

The conditions of arising of ferromagnetic instability are easy to obtain in the one-loop approximation if it is taken into account that, in the region $0 < n_e < 1$, one-particle occupation numbers n_e^{σ} enter into the equations of state through the end multiplier, which equals the sum of the mean occupation numbers for empty and one-particle states,

$$f_e^{\sigma} = n_0 + n_e^{\sigma}, \tag{15}$$

and therefore $\delta n_e^{\sigma} = \delta f_e^{\sigma}$.

In exactly the same way, one-particle occupation numbers n_z^{σ} in the region $1 < n_z < 2$ enter into the equations of state through the end multiplier, which is equal to the sum of the mean occupation numbers of two-particle states with a zero total spin projection,

$$f_z^{\sigma} = n_{\mathrm{II}} + n_z^{-\sigma}, \tag{16}$$

and therefore $\delta n_z^{\sigma} = -\delta f_z^{\sigma}$.

Note also that, in the region $1 < n_p < 2$, two-particle occupation numbers n_{II}^{σ} enter into the equations of state through the $g_1^2 f_1^{\sigma} + g_2^2 f_2^{\sigma}$ combinations of end multipliers. Two end multipliers $f_{1,\,2}^{\sigma}$ are expressed through the sums of one-particle and two-particle states,

$$f_1^{\sigma} = n_{\mathrm{II}}^{\sigma} + n_{\mathrm{I}}^{\sigma}, \quad f_2^{\sigma} = n_{\mathrm{II}}^{0} + n_{\mathrm{I}}^{-\sigma}. \tag{17}$$

Hence the variation of two-particle occupation numbers is given by

$$\delta n_{\mathrm{II}}^{\sigma} = \delta f_1^{\sigma} + \delta f_2^{\sigma}, \quad \delta n_{\mathrm{II}}^{0} = 0. \tag{18}$$

For MnB_2, these relations lead to the equations

$$\begin{aligned}\delta n_e^\sigma &= \delta f_e^\sigma = \tilde{K}_e \delta f_e^\sigma \\ &+ f_e D_{e,p} \sum_k g_k^2 \delta f_k^\sigma - f_e D_0^e \delta H,\end{aligned} \tag{19}$$

$$\begin{aligned}\delta n_{\rm II}^\sigma &= \sum_k \delta f_k^\sigma \\ &= \tilde{K}_p \sum_k g_k^2 \delta f_k^\sigma + g_p^2 f_p D_{p,e} \delta f_e^\sigma - g_p^2 f_p D_0^p \delta H.\end{aligned} \tag{20}$$

Here, we use the convenient notation

$$\begin{aligned}\tilde{K}_e &= K_e + f_e D_e, \quad \tilde{K}_p = K_p + g_p^2 f_p D_p, \\ g_p^2 &= \sum_k g_k^2 = \frac{3}{2}.\end{aligned} \tag{21}$$

The D_p, $D_{p,e}$ and D_d, $D_{e,p}$ coefficients are the variational derivatives of K_p and K_e, which are defined below.

The missing equation, which relates the variations of one-particle and two-particle p states, can be obtained according to the definition of the diagonal components of the one-particle Green function written with the use of auxiliary coefficients b_k satisfying the orthogonality condition $g_1 b_1 + g_2 b_2 = 0$.

In the zero-loop approximation, the sought equation has the form (see [4, 5])

$$b_1 g_1 \delta n_{\rm II}^\sigma = K_p (g_1 b_1 \delta f_1^\sigma + g_2 b_2 \delta f_2^\sigma). \tag{22}$$

Using the orthogonality conditions and relation (22), we find that the variations of the end multipliers are related as

$$\delta f_1^\sigma (1 - K_p) + \delta f_2^\sigma (1 + K_p) = 0. \tag{23}$$

Equations (19), (20), (22), and (23) allow three independent variations of the end multipliers to be determined. The condition of solvability of this system of equations at $\delta H = 0$ makes it possible to obtain the condition of arising of ferromagnetic instability ($n_e < 1$, $1 < n_p < 2$):

$$\begin{aligned}K_p(1 - K_p)(1 - K_e) &= f_e K_p (1 - K_p) D_e \\ &+ f_p g_p^2 (1 - K_e) D_p \left(\frac{1}{3} + K_p\right) \\ &- f_p g_p^2 f_e \left(\frac{1}{3} + K_p\right)(D_p D_e - D_{p,e} D_{e,p}).\end{aligned} \tag{24}$$

Here, $f_e = 1/(3K_e + 1)$, $f_p = 1/(4 - K_p)$, and $g_p^2 = 3/2$. At $T = 0$, when $D_e D_p - D_{p,e} D_{e,p} = 0$, we can also find the correction corresponding to the one-loop approximation for d electrons:

$$\begin{aligned}K_p(1 - K_p)(1 - K_e)(1 - S_e) &= f_e K_p (1 - K_p) D_e \\ &+ g_p^2 f_p (1 - K_e)\left(\frac{1}{3} + K_p\right) D_p,\end{aligned} \tag{25}$$

where

$$\begin{aligned}S_e &= \frac{\partial \Sigma}{\partial \varepsilon_e} = \frac{1}{f_e} \\ &\times \left\{ y\rho(y)\left[1 + \operatorname{sgn}(r + v)\frac{1}{\sqrt{1 + sy^2}}\right]\right. \\ &\left. - \frac{1}{4}\operatorname{sgn}(r + v) s \int_y^1 \frac{x^2 \rho(x) dx}{(1 + sx^2)^{3/2}}\right\}.\end{aligned} \tag{26}$$

Here, $\rho(y) = (4/\pi)\sqrt{1 - y^2}$ in the problem under consideration.

Taking into account one-loop corrections for p electrons leads to fairly cumbersome and partially canceling corrections, which will be ignored.

For CrB_2 with $1 < n_z < 2$ and $1 < n_p < 2$, the condition for ferromagnetic instability has the form

$$\begin{aligned}K_p K_z (1 - K_p) &= g_p^2 f_p K_z D_p \left(\frac{1}{3} + K_p\right) \\ &+ f_z K_p (1 - K_p) D_z \\ &- f_z g_p^2 f_p \left(\frac{1}{3} + K_p\right)(D_p D_z - D_{p,z} D_{z,p}).\end{aligned} \tag{27}$$

Here,

$$K_\nu = \sum_{p_z, \mathbf{p}, \lambda} A^{(-\lambda)}(\mathbf{p}, p_z) n_F(\xi^\lambda(\mathbf{p}, p_z)), \tag{28}$$

$$\begin{aligned}K_p &= \frac{1}{2} \\ &\times \left\{\sum_{\mathbf{p}}\left[n_F(\xi^\lambda(\mathbf{p})) + \sum_{p_z, \lambda} A^\lambda(\mathbf{p}, p_z) n_F(\xi^\lambda(\mathbf{p}, p_z))\right]\right\},\end{aligned} \tag{29}$$

$$\begin{aligned}D_\nu &= \frac{\delta K_\nu}{\delta f_\nu}, \quad D_p = \frac{\delta K_p}{\delta (g^2 f_p)}, \\ D_{\nu,p} &= \frac{\delta K_\nu}{\delta (g_p^2 f_p)}, \quad D_{p,\nu} = \frac{\delta K_p}{\delta f_\nu},\end{aligned} \tag{30}$$

where $\nu = e$ or z.

Table

Region	g_p^2	f_p	K_p	n_p	Γ_p	R_p
$0 < n_p < 1$	1	$\frac{4-3n_p}{4}$	$\frac{n_p}{4-3n_p}$	$\frac{4K_p}{1+3K_p}$	0	4
$1 < n_p < 2$	$\frac{3}{2}$	$\frac{2+n_p}{12}$	$\frac{4(n_p-1)}{2+n_p}$	$\frac{2(2+K_p)}{4-K_p}$	$\frac{1}{3}$	3
$2 < n_p < 3$	$\frac{3}{2}$	$\frac{6-n_p}{12}$	$\frac{3(n_p-2)}{6-n_p}$	$\frac{6(1+K_p)}{3+K_p}$	$-\frac{4}{3}$	4
$3 < n_p < 4$	1	$\frac{3n_p-8}{4}$	$\frac{4(n_p-3)}{3n_p-8}$	$\frac{4(3-2K_p)}{4-3K_p}$	–1	1
Region	g_z^2	f_z	K_z	n_z	Γ_z	R_z
$0 < n_z < 1$	1	$\frac{2-n_z}{2}$	$\frac{n_z}{2-n_z}$	$\frac{2K_z}{1+K_z}$	0	2
$1 < n_z < 2$	1	$\frac{n_z}{2}$	$2-\frac{2}{n_z}$	$\frac{2}{2-K_z}$	–1	1

The general conditions for the arising of ferromagnetism can be found through variations of the end multipliers in the equations of state written in the Hubbard I approximation,

$$n_p = [n_p] + R_p f_p \times\left\{\sum_{\mathbf{p}} n_F(\xi_\nu(\mathbf{p})) + \sum_{p_z,\mathbf{p},\lambda} A_\nu^{(-\lambda)}(\mathbf{p}, p_z) n_F(\xi^\lambda(\mathbf{p}, p_z))\right\}, \quad (31)$$

$$n_z = [n_z] + R_z f_z \times\left\{\sum_{p_z,\mathbf{p},\lambda} A^\lambda(\mathbf{p}, p_z) n_F(\xi^\lambda(\mathbf{p}, p_z))\right\}. \quad (32)$$

Here, $R_{p,z}$ is the degeneracy multiplicity of $([n_{p,z}] + 1)$-particle states, and $f_{p,z}$ are the end multipliers, which were determined for each integer interval and tabulated.

The condition of the arising ferromagnetism for the $n_{p,z} < 1$ region can easily be obtained by simply differentiating the equations of state.

At $T = 0$, the general equation for determining the boundaries of the paramagnetic and ferromagnetic phases has the form

$$K_pK_z(1-K_p)(1-K_z) - L_zK_p(1-K_p)(\Gamma_z + K_z) - L_pK_z(1-K_z)(\Gamma_p + K_p) = 0. \quad (33)$$

Here, $\Gamma_{p,z}$ are dimensionless amplitudes of scattering of high-spin excitations calculated for each integer interval of variations of mean occupation numbers $n_{p,z}$, $L_p = g_p^2 f_p D_p$, and $L_z = f_z D_z$. The amplitudes are listed in the table, which also contains the relation between the $K_{p,z}$ coefficients and the mean occupation numbers (for electrons, subscripts p in the table must be replaced by e).

Consider two cases.

(A) $0 < n_z < 1$, $\Gamma_z = 0$, and the d subsystem resonates between unoccupied and one-particle states. The condition for the arising of ferromagnetism has the form

$$K_p(1-K_p)(1-K_z) = f_zD_zK_p(1-K_p) + g_p^2 f_pD_p(1-K_z)(\Gamma_p + K_p). \quad (34)$$

This equation was used in studying MnB_2 (where $1 < n_p < 2$, $\Gamma_p = 1/3$, and $K_z \longrightarrow K_e < 1$).

(B) $1 < n_z < 2$, $\Gamma_z = -1$, and the d subsystem resonates between one-particle and two-particle states. The condition for the arising of ferromagnetism then takes the form

$$K_pK_z(1-K_p) = -f_zD_zK_p(1-K_p) + g_p^2 f_pD_pK_z(\Gamma_p + K_p). \quad (35)$$

This equation was applied to CrB_2, where $1 < n_p < 2$.

5. PHASE DIAGRAM

The most general property of systems with infinite Hubbard repulsion is a positive amplitude of scattering of excitations with opposite spin projections if the number of excitations is small, which corresponds to a tendency to ferromagnetism. For MnB_2, this tendency manifests itself by positive D_e and D_p values for filling both the lower hybrid subband and the lower half of the boron subband.

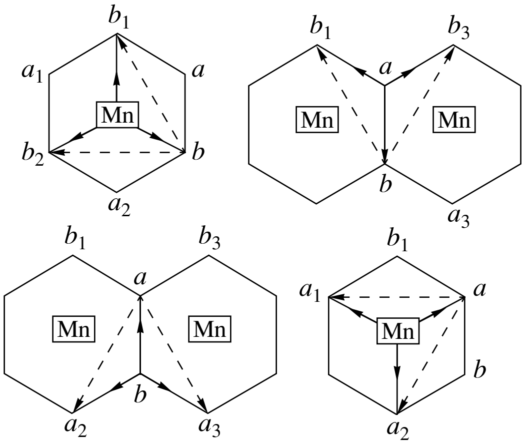

Fig. 2. Separate fragments of the structure of MnB_2. Solid lines with arrows are jump directions. Dashed lines are elementary translation vectors.

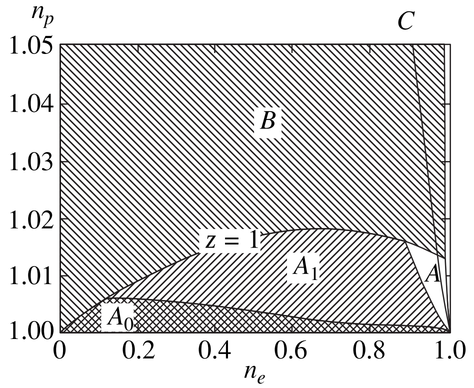

Fig. 3. Magnetic phase diagram at $T = 0$ and in the region of small $n_p - 1$ values. Ferromagnetic regions are hatched, $z = 1$ is the boundary at which filling of the p boron subband begins; A_0 is the ferromagnetic region in the zero-loop approximation; A_1 is the ferromagnetic region in the one-loop approximation; B is the ferromagnetic region; and C is the electrical neutrality line.

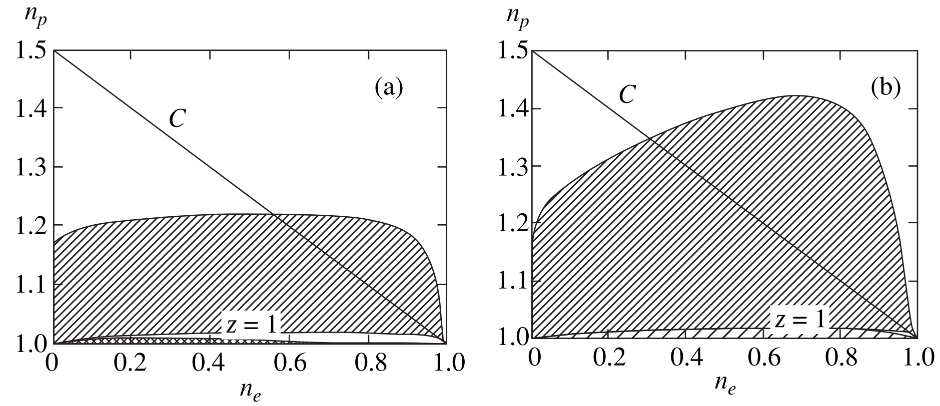

Fig. 4. Magnetic phase diagram of MnB_2 at $T = 0$; C is the electrical neutrality line: (a) zero-loop approximation and (b) one-loop approximation.

A comparison of the right-hand sides of (34) and (35) shows that, in the regions where D_e, D_z, and D_p have the same sign, there is a substantial compensation for CrB_2.

Direct calculations show that, exactly in the region where the n_z and n_p occupation numbers are related by the electrical neutrality condition $2n_p + n_z = 4$, the D_p and D_z coefficients are of the same order of magnitude and Eq. (35) does not have solutions.

It follows that the CrB_2 compound remains paramagnetic at all temperatures.

In the Appendix, we, by way of illustration, consider a particular case when the electron jump energy over boron layers equals the electron jump energy between the nearest boron and manganese layers; that is, $t_p = t$.

At $T = 0$, we will use the $y = \sqrt{\varepsilon}$ and $s = 4g_p^2 f_p f_d t^2/(r + v)^2$ variables, where $v = g_p^2 f_p f_d$ and $r = \varepsilon_p - \varepsilon_e$, instead of the ε_p and ε_e independent parameters.

First consider the region of energies where the lower hybrid subband is filled, whereas the boron subband remains unoccupied.

Figure 3 shows that, under these conditions, ferromagnetic ordering exists in a very narrow region of deviations of the number of p electrons from unity (region A_0).

The D_p value rapidly decreases as energy increases, and the system remains paramagnetic (region A) until, alongside filling of the lower subband, filling of the boron subband begins (region B).

According to Fig. 4, the line of electrical neutrality of MnB_2 intersects a fairly wide region of ferromagnetic ordering, in which the lower hybrid and boron subbands are occupied simultaneously. Taking into account one-loop corrections broadens the possible region of the existence of ferromagnetism, see Fig. 4b.

The ferromagnetic region obtained in the zero-loop approximation and shown in Fig. 4a covers a substantially smaller fraction of the phase diagram, but, in both cases, the line of MnB_2 electrical neutrality intersects the ferromagnetic region in its fairly extended part.

Figures 3 and 4 shown that the region of ferromagnetic instability is situated in the region of a small number of excitations for both p and e excitations.

The MnB_2 electrical neutrality line intersects the ferromagnetic part of the phase diagram in a fairly wide region, which corresponds to simultaneous filling of the lower hybrid and the broad boron p subband.

We therefore obtain a qualitative explanation of the existence of ferromagnetism in MnB_2, which is the only ferromagnetic diboride.

6. CONCLUSIONS

In both CrB_2 and MnB_2, p electrons resonate between one-particle ($S = 1/2$) and triplet two-particle ($S = 1$) states. For this reason, CrB_2 has a fairly substantial susceptibility, whereas MnB_2 is ferromagnetic in the whole region of n_p numbers for which the p–p scattering amplitude is positive.

As far as hybrid p–d excitations are concerned, the character of their interactions in MnB_2 is different in principle from that in CrB_2.

For MnB_2 in the region of small n_e numbers, the amplitude of scattering of hybrid excitations is positive, and, at small n_p and n_e, the scattering amplitudes are summed. Ferromagnetic ordering therefore exists in a fairly wide region of n_p and n_e variables, which intersects the $2n_p + n_e = 3$ electrical neutrality line, see Fig. 4b.

In CrB_2, in which the p subband and the upper half of the Hubbard ($3z^2 - r^2$) subband are filled simultaneously, the scattering amplitude is negative at small $n_z - 1$ numbers. For this reason, substantial compensation of the total scattering amplitude occurs at small n_p and $n_z - 1$, and the system remains paramagnetic in the region of intersection with the $2n_p + n_e = 4$ electrical neutrality line.

ACKNOWLEDGMENTS

This work was financially supported by the Russian Foundation for Basic Research (project no. 98-02-17388).

APPENDIX

Consider the special situation when jump integrals over boron layers and jump integrals between manganese and boron layers are equal in magnitude. Below, these integrals are set equal to one.

In this situation, $v = g_p^2 f_p$, and r is expressed through s as

$$r = -v + \operatorname{sgn}(r+v)2\sqrt{\frac{g_p^2 f_p f_e}{s}},$$

$$\text{so that}\quad \xi_{\mathbf{p}}^{\pm} = \frac{v}{2} \pm \frac{|r+v|}{2}\sqrt{1+sy^2} - \mu, \qquad \text{(A.1)}$$

$$\xi_p = \frac{r}{2} - vz - \mu.$$

Parameter s introduced in place of energy difference r varies from zero to infinity and actually determines the splitting of subbands.

The y and z values change from zero to one and are determined by the position of the Fermi level within the Brillouin zone.

Case A: $r > v$, $0 < s < 0.68$

Under these conditions, the lowest subband is ξ_s^-, which is occupied independently of the higher boron p subband.

*A*1. If $+v/2 - |r+v|\sqrt{1+s}/2 < \mu < v/2 - |r+v|/2$, we have

$$K_p = \frac{1}{2}J_s^-(y, 1), \quad K_e = J_s^+(y, 1),$$
$$\mu = \frac{v}{2} - \frac{1}{2}|r+v|\sqrt{1+sy^2}. \qquad \text{(A.2)}$$

Here and throughout, the following notation is used:

$$J_s^{\pm}(y, 1) = \frac{1}{2}\int_y^1 \rho(x)dx\left(1 \pm \frac{1}{\sqrt{1+sx^2}}\right),$$

$$\rho(x) = \frac{4}{\pi}\sqrt{1-x^2}.$$

The coefficients in the condition of the appearance of ferromagnetism are obtained by differentiating the equation of state:

$$f_e D_{ee} = -\operatorname{sgn}(r+v)\frac{s}{\pi}J'(y, 1)$$
$$+\frac{y}{\pi}\sqrt{1-y^2}\left[1 + \frac{\operatorname{sgn}(r+v)}{\sqrt{1+sy^2}}\right], \qquad \text{(A.3)}$$

$$g_p^2 f_p D_{pp} = s\frac{\operatorname{sgn}(r+v)}{2\pi}J'(y, 1)$$
$$\times\left[1 - \operatorname{sgn}(r+v)\sqrt{\frac{sg_p^2 f_p}{f_e}}\right] + y\frac{\sqrt{1-y^2}}{2\pi} \qquad \text{(A.4)}$$
$$\times\left[1 - \frac{\operatorname{sgn}(r+v)\sqrt{sg_p^2 f_p}}{\sqrt{f_e}(1-\operatorname{sgn}(r+v)\sqrt{1+sy^2})}\right]\left[1 - \frac{\operatorname{sgn}(r+v)}{\sqrt{1+sy^2}}\right],$$

$$S_e = \frac{1}{\pi f_e} \times \left\{ \operatorname{sgn}(r+\nu) y\sqrt{1-y^2}\left[1+\frac{\operatorname{sgn}(r+\nu)}{\sqrt{1+sy^2}}\right] - \operatorname{sgn}(r+\nu) s J'(y,1) \right\}. \tag{A.5}$$

In the case under consideration,

$$g_p^2 = \frac{3}{2}, \quad f_p = \frac{1}{4-K_p}, \quad f_e = \frac{1}{1+3K_e},$$
$$J'(y,1) = \int_y^1 \frac{x^2\sqrt{1-x^2}}{(1-sx^2)^{3/2}}dx. \tag{A.6}$$

The integrals that appear in these equations are reduced to elliptical integrals, after which computer calculations can be performed to determine the phase curve. We considered zero-loop and one-loop (for *d* electrons) approximations, see Fig. 4.

The hatched regions in Fig. 3 are ferromagnetic ordering regions. The ferromagnetic region obtained in the zero-loop approximation (A_0) is situated within the A_1 region whose boundary was calculated in the one-loop approximation.

Note that the electrical neutrality line intersects the *A* region at high energies, at which ferromagnetic instability does not arise.

*A*2. If $r/2 - \nu < \mu < r/2$, the broad nonhybrid *p* subband is occupied. For this subband, the condition of ferromagnetism is satisfied, but the electrical neutrality line does not intersect it.

Case B: $0 < r < \nu$, $0.68 < s < 2.47$

Under these conditions, the lowest subband is the lower ξ_s^- subband. Starting with a certain chemical potential value, it is filled simultaneously with the boron *p* band.

The upper edge of the boron subband is situated above the top of the lower hybrid subband.

*B*1. If $\nu/2 - (r+\nu)\sqrt{1+s}/2 < \mu < r/2 - \nu$, the lower hybrid subband is filled. The situation is indistinguishable from case *A1*. For this reason, the zero-loop approximation gives a narrow region adjoining the $K_p = 0$, or $n_p = 1$, line. This region is a continuation of the region considered under *A1*.

In the one-loop approximation, the whole *B*1 region is ferromagnetic and the boundary of the ferromagnetic region lies within region *B*2.

*B*2. If $r/2 - \nu < \mu < \nu/2 - |r+\nu|/2$, the ξ_s^- and boron *p* subbands are filled simultaneously,

$$K_p = \frac{1}{2}J_s^-(y,1) + \frac{1}{2}J_p(z,1), \quad K_d = J_s^+(y,1). \tag{A.7}$$

The *y* and *z* variables are related to each other and to the chemical potential as

$$\mu = \frac{\nu}{2} - \frac{|r+\nu|}{2}\sqrt{1+sy^2} = \frac{r}{2} - z\nu,$$
$$z = \frac{r}{2\nu} - \frac{1}{2} + \frac{|r+\nu|}{2\nu}\sqrt{1+sy^2}, \quad 0 < y < y_*. \tag{A.8}$$

An explicit dependence of *z* on *y* is found taking into account the definitions

$$J_p(z,1) = \int_z^1 [\rho_p(x)]dx = 1 - z,$$
$$K_p = \frac{1}{2}J_s^-(y,1) + \frac{1}{2}J_p(z,1) = \tilde{K}_p + \frac{1-z}{2}. \tag{A.9}$$

Combining this equation with the condition of the equality of the chemical potentials and the condition $\nu = f_p$ yields the equation

$$(1+z)^2 = \frac{f_d}{3s}(7 - 2\tilde{K}_p + z)(\sqrt{1+sy^2}+1)^2 \tag{A.10}$$

for determining *z*. Using (A.12), we obtain

$$z = -1 + B + \sqrt{B(B+12-4\tilde{K}_p)},$$
$$\text{where } B = \frac{(\sqrt{1+sy^2}+1)^2}{6s(1+3K_d)}, \tag{A.11}$$
$$\tilde{K}_p = \frac{1}{2}J_s^-(y,1);$$

the *z* value should be positive and should not exceed one.

In the (*s*, *y*) variables, the required boundaries can be determined by (A.8) with *z* set equal to 0 or 1. The conditions $z = 1$ and 0 correspond to the beginning and end of boron subband filling, respectively.

The coefficients present in the condition of the appearance of ferromagnetism are found by differentiating the equation of state,

$$f_e D_{ee} = -\operatorname{sgn}(r+\nu)\frac{s}{\pi}J'(y,1) + \frac{1}{\pi}y\sqrt{1-y^2}\left[1+\frac{\operatorname{sgn}(r+\nu)}{\sqrt{1+sy^2}}\right],$$
$$g_p^2 f_p D_{pp} = \frac{z}{2} + \operatorname{sgn}(r+\nu)\frac{s}{2\pi}J'(y,1)\left[1-\operatorname{sgn}(r+\nu)\sqrt{\frac{sg_p^2 f_p}{f_e}}\right] + \frac{yz\sqrt{1-y^2}}{2\pi(1+z)}\left[1-\frac{\operatorname{sgn}(r+\nu)}{\sqrt{1+sy^2}}\right], \tag{A.12}$$

$$S_e = \frac{1}{\pi f_e}$$
$$\times\left\{\operatorname{sgn}(r+V)y\sqrt{1-y^2}\left[1+\frac{\operatorname{sgn}(r+V)}{\sqrt{1+sy^2}}\right]\right.$$
$$\left.-\operatorname{sgn}(r+V)sJ'(y,1)\right\}.$$

These coefficients should be substituted into the condition of ferromagnetism, which allows the phase curve to be determined. The results of calculations show that the ferromagnetic phase boundary in both zero- and one-loop approximations occurs inside the *BZ* region.

Case C: $-V < r < 0$, $24 > s > 2.47$

Under these conditions, the lower ξ_s^- band is the lowest. Starting with a certain chemical potential value, its filling, however, occurs simultaneously with filling of the boron *p* band.

The bottom edge of the boron *p* subband is situated above the energy minimum of the lower ξ_s^- subband.

The top edge of the boron *p* subband is situated below the top of the lower ξ_s^- subband.

*C*1. If $V/2-(r+V)\sqrt{1+s}/2 < \mu < r/2 - V$, the lower hybrid subband is occupied,

$$K_p = \frac{1}{2}J_s^-(y,1), \quad K_d = J_s^+(y,1),$$
$$\mu = \frac{V}{2}-\frac{|r+V|}{2}\sqrt{1+sy^2}. \tag{A.13}$$

The last condition relates *y* to the chemical potential. The *y p*arameter varies in a limited region, namely, $y_* < y < 1$, where $y_*$is determined from the condition

$$V/2-|r+V|\sqrt{1+sy_*^2V}/2 = r/2 - V.$$

Case *C*1 only differs from *A*1 and *B*1 in that the narrow ferromagnetic region in the n_d and n_e variables now ends at the (0, 0) point, which corresponds to $s = 24$, see Fig. 3.

The curve corresponding to the condition $z = 1$ (at $z = 1$, filling of the lower hybrid subband continues and that of the boron subband begins) is shown in Fig. 3. Within this region, the condition of ferromagnetic instability is satisfied even in the zero-loop approximation.

Note that the ferromagnetic region boundary intersects the boundary at which filling of the boron *p* subband begins; within this subband, there exists ferromagnetic ordering caused by the boron–boron exchange scattering amplitude.

In the one-loop approximation, the whole *C*1 region remains ferromagnetic.

*C*2. If $r/2 - V < \mu < V/2 - |r+V|/2$, the ξ_s^- and boron *p* subbands are filled simultaneously,

$$K_p = \frac{1}{2}J_s^-(y,1)+\frac{1}{2}J_p(z,1), \quad K_d = J_s^+(y,1). \tag{A.14}$$

All dependences then coincide with those for case *B*2, see Eqs. (A.7)–(A.11).

In the one-loop approximation, a part of the boundary phase curve for case *C*2 intersects the MnB_2 electrical neutrality line.

An analysis of Figs. 3 and 4 leads us to conclude that, under the corresponding conditions, the electrical neutrality line passes through the ferromagnetic region.

The ferromagnetic region obtained in the zero-loop approximation lies completely within the ferromagnetic region of the one-loop approximation.

Case D: $-V < r < 0$, $24 < s < +\infty$

The broad *p* subband is the lowest; this subband is filled independently of hybrid subbands.

*D*1. If $-V + r/2 < \mu < V/2 - (r+V)\sqrt{1+s}/2$, we have

$$K_p = \frac{1}{2}J_p(z,1), \quad K_d = 0, \quad \mu = \frac{r}{2} - zV. \tag{A.15}$$

The last condition relates *z* to the chemical potential.

The boron subband is only filled. It follows that $K_e = 0$; that is, $n_d = 6$, and the number of *p* electrons changes from 1 to some finite value. The condition of ferromagnetism is satisfied even at a small number of excitations. At $n_p = 1$, all *p* electrons are in the state with spin 1/2, and when n_p increases, new states with spin 1 are formed. It follows that the system tends to ferromagnetic ordering from the outset.

In case *D*1, $K_d = D_{ee} = D_{ep} = D_{pe} = 0$,

$$K_p = \frac{1}{2}(1-z), \quad g_p^2 f_p D_{pp} = \frac{z}{2}. \tag{A.16}$$

This leads us to conclude that ferromagnetic instability exists for all $1 > z > 0.47$, or $0 < K_p < 0.27$.

*D*2. If $V/2 - (r+V)/2 < \mu < r/2$, the ξ_s^- and boron *p* subbands are filled simultaneously,

$$K_p = \frac{1}{2}J_s^-(y,1)+\frac{1}{2}J_p(z,1), \quad K_d = J_s^+(y,1). \tag{A.17}$$

This and all the other equations coincide with (A.7)–(A.12).

In the zero-loop approximation, the curve of the appearance of ferromagnetism begins at *s* equal to infinity and $y = 1$, which corresponds to $K_d = 0$ and $K_p = 0.21$, see Fig. 4a, where the whole zero-loop approximation curve is shown.

Case E: $b < -rV,\ r < -V,\ s > 21/4 = 5.25$

The lowest subband is the broad p subband, which is filled independently of hybrid subbands.

$E1$. If $-V + r/2 < \mu < V/2 + (r + V)\sqrt{1+s}/2$, we have

$$K_p = \frac{1}{2}J_p(z, 1), \quad K_d = 0, \quad \mu = \frac{r}{2} - zV. \qquad (A.18)$$

The last condition relates z to the chemical potential.

Case $E1$ is indistinguishable from $D1$; that is, $n_d = 0$, $0.21 < n_p < 1/2$, and the ferromagnetic region lies within the $0.21 < n_p < 0.27$ narrow interval.

$E2$. If $V/2 + |r + V|/2 < \mu < r/2$, the ξ_s^- and boron p subbands are filled simultaneously,

$$K_p = \frac{1}{2}J_s^+(y, 1) + \frac{1}{2}J_p(z, 1), \quad K_d = J_s^-(y, 1). \quad (A.19)$$

Here, the lower and the broad p subbands overlap. The z and y parameters are related to each other as

$$\mu = \frac{V}{2} - \frac{|r + V|}{2}\sqrt{1 + sy^2} = \frac{r}{2} - Vz. \qquad (A.20)$$

The last condition relates the y and z values to the chemical potential. An explicit dependence of z on y can be found taking into account the definitions

$$J_p(z, 1) = \int_z^1 [\rho_p(x)]dx = 1 - z,$$
$$K_p = \frac{1}{2}J_s^+(y, 1) + \frac{1}{2}J_p(z, 1) = \tilde{K}_p + \frac{1 - z}{2}. \qquad (A.21)$$

Combining these equations with the condition of the equality of the chemical potentials and the $V = f_p$ condition, we obtain the equation

$$(1 + z)^2 = \frac{f_d}{3s}(7 - 2\tilde{K}_p + z)(\sqrt{1 + sy^2} - 1)^2 \qquad (A.22)$$

for determining z. This equation yields

$$z = -1 + C + \sqrt{C(C + 12 - 4\tilde{K}_p)},$$
$$\text{where } C = \frac{(\sqrt{1 + sy^2} - 1)^2}{6s(1 + 3K_d)}, \qquad (A.23)$$
$$\tilde{K}_p = \frac{1}{2}J_s^+(y, 1).$$

The z value should be positive and should not exceed unity. In this region, no ferromagnetic instability is observed under the conditions studied.

At the level of the zero-loop approximation, there is no ferromagnetic instability in this region.

The phase curve obtained in the one-loop approximation begins at the same parameter values as in case $D2$; that is, $s = \infty$ and $y = 1$, or $K_d = 0$ and $K_p = 0.21$. Further, the phase curve deviates from the line corresponding to $s = \infty$ and then intersects this line at $y = 0.91$, or at the $K_d = 0.02$, $K_p = 0.32$ point.

The whole one-loop approximation curve is shown in Fig. 4b.

Case F: $0 < s < 21/4,\ r < -V$

The lowest subband is the broad p subband, which is filled independently of the hybrid subbands.

$F1$. If $-V + r/2 < \mu < r/2$, we have

$$K_p = \frac{1}{2}J_p(z, 1), \quad K_d = 0, \quad \mu = \frac{r}{2} - zV. \qquad (A.24)$$

The last condition relates z to the chemical potential value.

Case $F1$ is indistinguishable from $D1$: $n_d = 0$, $0.21 < n_p < 1/2$, and the ferromagnetic region lies in the narrow $0.21 < n_p < 0.27$ interval.

$F2$. If $V/2 + (r + V)\sqrt{1 + sy^2}/2 < \mu V/2 + (r + V)/2$, the lower hybrid subband is filled.

It can be shown that, under these conditions, the system remains paramagnetic at all temperatures and chemical potential values.

REFERENCES

1. G. V. Samsonov, T. N. Serebryakova, and V. A. Neronov, *Borides* (Atomizdat, Moscow, 1975), p. 83.
2. J. Hubbard, Proc. R. Soc. London, Ser. A **281**, 401 (1964).
3. V. J. Emery, Phys. Rev. Lett. **58**, 2794 (1987).
4. R. O. Zaĭtsev, Fiz. Tverd. Tela (Leningrad) **31**, 1725 (1989).
5. R. O. Zaĭtsev and N. V. Terekhina, Zh. Éksp. Teor. Fiz. **117**, 1018 (2000) [JETP **90**, 886 (2000)].

Translated by V. Sipachev

Journal of Experimental and Theoretical Physics, Vol. 92, No. 5, 2001, pp. 830–839.
Translated from Zhurnal Éksperimental'noĭ i Teoreticheskoĭ Fiziki, Vol. 119, No. 5, 2001, pp. 954–965.
Original Russian Text Copyright © 2001 by Krichevtsov.

SOLIDS
Electronic Properties

Anisotropy of the Linear and Quadratic Magnetic Birefringence in Rare-Earth Semiconductors γ-Ln_2S_3 (Ln = Dy^{3+}, Pr^{3+}, Gd^{3+}, La^{3+})

B. B. Krichevtsov
Ioffe Physicotechnical Institute, Russian Academy of Sciences, St. Petersburg, 194021 Russia
e-mail: Boris.@krich.ioffe.rssi.ru

Received November 16, 2000

Abstract—The field and angular dependence of the magnetic linear birefringence (MLB) in noncentrosymmetric cubic (symmetry class T_d) rare-earth (RE) semiconductors γ-Ln_2S_3 (Ln = Dy^{3+}, Pr^{3+}, Gd^{3+}, La^{3+}) was studied. The field dependence of the MLB in Dy_2S_3 and Pr_2S_3 is a combination of two contributions, quadratic and linear with respect to the magnetic induction B, both possessing a strong anisotropy. The quadratic birefringence related to the Cotton–Mouton effect manifestations at a wavelength of $\lambda = 633$ nm is characterized in Dy_2S_3 by the value of $\beta = 1.5$ deg/(cm T^2) and the anisotropy parameter $a = -0.7$ and in Pr_2S_3, by $\beta = 0.2$ deg/(cm T^2) and $a = 2$. The non-reciprocal MLB caused by the magnetic-field-induced spatial dispersion reaches $\gamma = 0.55$ and 0.71 deg/(cm T) in Dy_2S_3 and Pr_2S_3, respectively. The relationship between parameters A and g of the γ_{ijkl} tensor describing contributions of the B_ik_j type to the dielectric tensor $\varepsilon_{ij}(\omega, \mathbf{k}, \mathbf{B})$ is $A = 2g$ in Dy_2S_3 (as well as in boracite crystals containing 3d ions), which is characteristic of the second-order magnetoelectric permittivity manifestations in the optical frequency range. In Pr_2S_3, the relationship $A = 3.3g$ is evidence of manifestations of the additional quadrupole mechanism. A comparison of the Cotton–Mouton and Faraday effects in Ln_2S_3 and in magnetic semiconductors $Cd_{1-x}Mn_xTe$ shows a principal difference between these systems and indicates that both phenomena in Ln_2S_3 are determined by the optical transitions in RE ions rather than by the interband or exciton transitions. This is also confirmed by the comparison of the Cotton–Mouton effect manifestations in Ln_2S_3, in dielectric $Dy_3Ga_5O_{12}$ and $Dy_3Al_5O_{12}$ single crystal cubic garnets, and in Dy_2O_3. An analysis of the non-reciprocal MLB mechanisms related to manifestations of the local interconfiguration optical transitions $4f^N \longrightarrow 4f^{N-1}5d$ in RE ions showed that this phenomenon, in contrast to the Cotton–Mouton and Faraday effects, is caused by the presence of odd components of the crystal field acting upon the RE ion in Ln_2S_3. In Gd_2S_3, as well as in diamagnetic Ln_2S_3, neither the Cotton–Mouton effect nor the non-reciprocal MLB are manifested at $T = 294$ K, which is explained by different microscopic mechanisms of the magnetooptical phenomena for ions in the S-state and diamagnetic ions, on the one hand, and RE ions with nonzero orbital moment, on the other hand. *© 2001 MAIK "Nauka/Interperiodica".*

1. INTRODUCTION

Rare-earth (RE) sesquisulfides of the Ln_2S_3 system, where Ln^{3+} is a trivalent RE ion, may crystallize in a cubic noncentrosymmetric lattice of the Th_3P_4 type (symmetry class T_d) and represent wide-bandgap magnetic semiconductors with a band gap of $E_g \sim 2.5$–3 eV. These materials possess a high resistivity ($\rho \sim 10^{10}\ \Omega$ cm) and a broad transparency window in the visible spectral range. A detailed description of many physical properties of sesquisulfides can be found in reviews [1, 2]. The presence of trivalent RE ions with unfilled 4f electron shells in these compounds accounts for their paramagnetic properties and for a relatively large magnitude of the linear magnetooptical effects.

To our knowledge, only linear (with respect to the magnetic field strength) Faraday and Kerr effects in γ-Ln_2S_3 crystals were studied to date [3–6]. It should be noted that the linear magnetic Faraday effect is described by a third-rank axial tensor α_{ijk} possessing a singe independent parameter in cubic crystals. This circumstance accounts for the isotropic character of this phenomenon, whereby the magnitude of the Faraday effect is independent of the direction of light propagation relative to the crystallographic axes.

As is well known, the crystals containing RE ions may exhibit a large quadratic Cotton–Mouton effect (magnetic birefringence or double refraction), which is described by a fourth-rank tensor β_{ijkl} [7]. In cubic crystals belonging to the symmetry classes O_h or T_d, the β_{ijkl} tensor possesses three independent parameters. For this reason, the Cotton–Mouton (CM) effect can be anisotropic, whereby the magnetic birefringence depends on the direction of light propagation and on the magnetic field orientation relative to the crystallographic axes.

A phenomenological description of the CM effect in cubic magnetic crystals was reported in [7, 8]. However, this description is also valid in RE paramagnets exposed to a magnetic field, provided sufficiently high temperatures and low field strengths. A microscopic theory of the CM effect related to the optical transitions in RE ions was developed in [9]. Experimental investigations of the CM effect in cubic paramagnets were conducted for noncentrosymmetric RE gallates and aluminates with a garnet structure (symmetry class O_h) [10–13]. To our knowledge, no experimental investigations of the CM effect in RE sesquisulfides were reported.

In noncentrosymmetric crystals, in contrast to the structures with the center of inversion, the magnetic linear birefringence (MLB) can be determined both by the reciprocal CM effect and by the non-reciprocal magnetic birefringence (NMB) related to a magnetic-field-induced spatial dispersion [14, 15]. The latter effect is described by terms of the type $\delta\varepsilon_{ij} = \gamma_{ijkl}B_k k_l$ in the dielectric tensor expansion, where **B** is the magnetic induction and **k** is the light wavevector. In contrast to the CM effect, the NMB magnitude is described by an odd linear function of the magnetic induction. A phenomenological analysis of the NMB in crystals of the T_d symmetry was reported in [16, 17]. The phenomenon was experimentally studied in the cubic crystals of magnetic semiconductors (CdMnTe and ZnMnTe) [16–18], semiconductors (CdTe, ZnTe, GaAs) [19–21], and dielectrics (boracites $R_3B_7O_{13}X$, R = Co^{2+}, Cu^{2+}, Ni^{2+}; X = Br^-, I^-) [21, 22]. The results of these investigations showed that, in both semiconductors and magnetic semiconductors, the CM and NMB effects are determined primarily by the interband and exciton transitions, while the same effects in dielectric $R_3B_7O_{13}X$ are determined by the local electron transitions between states of the unfilled 3*d* electron shell of the R^{2+} ion. In RE compounds, the non-reciprocal birefringence effect has not been observed to the present.

Since the RE sesquisulfides are, on the one hand, semiconductors with the absorption edge determined by the interband transitions and, on the other hand, compounds exhibiting intense local transitions in RE ions and strong linear magnetooptical effects, we may expect manifestations of both the NMB and CM effects in these materials. It would be of interest to compare the Faraday effect and the MLB manifestations in RE semiconductors of the Ln_2S_3 system to the behavior of noncentrosymmetric magnetic semiconductors of the $Cd_{1-x}Mn_xTe$ type and dielectric $R_3B_7O_{13}X$ crystals (the magnetic and magnetooptical properties of which are determined by 3*d* ions) and to the properties of centrosymmetric dielectric RE garnets.

The purpose of this work was to study experimentally the magnetic linear birefringence in cubic noncentrosymmetric single crystals of γ-Ln_2S_3 with various RE ions (Ln = Dy^{3+}, Pr^{3+}, Gd^{3+}, La^{3+}). We compared the magnitudes of the linear and quadratic magnetooptical effects in these RE compounds to those in magnetic semiconductors of the $Cd_{1-x}Mn_xTe$ type and in dielectric crystals (boracites and paramagnetic RE garnets). We also aimed at elucidating the microscopic mechanisms responsible for the manifestations of magnetic-field-induced spatial dispersion in the transparency range of RE sulfides.

2. EXPERIMENTAL METHODS AND SAMPLE PREPARATION

The non-reciprocal magnetic birefringence and the CM effect were studied as described elsewhere [16, 17]. The method consists in measuring the rotation angle α of the polarization plane of the light passed through a crystal, placed in an external magnetic field with the induction **B**, and a quarter-wave ($\lambda/4$) plate. The direction of light propagation was perpendicular to the magnetic induction vector **B**, which was verified by a zero Faraday effect measured using the same optical scheme without the quarter-wave plate. The measurements were performed in two geometries: $\mathbf{E} \parallel \mathbf{B}$ (with the incident light polarized so that the **E** vector was parallel to **B**) and $\widehat{\mathbf{EB}} = 45°$ (with the **E** vector making an angle of 45° with the magnetic field direction). In both geometries, the light polarization direction was parallel to the principal axis of the $\lambda/4$ plate. In order to increase the sensitivity of α measurements, we used the Faraday polarization modulator and a lock-in detection scheme. The light source was a helium–neon laser (LGN-111) with an output power of up to 30 mW, operating at a wavelength of $\lambda = 633$ nm. A crystal placed into the gap of an electric magnet could be rotated about the axis parallel to the light wavevector **k** with an accuracy of approximately 0.1°.

In the absence of the magnetic field, the spontaneous birefringence related to the presence of internal stresses or defects produces an initial rotation of the polarization plane by an angle $\alpha_0(\theta)$ depending on the crystal azimuth θ. The angular dependence of this initial rotation, $\alpha_0(\theta)$, is described by second-order harmonics. Upon measuring this angular dependence, we can determine the magnitude of the spontaneous birefringence and the orientation of its principal directions. The spontaneous birefringence in γ-Ln_2S_3 crystals (Ln = Dy, Pr, Gd, Lu) amounted to $\Delta n \sim (3–5) \times 10^{-6}$. During the experiment, the spontaneous birefringence component was compensated by rotating the analyzer, after which the field dependence $\alpha(B) = \alpha_1(B) - \alpha_0$ was measured at various values of the crystal azimuth angle (θ $\alpha_1(B)$ is the angle of rotation of the polarization plane of the transmitted light relative to the **E** vector in the incident light beam). Using this technique, the field dependence $\alpha(B)$ could be measured with a maximum error of ~10″ seconds of arc.

Rare-earth (RE) sesquisulfides of the γ-Ln_2S_3 system crystallize in a structure of the Th_3P_4 type belong-

Table 1. The energy parameters of γ-Ln_2S_3 crystals [3–6]

Compound	E_g, eV	E_{eff}, eV
Dy_2S_3	2.5	3.8
Pr_2S_3	2.42	3.15
Gd_2S_3	2.7	3.2
La_2S_3	2.76	5.4

ing to the T_d symmetry class [1, 2]. In this structure, the RE ions are located at the centers of octahedra (formed by the S^{2-} ions) belonging to the noncentrosymmetric point group S_4 [23]. The RE ions occupy 8/9 of the possible central positions, while the remaining 1/9 of these sites are vacant (these vacancies are randomly distributed over the crustal volume). The presence of these vacancies does not change the crystal symmetry (T_d) according to the X-ray diffraction data. The γ-Ln_2S_3 (Ln = Dy, Pr, Gd, Lu) crystals used in our experiments were grown by the Czochralski method [24]. The samples with lateral dimensions 3 × 3 mm and thickness of 1 mm were cut from ingots along the (110) plane with an accuracy of 2°. The orientation and structural perfection of the samples were checked by X-ray diffraction measurements in the Laue geometry. It is important to note that NMB is extremely sensitive to the presence of twins and/or blocks in the crystals, for which reason special attention was paid to obtaining samples without blocks.

The absorption (transmission) and reflection spectra of the γ-Ln_2S_3 crystals were measured in [1, 25, 26]. The spectral dependences of the Faraday and Kerr effects were reported in [1, 3–6]. Table 1 presents data on the bandgap width E_g and the energy of the effective oscillator responsible for the frequency dependence (dispersion) of the Faraday effect in the crystals studied. The optical quality of the crystals was checked with the aid of a polarization microscope and by measuring the optical absorption spectra at $T = 294$ K. Data on the elastic, piezooptical, piezoelectric, and electrooptical properties of Dy_2S_3 were reported in [27, 28].

3. EXPERIMENTAL RESULTS

The magnetooptical phenomena in paramagnets at high temperatures and low field strengths are described in terms of expansion of the dielectric tensor $\varepsilon_{ij}(\omega, \mathbf{k}, \mathbf{B})$ with respect to components of the magnetic field $\mathbf{B}$:

$$\begin{aligned}\varepsilon_{ij}(\omega, \mathbf{k}, \mathbf{B}) &= \varepsilon_0(\omega) + \alpha_{ijk}B_k \\ &+ \gamma_{ijkl}B_k k_l + \beta_{ijkl}B_k B_l,\end{aligned} \tag{1}$$

where the tensors α_{ijk}, β_{ijkl}, and γ_{ijkl} refer to the Faraday effect, the CM effect plus the isotropic magnetic refraction birefringence, and the NMB, respectively. In the transverse geometry ($\mathbf{k} \perp \mathbf{B}$), the Faraday effect in cubic crystals is not manifested. Therefore, a change in the polarization of light passed through a crystal exposed to an external magnetic field $\mathbf{B}$ is due to the CM effect (quadratic with respect to the induction $\mathbf{B}$), the NMB effects (linear in $\mathbf{B}$), and a contribution of the second order in $\alpha_{ijk}B_k$. Thus, in a noncentrosymmetric crystal with an allowed γ_{ijkl} tensor, the MLB value may contain quadratic (even) and linear (odd) contributions with respect to the magnetic field induction $\mathbf{B}$.

Figure 1 shows the field dependence of $\alpha(B)$ measured for Dy_2S_3 at $\mathbf{k} \parallel [1\bar{1}0]$ in the $\mathbf{E} \parallel \mathbf{B}$ and $\widehat{\mathbf{EB}} = 45°$ geometries. The measurements were performed for various values of the angle θ between the magnetic field $\mathbf{B}$ and the [001] type crystal axis. The $\alpha(B)$ curves measured in both geometries can be described by combinations of the linear and quadratic functions, $\alpha(B) = \gamma B + \beta B^2$. The coefficients γ and β depend on the experimental geometry ($\mathbf{E} \parallel \mathbf{B}$ or $\widehat{\mathbf{EB}} = 45°$); in a certain geometry, the curves

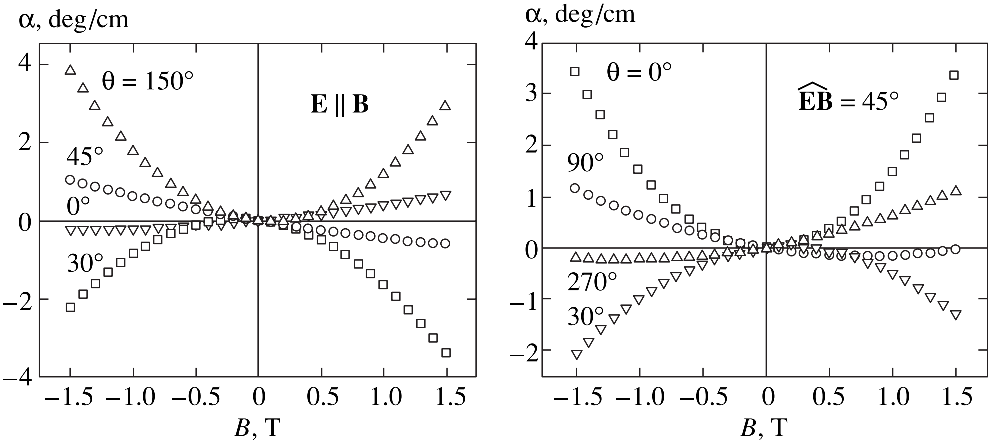

Fig. 1. The field dependences of $\alpha(B)$ measured in the (110) plane of Dy_2S_3 in the $\mathbf{E} \parallel \mathbf{B}$ and $\widehat{\mathbf{EB}} = 45°$ geometries at various angles θ between the magnetic field $\mathbf{B}$ and the [001] type crystal axis.

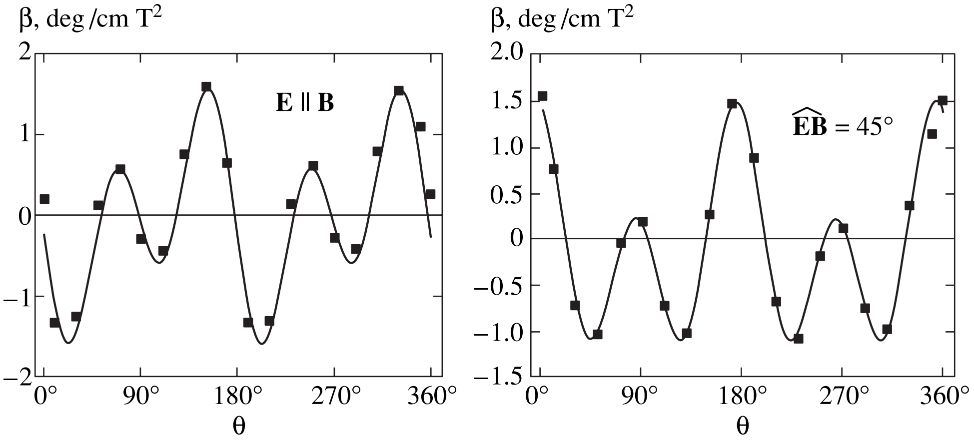

Fig. 2. The angular dependences of $\beta = \partial^2\alpha/\partial B^2|_{B=0}$ measured for Dy_2S_3 in the **E** || **B** and $\widehat{\mathbf{EB}}$ = 45° geometries.

may significantly (up to a change in the sign of α) depend on the angle θ, showing evidence of significantly different types of anisotropy.

Figure 2 presents angular dependences of the coefficient $\beta = \partial^2\alpha(B)/\partial B^2|_{B=0}$ measured for Dy_2S_3 in the **E** || **B** and $\widehat{\mathbf{EB}}$ = 45° geometries. The β(θ) curves, which describe anisotropy of the even contribution to α(*B*), exhibit a 180° periodicity and can be approximated by combinations of the zeroth, second-, and fourth-order harmonics. The quadratic magnetic birefringence in Dy_2S_3 at $B = 1$ T reaches $\Delta n = 5.3 \times 10^{-7}$. Using the known Verdet constant $V = 330$ deg/(cm T) for Dy_2S_3, we may readily show that the contribution to Δn due to the terms quadratic in α_{ijk} for this field must be two orders lower; this implies that the quadratic contribution to α(*B*) is related to the CM effect described by the β_{ijkl} tensor.

Note that the $\alpha(B^2)$ value related to the CM effect is determined both by the orientation of principal axes and by the magnitude of the magnetic birefringence $\Delta n(B^2)$. As is well known, the principal directions of birefringence in cubic crystals may deviate from the magnetic field **B**, except for the cases of **B** || [001], **B** || [111], and **B** || [110] [7, 8]. For these directions of the applied magnetic field, the birefringence components obey a relationship $\Delta n_{110} = (\Delta n_{111} + \Delta n_{001})/2$ and, in addition, the α value for the $\widehat{\mathbf{EB}}$ = 45° geometry is related to Δ*n* by the formula $\alpha = \pi\Delta n d/\lambda$, where *d* is the crystal thickness and λ is the light wavelength. In the general case, this relationship is not valid for other orientations of the magnetic field because deviation of the principal directions of birefringence from the field direction may reach up to 45°. As is seen from Fig. 2 for Dy_2S_3 measured in the $\widehat{\mathbf{EB}}$ = 45° geometry, $\alpha_{110} = (\alpha_{001} + \alpha_{111})/2$. This implies that anisotropy of the CM effect in this sample is the same as that in a cubic crystal. This fact, together with a small value of the spontaneous birefringence in the crystals studied, indicate that the presence of a large number of vacancies in Ln_2S_3 samples does not lead to deviation of the "optical" symmetry of these crystals from the "X-ray" symmetry. This provides additional evidence that the vacancies are randomly distributed over the crystal lattice volume.

Figure 3 shows the angular dependences of the coefficient β for Pr_2S_3 measured in the $\widehat{\mathbf{EB}}$ = 45° geometry. Similar to Dy_2S_3, this crystal obeys the rule of "even effects" $\alpha_{110} = (\alpha_{001} + \alpha_{111})/2$. However, Pr_2S_3 exhibits a markedly lower magnitude of the CM effect and a less pronounced anisotropy (being closer to the isotropic case).

Figure 4 presents angular dependences of the coefficient $\gamma = \partial\alpha/\partial B|_{B=0}$ describing the linear contribution to α(*B*), measured for Dy_2S_3 in the **E** || **B** and $\widehat{\mathbf{EB}}$ = 45°

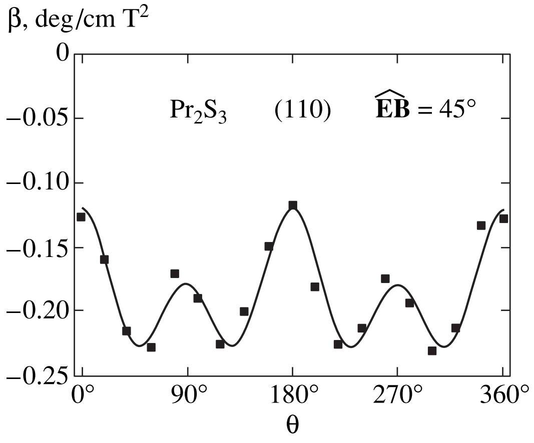

Fig. 3. The angular dependences of β(θ) measured for Pr_2S_3 in the $\widehat{\mathbf{EB}}$ = 45° geometry.

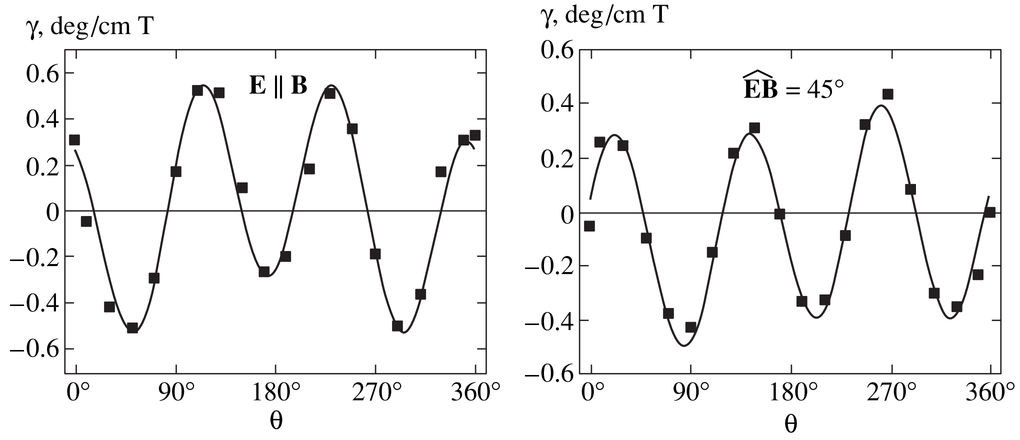

Fig. 4. The angular dependences of $\gamma = \partial\alpha/\partial B|_{B=0}$ for Dy_2S_3 measured in the **E** || **B** and $\widehat{\mathbf{EB}}$ = 45° geometries.

geometries. As is seen from these data, a 180° change in the crystal azimuth ($\theta \longrightarrow \theta + 180°$) leads to alternation of the sign of γ. The γ(θ)curves can be described by combinations of the first- and third-order harmonics: cosθ and cos3θ (in the **E** || **B** geometry) or sinθ and sin3θ (in the $\widehat{\mathbf{EB}}$ = 45° geometry). According to [16, 17], this type of the γ(θ) anisotropy is characteristic of the nonreciprocal birefringence in a cubic crystal of the T_d symmetry, which was related to the magnetic-field-induced spatial dispersion. In contrast to the CM effect, the NMB easy axes in a cubic crystal at **k** || $[1\bar{1}0]$ never coincide with the magnetic field direction, except for the case of **B** || [011]. For **B** || [001], the easy axes of birefringence make an angle of 45° with the direction of **B**. Thus, the relationship $\alpha = \pi\Delta nd/\lambda$ holds in the **E** || **B** geometry for **B** || [001] and in the $\widehat{\mathbf{EB}}$ = 45° geometry for **B** || [011]. The fact that the NMB anisotropy in Dy_2S_3 can be described by expressions similar to those for an ideal cubic crystal also indicates that the presence of vacancies in this crystal does not lead to deviation of the “optical” symmetry from the “X-ray” symmetry in this RE sesquisulfide.

It should be noted that the orientation of principal birefringence axes in a real crystal placed in an external magnetic field is determined by the field-independent spontaneous birefringence (always present due to the internal stresses and defects) or the Lorentz birefringence, as well as by the field-dependent CM and NMB effects. As a result, the orientation of the principal birefringence axes is a complicated function of **B** and θ. However, the results of model calculations using the experimental values of spontaneous birefringence and the parameters characterizing NMB and CF effects, the linear or quadratic contributions to α(*B*) can nevertheless be described using a formalism taking into account only a certain selected effect. For example, the quadratic contribution to α(*B*) is well described by expressions obtained for the ideal cubic crystal taking into account only the $\beta_{ijkl}B_kB_l$ terms, while the linear contribution is adequately described using the $\gamma_{ijkl}B_kk_l$ terms. This is explained by the fact that the spontaneous and induced birefringence components are small and the second-order terms can be neglected. Nevertheless, should the spontaneous birefringence be sufficiently large ($\Delta n \sim 10^{-4}$–10^{-3}), the field dependence of α(*B*) may be sensitive to the mutual influence of the spontaneous birefringence and the NMB and CM effects. However, no such mutual influence was manifested in the crystals studied in our experiments.

Figure 5 shows the angular dependences of the coefficient γ(θ) for Pr_2S_3. Similar to those for Dy_2S_3, these curves are described by the first- and third-order harmonics but with a somewhat different relative values of the harmonic amplitudes. This is manifested by a different ratio of the magnitudes of large and small extrema observed for the γ plots of Dy_2S_3 and Pr_2S_3. Note that the magnetic linear birefringence, as well as the CM and Faraday effects, in RE semiconductors must be independent of the incident light intensity. Indeed, it was experimentally established that an increase in the light intensity by two orders of magnitude led to no significant changes in the observed pattern. This result indicates, in particular, that NMB is a linear optical phenomenon and can be interpreted ignoring the “secondary” effects related, for example, to the light-induced internal electric fields or the electrooptical effect and its variations caused by the magnetic field application (the Kikoin effect).

In diamagnetic La_2S_3 crystals, as well as in Gd_2S_3, the magnitude of the CM and NMB effects in a magnetic field with *B* = 1.5 T did not exceed the sensitivity threshold. In the cubic centrosymmetric crystals of Dy_2O_3, DyAlG, and DyGaG, no NMB manifestations were observed at all.

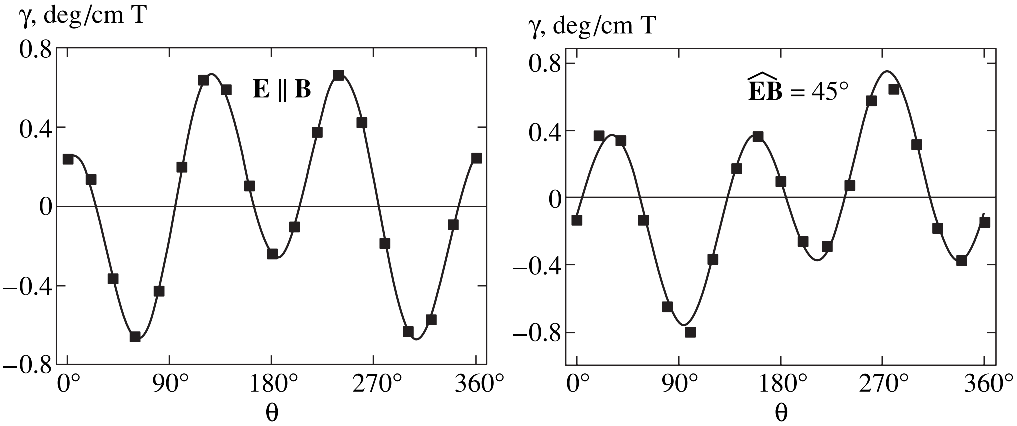

Fig. 5. The angular dependences of $\gamma(\theta)$ for Pr_2S_3 measured in the **E** || **B** and $\widehat{\mathbf{EB}} = 45°$ geometries.

4. DISCUSSION OF RESULTS

For crystals of the T_d symmetry, the tensors of α_{ijk}, β_{ijkl}, and γ_{ijkl} possess one, two, and three independent parameters, respectively. The γ_{ijkl} tensor components describing the NMB effect are as follows: $\gamma_{iijj} = -\gamma_{jjii} = A$, $\gamma_{ijij} = -\gamma_{ijji} = g$ ($ij = xy, yz, zx$); $\gamma_{ijkl} = \gamma_{jikl}$. The magnitudes and signs of the parameters A and g determine the value and anisotropy of $\gamma(\theta)$ in the **E** || **B** and $\widehat{\mathbf{EB}} = 45°$ geometries. Using the experimental angular dependences $\gamma(\theta)$, the parameters A and g can be determined by computer calculations with an accuracy of ~10%. The CM effect in cubic crystals of the O_h and T_d symmetry classes is determined by the values of β_{2323} and $\beta_{1111} - \beta_{1122}$ [7, 8]. Dependence of the orientation of principal axes and the magnitudes of the magnetic birefringence on the magnetic field direction is described by the anisotropy parameter $a = 2\beta_{2323}/(\beta_{1111} - \beta_{1122})$; the behavior of these characteristics for various values of a was reported in [8].

Table 2 presents data on the Faraday effect (the Verdet constant V), the maximum β and γ coefficients, the A and g parameters and the A/g ratio, and the a values for Dy_2S_3 and Pr_2S_3. As seen from these data, the linear Faraday effect and NMB in Pr_2S_3 are 1.5 times those in Dy_2S_3. The parameter A for Pr_2S_3 is also 1.7 times that for Dy_2S_3, whereas the g value for Pr_2S_3 is somewhat smaller than that for Dy_2S_3. A large difference is observed for parameters describing the CM effect in Dy_2S_3 and Pr_2S_3. In contrast to the Faraday effect and NMB, the maximum CM effect in Dy_2S_3 is 6 times that in Pr_2S_3; moreover, the magnetooptical anisotropy parameters of the two crystals differ both in magnitude and in sign. The Faraday effect in diamagnetic La_2S_3 and in Gd_2S_3 is lower by almost two orders of magnitude as compared to the same effect in Pr_2S_3 and Dy_2S_3. The NMB and CM effects on these crystals at $T = 294$ K are very small and are not manifested in the region of magnetic fields ($B = 1.5$ T) used in our experiments. This comparison shows that the MLB magnitude and anisotropy in Ln_2S_3 significantly depend on the RE ion type. Moreover, this dependence is different for the linear and quadratic magnetooptical phenomena in cubic RE sesquisulfides.

In RE semiconductors, the magnetooptical phenomena observed in the transparency range can be related to the interband and exciton optical transitions, as well as to the local optical transitions in RE ions. In this context, it was interesting to compare the behavior of the magnetooptical phenomena in RE semiconductors (Ln_2S_3) and in cubic magnetic semiconductors containing 3d ions of Mn^{2+} such as $Cd_{1-x}Mn_xTe$ or $Zn_{1-x}Mn_xTe$ (symmetry class T_d). In the latter case, the large magnitude of the magnetooptical phenomena is determined just by the interband and/or exciton transitions, which are related to a strong splitting of the energy bands and exciton states caused by the exchange and sp–d interactions [29], whereas the local transitions inside the 3d electron shell of manganese are insignificant. As was demonstrated in [16, 17], the CM effect in $Cd_{1-x}Mn_xTe$ and $Zn_{1-x}Mn_xTe$ at $T = 294$ K is observed near the fundamental absorption edge at $E_g - E < 0.2$ eV, sharply increases on approaching the band edge in proportion

Table 2. The parameters of non-reciprocal magnetic birefringence and the Cotton–Mouton and Faraday effects in Dy_2S_3 and Pr_2S_3 crystals

Parameter	Dy_2S_3	Pr_2S_3
γ_{max}, deg/(cm T)	0.55	0.73
A, 10^{-8} μm/T	5.3	7.7
g, 10^{-8} μm/T	2.7	2.3
A/g	1.9	3.3
β_{max}, deg/(cm T^2)	1.5	0.24
a	–0.7	1.9
V, deg/(cm T)	330	504

to $\propto(Eg - E)^{-3.5}$, and is virtually isotropic ($a = 1$). The latter implies that, irrespective of the magnetic field orientation, one of the principal birefringence axes is always parallel to **B** and the effect is constant. For this reason, the CM effect in these crystals is observed only in the $\widehat{\mathbf{EB}} = 45°$ geometry.

A quite different behavior of the CM effect is observed in Ln_2S_3. Here, the CM effect has a large magnitude in the region far from E_g ($E_g - E = 0.54$ eV and 0.48 eV for Dy_2S_3 and Pr_2S_3, respectively) and is characterized by a sharply pronounced anisotropy ($a = -0.7$ and +2 in Dy_2S_3 and Pr_2S_3, respectively). Note a very strong anisotropy of the CM effect in Dy_2S_3, where the magnetic birefringence for $\mathbf{B} \parallel [001]$ is close in magnitude but opposite in sign as compared to that for $\mathbf{B} \parallel [111]$. In Dy_2S_3, rotation of the magnetic field in a plane of the (110) type is accompanied by a large (~45°) deviation of the principal axes of birefringence from the magnetic field direction. As a result, comparable quadratic contributions to $\alpha(B)$ are observed in Dy_2S_3 for both $\mathbf{E} \parallel \mathbf{B}$ and $\widehat{\mathbf{EB}} = 45°$ geometries (Fig. 1).

It should be noted that the strong anisotropy of the CM effect is characteristic of the cubic dielectrics containing RE ions. In particular, the parameter of magnetooptical anisotropy in $Dy_3Ga_5O_{12}$ and $Dy_3Al_5O_{12}$ single crystal cubic garnets at $T = 294$ K and $\lambda = 633$ nm is $a = -6$ and +2, respectively. A maximum CM effect in these crystals, observed for $\mathbf{B} \parallel [111]$, amounts to $\beta = 0.3$ and 0.4 deg/(cm T^2) in $Dy_3Ga_5O_{12}$ and $Dy_3Al_5O_{12}$, respectively, which is somewhat lower as compared to $\beta = 1.5$ cm/(cm T^2) in Dy_2S_3. This is related to the fact that the allowed electric dipole transitions (responsible for the Faraday and CM effects in Dy^{3+} ions) are characterized by higher energies in dielectric crystals than in Dy_2S_3. In dielectric Dy_2O_3 (T_h symmetry class, $E_g = 4.9$ eV [1]), both the anisotropy parameter ($a = -5$) and the magnitude ($\beta = 0.7$ deg/(cm T^2)) are lower approximately by half as compared to the analogous values in Dy_2S_3. Thus, judging by the dispersion and anisotropy characteristics, the CM effect in RE semiconductors is essentially different from the magnetic birefringence effect in magnetic semiconductors of the $Cd_{1-x}Mn_xTe$ type and analogous to the effect in cubic dielectrics containing RE ions.

Dispersion of the Faraday effect in magnetic semiconductors of the $Cd_{1-x}Mn_xTe$ type is proportional to $\propto(E_g - E)^{-1.5}$ and strongly increases on approaching the band edge (E_g). On the contrary, investigations of the Faraday and Kerr effects in Dy_2S_3 and Pr_2S_3 [3–5] showed that the optical transitions responsible for the dispersion of the Faraday effect in the transparency range occur beyond the fundamental absorption edge ($E_0 = 3.8$ and 3.15 eV in Dy_2S_3 and Pr_2S_3, respectively) and can be related to the interconfiguration electron transitions of the $4f^N \longrightarrow 4f^{N-1}5d$ type., Therefore, there are grounds to believe that both linear and quadratic magnetooptical phenomena in the transparency range of sesquisulfides are primarily determined by the local optical transitions in RE ions.

A microscopic theory of the Faraday and CM effects taking into account the electric-dipole-allowed transitions in RE ions is based on an expression for the polarizability tensor α_{ij} [31]. In the transparency range far from the resonance transition frequencies ($\omega_{eg} - \omega \gg \Gamma_{eg}$), this tensor can be written as

$$\alpha_{ij} = \frac{2}{\hbar\Delta V} \times \sum_{\sigma ge} \rho_g \left[\frac{i\omega \,\mathrm{Im}(d^i_{ge} d^j_{eg})}{\omega^2 - \omega^2_{eg}} - \frac{\omega_{eg} \,\mathrm{Re}(d^i_{ge} d^j_{eg})}{\omega^2 - \omega^2_{eg}} \right], \tag{2}$$

where **d** is the dipole moment operator; $|g\rangle$ and $|e\rangle$ are the wavefunctions of the ground and excited states; ω_{eg} is the transition frequency; Γ_{eg} is the damping parameter; ρ_g is the ground state occupancy; ΔV is the unit cell volume; and σ denotes the RE in position in the unit cell. The first term in the square brackets of Eq. (2) refers to the imaginary antisymmetric part of α_{ij} and describes the ion contribution to the Faraday effect, while the second term determines the symmetric part of α_{ij} and describes the field-independent ion polarizability component and the β_{ijkl} tensor (that is, the isotropic magnetic birefringence and the CM effect). In the absence of an external magnetic field, the contribution of the first term to α_{ij} is zero.

The application of a magnetic field modifies the energy levels of the ground and excited states, perturbs their wavefunctions, and changes the occupancies ρ_g. Since the electric dipole transition is allowed, we may neglect (in a rough approximation) the effect of crystal fields upon the ion. This "free ion" approximation is frequently used to describe dispersion of the Faraday effect in RE compounds at high temperatures. In particular, this approximation was applied to Ln_2S_3 crystals [3]. However, the "free ion" model is inapplicable to description of the anisotropic magnetooptical phenomena even at high temperatures. Indeed, the CM effect in this model would be isotropic—in obvious discrepancy with experiment (see, e.g., Fig. 1). For adequate description of the anisotropic magnetooptical phenomena, as well as the field and temperature dependences of the Faraday effect, it is necessary (especially at low temperatures) to take into account the crystal field effects.

The eigenstates of an RE ion in a magnetic field are determined using the Hamiltonian

$$H = H_0 + V_{cr} + V_Z, \tag{3}$$

where H_0 is the free ion Hamiltonian including the Coulomb and spin–orbit interactions; V_{cr} is the crystal field potential; and $V_Z = \mu_B(\mathbf{L} + 2\mathbf{S})\mathbf{B}$ is the Zeeman interaction energy, **L** and **S** being the orbital and spin moment operators. The crystal field potential V_{cr} is determined by the point symmetry of the RE ion position and can be written as

$$V_{cr} = \sum_i \sum_{kn} B_n^k r_i^n Y_n^k(\theta_i, \varphi_i), \qquad (4)$$

where B_n^k are coefficients depending on the symmetry of the ion environment; Y_n^k are spherical harmonics; and r_i, θ_i, φ_i are the spherical coordinates of the *i*th electron of the RE ion.

In order to describe the multiplet splitting in the crystal field and the effect of applied magnetic field upon the resulting states, the $V_{\rm cr}$ operator is projected onto the space of wavefunctions of the corresponding multiplet. Since these wavefunctions are of the same parity, Eq. (4) will contain only components with even *n*. This implies that odd components of the crystal field do not lead to the splitting of states of the ground and excited multiplets. Therefore, the crystal-field-induced anisotropy of the CM effect is determined only by the even harmonics. In the Th_3P_4 type lattice, the RE ions occupy positions possessing the S_4 point symmetry and the crystal field potential $V_{\rm cr}$ depends on the parameters B_2^0, B_4^0, B_6^0, B_4^4, and B_6^4. As demonstrated in [32], a correct description (including the temperature and field dependences) of the magnetic Faraday effect in RE compounds must take into account the crystal field effects; however, the odd components of the crystal field potential are also not manifested in that phenomenon.

The non-reciprocal magnetic birefringence, related to the local optical transitions with the energies independent (unlike the case of interband or exciton transitions) of the wavevector **k**, is determined by the magnetoelectric and quadrupole mechanisms [21]. The contribution of these mechanisms to the symmetric art of the dielectric permittivity tensor ε_{ij} has the following form:

$$\delta\varepsilon_{ij}(\omega, \mathbf{k}) = \frac{1}{\varepsilon_0\omega} \times \left[-\varepsilon_{jlk}G_{ik} - \varepsilon_{ilk}G_{jk} + \frac{\omega}{2}(a'_{ijl} + a'_{jil})\right]k_l, \qquad (5)$$

where ε_{ijk} is a fully antisymmetric third-rank unit tensor,

$$G_{ik} = \frac{2}{\hbar\Delta V}\sum_{\sigma ge}\rho_g \operatorname{Re}(d_{ge}^{i,\sigma} m_{eg}^{j,\sigma})\frac{\omega_{eg}}{\omega_{eg}^2 - \omega^2}, \qquad (6)$$

$$a'_{ijk} = -\frac{2}{\hbar\Delta V}\sum_{\sigma ge}\rho_g \operatorname{Im}(d_{ge}^{i,\sigma} Q_{eg}^{jk,\sigma})\frac{\omega}{\omega_{eg}^2 - \omega^2}, \qquad (7)$$

m is the magnetic moment operator, and Q^{ij} is the quadrupole moment operator. In the absence of an external magnetic field, $G_{ij} = 0$ and $a'_{ijk} = 0$. The application of a magnetic field leads to the appearance of nonzero tensor components linearly depending on **B**:

$$G_{ij} = G_{ijk}B_k, \quad a'_{ijk} = a'_{ijkl}B_l,$$

where G_{ijk} is the second-order magnetoelectric permittivity in the optical frequency range [21]. As is seen from Eqs. (6) and (7), a transition will contribute to the non-reciprocal birefringence provided that it is simultaneously allowed in the electric dipole and magnetic dipole or quadrupole approximations. Since the magnetic moment operator **m** and the quadrupole moment operator Q^{ij} are even, while the operator d is odd, this requirement cannot be satisfied for the states with definite parity.

Thus, in the case of allowed electric dipole transitions, the NMB is due to the states of different parity being mixed by the odd crystal field components. These states include, in particular, the states of the $4f^N$ and $4f^{N-1}5d$ configurations. The RE ion positions in γ-Ln_2S_3 possess no center of inversion (symmetry class S_4) and the crystal field potential contains only the terms with odd *n*. Since the CM and NMB effects observed in Dy_2S_3 and Pr_2S_3 in a field of $B = 1$ T are comparable (see Table 1), we may conclude that an odd crystal field determines to a considerable extent the MLB in γ-Ln_2S_3 crystals. In contrast to the case of sesquisulfides, the CM effect is not observed at $B = 1$ T in the transparency range of boracites containing 3*d* ions, where the MLB is mostly determined by the NMB effect [22].

It must be noted that, for the appearance of NMB in the case of allowed electric dipole transitions, the odd crystal field is necessary in order to make these transitions allowed in the magnetic dipole and quadrupole approximations; in the case of intraconfiguration transitions between states of the same parity, the presence of this field provides for these transitions being allowed in the electric dipole approximation. In both cases, the NMB is determined by the degree of mixing of the wavefunctions of different parity. Therefore, we may expect that parameters describing NMB will have close values irrespective of whether the transition is allowed or forbidden in the electric dipole approximation. Indeed, a comparison of the *A* and *g* parameters for Dy_2S_3, Pr_2S_3 and those of $R_3B_7O_{13}I$ boracites (in which the NMB is due to transitions inside the 3*d* electron shell of a transition metal [21, 22]) shows that these quantities are approximately on the same order of magnitude. The absence of the CM effect in boracites can be explained by weak transitions in the 3*d* shell; making these transitions allowed in the electric dipole approximation would require taking into account the odd crystal field or the interaction with odd phonons.

In the general case, the electric dipole transitions inside the 3*d* or 4*f* shells can be rendered allowed by the action of the odd crystal field or by the interaction with odd phonons. However, the odd phonons by themselves cannot provide for the appearance of NMB. Indeed, the interaction with odd phonons may render the electric dipole transition allowed (and manifested in the absorption spectra) even for a centrosymmetric ion environment, but the NMB will not appear as long as the G_{ijk} and a'_{ijkl} tensors are forbidden in the centrosymmetric groups. In the case of a noncentrosymmetric environment, the V^n_{cr} components and γ_{ijkl} tensors will be proportional to odd powers of a certain parameter δ representing a shift (or a combination of shifts) of the RE ions from their positions corresponding to the centrosymmetric environment. For example, the parameter δ in boracites can be represented by the ion shift from the central position in the ferroelectric phase [33] or by pairwise ($\pm\delta$) ion shifts from the base plane in the paraelectric phase [21].

The odd phonons may produce a local (in time) change in the parameter δ but, in the approximation linear with respect to δ, this mechanism cannot account for NMB because the average δ value remains unchanged. Therefore, we may expect that NMB (in contrast to the absorption coefficient, Faraday effect, or CM effect) is determined primarily by purely electron transitions. It should be noted that methods available for determining parameters of the odd crystal field are very restricted. Thus, investigations of the NMB effect offer a possibility of evaluating these parameters, provided that the corresponding theory would be developed.

In crystals of the T_d symmetry, the G_{ijk} tensor describing the second-order magnetoelectric permittivity possesses a single independent coefficient G_{xyz}. Therefore, the magnetoelectric mechanism may give a contribution to the γ_{ijkl} tensor only with a strictly determined ratio of the parameters A and g: $A = 2g$. This was demonstrated by direct calculations for the boracite crystals with 3*d* ion positions possessing a D_{2d} symmetry [21]. Nevertheless, the relationship $A = 2g$ must be valid for crystals of the T_d symmetry irrespective of the particular symmetry of the ion environment. Indeed, the investigations of boracites with various 3*d* ions (Co^{2+}, Cu^{2+}, Ni^{2+}) [22] showed that this relationship holds with a good accuracy irrespective of the 3*d* ions type, which is evidence that the magnetoelectric mechanism of birefringence dominates. As is seen from Table 1, the relationship $A = 2g$ holds in Dy_2S_3, which is indicative that the magnetoelectric mechanism is operative in this crystal as well. At the same time, the analogous parameters in Pr_2S_3 obey a different relationship: $A = 3.3g$ (Table 1). Taking into account that the parameters are determined with an accuracy of 10%, so that $A/g = 3.3 \pm 0.6$, we may conclude that the NMB in Pr_2S_3 cannot be explained by the magnetoelectric mechanism alone and it is necessary to take into account the quadrupole mechanism related to matrix elements of the $\mathrm{Im}(d^i_{eg}Q^{jk}_{ge})$ type.

Zvezdin *et al.* [9] showed that the polarizability of an RE ion, described by the second term in Eq. (2) (responsible for the CM effect), for the interconfiguration electric dipole transitions of the $4f^N \longrightarrow 4f^{N-1}5d$ type far from resonance frequencies can be expressed through the quadrupole moment components Q_{ij}:

$$\alpha_{ij} = a_2\langle Q_{ij}\rangle, \quad (8)$$

where $\langle\ldots\rangle$ denotes averaging over levels of the ground state with the occupancy ρ_g (for notations see [9]). According to the experimental data, the CM effect is more pronounced in Dy_2S_3 than in Pr_2S_3, despite a lower effective oscillator energy in the latter compound (Table 1). This behavior can be related to different properties of the ground state multiplets in Dy^{3+} and Pr^{3+} ions. In a crystal field of low symmetry, the ${}^6H_{15/2}$ multiplet of Dy^{3+} (with an odd number of electrons on the 4*f* shell) splits into several Kramers doublets. For Pr^{3+} (with even number of electrons), the ground state multiplet ${}^4F_6$ represents a set of singlets.

As demonstrated in [9] for a singlet ground state, the field dependence of $\langle Q_{ij}\rangle$ at low temperatures is manifested in the second-order terms (for the Kramers doublets, in the first-order terms) with respect to $\mu_B B/E$, where E is the energy difference between the ground state levels. For RE ions in the *S*-state (Gd^{3+}), the dependence of $\langle Q_{ij}\rangle$ on B is manifested in the third-order terms, which accounts for the MLB in Gd_2S_3 being markedly lower than in Dy_2S_3 or Pr_2S_3. The linear magnetooptical phenomena caused by ions in the *S*-states, in contrast to the effects due to ions possessing nonzero orbital momentum in the ground state, are related only to the spin splitting [34]. For this reason, the crystals of compounds containing ions in the *S*-state are characterized by low magnitudes of the Faraday effect. According to the experimental data, this is also valid for the NMB. In La_2S_3, where the 4*f* shell is empty, the magnetooptical phenomena are purely of the diamagnetic nature, with a magnitude lower by at least two orders as compared to that in paramagnetic crystals of Ln_2S_3.

5. CONCLUSION

We have experimentally studied the non-reciprocal magnetic birefringence, related to the magnetic-field-induced spatial dispersion, and the CM effect in noncentrosymmetric sesquisulfides of the γ-Ln_2S_3 type. The NMB and CM effects (as well as the Faraday effect) depend on the type of RE ions entering into the crystal lattice. Both effects are more pronounced for ions possessing nonzero orbital moments in the ground state (Pr^{3+}, Dy^{3+}) than for ions in the *S*-state (Gd^{3+}) and diamagnetic ions (La^{3+}). A strong anisotropy of the CM effect in γ-Ln_2S_3 indicates that this phenomenon (as well as that observed in RE dielectrics) is related to electron transitions in RE ions. A decisive role is played by the crystal field, especially by the centrosymmetric crystal field components.

The non-reciprocal magnetic birefringence, in contrast to the CM effect, for both allowed and forbidden electric dipole transitions, is related to the presence of odd crystal field components. The NMB magnitude observed in Dy_2S_3 and Pr_2S_3 indicates that the odd crystal field components in these compounds are sufficiently large. Therefore, investigations of the NMB effect offer a possibility of evaluating the crystal field parameters, provided that the corresponding theory would be developed. The level of the NMB anisotropy in Dy_2S_3 corresponds to manifestations of the second-order magnetoelectric permittivity in the optical frequency range. At the same time, the NMB in Pr_2S_3 is partly due to the quadrupole mechanism. We expect that investigations of the spectral dependence of the Cotton–Mouton effect and the non-reciprocal magnetic birefringence in RE sesquisulfides may help to determine the values of various matrix elements of the optical transitions and the crystal field parameters

ACKNOWLEDGMENTS

The author is grateful to N.F. Kartenko for X-ray diffraction measurements and to A.Yu. Zyuzin for fruitful discussions.

This study was supported by the Russian Foundation for Basic Research (project no. 99-02-18028) and by the “Fundamental Spectroscopy” program.

REFERENCES

1. V. P. Zhuze and A. I. Shelykh, Fiz. Tekh. Poluprovodn. (Leningrad) **23**, 393 (1989) [Sov. Phys. Semicond. **23**, 245 (1989)].
2. S. Methfessel and D. C. Hattis, in *Handbuch der Physik*, Band XVIII/1: *Magnetism*, Ed. by H. P. J. Wijn (Springer-Verlag, New York, 1968), p. 517.
3. R. Dagis, G. Babonas, and G. Pukinskas, Litov. Fiz. Sb. **28**, 559 (1988).
4. Yu.-G. Babonas, R. Dagis, and G. Pukinskas, Opt. Spektrosk. **68**, 824 (1990) [Opt. Spectrosc. **68**, 481 (1990)].
5. G. Babonas, R. Dagys, and G. Pukinskas, Fiz. Tverd. Tela (Leningrad) **30**, 3460 (1988) [Sov. Phys. Solid State **30**, 1985 (1988)].
6. G. Babonas, R. Dagis, and G. Pukinskas, Phys. Status Solidi B **153**, 741 (1989).
7. R. V. Pisarev, in *Physics of Magnetic Dielectrics* (Nauka, Leningrad, 1974).
8. R. V. Pisarev, Fiz. Tverd. Tela (Leningrad) **17**, 1396 (1975) [Sov. Phys. Solid State **17**, 898 (1975)].
9. A. K. Zvezdin, A. I. Popov, and Kh. I. Turkmenov, Fiz. Tverd. Tela (Leningrad) **28**, 1760 (1986) [Sov. Phys. Solid State **28**, 974 (1986)].
10. N. F. Vedernikov, A. K. Zvezdin, S. V. Koptsik, *et al.*, Pis’ma Zh. Éksp. Teor. Fiz. **43**, 38 (1986) [JETP Lett. **43**, 48 (1986)].
11. N. P. Kolmakova, R. Z. Levitin, A. I. Popov, *et al.*, Phys. Rev. B **41**, 6170 (1990).
12. G. S. Krinchik, R. Z. Levitin, A. I. Popov, and A. K. Zvezdin, in *Abstracts of ISMO'91, Kharkov, 1991,* p. 131.
13. N. P. Kolmakova, R. Z. Levitin, and A. I. Popov, in *Abstracts of ISMO’91, Kharkov, 1991*, p. 75.
14. D. L. Portigal and E. Burstein, J. Phys. Chem. Solids **32**, 603 (1971).
15. V. M. Agranovich and V. L. Ginzburg, *Crystal Optics with Spatial Dispersion and Excitons* (Nauka, Moscow, 1979; Springer-Verlag, New York, 1984).
16. B. B. Krichevtsov, R. V. Pisarev, A. A. Rzhevsky, *et al.*, Phys. Rev. B **57**, 14611 (1998).
17. B. B. Krichevtsov, R. V. Pisarev, A. A. Rzhevskiĭ, *et al.*, Zh. Éksp. Teor. Fiz. **114**, 1018 (1998) [JETP **87**, 553 (1998)].
18. B. B. Krichevtsov, R. V. Pisarev, A. A. Rzhevskiĭ, and H.-J. Weber, Pis’ma Zh. Éksp. Teor. Fiz. **69**, 514 (1999) [JETP Lett. **69**, 551 (1999)].
19. O. V. Gogolin, V. A. Tsvetkov, and E. G. Tsitsishvili, Zh. Éksp. Teor. Fiz. **87**, 1038 (1984) [Sov. Phys. JETP **60**, 593 (1984)].
20. E. G. Tsitsishvili, Fiz. Tekh. Poluprovodn. (Leningrad) **20**, 650 (1986) [Sov. Phys. Semicond. **20**, 412 (1986)].
21. B. B. Krichevtsov, A. A. Rzhevskii, and H.-J. Weber, Phys. Rev. B **61**, 10084 (2000).
22. B. B. Krichevtsov, Fiz. Tverd. Tela (St. Petersburg) **43**, 75 (2001) [Phys. Solid State **43**, 76 (2001)].
23. P. P. Kripyakevich, Kristallografiya **7**, 686 (1962) [Sov. Phys. Crystallogr. **7**, 556 (1962)].
24. A. V. Mironov, A. A. Kamarzin, V. V. Sokolov, *et al.*, *Rare-Earth Semiconductors* (Baku, 1981).
25. J. R. Hendeson, M. Muramoto, and E. Loh, J. Chem. Phys. **47**, 3347 (1967).
26. J. R. Henderson, M. Muramoto, J. B. Gruber, and R. Menzel, J. Chem. Phys. **52**, 2311 (1970).
27. T. I. Volkonskaya, A. I. Shelykh, A. V. Sotnikov, *et al.*, Fiz. Tverd. Tela (Leningrad) **29**, 559 (1987) [Sov. Phys. Solid State **29**, 318 (1987)].
28. V. P. Zhuze, A. A. Kamarzin, V. V. Sokolov, *et al.*, Pis’ma Zh. Tekh. Fiz. **7**, 1435 (1981) [Sov. Tech. Phys. Lett. **7**, 613 (1981)].
29. J. K. Furdyna, J. Appl. Phys. **64**, R29 (1988).
30. B. B. Krichevtsov, R. V. Pisarev, A. A. Rzhevskiĭ, *et al.*, Pis’ma Zh. Éksp. Teor. Fiz. **67**, 569 (1998) [JETP Lett. **67**, 602 (1998)].
31. M. Born and K. Huang, *Dynamical Theory of Crystal Lattices* (Clarendon Press, Oxford, 1954; Inostrannaya Literatura, Moscow, 1958).
32. U. V. Valiev, A. K. Zvezdin, G. S. Krinchik, *et al.*, Zh. Éksp. Teor. Fiz. **85**, 311 (1983) [Sov. Phys. JETP **58**, 181 (1983)].
33. R. V. Pisarev, V. V. Druzhinin, S. D. Prochorova, *et al.*, Phys. Status Solidi **35**, 145 (1969).
34. A. K. Zvezdin and V. A. Kotov, *Modern Magnetooptics and Magnetooptical Materials* (Institute of Physics Publ., Bristol, 1997).

Translated by P. Pozdeev

Journal of Experimental and Theoretical Physics, Vol. 92, No. 5, 2001, pp. 840–843.
From Zhurnal Éksperimental'noĭ i Teoreticheskoĭ Fiziki, Vol. 119, No. 5, 2001, pp. 966–970.
Original English Text Copyright © 2001 by Falkovsky.

The Coulomb Effects in the Dynamics of Polar Lattices[¶]

L. A. Falkovsky
Landau Institute for Theoretical Physics, Moscow, 117337 Russia
e-mail: falk@itp.ac.ru

Received November 16, 2000

Abstract—The zone-center phonon frequencies of polar lattices are calculated for uniaxial crystals proceeding from the symmetry considerations. The long-range Coulomb forces and crystal anisotropy are explicitly taken into account. The free-carrier contributions to the dielectric constant are included. The angular dispersion of the optical-phonon modes is compared to data for a hexagonal 6*H*-SiC polytype. © *2001 MAIK “Nauka/Interperiodica”.*

1. INTRODUCTION

Electrostatic dipole–dipole interactions play an important role in the theory of lattice vibrations. It is common knowledge [1] that the degeneracy of phonon modes at the Brillouin zone center (e.g., in the cubic 3*C*-SiC crystal) is removed if the atomic displacements are accompanied by the Coulomb field. Then the frequency of the longitudinal optical mode becomes larger than the frequencies of transverse modes. For noncubic crystals (e.g., for the hexagonal or rhombohedral SiC polytypes), the long-range Coulomb field also gives rise to an angular dependence of the zone-center modes: at $\mathbf{k} = 0$, *the optical phonon frequencies depend on the direction of propagation.*

This phenomenon is rather unusual from both physical and mathematical standpoints: the eigenvalues of the dynamical matrix calculated for $\mathbf{k} = 0$ depend on the **k**-direction. This is caused by a nonanalytical **k**-dependence of the dynamical matrix which results from a long-range dipole–dipole interaction. In polar cubic crystals, the Coulomb field splits the threefold degeneracy of optical modes at the Brillouin zone center, but the frequency dependence on the propagation direction also appears in uniaxial crystals due to the long-range electrostatic field.

The electrodynamic part of the problem was formulated by Loudon [2]. The Coulomb contributions in the dynamical matrix are usually calculated by means of the Evald summation [1]. The angular dispersion of the optical modes is clearly demonstrated by the recent numerical calculations for the zone-center phonons [3] and for the entire Brillouin zone [4] in the case of $A^{III}B^{V}$ semiconductors with the wurtzite structure. The Coulomb field is also taken into account in the theory of phonon–plasmon coupled modes (polaritons) [5] when the effect of free carriers is studied.

The main purpose of this paper is (i) to calculate the angular dispersion for the zone-center phonons in uniaxial crystals using the symmetry arguments and (ii) to consider the effect of free carriers on these modes. For definiteness, we concentrate on the phonon modes of uniaxial SiC polytypes that are presently very popular in technical applications.

2. OPTICAL MODES AT THE ZONE CENTER OF CUBIC CRYSTALS

Among the hexagonal and rhombohedral SiC polytypes, there is the cubic 3*C*-SiC polytype with two atoms in the unit cell. First we consider the optical modes in this simplest case. For the nearest vicinity of the Brillouin zone center, $k \ll \pi/d$, where d is the lattice parameter, the acoustic and optical modes can be divided using the series expansion in **k** of the dynamical matrix. As the result, in the zero approximation in **k** we obtain the system of three equations for the optical displacements u_i $(i = x, y, z)$:

$$(\phi - M^*\omega^2)\mathbf{u} = \mathbf{f}, \tag{1}$$

where M^* is the reduced mass of two atoms (Si and C) in the unit cell, ϕ is the diagonal element of the force constant matrix (the only diagonal element of the 3×3 matrix existing in a cubic crystal). The value of ϕ can be calculated in the nearest neighbor approximation, but the long-range Coulomb interaction cannot be considered in this way. The Coulomb effect is described by the force $\mathbf{f} = Ze\mathbf{E}$ acting on an effective charge Z, where the electric field **E** is found from Maxwell's equations. Eliminating the magnetic field from Maxwell's equations, we can express the electric field **E** in terms of polarization **P** as

$$\mathbf{E} = \frac{-4\pi[\mathbf{k}(\mathbf{k}\cdot\mathbf{P}) - \omega^2\mathbf{P}/c^2]}{k^2 - \omega^2/c^2}. \tag{2}$$

We are interested in the ω values of the order of optical mode frequencies, such that $\omega/c \approx 10^3$ cm^{-1}. If the phonon is excited by light, its wave vector has the value

---

[¶] This article was submitted by the author in English.

of the photon wave vector, i.e., of the order of 10^5 cm^{-1}. The condition $k \gg \omega/c$ is then satisfied and the terms involving c^2 must be omitted in Eq. (2), which then becomes

$$\mathbf{E} = -4\pi\mathbf{k}(\mathbf{k}\cdot\mathbf{P})/k^2. \tag{3}$$

In the longwave limit ($k \ll \pi/d$), the polarization is related to the phonon displacement and the electric field by the macroscopic equation

$$\mathbf{P} = NZe\mathbf{u} + \chi\mathbf{E}, \tag{4}$$

where χ is the atomic permittivity and N is the number of unit cells per cm^3. Sometimes, the local field is used in equations similar to (4) instead of the macroscopic field **E**. For cubic crystals (for which only the simple Lorentz relationship exists), the local field can be eliminated by renormalizing the force constant ϕ.

Using Eqs. (3) and (4), we can express the electric field **E** in terms of **u**. Equation (1) then gives the frequencies of transverse and longitudinal optical modes in the cubic crystal as

$$\omega_{TO}^2 = \phi/M^* \text{ and } \omega_{LO}^2 = \phi/M^* + \rho, \tag{5}$$

where

$$\rho = 4\pi Z^2e^2N/\varepsilon^\infty M^* \text{ and } \varepsilon^\infty = 1 + 4\pi\chi. \tag{6}$$

Although relation (3) between **E** and **P** involves the **k**-direction explicitly, the frequencies of optical modes (5) are independent of the propagation direction, as it must be for a cubic crystal.

3. OPTICAL MODES AT THE ZONE CENTER OF UNIAXIAL CRYSTALS

The crystal anisotropy of the noncubic SiC polytypes is known to be small because the nearest neighbors of any given atom preserve the cubic symmetry. Let us introduce the strain tensor e_{ij} describing a small difference between the dynamic matrices for the noncubic polytype and the cubic one. The phonon spectrum of the noncubic polytype can then be obtained in the following way. At the first step, we transform the Brillouin zone of the cubic polytype (“the large zone”) using the strain e_{ij}. Hence, we find the frequencies of the so-called strong modes. For the zone-center, they can be obtained by expanding the dynamic matrix in the strain e_{ij}.

At the second step, we take into account that noncubic polytypes have more than two atoms in the unit cell and additional optic modes appear. Phonon branches of the large zone are folded [6] into the Brillouin zone of the noncubic polytype, thereby producing additional weak modes. The weak mode intensity in both optics and Raman scattering was calculated in [7]. In the present paper, we thus consider only strong modes.

The dynamic matrix can contain only the e_{ij} components that are invariant under the symmetry transformations of the crystal. There are two first-order invariants, e_{zz} and $e_{xx} + e_{yy}$, assuming that the z axis is parallel to the c axis. We can fix the crystal volume, i.e., impose the condition $e_{ii} = 0$. We then have only one invariant, for instance e_{zz}, which is involved only in the diagonal elements of the force-constant matrix in Eq. (1). The coefficients of the xx and yy elements are equal because of the rotation invariance around the c axis. Finally, we can omit the common frequency shift. Instead of Eq. (1), we thus obtain

$$\begin{pmatrix} \beta + \rho n_x^2 - \omega^2 & \rho n_x n_y & \rho n_x n_z \\ \rho n_x n_y & \beta + \rho n_y^2 - \omega^2 & \rho n_y n_z \\ \rho n_x n_z & \rho n_y n_z & \alpha + \rho n_z^2 - \omega^2 \end{pmatrix} \tag{7}$$

$$\times \begin{pmatrix} u_x \\ u_y \\ u_z \end{pmatrix} = 0,$$

where $\mathbf{n} = \mathbf{k}/k$ and

$$\alpha = \phi/M^*, \quad \beta = \alpha + be_{zz}. \tag{8}$$

We take the vector **k** in the yz plane and denote as θ the angle between **k** and the c axis,

$$n_x = 0, \quad n_z = \cos\theta, \quad n_y = \sin\theta.$$

We then see from Eq. (7) that there are one transverse mode (TO_1) vibrating in the x direction and two modes in the yz plane with the frequencies

$$\omega_{TO_1}^2 = \beta,$$

$$\omega_{y,z}^2(\theta) = \frac{1}{2}(\rho + \alpha + \beta) \tag{9}$$

$$\pm\frac{1}{2}\{[\rho + (\alpha - \beta)\cos 2\theta]^2 + (\alpha - \beta)^2\sin^2 2\theta\}^{1/2}.$$

We emphasize that Eqs. (9) give the phonon frequencies at the zone center, but these frequencies depend on the propagation direction θ. This dependence has its origin in the simultaneous effect of the Coulomb field (described by the constant ρ) and crystal anisotropy ($\beta \neq \alpha$). In the absence of the Coulomb field ($\rho = 0$), we have $\omega_z^2 = \alpha$, $\omega_y^2 = \beta$, and there is no angular dispersion. For the isotropic case ($\alpha = \beta$), Eq. (9) gives the modes for the cubic crystal.

If the Coulomb effect is small compared to the crystal anisotropy ($\rho \ll |\alpha - \beta|$), we can omit the off-diagonal terms in matrix (7). We then have one mode vibrating close to the c direction with the frequency $\omega_z^2 = \alpha + \rho\cos^2\theta$ (with an accuracy to $\rho^2/(\alpha - \beta)^2$), and the other mode near the y direction with the frequency $\omega_y^2 = \beta + \rho\sin^2\theta$.

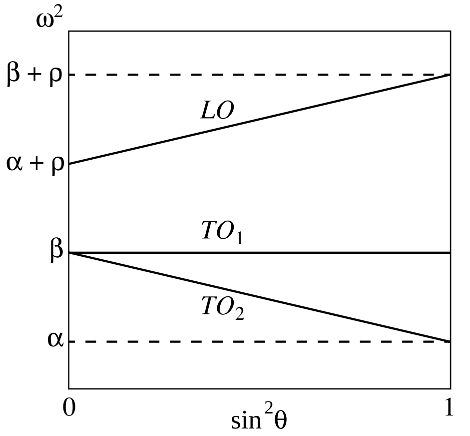

Angular dispersion of the optical phonon modes at the zone center in uniaxial crystals. The angle θ is the angle between the *c* axis and the wave vector **k** ⟶ 0. The TO_1 mode is polarized perpendicularly to the *c*–**k** plane. The *LO* and TO_2 modes have a nearly longitudinal and transverse character, respectively, if the Coulomb force effects dominate over the crystal anisotropy.

In the opposite limiting case of the small crystal anisotropy, it is useful to pass to the coordinate system with the *z*' axis along the **k** vector, subjecting Eq. (7) to the unitary transformation

$$U_{ij} = \begin{pmatrix} 1 & 0 & 0 \\ 0 & \cos\theta & \sin\theta \\ 0 & -\sin\theta & \cos\theta \end{pmatrix}. \tag{10}$$

We must then diagonalize the matrix

$$\begin{pmatrix} \beta & 0 & 0 \\ 0 & \beta\cos^2\theta+\alpha\sin^2\theta & (\beta-\alpha)\sin\theta\cos\theta \\ 0 & (\beta-\alpha)\sin\theta\cos\theta & \beta\sin^2\theta+\alpha\cos^2\theta+\rho \end{pmatrix}. \tag{11}$$

We see that in addition to the TO_1 mode, in the case where $|\alpha-\beta| \ll \rho$, there are another nearly transverse TO_2 mode and nearly longitudinal *LO* mode with the frequencies

$$\begin{aligned} \omega_{TO_2}^2(\theta) &= \beta\cos^2\theta+\alpha\sin^2\theta, \\ \omega_{LO}^2(\theta) &= \rho+\beta\sin^2\theta+\alpha\cos^2\theta, \end{aligned} \tag{12}$$

which can also be obtained by expanding Eq. (9) with an accuracy to $(\alpha-\beta)^2/\rho^2$. The dispersion curves corresponding to Eqs. (9) and (12) are shown schematically in the figure. The angular dispersions of form (12) were obtained by Loudon [2].

One can see from Eq. (9) that a conservation law exists. Namely, the sum of the squared frequencies of the *y* and *z* modes is independent of the propagation direction, e.g.,

$$\begin{aligned} &\omega_y^2(\theta=0)+\omega_z^2(\theta=0) \\ &= \omega_y^2(\theta=\pi/2)+\omega_z^2(\theta=\pi/2). \end{aligned} \tag{13}$$

As an example, we consider the 6*H*-SiC polytype. The angular dispersion of its optical modes is known from the experiment [5, 6]. For $\theta = 0$ (propagation parallel to the *c* axis), the TO_1 and *y* modes are degenerate and their frequencies are equal to $\sqrt{\beta}$. The experimental value is 797 cm^{-1} (with the uncertainty about 1 cm^{-1}). The corresponding value of the longitudinal mode is

$$\omega_{LO}(\theta=0) = \sqrt{\rho+\alpha}.$$

For $\theta = \pi/2$ (propagation perpendicular to the *c* axis),

$$\omega_{TO_2}(\theta=\pi/2) = \sqrt{\alpha}$$

(the experimental value is 788 cm^{-1}) and

$$\omega_{LO}(\theta=\pi/2) = \sqrt{\rho+\beta}$$

(the experimental value is 970 cm^{-1}). It immediately follows that $\rho = 552.9^2$ cm^{-2}, $\alpha = 788^2$ cm^{-2}, and $\beta = 797^2$ cm^{-2}.

We then find

$$\omega_{LO}(\theta=0) = \sqrt{\rho+\alpha} = 962.6\ \text{cm}^{-1},$$

which should be compared with the experimental value 964 cm^{-1}. The small difference between these two values can be attributed to the anisotropy in the atomic permittivity, which is considered in the next section.

4. EFFECTS OF THE PERMITTIVITY ANISOTROPY AND FREE CARRIERS

In the previous section, we assumed that the uniaxial anisotropy affects only the short-range contribution to the force constant matrix, but in uniaxial crystals, the atomic permittivity χ is a tensor with two independent components, $\chi_\parallel$ and $\chi_\perp$, corresponding to the crystal axes. This effect is small because each atom has nearly cubic surroundings, but it must be included for a careful comparison with experiments. In a similar way, free carriers contribute to the angular dispersion of the longitudinal optical mode.

To take into account both the anisotropy of atomic permittivity and the conductivity of free carriers σ, we replace Eq. (4) with

$$\begin{aligned} P_\parallel &= NZeu_\parallel+\left(\chi_\parallel+i\frac{\sigma_\parallel}{\omega}\right)E_\parallel, \\ P_\perp &= NZeu_\perp+\left(\chi_\perp+i\frac{\sigma_\perp}{\omega}\right)E_\perp. \end{aligned} \tag{14}$$

Using Eqs. (3) and (14), we obtain the equation of motion in form (7) and phonon frequencies (9), but the conservation law (13) does not apply now because ρ becomes a function of θ,

$$\rho(\theta) = \frac{4\pi Z^2 e^2 N}{M^*}\left[\left(\varepsilon_{\parallel}^{\infty} + 4\pi i\frac{\sigma_{\parallel}}{\omega}\right)\cos^2\theta + \left(\varepsilon_{\perp}^{\infty} + 4\pi i\frac{\sigma_{\perp}}{\omega}\right)\sin^2\theta\right], \tag{15}$$

where $\varepsilon_{\parallel}^{\infty} = 1 + 4\pi\chi_{\parallel}$ and $\varepsilon_{\perp}^{\infty} = 1 + 4\pi\chi_{\perp}$. We note that the vibration modes acquire some damping due to conductivity. In addition, the optical phonon has a natural width Γ given by its probability to decay into lower energy phonons, and the term $i\Gamma/2$ must be added to ω in Eq. (7).

We can then use transformation (10) and obtain matrix (11) with the function ρ(θ) instead of constant ρ. We see that in the limiting case of the weak anisotropy, $|\alpha - \beta| \ll \rho(\theta)$, the Coulomb field (and therefore the carriers) affects only the longitudinal mode. Its frequency is determined by the equation

$$R(\omega) \equiv \rho(\theta) + \beta\sin^2\theta + \alpha\cos^2\theta - i\omega\Gamma - \omega^2 = 0, \tag{16}$$

where ρ(θ) given by Eq. (15) depends on ω explicitly and through the conductivity σ.

Equation (16) gives the frequency of the *LO* phonon–plasmon coupled mode in uniaxial semiconductors. Notice that in the isotropic case, Eq. (16) coincides with the condition ε(ω)= 0, where the dielectric function ε(ω) is given by the well-known expression

$$\varepsilon(\omega) = \varepsilon^{\infty}\left[1 + \frac{\omega_{LO}^2 - \omega_{TO}^2}{\omega_{TO}^2 - \omega^2 - i\omega\Gamma} - \frac{\omega_p^2}{\omega(\omega + i\gamma)}\right],$$

and the plasmon frequency is

$$\omega_p^2 = \frac{4\pi n e^2}{\varepsilon^{\infty} m}.$$

In this case, Eqs. (5), (6), and (8) give

$$\omega_{TO}^2 = \alpha = \beta, \quad \omega_{LO}^2 = \omega_{TO}^2 + \frac{4\pi Z^2 e^2 N}{\varepsilon^{\infty} M^*},$$

and the Drude formula for the conductivity reads

$$\sigma = \frac{ne^2}{m(-i\omega + \gamma)}.$$

The function *R*(ω) in Eq. (16) is measured in Raman experiments. Namely, the Raman intensity considered as a function of frequency transfer ω is

$$I(\omega, \theta) \approx \mathrm{Im}\frac{1}{R(\omega)} \tag{17}$$

for the *LO* mode excitation with the propagation direction θ. If the incident or scattered light has a finite aperture, Eq. (17) must be integrated over the allowed range of θ.

Equation (17) can be used in experimental studying the effect of carriers on the Raman scattering in uniaxial semiconductors. The conductivity tensor in Eq. (15) is given by the Drudelike formula with the diagonal components $m_{\parallel,\perp}$ and $\gamma_{\parallel,\perp}$, for instance, $\sigma_{\parallel} = ne^2/m_{\parallel}(-i\omega + \gamma_{\parallel})$.

Let us summarize the main result of the paper: the effects of crystal anisotropy ($\alpha \neq \beta$) and Coulomb field ρ(θ) on the phonon dispersion are explicitly separated, as one can see in Eqs. (9) and (16).

ACKNOWLEDGMENTS

This study was initiated by discussions with J. Camassel and P. Vicente (GES, Montpellier, France), and the author would like to thank them. The author acknowledges the kind hospitality of the Max-Plank-Institut für Physik Komplexer Systeme (Dresden, Germany), where this work was completed. The work was also supported by the Russian Foundation for Basic Research (project no. 01-02-16211).

REFERENCES

1. M. Born and K. Huang, *Dynamical Theory of Crystal Lattices* (Clarendon Press, Oxford, 1954; Inostrannaya Literatura, Moscow, 1958).
2. R. Loudon, Adv. Phys. **13**, 423 (1964).
3. H. Grille, Ch. Schnittler, and F. Bechstedt, Phys. Rev. B **61**, 6091 (2000).
4. C. Bungaro, K. Rapcevicz, and J. Bernholc, Phys. Rev. B **61**, 6720 (2000).
5. H. Harima, S. Nakashima, and T. Uemura, J. Appl. Phys. **78**, 1996 (1995).
6. D. W. Feldman, J. H. Parker, W. J. Choyke, and L. Patrick, Phys. Rev. **170**, 698 (1968); Phys. Rev. **173**, 787 (1968).
7. L. A. Falkovsky, Pis'ma Zh. Eksp. Teor. Fiz. **69**, 247 (1999) [JETP Lett. **69**, 268 (1999)].

Journal of Experimental and Theoretical Physics, Vol. 92, No. 5, 2001, pp. 844–850.
Translated from Zhurnal Éksperimental'noĭ i Teoreticheskoĭ Fiziki, Vol. 119, No. 5, 2001, pp. 971–978.
Original Russian Text Copyright © 2001 by Eleonskiĭ, Kulagin.

SOLIDS
Electronic Properties

The Spectrum of Speeds of Topological Solitons in Nonlocal Josephson Electrodynamics

V. M. Eleonskiĭ* and N. E. Kulagin**

Lukin Scientific Research Institute of Physical Problems, Zelenograd, Moscow, 103460 Russia
**e-mail: eleon@nonlin.msk.ru*
***e-mail: kulagin@nonlin.msk.ru*

Received November 23, 2000

Abstract—For the model [6] of nonlocal electrodynamics with nonsmooth (piecewise linear) nonlinearity, the problem of point spectrum of speeds of topological solitons with the minimal topological charge is analyzed. The variation of the spectrum of speeds under one-parameter deformation of such a nonlinearity is determined. *© 2001 MAIK "Nauka/Interperiodica".*

1. Recently, various piecewise linear approximations of the nonlinearity determining the dependence of the Josephson current on the phase difference of superconductor pairs have been often used for analyzing the dynamics of Josephson vortices [1–6]. This approach was largely stimulated by studies of the dynamics of topological solitons in dislocation theory [1]. Note that piecewise linear approximations of nonlinearities in wave equations were earlier widely used for the analysis of wave propagation in nonlinear signal transmission lines [7].

In our opinion, the most interesting line of investigations is connected to the use of piecewise linear approximations of nonlinearity in problems of nonlocal Josephson electrodynamics; this approach is described in the works by Silin and his associates [4–6]. This approach enables one to perform a comparitive analysis of the vortex dynamics under various models of nonlocal effects (differential and integral).

In this work, we use a simple generalization of one model of nonlocal electrodynamics suggested in [6] as a basis for analyzing the influence of one-parameter deformation of the piecewise linear approximation of the nonlinearity on the spectrum of speeds and internal structure of the 2π-kink (topological soliton). This generalization makes it possible, in particular, to trace the variation of the spectrum of speeds of the 2π-kink when passing from the piecewise linear approximation of the nonlinearity used in [6, 7] to the approximation used by Aubry [1] and Volkov [2].

In the model under consideration, nonlocal effects are responsible for the appearance of higher order derivatives in the wave equation with a nonsmooth nonlinearity. This situation requires that the notions used to describe soliton solutions be refined (in contrast to the case of the nonlinear Klein–Gordon wave equation).

For example, in the case of steady waves, the nonlinear wave equation of our model leads to a Lagrangian (or Hamiltonian) dynamical system with two degrees of freedom. The corresponding equations of motion are locally integrable under a piecewise linear approximation of the potential. When constructing the complete solution (the entire trajectory), we use the conditions of smoothness of the function and its three derivatives at the points where the potential is not smooth. In the regions of local integrability, the dynamical system possesses a pair of first integrals. One of them is global, but the other is not conserved. More precisely, the second integral has finite discontinuities at the points where the potential is not smooth. This situation is typical for other models in which taking into account nonlocal effects is related to the appearance of a finite number of higher order derivatives in the nondissipative nonlinear wave equation under a piecewise linear approximation of the nonlinearity.

We call attention to a yet unstudied possibility of renouncing the condition of the maximum smoothness of the trajectory and replacing it by the condition of the conservation of both first integrals. In the model under consideration, this means the continuity of the global solution and its derivative and finite discontinuities of the second and third derivatives. In this work, we use the condition of the maximum smoothness of the solution.

Finally, we note that the rigorous passing from the problem with asymptotic boundary conditions at infinity to the problem with boundary conditions on a finite interval (with its length to be determined) can be effectively used in the analysis of soliton solutions. This possibility derives from the piecewise linear approximation of the potential and was realized in numerical calculations. An alternative approach based on the numerical analysis of the transcendental solvability equations of the problem was used to verify the numerical results and construct asymptotics only. The results obtained confirm certain results and assumptions presented in [6, 7] for the value of the structure parameter corresponding to the values given therein.

In particular, this approach makes it possible to relate the description of the influence of Cherenkov's wave capture on the structure of the 2π-kink described in [4–6] with the fact that the trajectory of the 2π-kink temporary lies on a torus in the four-dimensional phase space. For smooth trajectories, the realization of this possibility in our model is related to the discontinuity of one of the first integrals at the point where the nonlinearity is not smooth.

2. We consider the following generalization of the nonlinear wave equation as the basic model:

$$\ell^4 u_{xxxx} + \ell_0^2\left(u_{xx} - \frac{1}{c^2}u_{tt}\right) + f(u) = 0. \tag{1}$$

Here ℓ, ℓ_0, and c are the characteristic lengths and speed. For solutions of the form $u(x, t) = u(x - vt)$, Eq. (1) can be written in the form

$$\varepsilon u_{xxxx} + u_{xx} + f(u) = 0. \tag{2}$$

Here, the parameter ε is defined by the formula

$$\varepsilon = \left(\frac{\ell}{\ell_0}\right)^4\left(1 - \frac{v^2}{c^2}\right)^{-2}, \tag{3}$$

and the transformation of the independent variable is given by the relation

$$x \longrightarrow x\ell_0^{-1}\left(1 - \frac{v^2}{c^2}\right)^{-1/2}.$$

Equation (2) is a Lagrange equation

$$\frac{\partial\mathcal{L}}{\partial u} - \frac{d}{dx}\left(\frac{\partial\mathcal{L}}{\partial u_x}\right) + \frac{d^2}{dx^2}\left(\frac{\partial\mathcal{L}}{\partial u_{xx}}\right) = 0. \tag{4}$$

For the Lagrangian $\mathcal{L} = \mathcal{L}(u, u_x, u_{xx})$, we have

$$\mathcal{L} = -\frac{1}{2}\varepsilon u_{xx}^2 + \frac{1}{2}u_x^2 - U(u), \quad U(u) = \int f(u)du. \tag{5}$$

Note that in our model, nonlocal effects lead to the dependence of the Lagrangian on higher derivatives. Defining the canonical variables (q_1, q_2, p_1, p_2) by the equations (see, e.g., [8])

$$\begin{gathered} q_1 = u, \\ p_1 = \frac{\partial\mathcal{L}}{\partial u_x} - \frac{d}{dx}\left(\frac{\partial\mathcal{L}}{\partial u_{xx}}\right) = u_x + \varepsilon u_{xxx}, \\ q_2 = u_x, \quad p_2 = \frac{\partial\mathcal{L}}{\partial u_{xx}} = -\varepsilon u_{xx}, \end{gathered} \tag{6}$$

we write Eq. (2) in the Hamiltonian form

$$\begin{aligned} \frac{dq_1}{dx} &= \frac{\partial H}{\partial p_1} = q_2, \quad \frac{dp_1}{dx} = -\frac{\partial H}{\partial q_1} = -\frac{\partial U}{\partial q_1}, \\ \frac{dq_2}{dx} &= \frac{\partial H}{\partial p_2} = -\frac{1}{\varepsilon}p_2, \quad \frac{dp_2}{dx} = -\frac{\partial H}{\partial q_2} = -p_1 + q_2 \end{aligned} \tag{7}$$

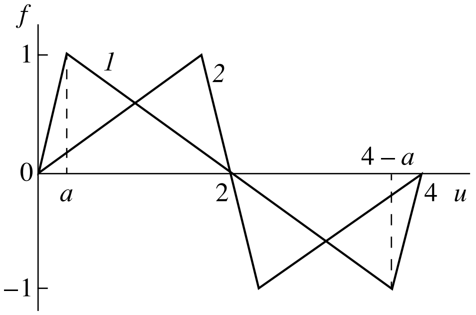

Fig. 1. The dependence $f(u)$ for the values of the parameter $a \gtrsim 0$ (curve *1*) and $a \lesssim 2$ (curve *2*).

with the Hamiltonian

$$H = p_1q_2 - \frac{1}{2\varepsilon}p_2^2 - \frac{1}{2}q_2^2 + U(q_1), \tag{8}$$

which is linear in the momentum p_1.

In the case when $f(u)$ is a piecewise linear function (see Fig. 1) of the form

$$f(u) = \begin{cases} -\dfrac{1}{a}u, & u \in [0, a), \\ -\dfrac{2-u}{2-a}, & u \in [a, 4-a), \\ -\dfrac{1}{a}(u-4), & u \in [4-a, 4] \end{cases} \tag{9}$$

or its periodic extension ($f(u + 4) = f(u)$), Eq. (2) can be integrated on each of the three linearity intervals or their shifts by the period. Moreover, Eq. (2) has two first integrals on each of these intervals:

$$\begin{aligned} I_1 &= \varepsilon u_{xxx}u_x - \frac{1}{2}\varepsilon u_{xx}^2 + \frac{1}{2}u_x^2 + U(u), \\ I_2 &= \frac{1}{2}\varepsilon u_{xxx}^2 + \frac{1}{2}u_{xx}^2 + V(u, u_x, u_{xx}). \end{aligned} \tag{10}$$

Here

$$U(u) = \begin{cases} -\dfrac{1}{2a}u, & u \in [0, a), \\ \dfrac{(2-u)^2}{2(2-a)} - 1, & u \in [a, 4-a), \\ \dfrac{1}{2a}(4-u)^2, & u \in [4-a, 4], \end{cases} \tag{11}$$

$$V(u, u_x, u_{xx}) = \begin{cases} -\dfrac{1}{a}uu_{xx} + \dfrac{1}{2a}u_x^2, & u \in [0, a), \\ -\dfrac{2-u}{2-a}u_{xx} - \dfrac{u_x^2}{2(2-a)}, & u \in [a, 4-a), \\ \dfrac{4-u}{a}u_{xx} - \dfrac{1}{2a}u_x^2, & u \in [4-a, 4]. \end{cases} \tag{12}$$

Completing the solution at the break points of the function $f(u)$ by the continuity condition of the function u_x and its derivatives u_x, u_{xx}, and u_{xxx}, we see that the first integral I_1 preserves its value on all three intervals of linearity of $f(u)$. This means that I_1 is the global first integral. However, the first integral I_2 is discontinuous at the points $u = a$ and $u = 4 - a$. More precisely,

$$\begin{gathered} I_2|_{u=a+} - I_2|_{u=a-} = -\frac{1}{a(2-a)}u_x^2(a), \\ I_2|_{u=(4-a)+} - I_2|_{u=(4-a)-} \\ = \frac{1}{a(2-a)}u_x^2(4-a). \end{gathered} \tag{13}$$

where $a_\pm = a \pm 0$.

In terms of the canonical variables (q_1, q_2, p_1, p_2), the first integrals (10)–(12) have the form

$$\begin{gathered} I_1 = H = p_1 q_2 - \frac{1}{2\varepsilon}p_2^2 - \frac{1}{2}q_2^2 + U(q_1), \\ I_2 = \frac{1}{2\varepsilon}(p_1 - q_2)^2 + \frac{1}{2\varepsilon^2}p_2^2 + V(q_1, q_2, p_2). \end{gathered} \tag{14}$$

Here

$$V(q_1, q_2, p_2) = \begin{cases} -\dfrac{1}{a\varepsilon}q_1 p_2 + \dfrac{1}{2a}q_2^2, & u \in [0, a), \\ \dfrac{2-q_1}{\varepsilon(2-a)}p_2 - \dfrac{6q_2^2}{2(2-a)}, & u \in [a, 4-a), \\ \dfrac{4-q_1}{a\varepsilon}p_2 - \dfrac{1}{2a}q_2^2, & u \in [4-a, 4], \end{cases} \tag{15}$$

and the discontinuities the local first integral I_2 are determined by the expressions

$$\begin{gathered} I_2|_{q_1=a+} - I_2|_{q_1=a-} = -\frac{1}{a(2-a)}q_2^2(a), \\ I_2|_{q_1=(4-a)+} - I_2|_{q_1=(4-a)-} \\ = \frac{1}{a(2-a)}q_2^2(4-a). \end{gathered} \tag{16}$$

These formulas for the first integrals (I_1, I_2) and for the discontinuities of the local integral I_2 can be easily generalized for the case of other piecewise linear approximations of the nonlinearity $f(u)$, for example, for the case of the two-parameter piecewise linear approximation $f(u)$ defined as

$$f(u) = \begin{cases} -\dfrac{(4-a)u}{ab}, & u \in [0, a), \\ \dfrac{(4-a+b)u - 4b}{b(b-a)}, & u \in [a, b), \\ \dfrac{4-u}{4-b}, & u \in [b, 4], \end{cases} \tag{17}$$

which satisfies (as well as nonlinearity (9)) the condition

$$\int_0^4 f(u)du = 0. \tag{18}$$

Due to this condition, the equilibrium states $u = 0$ and $u = 4$ are at the same level of the global first integral I_1.

3. Let us consider the problem on the topological soliton for Eqs. (2), (9) with the conditions

$$\lim_{x \to -\infty} = 0, \quad \lim_{x \to +\infty} = 4. \tag{19}$$

From the viewpoint of the Hamiltonian dynamical system (7), (8), (11), this problem corresponds to that [9] of determining the heteroclinic trajectory in the phase space $\{(q_1, q_2, p_1, p_2)\}$ that is biasymptotic for the equilibrium states $O_0(0, 0, 0, 0)$ and $O_4(4, 0, 0, 0)$, which are singular points of the saddle–center type (see [9]). We note that such trajectories are sought in the space of dynamical systems [9], which are, in this case, indexed by the values of the structure parameters (ε, a). When $f(u)$ is a periodic function, the solutions to this problem are associated with topological solitons with the minimal charge (analogues of 2π-kinks). For the intervals $u \in [0, a]$ and $u \in [4 - a, 4]$, we have for $x \in (-\infty, 0]$,

$$\begin{gathered} q_1(x) = u(x) = a\exp\{kx\}, \\ q_2(x) = u_x = kq_1, \\ p_1(x) = u_x + \varepsilon u_{xxx} = (1 + \varepsilon k^2)kq_1, \\ p_2(x) = -\varepsilon u_{xx} = -\varepsilon k^2 q_1; \end{gathered} \tag{20}$$

for $x \in [l, +\infty)$, we have

$$\begin{gathered} q_1(x) = 4 - a\exp\{k(x-l)\}, \\ q_2(x) = k(4 - q_1), \\ p_1(x) = (1 + \varepsilon k^2)k(4 - q_1), \\ p_2(x) = \varepsilon k^2(4 - q_1). \end{gathered} \tag{21}$$

Here

$$\begin{gathered} k^2 = \frac{1}{2\varepsilon}\left(\sqrt{1 + \frac{4\varepsilon}{a}} - 1\right), \\ q_1(0) = u(0) = a, \quad q_1(l) = u(l) = 4 - a. \end{gathered} \tag{22}$$

On the interval $q_1 \in [a, 4 - a]$, the solution has the form

$$\begin{gathered} q_1(x) = 2 + a_+\sin(k_+x + \alpha_+) \\ + a_-\sin(k_-x + \alpha_-), \\ q_2(x) = k_+a_+\cos(k_+x + \alpha_+) \\ + k_-a_-\cos(k_-x + \alpha_-), \\ p_1(x) = \varepsilon k_+k_-(k_-a_+\cos(k_+x + \alpha_+) \end{gathered} \tag{23}$$

$$+ k_+ a_- \cos(k_- x + \alpha_-)),$$

$$p_2(x) = \varepsilon(k_+^2 a_+ \sin(k_+ x + \alpha_+) + k_-^2 a_- \sin(k_- x + \alpha_-))$$

for $x \in [0, l]$. Here

$$k_\pm^2 = \frac{1}{2\varepsilon}\left(1 \pm \sqrt{1 - \frac{4\varepsilon}{2-a}}\right). \tag{24}$$

In essence, the initial problem (19) on the line $x \in (-\infty, +\infty)$ is reduced to an overdetermined boundary value problem on the interval $u \in [a, 4 - a]$, which depends on two structure parameters (ε, a). Indeed, in accordance with (23), the unknown amplitudes $a_\pm$, phases $\alpha_\pm$, and l (the unknown length of the region of possible oscillations of the function $u(x)$ and its derivatives u_x, u_{xx}, and u_{xxx}) satisfy four conditions on each of the internal boundaries (i.e., at $x = 0$ and $x = l$). The boundary conditions depend on the structure parameters (ε, a). In the phase space $\{(q_1, q_2, p_1, p_2)\}$, formulas (23) determine a segment of the trajectory belonging to the torus that must be sewed (by continuity) with the half-trajectories defined by formulas (20) and (21). The length of the trajectory segment belonging to the torus is not known in advance.

The following four expressions are implied by (23):

$$(k_\pm a_\pm)^2 = \frac{k_\pm^2(p_2 - (q_1 - 2)k_\mp^2)^2 + (p_1 - q_2\varepsilon k_\pm^2)^2}{\varepsilon^2(k_+^2 - k_-^2)^2}, \tag{25}$$

$$\tan(k_\pm x + \alpha_\pm) = -k_\pm \frac{p_2 - (q_1 - 2)\varepsilon k_\mp}{p_1 - q_2 \varepsilon k_\pm^2} \equiv \Delta_\pm(q_1, q_2, p_1, p_2). \tag{26}$$

Formulas (25) determine two local first integrals in the domain of the phase space defined by the inequalities $a < q_1 < 4 - a$. Actually, these integrals are the constant amplitudes $a_\pm$. It is evident that $a_\pm$ must be functions of the first integrals I_1, I_2 and the structure parameters ε and a. It is easy to show that

$$\frac{1}{2}k_\pm^2 a_\pm^2 = \frac{\varepsilon}{1 - 4\varepsilon/(2-a)}((H+1)k_\mp^2 + I_2). \tag{27}$$

The proof is based on the comparison of expressions (25) with expressions (14), (15), and (11) with regard for the relations

$$\varepsilon(k_+^2 + k_-^2) = 1, \quad \varepsilon(k_+ k_-)^2 = \frac{1}{2-a},$$

$$\varepsilon k_\pm^4 = k_\pm^2 - \frac{1}{2-a}, \tag{28}$$

$$\varepsilon(k_+^2 - k_-^2) = \sqrt{1 - \frac{4\varepsilon}{2-a}}.$$

Note that

$$\frac{1}{2}k_+^2 a_+^2 + \frac{1}{2}k_-^2 a_-^2 = \frac{H + 1 + \varepsilon I_2}{1 - 4\varepsilon/(2-a)}. \tag{29}$$

For half-trajectories (20) and (21), the constants of the first integrals $I_1 = H$ and I_2 are zero. Since H is the global first integral, we have that $H = 0$ for the required trajectories in (27). The constant of the first integral I_2 is determined from the discontinuity conditions (14), which imply that $I_2 = -ak^2/(2 - a)$ on the internal interval $[a, 4 - a]$. Therefore, for the required trajectories, formulas (27) have the form

$$\frac{1}{2}k_\pm^2 a_\pm^2 = \frac{\varepsilon}{1 - 4\varepsilon/(2-a)}\left(k_\mp^2 - \frac{ak^2}{2-a}\right). \tag{30}$$

The sewing conditions for the solutions of the internal boundary value problem with the solutions with the external one imply, by (26), the four equations

$$\tan(\alpha_\pm) = \delta_\pm(\varepsilon, a), \quad \tan(k_\pm l + \alpha_\pm) = -\delta_\pm(\varepsilon, a), \tag{31}$$

where

$$\delta_\pm(\varepsilon, a) = k_\pm \frac{ak^2 - (2-a)k_\mp^2}{(k^2 + k_\mp^2)ka} = \Delta_\pm(q_1, q_2, p_1, p_2)\big|_{q_1 = a}. \tag{32}$$

Assuming that the phase variables can rotate on the length l, we write (31) in the form

$$\alpha_\pm = \arctan\delta_\pm(\varepsilon, a), \qquad \alpha_\pm + k_\pm l = -\arctan\delta_\pm(\varepsilon, a) + \pi m_\pm, \tag{33}$$

where $m_\pm$ are integers. Relations (33) constitute an overdetermined system of linear inhomogeneous equations in three unknowns ($\alpha_\pm$, l). It is consistent if

$$k_-\left(\arctan\delta_+(\varepsilon, a) - \frac{\pi}{2}m_+\right) = k_+\left(\arctan\delta_-(\varepsilon, a) - \frac{\pi}{2}m_-\right). \tag{34}$$

Under this condition, the internal boundary value problem is defined on the segment with the length l determined by the equation

$$(k_+ k_-)l = -k_-\left(\arctan\delta_+(\varepsilon, a) - \frac{\pi}{2}m_+\right) - k_+\left(\arctan\delta_-(\varepsilon, a) - \frac{\pi}{2}m_-\right). \tag{35}$$

Note that

$$k_-\alpha_+ - k_+\alpha_- = \frac{\pi}{2}(m_+ k_- - m_- k_+). \tag{36}$$

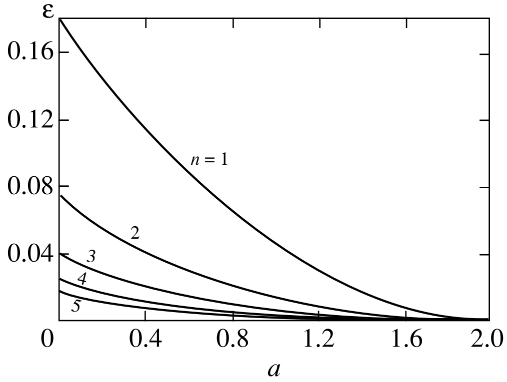

Fig. 2. The dependence of the eigenvalues ε on a for the first five modes.

Thus, the solution to the internal boundary value problem is written in the form

$$u(x) = 2 + a_+ \sin(k_+ x + \arctan\delta_+) \\ + a_- \sin(k_- x + \arctan\delta_-). \tag{37}$$

Moreover, the values of the parameters (ε, a) and the pairs of even integers must satisfy the consistency conditions (34) and the condition $l > 0$. The requirement that the integers must be even derives from the fact that the phase variables can rotate by an angle multiple of 2π.

Thus, in the model under consideration, the phase half-trajectories of the saddle singular points O_0 and O_4 are sewed with the segment of the trajectory that lies on the torus (due to the continuity of the phase trajectory) when reaching the surface of the torus with the parameters (a_+, a_-), (k_+, k_-). This is achieved at the expense of a finite discontinuity of the additional first integral. Such a simple and demonstrative interpretation of the internal structure of the topological soliton is possible only for nonsmooth (piecewise linear) dynamical systems. For the case of a smooth nonlinearity $f(u)$, the situation is more complex. It is not clear which forms of smooth nonlinearities $f(u)$ can lead to solutions of the type of a topological soliton with an internal structure and a given topological charge. This issue is discussed in more detail in [10] and the literature cited therein.

4. In this section, we cite the results of the numerical analysis of the problem on topological solitons (19). We used the boundary conditions at $x = 0$ as the initial conditions of the Cauchy problem; the integration was performed (for arbitrary values of the parameters ε and a) until the trajectory reached the plane of symmetry $u = 2$ for $u_{xx} = 0$. This means that the points corresponding to the flex points of the function $u(x;\, \varepsilon,\, a)$ were determined on the plane of symmetry. Then, the trajectory was extended up to $x = l$ using the symmetry of the problem.

For the values $a \in [0, 2]$, the point spectrum of the parameter $\varepsilon_n(a)$ and the corresponding eigenfunctions $u_n(x; a)$ were determined for $n = 1, 2, \ldots, 10$. The values $a \ll 1$, $a \sim 1$, and $a \sim 2$ were analyzed in more detail.

The variation of the point spectrum $\varepsilon_n(a)$ depending on the parameter a (the deformation of the nonlinearity $f(u, a)$) is presented in Fig. 2. As a increases, all eigenvalues $\varepsilon_n(a)$ decrease, and tend to the limit $\varepsilon = 0$ as $a \longrightarrow 2$.

From the viewpoint of the initial wave equation (1), the point spectrum $\varepsilon_n(a)$ of speeds

$$v_n = c\left(1 - \left(\frac{\ell}{\ell_0}\right)^2 \varepsilon_n^{-1/2}(a)\right)^{1/2} \tag{38}$$

of the family of topological solitons characterized by the eigenfunctions (modes) $u_n(x;\, \varepsilon_n,\, a)$ corresponds to the point spectrum ε $\varepsilon_n(a)$. For fixed values of the parameters ($\ell/\ell_0 < 1$, a), the speed of the solitons decreases as n increases (due to the decrease of $\varepsilon_n(a)$ with increasing n). Moreover, there exists a maximum

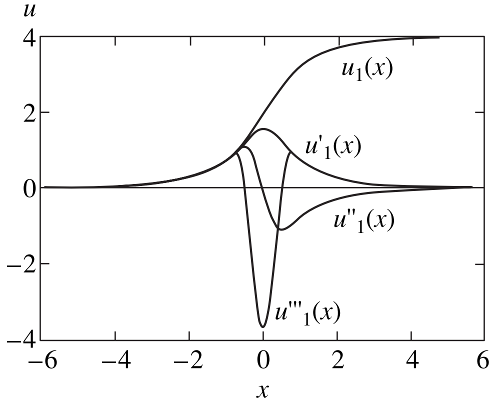

Fig. 3. The plots of the first eigenfunction $u_1(x)$ and its three derivatives u'_1, u''_1, and u'''_1 for $a = 1$. The eigenvalue is $\varepsilon = 0.047$.

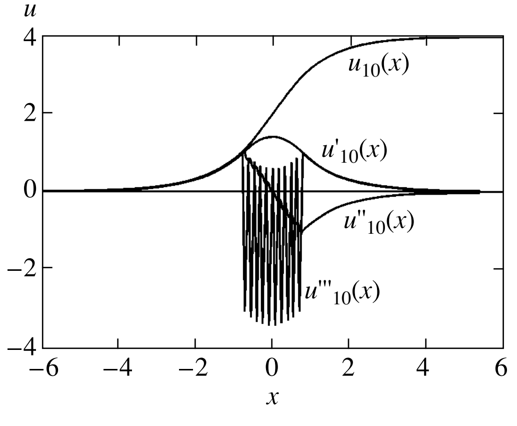

Fig. 4. The plots of the tenth eigenfunction $u_{10}(x)$ and its three derivatives u'_{10}, u''_{10}, and u'''_{10} for $a = 1$. The eigenvalue is $\varepsilon = 0.00062$.

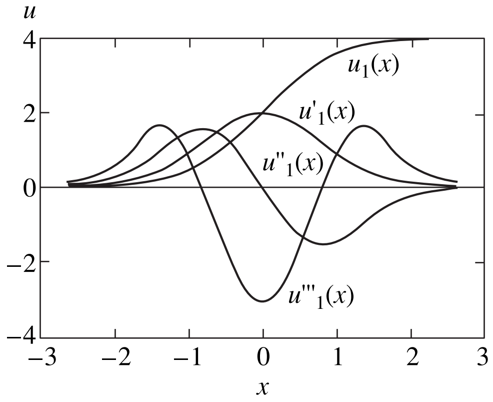

Fig. 5. The plots of the first eigenfunction $u_1(x)$ and its three derivatives u'_2, u''_2, and u'''_2 for $a = 0.1$. The eigenvalue is $\varepsilon = 0.160$.

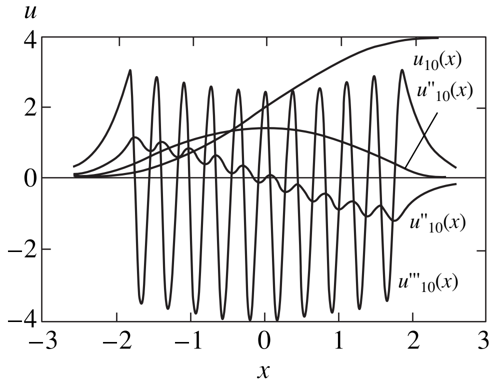

Fig. 6. The plots of the tenth eigenfunction $u_{10}(x)$ and its three derivatives u'_{10}, u''_{10}, and u'''_{10} for $a = 0.1$. The eigenvalue is $\varepsilon = 0.0034$.

value $n_c = n(\ell/\ell_0, a)$ that corresponds to the lower bound of the spectrum of speeds, which is, generally, not equal to zero. At a fixed value of the nonlocality parameter ℓ/ℓ_0, the increase of the parameter a results in the decrease of the speed of solitons and the number of modes. For every mode, there exists a critical value of the parameter $a_c = a_c(\ell/\ell_0, n)$; when this value is attained, the speed of the soliton becomes zero. It is evident that $a_c \sim 2$ for $\ell/\ell_0 \ll 1$.

For $a = 1$, the spectrum of the eigenvalues for $n > 1$ (which was determined numerically) is described by the formula $1/4\sqrt{\varepsilon_n} = n$ with a high degree of accuracy. This expression is obtained in the process of the analysis of solvability conditions of the problem in the limit $\varepsilon \ll 1$.

Figures 3 and 4 present the plots of the dependence of $u_n(x)$, $(u_n(x))x$, $(u_n(x))_{xx}$, and $(u_n(x))_{xxx}$ for $n = 1$ ($\varepsilon = 0.047$) and $n = 10$ ($\varepsilon_{10} = 0.00062$) for $a = 1$. The comparison of the plots shows that the eigenfunction and its derivative retain its superficially simple behavior when passing from the first mode to the tenth one; however, the second and the third derivatives of $u_1(x)$ and $u_{10}(x)$ are substantially different from each other. More precisely, when passing to higher modes, a more complex small-scale structure (in particular, high-frequency oscillations of the third derivative whose characteristic amplitude slightly varies when passing from lower modes to higher ones) appears almost on the same length.

Figures 5 and 6 present the plots of the dependence of $u_n(x)$, $(u_n(x))x$, $(u_n(x))_{xx}$, and $(u_n(x))_{xxx}$ for $n = 1$ ($\varepsilon_1 = 0.160$) and $n = 10$ ($\varepsilon_{10} = 0.0034$) for $a = 0.1$. The general tendency to forming a small-scale structure of the second and third derivatives of the eigenfunctions is retained when passing to higher modes. However, in the process, the increase of the oscillation amplitude of the third derivative is observed. Another difference can be seen when looking at the dependence of the first derivative of $(u_2(x))_x$ on x (see Fig. 7). It is characterized by three points of extremum. Such a behavior of $((u_2(x))_x$ is retained for the third mode and disappears only for higher modes.

When passing to the domain $a \lesssim 2$, the eigenfunction and its first derivative retain the characteristic size of the localization region and their superficially simple form. However, its second and third derivatives undergo sharp variations (of the type of a finite discontinuity for the second derivative and a deltalike spike for the third one) in a small neighborhood of $x = 0$. Figure 8 illustrates the behavior for the first eigenfunction ($a = 1.8$ and $\varepsilon = 0.001992$). It is not clear whether or not this behavior of the solutions in the domain $a \lesssim 2$ can be considered as an indication of the existence of solutions with discontinuities of higher derivatives.

In conclusion, we note that our simple model of the nonlocal Josephson electrodynamics in the problem on the topological soliton with the minimal topological

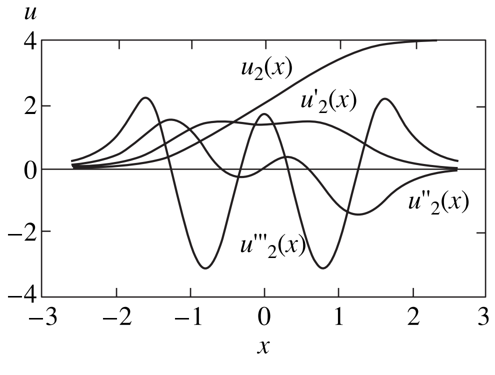

Fig. 7. The plots of the second eigenfunction $u_2(x)$ and its three derivatives u'_2, u''_2, and u'''_2 for $a = 0.1$. The eigenvalue is $\varepsilon = 0.063$.

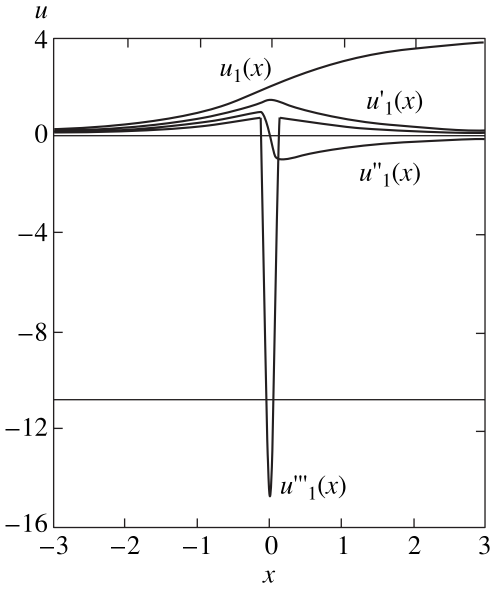

Fig. 8. The plots of the first eigenfunction $u_1(x)$ and its three derivatives s u'_1, u''_1, and u'''_1 for $a = 1.8$. The eigenvalue is $\varepsilon = 0.001992$.

charge (2π-kink) actually leads to a point spectrum of speeds and a peculiar internal structure of the soliton (vortex). However, it is important that one-parameter deformation of the piecewise linear function approximating the Josephson current generally leads to a corresponding deformation of the point spectrum of speeds and qualitatively the same internal structure of the soliton. However, it is not clear whether or not such a structural stability of the object of interest under study is retained under deformations of piecewise linear nonlinearities in more general models (for example, those that take account of higher spatial derivatives in the initial wave equation or nonlocal effects in the integral form).

ACKNOWLEDGMENTS

This work was supported in part by the Russian Foundation for Basic Research, project no. 99-01-00342.

REFERENCES

1. S. Aubry and P. J. L. Daeron, Physica D (Amsterdam) **7**, 240 (1983); S. Aubry, J. Phys. C **16**, 2497 (1983).
2. A. F. Volkov, Physica C (Amsterdam) **183**, 177 (1991); **192**, 306 (1992).
3. S. Sakai and H. Tateno, Jpn. J. Appl. Phys. **22**, 1374 (1983); S. Sakai and N. F. Pedersen, Phys. Rev. B **34**, 3506 (1986).
4. A. S. Malishevskiĭ, V. P. Silin, and S. A. Uryupin, Phys. Lett. A **253**, 333 (1999).
5. A. S. Malishevskiĭ, V. P. Silin, and S. A. Uryupin, Zh. Éksp. Teor. Fiz. **117**, 711 (2000) [JETP **90**, 671 (2000)].
6. V. P. Silin and A. V. Studenov, Zh. Éksp. Teor. Fiz. **117**, 1230 (2000) [JETP **90**, 1071 (2000)].
7. M. I. Rabinovich and D. I. Trubetskov, *An Introduction to the Theory of Oscillations and Waves* (Nauka, Moscow, 1984).
8. B. A. Dubrovin, A. T. Fomenko, and S. P. Novikov, *Modern Geometry—Methods and Applications* (Nauka, Moscow, 1979; Springer-Verlag, New York, 1984, 1985, 1990), Parts 1–3.
9. N. N. Bautin and E. A. Leontovich, *Methods and Techniques of Qualitative Investigation of Dynamic Systems on a Plane* (Nauka, Moscow, 1976); N. V. Butenin, Yu. I. Naĭmark, and N. A. Fufaev, *An Introduction to the Theory of Nonlinear Oscillations* (Nauka, Moscow, 1976).
10. G. L. Alfimov, V. M. Eleonsky, and L. M. Lerman, Chaos **8**, 257 (1998).

Translated by A. Klimontovich

Journal of Experimental and Theoretical Physics, Vol. 92, No. 5, 2001, pp. 851–857.
From Zhurnal Éksperimental'noĭ i Teoreticheskoĭ Fiziki, Vol. 119, No. 5, 2001, pp. 979–986.
Original English Text Copyright © 2001 by S. Vedeneev, Szabó, Jansen, I. Vedeneev.

SOLIDS
Electronic Properties

Tunneling in Single-Layer $Bi_2Sr_2CuO_{6+\delta}$ Single Crystals in High Magnetic Field[¶]

S. I. Vedeneev[a, b, *], P. Szabó[b, c], A. G. M. Jansen[b], and I. S. Vedeneev[a]

[a]Lebedev Physical Institute, Russian Academy of Sciences, Moscow, 117924 Russia
*e-mail: vedeneev@sci.lebedev.ru

[b]High Magnetic Field Laboratory, Max-Planck-Institut für Festkörperforschung/Centre National de la Recherche Scientifique, B. P. 166, F-38042 Grenoble Cedex 9, France

[c]Institute of Experimental Physics, Slovak Academy of Sciences, SK-04353 Košice, Slovakia

Received December 25, 2000

Abstract—In tunneling experiments with high-quality single crystals of a single-layer cuprate superconductor $Bi_2Sr_2CuO_{6+\delta}$ using the break junction and point-contact techniques at $T < T_c$, the coexistence of the superconducting-state gap and the normal-state gap was observed. The values of the superconducting energy gap $2\Delta_{p-p}$ are in the range from 13.4 to 15 meV (Δ_{p-p} = 6.7–7.5 meV). The values of $2\Delta_{p-p}$ are similar for two samples with T_c = 4 K and for two samples with T_c = 9–10 K and are independent of the carrier concentration. The normal-state gap, with the magnitude approximately equal to 50 meV, persists at $T < T_c$ and in the magnetic field $H \gg H_{c2}$ up to 28 T. After the transition of the sample to the normal state, the intensity of the tunneling conductance rapidly decreases with increasing magnetic field strength and temperature. The observed large broadening of the tunneling spectra and large zero-bias conductances can be caused by a strong angular dependence of the superconducting gap. The tunneling results are in full agreement with the data of the angle-resolved photoemission spectroscopy measurements. *© 2001 MAIK “Nauka/Interperiodica”.*

It is known that tunneling spectroscopy has been used successfully in studying the superconducting state in conventional superconductors. However, this method has encountered considerable difficulties in the case of high-temperature superconductors (HTSC) due to an extremely small coherence length ξ and high inhomogeneity of samples. At present, more reproducible results are only obtained for the bilayered cuprate $Bi_2Sr_2\,CaCu_2O_{8+\delta}$ (Bi2212). Previously [1, 2], we have performed an extensive tunneling study on high-quality Bi2212 single crystals using the break junction technique. Our experiments show that the presently available quality of Bi2212 samples enables fabricating good-quality tunnel junctions in the *ab*-plane with a low or almost zero leakage current and a well developed gap structure in the tunneling spectra. The angle-resolved photoemission spectroscopy (ARPES) measurements [3–6] confirmed the energy gap value found but, on the other hand, gave evidence of a strong angular dependence of the gap consistent with a four-lobed $d_{x^2-y^2}$ order parameter. In addition, many experiments (e.g., NMR [7], photoemission [5], and tunneling [8]) have provided evidence that in the normal state of the underdoped Bi2212, a pseudogap exists in the electronic excitation spectra at temperatures T^* above the superconducting transition temperature T_c. In scanning tunneling measurements on Bi2212, Renner *et al.* [8] have found this pseudogap to be present both in underdoped and overdoped samples, and to scale with the superconducting gap. It has been proposed that the pseudogap in the normal state can be seen as a precursor for the occurrence of superconductivity where the superconducting phase-coherence is suppressed by thermal or quantum fluctuations [9–11]. In the case of a nonsuperconducting origin, the pseudogap can be formed in the spin part of the excitation spectrum.

The situation for the low-T_c single-layer cuprate superconductor $Bi_2Sr_2CuO_{6+\delta}$ (Bi2201) is more complicated. The first point contact tunneling measurements of the superconducting energy gap in imperfect Bi2201 crystals were performed long ago [12]; up to now, however, it has been impossible to fabricate a high-quality tunnel junction using the break junction method. Because the coherence length ξ_{ab} in Bi2201 is larger than in Bi2212 and reaches 45 Å [13], it is very difficult to directly prepare a quality tunnel barrier in liquid helium. In ARPES experiments, Harris *et al.* [14] have observed highly anisotropic superconducting gaps of 10 ± 2 and 7 ± 3 meV in optimally doped and underdoped $Bi_2Sr_{2-x}La_xCuO_{6+\delta}$ (Bi,La2201), respectively. They have also found a pseudogap above T_c and assumed that these two energy gaps can have a common origin in the pairing interaction. However, on the basis of the experimental study of the *c* axis resistivity ρ_c in the normal state of nondoped Bi2201 single crystals under continuous high magnetic fields, we recently

---

[¶] This article was submitted by the authors in English.

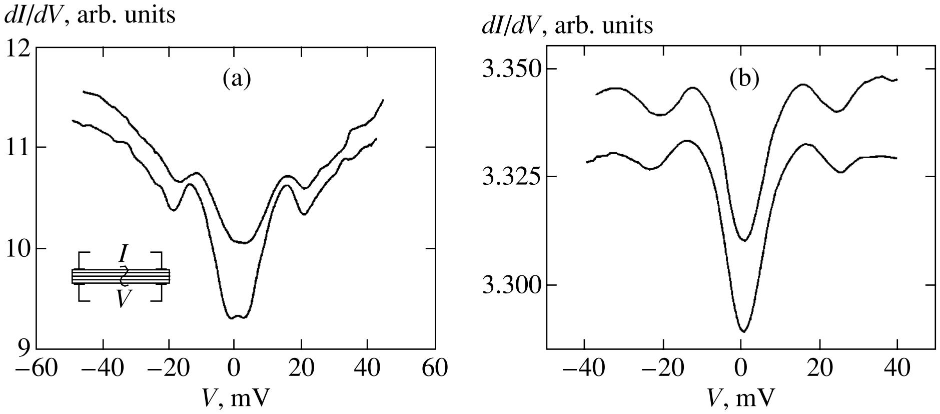

Fig. 1. Differential conductances dI/dV as functions of V for four break junctions at (a) $T = 2.6$ and (b) $T = 1.6$ K for Bi2201 single crystals (a) No. 1 and (b) No. 2 with $T_c = 3.5$ and 4 K, respectively. For clarity, the curves are shifted vertically with respect to the lower curves. The inset shows the geometry of the break junction.

concluded [15] that superconductivity is probably not at the origin of the pseudogap. The tunneling study of high-T_c superconductors in the normal state under high magnetic fields can give important information on the nature of the pseudogap.

In this paper, we describe the tunneling measurements for several high-quality $Bi_2Sr_2La_xCuO_{6+\delta}$ single crystals with midpoint $T_c = 3.5$–4 K (overdoped) and 9–10 K (near optimally doped) using the break junction and point-contact techniques under continuous magnetic fields H up to 28 T. A low T_c value for these crystals permits us to investigate the gap structures of a cuprate superconductor in the normal state down to low temperatures. In magnetic fields, we observed a different behavior of the superconducting and normal-state gaps. The previous results of the tunneling study using the break junction in lower magnetic fields were published in [16]. However, here we give a selection of these results because later magnetotransport measurements [13] allow us to understand an unusual behavior of differential conductances dI/dV in magnetic fields.

The Sr-deficient $Bi_{(2+x)}Sr_{2-(x+y)}Cu_{(1+y)}O_{6+\delta}$ single crystals with a Bi/Sr ratio of 1.4–1.5 for samples with $T_c = 9$–10 K and 1.7 for samples with $T_c = 3.5$–4 K (with the Bi excess localized at the Sr positions) were grown in a gaseous phase in closed cavities of the KCl solution–melt [17]. Because of a long growing time, the single crystals have a high cation ordering. The crystal sizes are around (0.5–2.5) mm × (0.4–2) mm × (1.5–5) μm. The half-widths of main reflections in the X-ray rocking curves for single crystals do not exceed 0.3–0.1°, which is the minimum value reported so far. The crystal lattice parameters are $a = 5.353$–5.385 Å and $c = 24.600$–24.638 Å, and the superlattice periodicity is $\tilde{a} = 4.75a$. The superconducting transition width defined by 10% and 90% of the superconducting transition points ranges from 0.5 to 1.5 K. The onset temperatures in the superconducting transition for the dc-resistance and ac-susceptibility are close, and the transition widths are almost the same. The in-plane resistivity ρ_{ab} of the crystals shows a linear temperature dependence at high temperatures and saturates to the residual resistivity below 20–40 K. The in-plane resistivity slope $\Delta\rho_{ab}/\Delta T = 0.5$–1.5 μΩ cm/K was obtained at high temperatures. The residual resistivity $\rho_{ab}(0)$ is between 80 and 180 μΩ cm. By measuring the normal-state Hall coefficient in our crystals in the temperature region of 4.2–50 K, we have found that the concentration of the carriers equals $n = (4.8$–$6.3) \times 10^{21}$ cm^{-3}. The carrier density in low-T_c samples was larger than in the samples with $T_c = 9$–10 K. It is believed [18] that single crystals of pure Bi-excess Bi2201 phase are always overdoped because Bi gives some intrinsic doping. This is reasonable if one considers the optimally La-doped Bi2201 polycrystal samples with the maximum value for Bi2201 $T_c \approx 25$ K and the carrier density $n \approx 3 \times 10^{21}$ cm^{-3} [18]. Our single crystals with $T_c = 3.5$–4 K must therefore be assigned to heavily overdoped ones. On the other hand [19], the carrier concentrations in the underdoped Bi,La2201 single crystals with $T_c = 13$ K are similar. Because the magnitude of T_c in nondoped Bi2201 single crystals approximately equals 13 K, the samples with $T_c = 9$–10 K studied here are most likely to be slightly underdoped or nearly optimally doped. The tunneling junctions were made *in situ* at 1.5 K by the superconductor–insulator–superconductor (SIS type) break junction [2] or the superconductor–insulator–normal metal (SIN type) tunnel point contact techniques [12], using a Cu needle as a counter electrode. The current–voltage (I–V) characteristics and derivatives dV/dI were measured by the usual phase-sensitive detection technique. The tunneling in the break junction geometry used in our experiments is supposed to probe the superconducting state in the *ab* plane [2].

The typical differential conductances dI/dV as functions of V for four break junctions at $T = 2.6$ and 1.6 K for two single crystals (Nos. 1 and 2) with $T_c = 3.5$ and 4 K are shown in Fig. 1. Although the measurements were carried out at low (≈0.2 kΩ, Fig. 1a) and moderately high (≈0.5 kΩ, Fig. 1b) resistances of the tunnel barrier, the spectra reveal a very large zero-bias conductance (80–90% of the conductance), the gap structure is strongly smeared and the conductance of the low-resistance junctions (Fig. 1a) has the V-shaped background. We have not observed anything similar in the tunneling experiments with Bi2212 single crystals [1, 2]. Recently, Mallet *et al.* [20] analyzed in detail the influence of different channels of a current leakage on the tunneling spectra of HTSC and suggested some correction procedure in order to extract the real tunneling density of states. However, in the given case, the zero-bias conductance is too large to be completely ascribed to the leakage current. In spite of numerous attempts, we could not obtain the curves of dI/dV versus V with the same clear gap structure and small zero-bias conductance as for Bi2212. Taking this circumstance into account, it seems that the large zero-bias conductance and strongly smeared gap structure in the tunneling spectra in Fig. 1 are more probably related to a high anisotropy of the superconducting gap in Bi2201 observed recently in ARPES experiments by Harris *et al.* [14]. In the underdoped Bi,La2201 single crystals, they observed not a sharp gap, but a reproducible gap of 7 ± 3 meV along the $(\pi, 0)$ symmetry line of the **k**-space and a zero gap at 45°. For the SIS junctions studied here, the peak-to-peak distance between the two main maxima on the dI/dV curves must correspond to $4\Delta_{p-p}$. As can be seen in Fig. 1, the value of the superconducting energy gap $2\Delta_{p-p}$ is in the range of 13.4–15 meV (with Δ_{p-p} = 6.7–7.5 meV). The break junction method is a technique that probes the tunneling density of states integrated over the polar angle in the k_{ab}-space. The strong angular dependence of the energy gap with zero value in some directions must result in a high density of states inside the gap [20] (large zero-bias conductance in tunneling spectra) and to a strongly smeared gap structure corresponding to the upper limit of Δ_{p-p}. This is in full agreement with the APRES measurements [14]. Both our tunneling spectra and APRES spectra have a broad gap structure that is difficult to describe within a simple BCS model. We have used only the phenomenological parameter Γ to take the pair breaking effects into account [21] and obtained an energy gap of 3.5–4 meV that is very close to that measured by us in the point-contact tunneling experiments on Bi2201 [12].

To prove a relation between the energy gap and T_c, we have measured the tunneling conductances dI/dV at different temperatures shown in Fig. 2. It can be seen that the gap structure (marked by arrows) broadens and diminishes as the temperature increases with a small decrease in the feature position. Because T_c = 4 K for the given sample and the gap structure disappears at T near T_c, we can assume that the observed energy gap is definitely the superconducting state gap of Bi2201. Because the gap structure is smeared out and the zero-bias conductance is high, it is impossible to investigate the temperature dependence of the superconducting gap in detail.

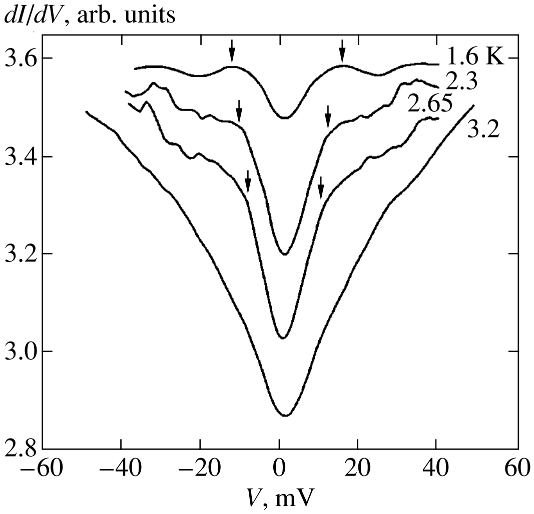

Fig. 2. Tunneling conductances dI/dV versus V at different temperatures for sample No. 2. The curves are shifted with respect to the upper one. The gap structure is marked by arrows.

The tunneling spectrum of the superconductor outside the gap for high-ohmic junctions with a good tunneling barrier is known to be flat [22] because this is expected for a Fermi liquid. The V-shaped form of the conductance for the low-resistance junctions comes from the bias voltage-induced barrier decreasing. However, the results in Fig. 2 show that the form of the background changes from flat to V-shaped with increasing temperature. Moreover, the V-shaped background conductance increases remarkably with increasing temperature. One of the reasons for the observed change can be a temperature-induced barrier damping or the temperature dependence of the coherence length ξ. Near T_c, ξ is large and the measured tunneling density of states is determined not only by the CuO_2 planes but also by the nonmetallic Bi–O layers. To exclude the influence of the temperature-induced barrier transparency change, we have measured the tunneling spectra of the break junction in magnetic fields above the upper critical field H_{c2} at a given temperature in the geometry when **H** is parallel to the c axis.

The effect of the magnetic field on the tunneling conductance dI/dV at T = 1.4 K is shown in Fig. 3. As can be seen, the behavior of the Bi2201 break junction in the magnetic field sharply differs from that for Bi2212 [1, 2]. First, the magnitude of the tunnel-junction conductance decreases with increasing magnetic field and the curves of dI/dV versus V significantly shift down, thereby decreasing the zero-bias conductance. Second, in the magnetotransport experiments [13] carried out after the tunneling measurements [16], we have found that the ab-plane H_{c2} in our low-T_c Bi2201 single crystals equals 10 T at T = 1.4 K, but the gap structure in

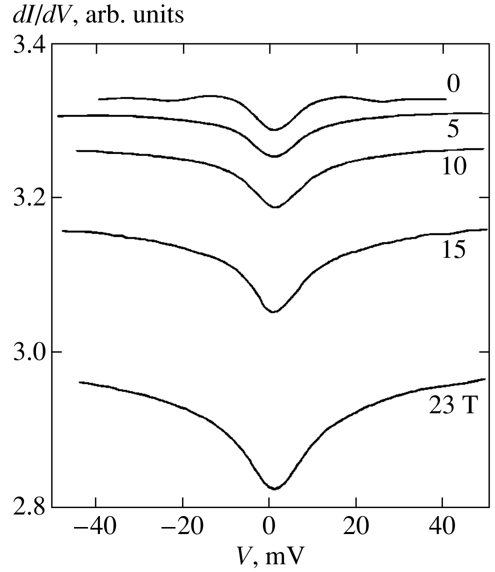

Fig. 3. The effect of the magnetic field on tunneling conductances dI/dV as functions of V at $T = 1.4$ K (**H** is parallel to the c-axis), sample No. 2.

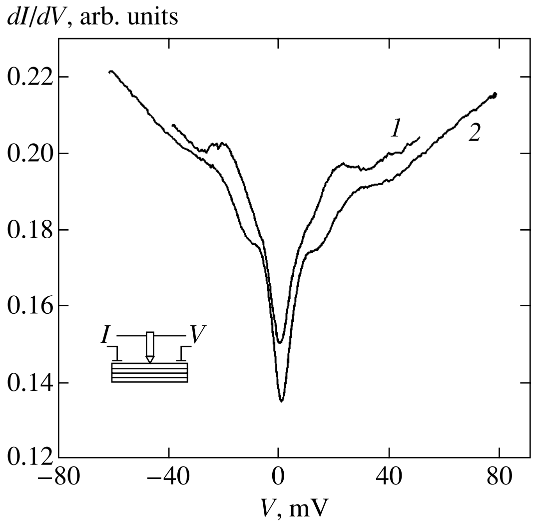

Fig. 4. Differential conductances dI/dV versus V for Bi2201-Cu tunnel point contacts fabricated on single crystals No. 24 (curve *1*) and No. 44 (curve *2*) with $T_c = 9$ and 10 K, respectively ($T = 1.6$ K, $H = 0$, $R_t = 0.6$ kΩ). The inset schematically shows the geometry of the point contact.

Fig. 3 practically disappears already at 5 T. As was mentioned above, the tunnel current probes a region of the order of the coherence length. For the break junction in the mixed state, the conductance dI/dV corresponds to the tunneling density of states for an isolated vortex with a normal core and the superconducting density of states near the vortex is broadened by the pair-breaking effect of the local magnetic field. Thus, the superconducting gap structure can be already smeared at $H \ll H_{c2}$. We note that the barrier transparency at constant temperature remains unchanged and the general form of tunneling conductances is preserved. In the tunneling measurements of the conventional superconductors in magnetic fields $H > H_{c2}$, the differential conductance dI/dV is constant at eV from zero to Δ. In the present case, a large dip around $V = 0$, seen in Fig. 3, indicates the existence of an energy gap in high magnetic fields up to 23 T. Although the spectra are so broad that it is difficult to define the gap value exactly, we can say that this gap persists even in the normal state at $H \gg H_{c2}$. At the same time, we found that the V-dependences of the differential resistance dV/dI at two points with $V = 0$ and 40 mV extracted from Fig. 3 are quadratic in the magnetic field in a wide range of fields without the saturation occurring for the classical magnetoresistivity of a normal metal in the transverse configuration. The data in Fig. 3 point out that, due to a large anisotropy of the resistance of Bi2201 single crystals ($\rho_c/\rho_{ab} \sim 10^3$–$10^4$ [13]), the measurement current in the break junction geometry flows in a very thin layer of the sample. In high magnetic fields, the resistance of this near-barrier region can be of the order of or larger than the resistance R_t of the tunneling barrier. In this case, the break junction is not quite a four-probe junction, and the applied voltage drops partially across the bulk of the crystal and not only across the tunneling barrier, especially at low temperatures, where the nonmetallic resistance along the c axis becomes very large.

To partially exclude the influence of the crystal resistance on the measured tunneling spectra, we have studied the point-contact tunnel junctions in which the four-probe contact method can be better realized. The tip of a copper wire needle was pressed perpendicularly to the crystal surface (parallel to the c axis). The magnetic field was also oriented parallel to the c axis. The point-contact tunnel junctions use the natural oxide layer on the contact-forming electrodes as a tunneling barrier. In our experiments, the point contacts revealed a high resistance after the first touch in liquid helium at 1.5 K; the background conductance only increased with increasing bias voltage. After a further increase of the pressure applied to the tip, a gaplike structure appeared in the I–V characteristics of the contacts.

The differential conductances dI/dV of the Bi2201-Cu tunnel point contacts fabricated on two single crystals, Nos. 24 and 44, with $T_c = 9$ and 10 K, respectively, are shown in Fig. 4. The tunneling barrier resistance R_t for these contacts at $T = 1.6$ K is equal to about 0.6 kΩ. The gap structure on the characteristics of the SIN-type tunnel junctions is always smeared larger than in the case of SIS-type junctions. Nevertheless, the zero-bias conductance for our point-contact tunnel junctions was less than for the break junctions. Two pairs of symmetric features on the curves plotted in Fig. 4 can be easily seen, and we believe we have observed two energy gaps. The peak-to-peak distances between the symmetric maxima on the curves of dI/dV versus V lie in the range of 15–18 and 45–50 mV. The magnitude of the first gap is in close agreement with data in Fig. 1, although the T_c value of the given crystal is nearly twice as that of crystal No. 2 in Fig. 1. The second pair of gap features in the SIS break junctions in case of a true gap must be located near 100 mV ($4\Delta_{p-p}$), which we did not study for break junctions.

In Fig. 5, we have plotted the differential conductances dI/dV for the Bi2201–Cu tunnel point contact at different temperatures. It can be seen that the gap structure again broadens and rapidly vanishes with increasing temperature. At low temperatures away from T_c, the tunneling barrier transparency does not change because the conductance spectra shapes are preserved. However, starting from $T \geq 5$ K, the V-shaped background conductance is slightly enhanced with increasing temperature, the differential conductances at zero bias $V = 0$ change, and the curves shift down. Since $T_c = 9$ K for the given sample (No. 24), the gap structure is believed to vanish at $T < T_c$, but this is not the case. Inset *a* in Fig. 5 shows I–V characteristics of the low-resistance (<0.1 Ω) tunnel break junction fabricated from the same single crystal where the superconducting energy gap is well seen at 6 K. In inset *b* in Fig. 5, we have plotted the temperature dependence of the differential resistance dV/dI at $V = 0$ extracted from the experimental data in combination with the *ab*-plane superconducting transition curve of the given single crystal. It is easy to verify that the crystal resistance rise and the shift of the dI/dV curves in Fig. 5 with increasing temperature are caused by the superconducting transition of the Bi2201 crystal region near the tunneling barrier as before even if $R_t \approx 0.6$ kΩ. The tunneling conductance behavior at temperatures near and above T_c for the point contacts (Fig. 5) is identical to that for break junctions (Fig. 2).

The effect of the magnetic field on the gap structure at $T = 1.6$ K is illustrated in Fig. 6, where we show the differential conductances dI/dV for the Bi2201–Cu tunnel point contact at different fields oriented along the crystal *c* axis ($R_t \approx 0.6$ kΩ). In moderate magnetic fields (up to 6 T), the dI/dV curves did not shift with respect to each other; for clarity, the curves in Fig. 6 have been shifted vertically by the same value with respect to the $H = 0$ curve. As earlier, the gap features broaden and practically diminish already at 4 T, although the respective values of T_c and *ab*-plane H_{c2} at 1.6 K are equal to 10 K and 22 T for crystal No. 44. In the point junction region of the crystal, additional pinning centers are produced by the pressure between the contact-forming electrodes. In this case, the tunneling conductance dI/dV mainly conforms to the density of states in the normal vortex cores near the contact already at $H > H_{c1}$. As is illustrated by the inset in Fig. 6, the *ab*-plane resistance of the same Bi2201 crystal in magnetic field 4 T still equals zero, but the gap structure is hardly visible.

A steady value and the general shape of the conductance spectra in the magnetic field up to 6 T made it possible to normalize the last dI/dV curves at $H = 0$–5 T by the conductance at $H = 6$ T, where the gap structure is no longer visible, in order to see the magnetic field influence on the gap features more clearly. In the normalized conductances, the gap structure broadens and diminishes gradually at increasing fields with a decrease in peak positions. The peak-to-peak distance between the two main maxima of the dI/dV curve at $H = 0$ is equal to 14.8 mV ($\Delta_{p-p} = 7.4$ meV). As noted above, this value

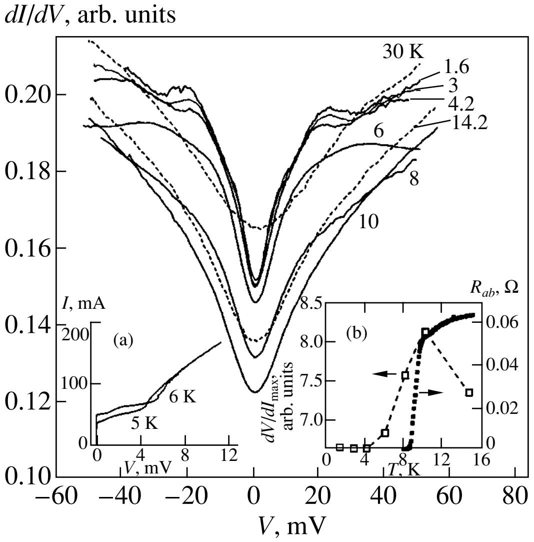

Fig. 5. Differential conductances dI/dV as functions of V for Bi2201–Cu tunnel point contacts at different temperatures (sample No. 24, $H = 0$). Inset *a* shows the I–V characteristics of the tunnel break junction with a very low resistance (< 0.1 Ω) fabricated from the same single crystal where the superconducting energy gap is well seen at 6 K. In inset *b*, we have plotted the temperature dependence of the differential resistance dI/dV at $V = 0$ extracted from the experimental data in combination with the *ab*-plane superconducting transition curve of the given single crystal.

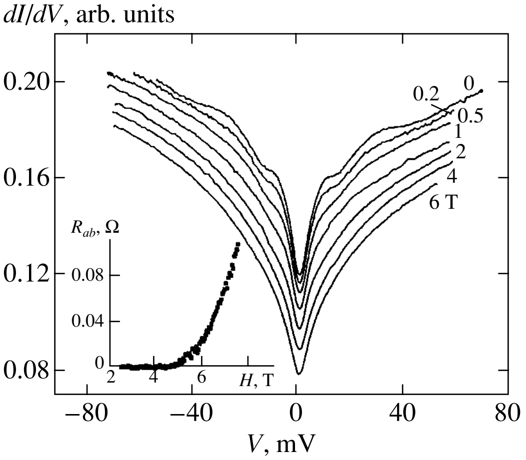

Fig. 6. Differential conductances dI/dV as functions of V for the Bi2201–Cu tunnel point contacts at $T = 1.6$ K and for different values of the field oriented along the *c*-axis of the crystal (No. 44). The curves are shifted vertically by the same value with respect to the $H = 0$ curve. The inset shows the *ab*-plane resistance of the same Bi2201 crystal.

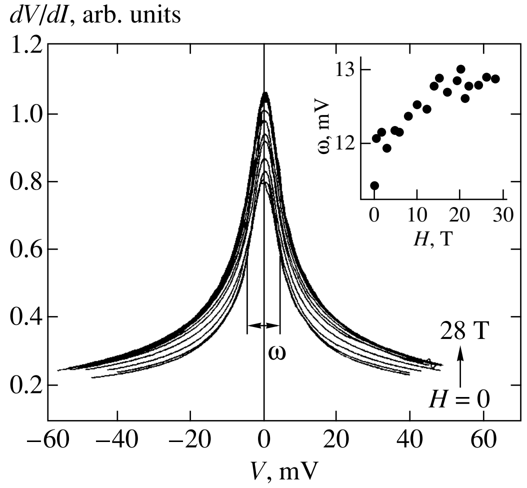

Fig. 7. Differential resistances dI/dV as functions of V for Bi2201–Cu contacts at 1.6 K in different magnetic fields (sample No. 44, $R_t = 4.5$ kΩ, $T = 1.6$ K), H is parallel to the c-axis. A variation of the half-width of the gap versus magnetic field is shown in the inset.

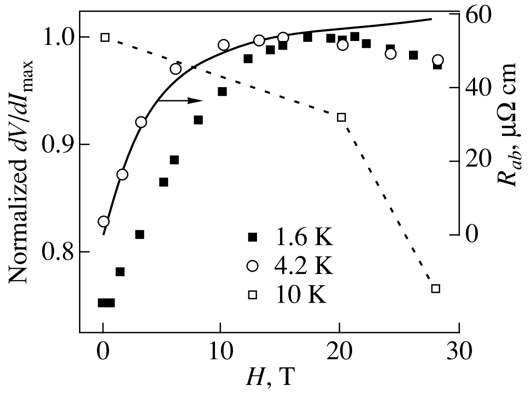

Fig. 8. The magnetic field dependences of the zero-bias differential resistances dI/dV at temperatures 1.6 K (full squares), 4.2 K (circles), and 10 K (open squares) normalized to the respective maximum values. The solid line shows the ab-plane superconducting transition of the same crystal in the magnetic field at 4.2 K.

is coincident with that measured by the break junction technique. It is surprising that the magnitude of $2\Delta_{p-p}$ is similar for two samples with $T_c = 4$ K and two samples with $T_c = 9$–10 K and is independent of the carrier concentration. So far as our normalization is not quite correct, it is difficult to give a quantitative analysis of the magnetic field effect on the gap value. However, the shift in the position of the features in the normalized conductance in Fig. 6 reflects the reduction of the order parameter in the point-contact region in the magnetic field. It is reasonable to expect that there are additional pinning centers in the point junction region of the crystal, and hence, the number of fixed vortices rapidly increases with the magnetic field. This leads to a fast suppression of the order parameter and the closing of the superconducting energy gap in the magnetic field $H \ll H_{c2}$.

The second pair of maxima in the upper part of the dI/dV curves in Figs. 4–6 is related to the large dip around zero voltage, the main shape of which does not vary with the magnetic field and temperature. The peak-to-peak distance between the second maxima in zero field is approximately equal to 52 mV. As the main maxima, these maxima broaden with increasing magnetic field, but the shift in the position of peaks in the normalized conductances is only slight. This gap does not close above T_c and H_{c2}, as indicated by Figs. 3 and 5, and can be identified with the normal-state gap of Bi2201 observed in ARPES experiments by Harries *et al.* [14]. Because this gap occurring in the tunneling spectra is so broad and the zero-bias conductance is so large, there is a nonzero state density at the Fermi energy, i.e., the true gap does not exist [5]. Our point-contact tunneling spectra at low temperatures and zero magnetic field can be presumably described by a representative background, two broad peaks near the energies ±25 meV, and sharper peaks at the energies ±7.4 meV, as was done in ARPES experiments with Bi2212 [6].

Next, we studied the magnetic field dependence of the normal-state gap in more detail using a sufficiently high-Ohmic point-contact tunnel junction with $R_t = 4.5$ kΩ. Such large resistance makes the observation of the superconducting gap difficult but ensures only a negligible effect of the crystal magnetoresistance on the main shape of the tunneling spectra. Figure 7 shows the series of the differential resistances dV/dI as functions of V for this Bi2201–Cu contact at 1.6 K in different magnetic fields. It can be seen that the shape of the tunneling spectra does not vary with the magnetic field and the data provide clear evidence that the normal-state gap still exists up to 28 T. A variation of the half-width of the gap versus magnetic field is shown in the inset in Fig. 7. In Fig. 8, we have plotted the magnetic field dependences of the zero-bias differential resistances dV/dI at $T = 1.6$ K, 4.2 K, and 10 K normalized to the corresponding maximum values. Here, we also show the ab-plane superconducting transition of the same crystal in the magnetic field at 4.2 K (solid line). From Fig. 8 and the inset in Fig. 7, it is clear that the transition of the sample to the normal state is responsible for a small increase in the gap half-width and the enhancement of the differential resistance at $V = 0$. However, after the transition of the sample to the normal state, the intensity of the dV/dI curves (the dip amplitude in tunneling conductance) starts to decrease rapidly with the magnetic field. Furthermore, we note that the intensity of the tunneling spectra at $V = 0$ also undergoes a rapid decline at $T > T_c$. This is in contrast with heavily underdoped Bi2212 samples with $T_c = 10$ K [5], where the large normal-state gap does not close even at 301 K. Our last result agrees well with the data of ARPES measurements of optimally doped Bi2212 [6].

It is probable that the normal-state gap observed in tunneling experiments is the pseudogap that has been widely discussed recently. It is worth mentioning that many tunneling conductances with a similar shape and a large dip in the vicinity of the zero-bias voltage have been observed in the metal–insulator–semiconductor tunnel junctions [23]. In particular, the conductance peaks and a large dip on the tunneling spectra of the Bi alloy junction [24] were attributed to the energy gap and to the band bending near the surface due to the applied voltage, respectively. It is interesting that with an increasing magnetic field, the conductance peaks tend to be washed away, whereas the dip due to the energy gap is deepened. Therefore, it is quite possible that a normal gap in BiO layers manifests itself in our measurements as the large dip near the zero-bias voltage.

To summarize, in the tunneling experiments with high-quality single crystals of single-plane Bi2201 cuprate superconductor using the break junction and point-contact techniques at $T < T_c$, we observed the coexistence of the superconducting-state gap and the normal-state gap. The value of the superconducting energy gap $2\Delta_{p-p}$ is in the (13.4–15)-meV range (Δ_{p-p} = 6.7–7.5 meV). The values of $2\Delta_{p-p}$ are similar for two samples with $T_c = 4$ K and two samples with T_c = 9–10 K and are independent of the carrier concentration. At $T < T_c$, the normal-state gap with the magnitude approximately equal to 50 meV persists in the magnetic field $H \gg H_{c2}$ up to 28 T. However, after the transition of the sample to the normal state, the intensity of the dV/dI versus V curves (the dip amplitude in the tunneling conductance) starts to decrease rapidly with the increasing magnetic field and temperature. The observed large broadening of the tunneling spectra and large zero-bias conductances can be caused by a strong angular dependence of the superconducting gap. The tunnel results are in full agreement with the angle-resolved photoemission spectroscopy measurements [14].

ACKNOWLEDGMENTS

One of the authors (S.I.V.) was partially supported by the Russian Ministry of Science and Technical Policy under the Program for Actual Problems in Condensed Matter Physics (grant no. 96001) and by the Russian Foundation for Basic Research (project no. 99-02-17877).

REFERENCES

1. S. I. Vedeneev, K. A. Kuznetsov, V. A. Stepanov, *et al.*, Pis’ma Zh. Éksp. Teor. Fiz. **57**, 338 (1993) [JETP Lett. **57**, 352 (1993)].
2. S. I. Vedeneev, A. G. M. Jansen, P. Samuely, *et al.*, Phys. Rev. B **49**, 9823 (1994).
3. J. M. Harris, Z.-X. Shen, P. J. White, *et al.*, Phys. Rev. B **54**, 15665 (1996).
4. D. S. Marshall, D. S. Dessan, A. G. Loeser, *et al.*, Phys. Rev. Lett. **76**, 4841 (1996).
5. H. Ding, T. Yokoya, J. C. Campuzano, *et al.*, Nature (London) **382**, 51 (1996).
6. A. V. Fedorov, T. Valla, P. D. Johnson, *et al.*, Phys. Rev. Lett. **82**, 2179 (1999).
7. C. Berthier, M.-H. Julien, O. Bakharev, *et al.*, Physica C (Amsterdam) **282-287**, 227 (1997).
8. Ch. Renner, B. Revaz, J.-Y. Genoud, *et al.*, Phys. Rev. Lett. **80**, 149 (1998).
9. V. Emery and S. A. Kivelson, Nature (London) **374**, 434 (1995).
10. T. Hotta, M. Mayr, and E. Dagotto, Phys. Rev. B **60**, 13085 (1999).
11. J. Maly, B. Jankó, and K. Levin, Phys. Rev. B **59**, 1354 (1999).
12. S. I. Vedeneev, P. Samuely, A. G. M. Jansen, *et al.*, Z. Phys. B: Condens. Matter **83**, 343 (1991).
13. S. I. Vedeneev, A. G. M. Jansen, E. Haanappel, *et al.*, Phys. Rev. B **60**, 12467 (1999).
14. J. M. Harris, P. J. White, Z.-X. Shen, *et al.*, Phys. Rev. Lett. **79**, 143 (1997).
15. S. I. Vedeneev, A. G. M. Jansen, and P. Wyder, Phys. Rev. B **62**, 5997 (2000).
16. S. I. Vedeneev, Pis’ma Zh. Eksp. Teor. Fiz. **68**, 217 (1998) [JETP Lett. **68**, 230 (1998)].
17. V. P. Martovitsky, J. I. Gorina, and G. A. Kaljuzhnaia, Solid State Commun. **96**, 893 (1995); J. I. Gorina, G. A. Kaljuzhnaia, V. P. Martovitsky, *et al.*, Solid State Commun. **108**, 275 (1998).
18. A. Maeda, M. Hase, I. Tsukada, *et al.*, Phys. Rev. B **41**, 6418 (1990).
19. Y. Ando, G. S. Boebinger, A. Passner, *et al.*, Phys. Rev. B **56**, 8530 (1997).
20. P. Mallet, D. Roditchev, W. Sacks, *et al.*, Phys. Rev. B **54**, 13324 (1996).
21. R. C. Dynes, V. Narayanamurti, and J. P. Garno, Phys. Rev. Lett. **41**, 1509 (1978).
22. K. Kitazawa, Science **271**, 313 (1996).
23. E. L. Wolf, *Principles of Electron Tunneling Spectroscopy* (Oxford Univ. Press, New York, 1985; Naukova Dumka, Kiev, 1990).
24. L. Esaki and P. J. Stiles, Phys. Rev. Lett. **16**, 574 (1966).

Journal of Experimental and Theoretical Physics, Vol. 92, No. 5, 2001, pp. 858–865.
From Zhurnal Éksperimental'noĭ i Teoreticheskoĭ Fiziki, Vol. 119, No. 5, 2001, pp. 987–994.
Original English Text Copyright © 2001 by Ovchinnikov.

SOLIDS
Electronic Properties

The Instability Point H_s of the Meissner State for Large-κ Superconductors[¶]

Yu. N. Ovchinnikov
Centre de Recherches sur les Tres Basses Temperatures, associe a l'UIF, CNRS BP166, 38042 Grenoble-Cedex 9, France
Landau Institute for Theoretical Physics, Russian Academy of Sciences, Moscow, 117940 Russia
e-mail: ovchin@labs.polycnrs_gre.fr

Received January 8, 2001

Abstract—The critical field H_s corresponding to the emergence of vortices in a superconductor without a threshold is found near the transition temperature and in the limit as $T \longrightarrow 0$ for an arbitrary value of the depairing factor Γ. In superconductors of the second kind, this field value coincides with the absolute instability point of the Meissner state. In large-κ superconductors, the order parameter tends to zero on the surface of the superconductor if the external magnetic field reaches the value H_s. We obtain that $H_s = H_{cm}$ (where H_{cm} is the thermodynamic critical field) for an arbitrary value of the depairing factor Γ in the temperature region near T_c and at $T = 0$. *© 2001 MAIK "Nauka/Interperiodica".*

1. INTRODUCTION

In superconductors with a large value of the Ginzburg–Landau parameter κ, the critical magnetic fields H_{c1}, H_{cm}, H_{c2} are widely separated by their κ-values [1, 2]. Here, H_{c1} is the magnetic field value for the transition to the Shubnikov phase (vortex state), H_{cm} is the thermodynamic critical field, and H_{c2} is the bifurcation point corresponding to the formation of a vortex state in the volume of the superconductor. If $\kappa = 1$, all three magnetic field values coincide. An isolated vortex is attracted to the boundary of a superconductor if the external magnetic field is weaker than a certain critical value H_s, the field of a barrierless penetration of vortices into the superconductor [3]. Near the transition temperature T_c, the problem of entering a vortex into the superconductor was considered by de Gennes [3]. He estimated that H_s is of the same order as the thermodynamic critical field H_{cm}. The exact value has not been found, because this requires considering small distances of the order of the correlation length. The value of the critical field H_s can be found as the linear instability point of the Meissner state. This means that there exists a stage of the transformation of the linear instability to the formation of a single vortex.

From this standpoint, the problem of calculating the critical field H_s is closely related to the problem of determining the superheating field H_{sh}. The last problem was considered by Ginzburg [4]. In what follows, we show that both problems (the calculation of the critical field H_s in the $\kappa \gg 1$ limit and the calculation of the critical field H_{sh} in the $\kappa \ll 1$ limit) can be solved using a single method near the transition temperature T_c, where the Ginzburg–Landau equations are applicable. The linear instability problem is simpler than the calculation of the vortex energy and some results for the H_s value can be found outside the framework of the Ginzburg–Landau free energy. We also find H_s in the zero-temperature limit. We show that near T_c, we have $H_s = H_{cm}$ and $H_{sh} = H_{cm}/\sqrt{\kappa}$, with the κ value related to the original definition of κ_{GL} as $\kappa_{GL} = \kappa/\sqrt{2}$.

2. THE CRITICAL FIELD H_s NEAR THE TRANSITION TEMPERATURE

The Ginzburg–Landau equations valid near the transition temperature can be written as

$$\left\{-\tau - \frac{\pi D}{8T}\left(\frac{\partial}{\partial r} - 2ieA\right)^2 + \frac{7\zeta(3)|\Delta|^2}{8\pi^2 T^2}\right\}\Delta = 0,$$

$$j = -ie\frac{\pi\nu D}{4T}(\Delta^*\partial_-\Delta - \Delta\partial_+\Delta^*), \qquad (1)$$

$$\mathrm{rot}\,\mathrm{rot}A = 4\pi j$$

where

$$\tau = 1 - T/T_c, \quad \partial_\pm = \frac{\partial}{\partial r} \pm 2ieA,$$

D is the effective diffusion coefficient, A is the vector potential, $\zeta(x)$ is the Riemann zeta function, and $\nu =$

[¶]This article was submitted by the author in English.

1063-7761/01/9205-0858$21.00 © 2001 MAIK "Nauka/Interperiodica"

$mp/2\pi^2$ is the density of states on the Fermi surface. The value of D was found by Gor'kov [5] and is equal to

$$D = \frac{vl_{tr}}{3} \times \left\{1 + \frac{8T\tau_{tr}}{\pi}\left[\psi(1/2) - \psi\left(\frac{1}{2} + \frac{1}{4\pi T\tau_{tr}}\right)\right]\right\}, \tag{2}$$

where v is the Fermi velocity, τ_{tr} is the transport collision time, and $\psi(x)$ is the Euler psi-function.

We use the gauge where

$$A = (A(y), 0, 0), \quad H = (0, 0, -\partial A/\partial y). \tag{3}$$

In the extreme case of large κ, we can use the local relation between A and Δ,

$$\Delta^2 = \frac{8\pi^2T^2}{7\zeta(3)}\left[\tau - \frac{\pi De^2}{2T}A^2\right]. \tag{4}$$

As a result, we obtain only one equation for the vector potential A instead of system (1),

$$-\frac{\partial^2\tilde{A}}{\partial Y^2} + \frac{1}{\kappa^2}\tilde{A}\left[1 - \frac{1}{2}\tilde{A}^2\right] = 0, \qquad \tilde{H} = -\kappa\frac{\partial\tilde{A}}{\partial Y}. \tag{5}$$

In Eq. (5), we use the dimensionless variables

$$y = \xi Y, \quad A = H_{cm}\kappa\xi\tilde{A}(Y), \quad \xi = \sqrt{\frac{\pi D}{16T\tau}},$$

$$\lambda_L^2 = \frac{7\zeta(3)}{32\pi^4e^2\nu DT\tau}, \quad \kappa = \frac{\lambda_L}{\xi} = \sqrt{\frac{7\zeta(3)}{2\pi^5e^2\nu D^2}}, \tag{6}$$

$$\frac{H_{cm}^2}{8\pi} = \frac{4\pi^2T^2\nu\tau^2}{7\zeta(3)}, \quad H = H_{cm}\tilde{H}.$$

The definition of κ in Eq. (6) differs from the original definition of κ_{GL} by the factor $\sqrt{2}$:

$$\kappa_{GL} = \kappa/\sqrt{2}.$$

With this definition of κ, the boundary between superconductors of the first and the second kind is at $\kappa = 1$. For $\kappa = 1$, all the critical fields H_{c1}, H_{cm}, and H_{c2} coincide. The definitions of ξ and κ in Eq. (6) can be continued in a natural way for the entire temperature region [6, 7].

Equation (5) can be reduced to the first-order equation

$$\frac{\partial\tilde{A}}{\partial Y} = -\frac{1}{\kappa}\tilde{A}\sqrt{1 - \frac{1}{4}\tilde{A}^2}. \tag{7}$$

The solution of (7) is

$$\tilde{A} = \frac{4C\exp(-Y/\kappa)}{1 + C^2\exp(-2Y/\kappa)}, \qquad \left.\frac{\partial\tilde{A}}{\partial Y}\right|_{Y=0} = -\frac{4C}{\kappa}\frac{1 - C^2}{(1 + C^2)^2}, \tag{8}$$

where C is an arbitrary positive constant. The function

$$\tilde{A}_1 = \frac{\partial}{\partial C}\tilde{A} = \frac{4\exp(-Y/\kappa)[1 - C^2\exp(-2Y/\kappa)]}{[1 + C^2\exp(-2Y/\kappa)]^2} \tag{9}$$

is a solution of system (1) linearized near $\tilde{A}$ with Δ given by Eqs. (4) and (8). The function $\tilde{A}$ is the eigenfunction of this system of equations with zero eigenvalue if the boundary condition

$$\left.\frac{\partial\tilde{A}_1}{\partial Y}\right|_{Y=0} = 0 \tag{10}$$

is satisfied. Using Eqs. (8) and (10), we obtain the critical value of the coefficient C,

$$C^2 = 3 - 2\sqrt{2}. \tag{11}$$

Therefore, the Meissner state becomes absolutely unstable at the magnetic field value

$$H_s = H_{cm}. \tag{12}$$

This linear instability leads to the formation of vortices. Hence, there exists some stage of the transformation from the linear instability to the formation of vortices. This stage cannot be studied in the framework of the Ginzburg–Landau equations. The energy δE of the vortex antivortex pair at distances $2a$ such that $2a \ll \xi$ decreases very slowly with a, only as $1/\ln(\xi/2a)$ [8]. This energy was found as the minimum of the Ginzburg–Landau free energy for fixed positions of zeros of Δ and fixed vorticities (± 1) [8]. From this point of view, a single vortex enters the superconductor without a threshold only if the order parameter Δ is equal to zero at the boundary.

Using Eqs. (4), (8), and (11), it is easy to prove that the condition

$$\Delta|_{y=0} = 0$$

is satisfied in the case under consideration. Our conjecture is that this condition is the boundary condition for the problem of calculating the critical field H_s for $\kappa \gg 1$. It is satisfied in all the cases considered in what follows. We note that the critical field H_s is separated from the critical fields H_{c1} and H_{c2} by the large parameter κ. The critical field H_{c2} was introduced in [1] as

$$H_{c2} = \frac{4}{\pi eD}(T_c - T). \tag{13}$$

Therefore,

$$\frac{H_{c2}}{H_s} = \frac{H_{c2}}{H_{cm}} = \kappa. \tag{14}$$

The critical field H_{c1} was found in [2] as

$$\frac{H_{c1}}{H_{cm}} = \frac{\ln\kappa + 0.146}{\kappa}. \tag{15}$$

3. THE SUPERHEATING FIELD H_{sh} FOR $\kappa \ll 1$

The superheating field H_{sh} was found by Ginzburg [4]. In the range $\kappa \ll 1$, this problem can be solved analytically. In a superconductor with a small value of κ, the magnetic field is screened near the surface at the distances much smaller than the correlation length ξ. In the leading approximation, we then obtain

$$A(y) = A_0 \exp\left(-\sqrt{\frac{4\pi^2 e^2 \nu D}{T}\Delta^2(0)}y\right), \tag{16}$$

where $\Delta(0)$ is the order parameter on the surface of the superconductor. With the help of Eq. (16), we reduce the system of equations (1) to one equation for the order parameter Δ and to the effective boundary condition for this equation,

$$\begin{gathered}\left(-1 - 2\frac{\partial^2}{\partial\tilde{Y}^2} + \tilde{\Delta}^2\right)\tilde{\Delta} = 0, \\ \tilde{\Delta}^2 \frac{\partial\tilde{\Delta}}{\partial Y}\bigg|_{Y=0} = \frac{\tilde{H}^2\kappa}{8},\end{gathered} \tag{17}$$

where

$$\Delta = \left(\frac{8\pi^2 T^2 \tau}{7\zeta(3)}\right)^{1/2}\tilde{\Delta}$$

and the quantities ξ, κ, Y, and $\tilde{H}$ are defined in Eqs. (6). Equation (17) has the solution

$$\tilde{\Delta} = \frac{C\exp Y - 1}{1 + C\exp Y}, \quad \frac{\partial\tilde{\Delta}}{\partial Y}\bigg|_{Y=0} = \frac{2C}{(1+C)^2}, \tag{18}$$

where $C > 1$ is an arbitrary parameter related to the external magnetic field by Eq. (17). The function

$$\tilde{\Delta}_1 = \frac{\partial\tilde{\Delta}}{\partial C} = \frac{2\exp Y}{(1 + C\exp Y)^2} \tag{19}$$

is the solution of system (1) linearized near the function $\tilde{\Delta}$ given by Eq. (18).

This function becomes the eigenfunction of this system of equations with zero eigenvalue if the boundary condition

$$\left(\frac{\partial\tilde{\Delta}_1}{\partial Y} + 2\frac{\tilde{\Delta}_1}{\tilde{\Delta}}\frac{\partial\tilde{\Delta}}{\partial Y}\right)\bigg|_{Y=0} = 0 \tag{20}$$

is satisfied. With the help of Eqs. (18), (19), and (20), we obtain the critical value of the coefficient C as

$$C = 3 + 2\sqrt{2}. \tag{21}$$

The superheating field H_{sh} is therefore related to the field H_{cm} by the simple equation

$$\frac{H_{sh}}{H_{cm}} = \frac{1}{\sqrt{\kappa}} = \frac{2^{-1/4}}{\sqrt{\kappa_{GL}}}. \tag{22}$$

4. CRITICAL FIELD H_s: THE GENERAL ANALYSIS

The general strategy of calculating H_s is as follows. First, the expression for the current density j must be found as a function of the vector potential A and the order parameter Δ,

$$j = Q(A, \Delta)A. \tag{23}$$

Equation (23) is formal and the relation can be nonlocal. In Eq. (23), the order parameter Δ must be considered as a functional of the vector potential A. Next, we solve the Maxwell equation for A,

$$\begin{gathered}\frac{\partial^2 A}{\partial y^2} + 4\pi Q(A, \Delta)A = 0, \\ -\frac{\partial A}{\partial y} = H, \quad H(0) = H_{\text{ext}},\end{gathered} \tag{24}$$

where H_{ext} is the external magnetic field. Solutions of Eq. (24) form a one-parameter family. The value of $A(y)$ at the point $y = 0$ can be considered as this parameter, and hence, the function

$$A_1 = \frac{\partial A}{\partial A(0)} \tag{25}$$

is a solution of linearized equation (24). It is an eigenfunction of this equation if the boundary condition

$$\frac{\partial A_1}{\partial y}\bigg|_{y=0} = \frac{\partial^2 A}{\partial A(0)\partial y}\bigg|_{y=0} = 0 \tag{26}$$

is satisfied. Equation (26) determines the critical field H_s (if $\kappa > 1$). We apply this strategy in the extreme case where $\kappa \gg 1$ and in the case where the superconductor can be considered as “dirty” material. The system of equations for the Green functions α and β can then be taken in the form [9]

$$\alpha\Delta - \beta\omega + \frac{D}{2}\left(\alpha\partial_-^2\beta - \beta\frac{\partial^2\alpha}{\partial r^2}\right) = \alpha\beta\Gamma,$$

$$\Delta = 2\pi T|\lambda|\sum_{\omega>0}\beta(\omega), \quad \alpha^2 + |\beta|^2 = 1, \tag{27}$$

$$j = -ie\nu D 2\pi T\sum_{\omega>0}(\beta^*\partial_-\beta - \beta\partial_+\beta^*).$$

For $\kappa \gg 1$, the relation of the vector potential to the order parameter Δ is local in the leading approximation and α and β can be taken as real functions. In this case, the system of equations (27) can be essentially simplified to

$$\begin{gathered}\Delta\tan\varphi - \omega = \sin\varphi(\Gamma + 2e^2DA^2).\\ \Delta = 2\pi T|\lambda|\sum_{\omega>0}\cos\varphi,\\ j = -e^2\nu D 8\pi T\sum_{\omega>0}A\cos^2\varphi, \quad -\frac{\partial^2 A}{\partial y^2} = 4\pi j,\\ \alpha = \sin\varphi, \quad \beta = \cos\varphi,\end{gathered} \tag{28}$$

where $\Gamma = \tau_s^{-1}$, with τ_s being the electron spin flip scattering time.

In what follows, we restrict ourselves to the zero-temperature limit. There are two regions

$$\begin{gathered}\Delta > \Gamma + 2e^2DA,\\ \Delta < \Gamma + 2e^2DA.\end{gathered} \tag{29}$$

In the first region, we have

$$\begin{gathered}A = \sqrt{\frac{2}{\pi e^2 D}}\left(\Delta\ln\left(\frac{\pi T_c^0}{\gamma\Delta}\right) - \frac{\pi\Gamma}{4}\right)^{1/2},\\ \frac{\partial}{\partial y}\left(\Delta\ln\left(\frac{\pi T_c^0}{\gamma\Delta}\right) - \frac{\pi\Gamma}{4}\right)^{1/2} = -\Phi(\Delta),\end{gathered} \tag{30}$$

where γ is the Euler constant, $\ln\gamma = 0.577216\ldots$, and T_c^0 is the transition temperature for the superconductor without paramagnetic impurities,

$$\begin{gathered}\Phi(\Delta) = (4\pi^2e^2\nu D)^{1/2}\\ \times\left\{\frac{\Delta_\infty}{2}\left(\Delta_\infty - \frac{\pi\Gamma}{2}\right) + \Delta^2\left(\ln\left(\frac{\pi T_c^0}{\gamma\Delta}\right) - \frac{1}{2}\right)\right.\\ -\frac{8}{3\pi}\left[\Gamma\left(\Delta\ln\left(\frac{\pi T_c^0}{\gamma\Delta}\right) - \frac{\pi\Gamma}{4}\right)\right.\\ \left.\left.+\frac{2}{\pi}\left(\Delta\ln\left(\frac{\pi T_c^0}{\gamma\Delta}\right) - \frac{\pi\Gamma}{\Delta}\right)^2\right]\right\}^{1/2},\end{gathered} \tag{31}$$

where Δ_∞ is the value of the order parameter as $y \longrightarrow \infty$.

We define the quantity Y as the point where

$$\Delta(Y) = \Gamma + 2e^2DA^2(Y). \tag{32}$$

At this point, we have

$$\Delta(Y) = \frac{\pi T_c^0}{\gamma}\exp\left(-\frac{\pi}{4}\right). \tag{33}$$

In the region $y > Y$, the order parameter Δ is the solution of the equation

$$\int_{\Delta(Y)}^{\Delta}\frac{d\left(\Delta\ln\frac{\pi T_c^0}{\gamma\Delta} - \frac{\pi\Gamma}{4}\right)^{1/4}}{\Phi(\Delta)} = -(y - Y). \tag{34}$$

We now consider the region $y > Y$. In this region, the system of equations (30) for the order parameter Δ and the vector potential A is more complicated,

$$\begin{gathered}\Delta\ln\frac{\pi T_c^0}{\gamma((\Gamma + 2e^2DA^2) + ((\Gamma + 2e^2DA^2)^2 - \Delta^2)^{1/2})}\\ = \frac{\Gamma + 2e^2DA^2}{2}\left\{\arcsin\left(\frac{\Delta}{\Gamma + 2e^2DA^2}\right)\right.\\ \left.-\frac{\Delta}{\Gamma + 2e^2DA^2}\left(1 - \left(\frac{\Delta}{\Gamma + 2e^2DA^2}\right)^2\right)^{1/2}\right\},\\ -\frac{\partial^2 A}{\partial y^2} + 16\pi e^2\nu DA\left\{\Delta\arcsin\left(\frac{\Delta}{\Gamma + 2e^2DA^2}\right)\right.\\ -(\Gamma + 2e^2DA^2)\left[\frac{2}{3} - \left(\left(1 - \left(\frac{\Delta}{\Gamma + 2e^2DA^2}\right)^2\right)^{1/2}\right.\right.\\ \left.\left.\left.-\frac{1}{3}\left(1 - \left(\frac{\Delta}{\Gamma + 2e^2DA^2}\right)^2\right)^{3/2}\right)\right]\right\} = 0.\end{gathered} \tag{35}$$

For $y > Y$, we have obtained the first integral of the equation for A (see Eq. (34)). We now show how to obtain the first integral in the region $y < Y$. To simplify the calculations, we set $\Gamma = 0$ in what follows. We then obtain

$$\begin{gathered}\frac{H_{cm}^2}{8\pi} = \frac{\nu\Delta_\infty^2}{2}, \quad \Delta_\infty = \frac{\pi T_c^2}{\gamma},\\ \lambda_L^{-2} = 8\pi^2e^2\nu D\Delta_\infty.\end{gathered} \tag{36}$$

Equations (36) allow us to pass to the dimensionless variables

$$\begin{gathered}\Delta = \Delta_\infty\tilde{\Delta}, \quad y = \lambda_L\tilde{y}, \quad Y = \lambda_L\tilde{Y},\\ H = H_{cm}\tilde{H}, \quad A = H_{cm}\lambda_L\tilde{A}.\end{gathered} \tag{37}$$

Equations (35) and (37) imply

$$\ln\left(\frac{\pi}{\tilde{A}^2 + (\tilde{A}^4 - \pi^2\tilde{\Delta}^2)^{1/2}}\right) = \frac{\tilde{A}^2}{2\pi\tilde{\Delta}} \times \left\{\arcsin\left(\frac{\pi\tilde{\Delta}}{\tilde{A}^2}\right) - \frac{\pi\tilde{\Delta}}{\tilde{A}^2}\left(1 - \left(\frac{\pi\tilde{\Delta}}{\tilde{A}^2}\right)^2\right)^{1/2}\right\},$$

$$-\frac{\partial^2\tilde{A}}{\partial\tilde{y}^2} + \frac{2}{\pi}\tilde{A}\tilde{\Delta}\left\{\arcsin\left(\frac{\pi\tilde{\Delta}}{\tilde{A}^2}\right) - \frac{\tilde{A}^2}{\pi\tilde{\Delta}} \times \left[\frac{2}{3} - \left(\left(1 - \left(\frac{\pi\tilde{\Delta}}{\tilde{A}^2}\right)^2\right)^{1/2} - \frac{1}{3}\left(1 - \left(\frac{\pi\tilde{\Delta}}{\tilde{A}^2}\right)^2\right)^{3/2}\right)\right]\right\} = 0. \quad (38)$$

The problem of calculating the critical field H_s is thus reduced to solving system (38) on the interval $\{0, \tilde{Y}\}$ with the boundary conditions

$$\tilde{\Delta}(\tilde{Y}) = \exp(-\pi/4), \quad \tilde{A}(\tilde{Y}) = \sqrt{\pi}\exp(-\pi/8),$$
$$\left.\frac{\partial\tilde{A}}{\partial\tilde{y}}\right|_{\tilde{y} = \tilde{Y}} = -\left\{1 + \left(\frac{\pi}{2} - \frac{5}{3}\right)\exp\left(-\frac{\pi}{2}\right)\right\}^{1/2}. \quad (39)$$

We must find the point $\tilde{Y}_{cr}$ such that

$$\left.\frac{\partial^2\tilde{A}}{\partial\tilde{Y}\partial\tilde{y}}\right|_{\tilde{y} = 0,\ \tilde{Y} = \tilde{Y}_{cr}} = 0. \quad (40)$$

The value of the derivative $\partial\tilde{A}/\partial\tilde{y}$ at the point $\tilde{y} = 0$ gives the field H_s via

$$\frac{H_s}{H_{cm}} = -\left.\frac{\partial\tilde{A}}{\partial\tilde{y}}\right|_{\tilde{y} = 0,\ \tilde{Y} = \tilde{Y}_{cr}}. \quad (41)$$

To solve this problem, we set

$$Z = \frac{\pi\tilde{\Delta}}{\tilde{A}^2}. \quad (42)$$

The system of equations (38) implies

$$\tilde{A}^2 = \frac{\pi}{1 + \sqrt{1 - Z^2}} \times \exp\left[-\frac{1}{2Z}(\arcsin Z - Z\sqrt{1 - Z^2})\right], \quad (43)$$
$$\frac{\partial\tilde{A}}{\partial\tilde{y}} = -\left[1 + \left(\frac{\pi}{2} - \frac{5}{3}\right)\exp\left(-\frac{\pi}{2}\right) + \Phi_1(Z)\right]^{1/2},$$

where

$$\Phi_1(Z) = 2\int_Z^1 dZR(Z),$$

$$R(Z) = \frac{Z}{(1 + \sqrt{1 - Z^2})^2} \times \exp\left[-\frac{1}{Z}(\arcsin Z - Z\sqrt{1 - Z^2})\right] \quad (44)$$
$$\times \left[\frac{Z}{1 + \sqrt{1 - Z^2}} - \frac{1}{2Z^2}(\arcsin Z - Z\sqrt{1 - Z^2})\right]$$
$$\times \left\{\arcsin Z - \frac{1}{Z}\left[\frac{2}{3} - \left((1 - Z^2)^{1/2} - \frac{1}{3}(1 - Z^2)^{3/2}\right)\right]\right\}.$$

The second equation in (43) is in fact an equation for Z,

$$\frac{\partial Z}{\partial\tilde{y}} = \frac{2}{\sqrt{\pi}}(1 + \sqrt{1 - Z^2})^{1/2} \times \exp\left[\frac{1}{4Z}(\arcsin Z - Z\sqrt{1 - Z^2})\right]$$
$$\times \left[1 + \left(\frac{\pi}{2} - \frac{5}{3}\right)\exp\left(-\frac{\pi}{2}\right) + \Phi_1(Z)\right]^{1/2}\left\{\frac{Z}{1 + \sqrt{1 - Z^2}} - \frac{1}{2Z^2}(\arcsin Z - Z\sqrt{1 - Z^2})\right\}^{-1}. \quad (45)$$

Condition (40) implies that

$$\left.\frac{\partial Z}{\partial\tilde{Y}}\right|_{\tilde{y} = 0} = 0 \quad \text{or} \quad \left.\frac{\partial\Phi_1}{\partial Z}\right|_{\tilde{y} = 0} = 0. \quad (46)$$

The function Z is a monotonic function of $\tilde{y}$, and hence, the first equation in (46) cannot be satisfied. It follows from Eq. (44) and the second equation in (46) that

$$Z = 0 \quad (47)$$

at the critical point, and therefore,

$$\frac{H_s}{H_{cm}} = \left\{1 + \left(\frac{\pi}{2} - \frac{5}{3}\right)\exp\left(-\frac{\pi}{2}\right) + \Phi_1(0)\right\}^{1/2} = 1. \quad (48)$$

We note that the $T = 0$, the order parameter behaves as

$$\Delta(y) \propto y^{1/2} \quad (49)$$

for small values of y.

5. THE CRITICAL FIELD H_s IN A SUPERCONDUCTOR WITH MAGNETIC IMPURITIES

The system of equations (35) can be solved for an arbitrary value of the spin flip scattering time $\Gamma = \tau_s^{-1}$. To do this, we put

$$Z = \frac{\Delta}{\Gamma + 2e^2DA^2}. \tag{50}$$

From the first equation in (35), we obtain

$$\begin{aligned}\Gamma + 2e^2DA^2 &= \frac{\pi T_c^0}{\gamma}\frac{1}{1+\sqrt{1-Z^2}}\\ &\times \exp\left[-\frac{1}{2Z}(\arcsin Z - Z\sqrt{1-Z^2})\right].\end{aligned} \tag{51}$$

With the help of Eq. (51), we obtain the first integral of the second equation in (35),

$$\frac{\partial A}{\partial y} = -[B + \tilde{\Phi}_1(Z)]^{1/2}, \tag{52}$$

where

$$\tilde{\Phi}_1(Z) = 8\pi\nu\left(\frac{\pi T_c^0}{\gamma}\right)^2\int_Z^b dZR(Z), \tag{53}$$

$$B = \begin{cases} 8\pi\nu\left\{\Delta_\infty\left(\dfrac{\Delta_\infty}{2} - \dfrac{\pi\Gamma}{4}\right) + \left(\dfrac{\pi T_c^0}{\gamma}\right)^2\right.\\ \left.\times\left(\dfrac{\pi}{4} - \dfrac{5}{6}\right)\exp\left(-\dfrac{\pi}{2}\right) + \dfrac{\Gamma^2}{3}\right\} \text{ if } \Delta_\infty > \Gamma,\\ 0 \text{ if } \Delta_\infty < \Gamma.\end{cases}$$

The upper integration limit in Eq. (53) is defined as

$$b = \begin{cases} 1 \text{ if } \Delta_\infty > \Gamma,\\ \dfrac{\Delta_\infty}{\Gamma} \text{ if } \Delta_\infty < \Gamma.\end{cases} \tag{54}$$

In Eqs. (53) and (54), the quantity Δ_∞ is the value of the order parameter in the Meissner state at large distances from the surface. The value of Δ_∞ can be found from Eqs. (30) and (35) as

$$\begin{aligned}\Delta_\infty\ln\left(\frac{\pi T_c^0}{\gamma\Delta_\infty}\right) &= \frac{\pi\Gamma}{4} \text{ if } \Delta_\infty > \Gamma,\\ \Delta_\infty\ln\left(\frac{\pi T_c^0}{\gamma(\Gamma + \sqrt{\Gamma^2 - \Delta_\infty^2})}\right) &= \frac{\Gamma}{2}\left\{\arcsin\left(\frac{\Delta_\infty}{\Gamma}\right)\right.\\ &\left.-\frac{\Delta_\infty}{\Gamma}\sqrt{1-\left(\frac{\Delta_\infty}{\Gamma}\right)^2}\right\} \text{ if } \Delta_\infty < \Gamma.\end{aligned} \tag{55}$$

The quantity B was found with the help of Eqs. (30), which were used to obtain the boundary conditions for the vector potential A at the point y such that $Z = 1$. It is easy to obtain that

$$\begin{aligned}\Gamma + 2e^2DA^2\big|_{Z=1} &= \frac{\pi T_c^0}{\gamma}\exp\left(-\frac{\pi}{4}\right),\\ \Delta\big|_{Z=1} &= \frac{\pi T_c^0}{\gamma}\exp\left(-\frac{\pi}{4}\right),\\ \frac{\partial A}{\partial y}\bigg|_{Z=1} &= -\sqrt{8\pi\nu}\left\{\Delta_\infty\left(\frac{\Delta_\infty}{2} - \frac{\pi\Gamma}{4}\right)\right.\\ &\left.+\left(\frac{\pi T_c^0}{\gamma}\right)^2\left(\frac{\pi}{4} - \frac{5}{6}\right)\exp\left(-\frac{\pi}{2}\right) + \frac{\Gamma^2}{3}\right\}^{1/2}.\end{aligned} \tag{56}$$

Using boundary condition (26) in Eq. (52), we immediately obtain the critical field H_s as

$$H_s = (B + \tilde{\Phi}_1(0))^{1/2}. \tag{57}$$

At the critical point H_s, the condition $\Delta|_{y=0} = 0$ is satisfied for all values of Γ. Equation (57) can be checked in the simplest case where $\Gamma \gg \Delta_\infty$. We have

$$\begin{aligned}A &= \left(\frac{\pi T_c^0}{48e^2D\gamma}\right)^{1/2}\left(\left(\frac{\Delta_\infty}{\Gamma}\right)^2 - Z^2\right)^{1/2},\\ \tilde{\Phi}_1(Z) &= \frac{\pi\nu}{12}\left(\frac{\pi T_c^0}{\gamma}\right)^2\left(\left(\frac{\Delta_\infty}{\Gamma}\right)^4 - Z^4\right).\end{aligned} \tag{58}$$

The solution of Eq. (52) is given by

$$A = \frac{\Delta_\infty}{\Gamma}\left(\frac{\pi T_c^0}{6e^2D\gamma}\right)^{1/2}\frac{C\exp(y/\tilde{\lambda})}{C^2 + \exp(2y/\tilde{\lambda})}, \tag{59}$$

where $0 < C < 1$ is an arbitrary constant and the penetration depth $\tilde{\lambda}$ is given by

$$\tilde{\lambda}^{-1} = (8\pi\nu e^2D)^{1/2}\left(\frac{\pi T_c^0}{\gamma}\right)^{1/2}\frac{\Delta_\infty}{\Gamma}. \tag{60}$$

Using Eq. (59), we find the magnetic field value at the point $y = 0$ as

$$H(0) = \frac{C(1-C^2)}{(1+C^2)^2}\frac{\Delta_\infty}{\Gamma\tilde{\lambda}}\left(\frac{\pi T_c^0}{6e^2D\gamma}\right)^{1/2}. \tag{61}$$

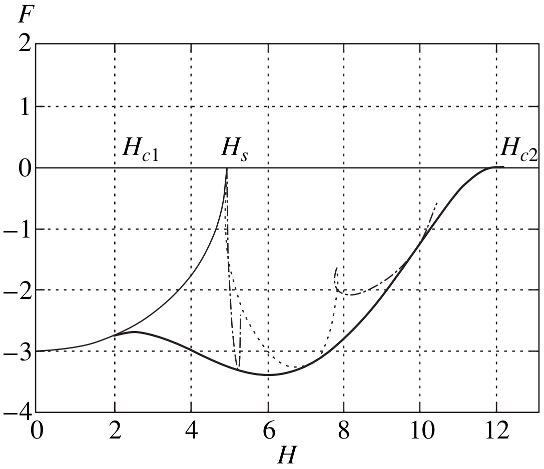

Energies of the Shubnikov phase (thick solid line), the Meissner state (thin line), and the states with different values of the vortex density (dashed lines).

The condition $\partial H(0)/\partial C = 0$ determines the value of the critical field H_s. With the help of Eq. (61), we obtain

$$C^2 = 3-2\sqrt{2},$$
$$H_s^2 = \left(\frac{\Delta_\infty}{4\Gamma\tilde{\lambda}}\right)^2 \frac{\pi T_c^0}{6e^2 D\gamma} = \frac{\pi\nu}{3}\frac{\Delta_\infty^4}{\Gamma^2}. \tag{62}$$

This value of H_s corresponds to the point $Z = 0$ and coincides with the value given by Eqs. (57) and (58). To complete the calculation, we give the equation for the thermodynamic field H_{cm} [10],

$$-\delta\mathcal{F} = \nu\int\limits_{2\gamma\Gamma/\pi}^{T_c^0}\frac{dT_c}{T_c}|\Delta|^2 = \frac{H_{cm}^2}{8\pi}, \tag{63}$$

where $\Delta = \Delta_\infty$ can be found from Eq. (55) with the replacement $T_c^0 \longrightarrow T_c$.

In the extreme case where $\Gamma \gg \Delta_\infty$, we find from Eqs. (55) and (63) that

$$\frac{dT_c}{T_c} = \frac{1}{12}d\left(\frac{\Delta}{\Gamma}\right)^2, \quad \delta\mathcal{F} = -\frac{\nu}{24}\frac{\Delta_\infty^2}{\Gamma^2}. \tag{64}$$

As before, we obtain

$$\frac{H_s}{H_{cm}} = 1, \quad \Gamma \gg \Delta_\infty. \tag{65}$$

We now prove that for an arbitrary value of the depairing factor Γ, we have the relation

$$H_s = H_{cm}. \tag{66}$$

Using Eqs. (55), (57), and (63), we verify that in both regions $\Delta_\infty > \Gamma$ and $\Delta_\infty < \Gamma$, the derivatives of H_s^2 and H_{cm}^2 with respect to T_c^0 coincide,

$$\frac{\partial H_s^2}{T_c^0} = \frac{\partial H_{cm}^2}{\partial T_c^0}. \tag{67}$$

This proves Eq. (66). Equation (57) allows us to take the integral over T_c in expression (63) for the free energy and to obtain the critical field H_{cm} in the explicit form if

$$\frac{H_{cm}^2}{4\pi\nu} = \Delta_\infty^2 - \frac{\pi\Delta_\infty\Gamma}{2} + \frac{2\Gamma^2}{3}\quad \Delta_\infty > \Gamma, \tag{68a}$$

and

$$\frac{H_{cm}^2}{4\pi\nu} = \left[\Delta_\infty^2 - \left(\frac{\pi T_c^0}{\gamma}\right)^2 R(Z)\left(\frac{Z}{1+\sqrt{1-Z^2}}\right.\right.$$
$$\left.\left.-\frac{1}{2Z^2}(\arcsin Z - Z\sqrt{1-Z^2})\right)^{-1}\right]_{Z=\Delta_\infty/\Gamma} \quad \text{if } \Delta_\infty < \Gamma, \tag{68b}$$

where Δ_∞ and T_c^0 are related by Eq. (55).

6. CONCLUSION

We have found the general method of calculating the critical field H_s in the entire range of κ values and given the results for H_s in the temperature region near T_c and $T = 0$. For an arbitrary value of the depairing factor Γ, the quantities H_s and H_{cm} are equal in both temperature regions. The initial definition of H_s is the value of the external magnetic field at which vortices can penetrate into the superconductor without a threshold. In superconductors of the second kind, the value of this field coincides with the critical field value of the absolute instability of the Meissner state. In a superconductor of the first kind, the field of the absolute instability of the Meissner state is the overheating field. If the order parameter Δ is nonzero at the boundary of the superconductor, the energy of a vortex-antivortex pair (at least in the $\kappa \gg 1$ limit) decreases very slowly with the distance $2a$ between them in the range $2a \ll \xi$ [8]. As the result, the order parameter Δ is zero on the boundary of the superconductor at the point H_s. The point H_s is an essentially singular point because an infinite number of states with different numbers of vortices in the sample go out of this point (the number of states is of the order SH_s/Φ_0, where S is the area of the sample and $\Phi_0 = \pi/e$ is the flux quantum). The free energy of the Shubnikov phase is the envelope curve for all these states.

By the Shubnikov phase, we mean the state with the minimum value of the free energy in a given external magnetic field. The disappearance of the threshold in the Meissner state at the point H_s does not mean that vortices can freely enter the superconductor in the Shubnikov phase as the external magnetic field changes. In the figure, we present the free energy as a function of the magnetic field for the Shubnikov phase (solid line), the Meissner state energy (thin line), and the energy of states with different densities of vortices in the superconductor (dashed line).

ACKNOWLEDGMENTS

The research described in this publication was made possible in part by Award RP1-2251 of the U.S. Civilian Research & Development Foundation for the Independent States of Former Soviet Union (CRDF). The research was also supported by the Russian Foundation for Basic Research (project no. 00-02-177-29).

REFERENCES

1. V. L. Ginzburg and L. D. Landau, Zh. Éksp. Teor. Fiz. **20**, 1064 (1950).
2. A. A. Abrikosov, Zh. Éksp. Teor. Fiz. **32**, 1442 (1957) [Sov. Phys. JETP **5**, 1174 (1957)].
3. P. G. de Gennes, *Superconductivity of Metals and Alloys* (Benjamin, New York, 1966; Mir, Moscow, 1968).
4. V. L. Ginzburg, Zh. Éksp. Teor. Fiz. **34**, 113 (1958) [Sov. Phys. JETP **7**, 78 (1958)].
5. L. P. Gor'kov, Zh. Éksp. Teor. Fiz. **36**, 1918 (1959) [Sov. Phys. JETP **9**, 1364 (1959)].
6. L. G. Aslamazov, A. I. Larkin, and Yu. N. Ovchinnikov, Zh. Éksp. Teor. Fiz. **55**, 323 (1968) [Sov. Phys. JETP **28**, 171 (1968)].
7. Yu. N. Ovchinnikov and V. Z. Kresin, Eur. Phys. J. B **14**, 203 (2000).
8. Yu. N. Ovchinnikov and I. M. Sigal, Physica A (Amsterdam) **261**, 143 (1998); Eur. J. Appl. Math. (2000) (in press).
9. A. I. Larkin and Yu. N. Ovchinnikov, Zh. Éksp. Teor. Fiz. **64**, 1096 (1973) [Sov. Phys. JETP **37**, 557 (1973)].
10. A. A. Abrikosov, L. P. Gor'kov, and I. E. Dzyaloshinskii, *Methods of Quantum Field Theory in Statistical Physics* (Fizmatgiz, Moscow, 1962; Prentice-Hall, Englewood Cliffs, 1963).

Journal of Experimental and Theoretical Physics, Vol. 92, No. 5, 2001, pp. 866–870.
Translated from Zhurnal Éksperimental'noĭ i Teoreticheskoĭ Fiziki, Vol. 119, No. 5, 2001, pp. 995–1000.
Original Russian Text Copyright © 2001 by Kosevich.

NONLINEAR PHYSICS

The Hamiltonian Dynamics of the Soliton of the Discrete Nonlinear Schrödinger Equation

A. M. Kosevich
Verkin Physicotechnical Institute of Low Temperatures, National Academy of Sciences of Ukraine, Kharkov, 61164 Ukraine
Max-Plank-Institut für Physik Komplexer Systeme, D01187, Dresden, Germany
e-mail: kosevich@ilt.kharkov.ua

Received September 28, 2000

Abstract—Hamiltonian equations are formulated in terms of collective variables describing the dynamics of the soliton of an integrable nonlinear Schrödinger equation on a 1D lattice. Earlier, similar equations of motion were suggested for the soliton of the nonlinear Schrödinger equation in partial derivatives. The operator of soliton momentum in a discrete chain is defined; this operator is unambiguously related to the velocity of the center of gravity of the soliton. The resulting Hamiltonian equations are similar to those for the continuous nonlinear Schrödinger equation, but the role of the field momentum is played by the summed quasi-momentum of virtual elementary system excitations related to the soliton. © *2001 MAIK "Nauka/Interperiodica".*

1. INTRODUCTION

Some nonlinear differential equations in partial derivatives important for physical applications [the nonlinear Schrödinger equation, the Landau–Lifshits equations in the theory of magnetization, etc.] possess so-called dynamic solitons. Dynamic solitons are understood to be nonlinear spatially localized perturbations of the system under study whose stability is ensured by the presence of simple additive integrals of motion. The dynamics of the soliton of the nonlinear Schrödinger equation has been described in detail for both its free motion (e.g., see [1]) and motion in an external field [2]. The dynamics of the magnetic dynamic soliton has been studied no less thoroughly [3, 4].

The motion of the dynamic soliton is usually characterized by the speed of motion of its center of gravity V and internal eigenfrequency ω (the frequency of precession for a magnetic soliton) in the laboratory frame of reference. These two mechanical characteristics of solitons can be put in correspondence to two integrals of motion: total soliton momentum P and soliton mass N [the number of virtual elementary excitations of the system (quasi-particles) bound in the soliton]. The remarkable property of the soliton as a particle-like excitation is the presence of an important relation between these integrals of motion, the V and ω parameters, and soliton energy E. If E is written in terms of integrals of motion (total momentum and mass) as independent dynamic variables, small variations in P, N, and E are related as [2, 3]

$$\delta E = V\delta P + \Omega\delta N, \tag{1}$$

where Ω is the soliton frequency in the frame of reference moving at speed V (the Planck constant is assumed to equal one). If the phase of the soliton is $kx - \omega t$, then $\Omega = \omega - kV$.

In this respect, the energy of soliton free motion, that is, its kinetic energy, plays the role of the Hamiltonian function. Equation (1) gives the equations of motion

$$V = \frac{\partial E}{\partial P}, \quad \Omega = \frac{\partial E}{\partial N}. \tag{2}$$

The first equation in (2) is the usual Hamiltonian equation of motion. The second equation determines the physical meaning of Ω; namely, soliton energy $E(P, N)$ increases by $\Omega(P, N)$ when the number of quasi-particles bound in the soliton increases by one.

We are going to generalize the Hamiltonian description of solitons to the dynamics of particle-like solutions (solitons) of nonlinear discrete equations on a lattice; that is, of finite-difference rather than differential equations. Such a generalization is nontrivial because one of the integrals of motion used above, namely, the field soliton momentum, is related to continuity of systems and is meaningless for a discrete periodic lattice. This raises the problem of defining the integral of motion conjugate to soliton velocity V. We will show how the corresponding integral of motion is introduced and what physical meaning it has.

One of the simplest nonlinear differential equations well studied as regards the dynamics of solitons is the nonlinear Schrödinger equation, which is completely integrable. However, the transition from a continuous nonlinear Schrödinger equation to its discrete (lattice) analogue is not unambiguous. If we start with a close-coupling-type model, the discrete analogue of the Schrödinger equation (taking into account the nonlinear term) should be written as

$$i\frac{\partial \Psi_n}{\partial t} = 2\Psi_n - \Psi_{n+1} - \Psi_{n-1} - 2g|\Psi_n|^2\Psi_n. \tag{3}$$

An analogue of precisely this equation is used in the nonlinear optics of a system of parallel waveguides [5]. Unfortunately, (3) is not completely integrable and does not have exact soliton solutions of the type of the soliton of the continuous nonlinear Schrödinger equation. There is, however, an exactly integrable version of the nonlinear Schrödinger equation on a lattice [6–8],

$$i\frac{\partial\Psi_n}{\partial t} = (\Psi_{n+1}+\Psi_{n-1})(1+|\Psi_n|^2)+\omega_0\Psi_n. \qquad (4)$$

The $\omega_0 + 2$ frequency shift used in (4) is of no consequence; we give it for convenience of references to [8], where this equation is discussed from the point of view of interest to us.

The linearized equation has the dispersion law

$$\omega = \omega_0+\varepsilon(k), \quad \varepsilon(k) = -2\cos k, \qquad (5)$$

which determines the spectrum of elementary excitations corresponding to the $(\omega_0 - 2 < \omega < \omega_0 + 2)$frequency interval.

Equation (4) has a dynamic soliton-type solution [6] and allows Hamiltonian equations of motion for such a soliton to be derived.

2. MECHANICAL INTEGRALS OF MOTION

Equation (4) has two additive integrals of motion, namely, the integral

$$N = \sum_n \ln(1+|\Psi_n|^2), \qquad (6)$$

mentioned above, which plays the role of the norm of the wave function and determines the number of soliton-related elementary excitations, and the $\mathcal{H}$ integral defined by

$$\mathcal{H} = E+\omega_0 N, \quad E = -\sum_n(\Psi_n\Psi^*_{n+1}+\Psi^*_n\Psi_{n+1}). \qquad (7)$$

This integral can be treated as the Hamiltonian of the system.

Hamiltonian (7) generates (4) in conformity with the usual definition

$$\frac{\partial\Psi_n}{\partial t} = \{\mathcal{H}, \Psi_n\}, \qquad (8)$$

but Poisson brackets $\{\ldots, \ldots\}$ are defined in a nonstandard way, namely,

$$\{\Psi_m, \Psi^*_n\} = i(1+|\Psi_n|^2)\delta_{mn},$$

$$\{\Psi_m, \Psi_n\} = \{\Psi^*_m, \Psi^*_n\} = 0.$$

Let us take into account the distinguishing property of discrete chains, namely, their periodicity. Because of translational periodicity, there is obvious symmetry in an infinite uniform chain related to the displacement by the period of the lattice; that is, to the $n \longrightarrow n + 1$ transition. Let T be the operator of this displacement,

$$T\Psi_n = \Psi_{n+1}. \qquad (9)$$

Its eigenfunctions e^{ikn} correspond to eigenvalues e^{ik} $(-\pi < k < \pi)$, where k is the quasi-wave number.

Operator T generates the additional additive integral of motion

$$\sum_n \Psi^*_n T\Psi_n,$$

which can conveniently be written as

$$S = -i\sum_n[\Psi^*_n(\Psi_{n+1}-\Psi_n)-\Psi_n(\Psi^*_{n+1}-\Psi^*_n)]$$

$$= -i\sum_n(\Psi^*_n\Psi_{n+1}-\Psi_n\Psi^*_{n+1}) \qquad (10)$$

$$= -i\sum_n\Psi^*_n(\Psi_{n+1}-\Psi_{n-1}).$$

Note that the $j_n = -i[\Psi^*_n(\Psi_{n+1} - \Psi_n) - \Psi_n(\Psi^*_{n-1} - \Psi^*_n)]$ value in a discrete chain is an analogue of the density of the flux of particles in a continuous medium. The S value therefore has the meaning of the total momentum in an excited chain.

Clearly, the definitions of finite integrals of motion (6), (7), and (10) refer to an arbitrary solution to (4) localized in space. We will, however, be interested in their use to describe the dynamics of a separate soliton.

Consider a stationary solution to (4) of the type

$$\Psi_n(t) = \Phi^\omega_n(t)\exp(ikn-i\omega t-i\theta), \qquad (11)$$

where $\Phi^\omega_n(t)$ is a real function and θ is an arbitrary constant phase. The Φ_n function and the relation between ω and k are determined by two real equations

$$(\omega_0-\omega)\Phi_n = \cos k(\Phi_{n+1}+\Phi_{n-1})(1+\Phi^2_n), \qquad (12)$$

$$\frac{\partial}{\partial t}\ln(1+\Phi^2_n) = -2\sin k\Phi_n(\Phi_{n+1}-\Phi_{n-1}). \qquad (13)$$

The Φ_n function that vanishes at infinity, $\Phi_n = 0$ as $n \longrightarrow \pm\infty$, corresponds to soliton solutions. The N, E, and S integrals of motion depend on both the form of Φ_n and the k value,

$$N = \sum_n\ln(1+\Phi^2_n), \qquad (14)$$

$$E = -2\cos k\sum_n\Phi_n\Phi_{n+1}, \qquad (14a)$$

$$S = 2\sin k\sum_n\Phi_n\Phi_{n+1}. \qquad (14b)$$

Consider small changes in the integrals of motions related to small wave function Ψ variations; that is, changes caused by small variations in Φ_n and wave number k. It follows from (12) and (14) that

$$(\omega_0 - \omega)\delta N = \cos k \sum_n (\Phi_{n+1} + \Phi_{n-1})\delta\Phi_n. \qquad (15)$$

Similarly, (14a), (14b), (15), and (7) yield

$$\delta\mathcal{H} = \omega\delta N + S\delta k. \qquad (16)$$

Clearly, the most important parameters of solution (11) (that is, ω and k) are related by two dynamical Hamiltonian equations

$$\omega = \frac{\partial\mathcal{H}}{\partial N} = \omega_0 + \frac{\partial E}{\partial N}, \quad S = \frac{\partial\mathcal{H}}{\partial k} = \frac{\partial E}{\partial k}, \qquad (17)$$

if the Hamiltonian is treated as a function of the N and k independent variables, $\mathcal{H} = \mathcal{H}(N, k)$. Note that the derivations of both (14)–(14b) and equations of motion (17) are not explicitly related to the complete integrability of the initial nonlinear equation. They, however, imply that the infinite sums in (14)–(14b) converge, that is, that this equation has a solution or solutions that vanish at infinity. In particular, the existence of a dynamic soliton is implied. In other words, it is assumed that there exists a solution of type (11) localized in space and not accompanied by emission of small-amplitude waves of the phonon type. Such solutions are not known for discrete nonlinear equations that do not possess complete integrability. Precisely for this reason, we turn to (4).

3. HAMILTONIAN EQUATIONS IN TRADITIONAL VARIABLES

As we treat a dynamic soliton as a particle-like excitation with an internal vibrational mode, it would be expedient to have equations of motion for a traditional pair of canonical variables, one of which is the velocity of the center of gravity of the soliton.

If (4) has a stationary localized solution traveling along the chain at rate V, its amplitude should, as with the continuous nonlinear Schrödinger equation, be expected to have the form

$$\Phi_n(t) = \Phi(n - Vt). \qquad (18)$$

Indeed, such a solution does exist [8],

$$\Phi(x) = A\,\mathrm{cn}[\beta(x - x_0), \kappa], \qquad (19)$$

where $A = \mathrm{const}$ and $\mathrm{cn}(z, \kappa)$ is the Jacobi elliptic cosine whose parameter κ lies in the interval $0 < \kappa < 1$. At $\kappa \ll 1$, the elliptic cosine becomes the trigonometric cosine, and (19) becomes a solution to the linear equation. In the opposite limiting case ($\kappa \longrightarrow 1$), we have the $\mathrm{cn}(z, \kappa) \longrightarrow 1/\cosh z = \mathrm{sech}\, z$ transition and the solution [8]

$$\Psi_n(t) = \sinh\beta\,\mathrm{sech}[\beta(n - Vt - x_0)] \times \exp(ikn - i\omega t + i\theta), \qquad (20)$$

where $x_0 = \mathrm{const}$, $\theta = \mathrm{const}$, and the β, V, ω, and k parameters are related to each other by two equations,

$$\omega = \omega_0 - 2\cosh\beta\cos k, \qquad (21)$$

$$V = (2/\beta)\sinh\beta\sin k. \qquad (22)$$

If the soliton solution has form (20), the integrals of motion are invariant under continuous translations and can therefore be calculated by the integration [8], the sums in (14)–(14b) being replaced by integrals,

$$\sum_n \ldots = \int dn \ldots.$$

We then have

$$N = 2\beta, \quad E = -4\sinh\beta\cos k, \quad S = 4\sinh\beta\sin k. \qquad (23)$$

It follows that three of four parameters β, V, ω, and k are determined by fixed integrals of motion, and the fourth one (quasi-wave number k) remains free. Clearly, the width of the soliton $\lambda = 1/\beta$ is only determined by N, and the energy of the soliton and its velocity are periodic functions of k (as it should be in a uniform periodic structure).

Clearly, (21) follows from the first Hamiltonian equation (17), whereas the second Hamiltonian equation and (22) lead us to conclude that

$$S = NV. \qquad (24)$$

This result harmonizes with treating S as the total momentum.

Equation (24) allows Hamiltonian equations (16) and (17) to be written in a more familiar form. Let us introduce $P = Nk$ (the total quasi-momentum of elementary excitations related to the soliton[1] as an independent variable in place of k. We will assume that the new Hamiltonian ($\mathcal{E}$) is a function of independent variables P and N; that is, $\mathcal{E}(N, P) = \mathcal{H}(N, P/N)$. This replaces (16) and (17) by

$$\delta\mathcal{E} = \Omega\delta N + V\delta P, \quad \Omega = \frac{\partial\mathcal{E}}{\partial N}, \quad V = \frac{\partial\mathcal{E}}{\partial P}, \qquad (25)$$

where Ω is, as in the continuous nonlinear Schrödinger equation, the frequency of the soliton in the frame of reference moving at velocity V.

---

[1] The physical meaning of the field momentum as the total quasi-momentum of elementary excitations of a discrete system is known in the dynamics of crystal lattice [9], and the relations obtained in this work substantiate that this circumstance is of a general physical character.

We arrive at the conclusion that the Hamiltonian equations for the soliton of the discrete nonlinear Schrödinger equation in a uniform chain are formally fully identical to those for the continuous nonlinear Schrödinger equation, but the role of the field momentum is now played by the total quasi-momentum P of soliton linear excitations. Such a definition of P is attached to the special form of the solution to the discrete nonlinear Schrödinger equation and uses a definite dependence of the phase of the solution on the chain node number; this dependence determines the physical meaning of quasi-momentum k.

4. MOTION IN AN EXTERNAL UNIFORM FIELD

Next, let us analyze the equations that describe the dynamics of a soliton in a nonuniform chain, in which the quasi-wave number k is not conserved. Suppose that the ω_0 value weakly varies along the chain, that is, weakly depends on node number n. At small chain length intervals, this dependence can be considered linear,

$$\omega_n = \omega_0 + \eta n. \tag{26}$$

For convenience, we introduce small gradient η of the ω_n function. The Hamiltonian that generates (4) with ω_n of type (26) has the form [8]

$$\begin{aligned}\mathcal{H} &= E + \sum_n \omega_n \ln(1 + |\Psi_n|^2)\\ &= E + \omega_0 N + \eta \sum_n n \ln(1 + |\Psi_n|^2),\end{aligned} \tag{27}$$

where the last term describes the nonuniform potential U in whose field the soliton moves.

Let us use the representation

$$\Psi_n = \Phi_n^{\omega} \exp[i(kn - \omega t - \omega_0 t)]$$

to write the equation that generalizes (12):

$$(\eta n - \omega)\Phi_n^{\omega} = \cos k(\Phi_{n+1}^{\omega} + \Phi_{n-1}^{\omega})[1 + (\Phi_n^{\omega})^2]. \tag{28}$$

If gradient η is small, an approximate method for analyzing this situation can be suggested. This method is also applicable to more complex $U(n)$ potentials. This is the so-called adiabatic approximation, which recommended itself as an effective tool for handling continuous systems. If $\eta \ll \omega_0$, the soliton only senses the ω_n local constant value at the point at which its center is situated. We can therefore assume that its form is as previously described by a solution of type (20), in which the k and V parameters slightly vary with time. Let us write the solution in the form

$$\Psi_n^0 = \Phi(n - X(t))\exp[i(kn - \phi(t) - \omega_0 t], \tag{29}$$

where $X(t)$ is the coordinate of the center of the soliton. Obviously, its velocity V and frequency ω are given by

$$V = \frac{dX}{dt}, \quad \omega = \frac{d\phi}{dt}.$$

First, let us show that a nonuniform potential [the last term in (27)] leads to a nonconserved total momentum S and determines the equation of motion of the quasi-wave number k. Based on definition (14)–(14b), let us calculate the derivative of S with respect to time,

$$\begin{aligned}\frac{dS}{dt} &= \{\mathcal{H}, S\} = \eta \sum_n n[\Psi_n^*(\Psi_{n+1} + \Psi_{n-1})\\ &\quad + \Psi_n(\Psi_{n+1}^* + \Psi_{n-1}^*)].\end{aligned} \tag{30}$$

Substituting (29) into (30) and replacing the summation by the integration, we obtain

$$\frac{dS}{dt} = 2\eta \cos k \int_{-\infty}^{\infty} n\Phi(n)[\Phi(n+1) - \Phi(n-1)]dn. \tag{31}$$

Retaining the leading terms of the expansion in powers of η, we can use the solutions to (11) and (28), in which $\omega_n = \omega_0 = \text{const}$, in the right-hand side of (31). Using (11) and the equality $(\partial\Phi/\partial t) = -V(d\Phi/dn)$ yields

$$\begin{aligned}\frac{dS}{dt} &= \eta V \cot k \int_{-\infty}^{\infty} n \frac{d}{dn} \ln(1 + \Phi_n^2) dn\\ &= -\eta V N \cot k.\end{aligned} \tag{32}$$

According to (24), we have $NV = S$ in the right-hand side of (32). It is, in addition, clear that the nonuniform character of ω_n has no effect on the conservation of N as an integral of motion. This simplifies (32), which becomes

$$\frac{dV}{dt} = -\eta V \cot k.$$

Lastly, relation (22) between the velocity and the wave number can be used to obtain the final equation

$$\frac{dk}{dt} = -\eta. \tag{33}$$

It follows that the quasi-wave number of the soliton in a nonuniform external field linearly depends on time, as it should in the quasi-classical approximation.

Let us transform the nonuniform potential in (27),

$$U(X) = \eta \int n \ln[1 + \Phi^2(n - X)]dn, \tag{34}$$

where the $\Phi(n)$ function in the approximation that we use is determined by (19) or (20). Taking into account that, in this approximation, $\Phi(\xi) = \Phi(-\xi)$, we obtain

$$U(X) = \eta N X. \tag{35}$$

It follows that total energy (27) can be written in the form

$$\mathcal{E} = E(N, P/N) + \omega_0 N + U(X) \qquad (36)$$

and can be treated as a function of three independent variables, N, P, and X. As $P = Nk$ and X only depend on time in sum (36), the derivative of the wave number with respect to time, Eq. (33), plays the role of one of the canonical Hamiltonian equations

$$\frac{dP}{dt} = -\frac{\partial\mathcal{E}}{\partial X}, \quad \frac{dX}{dt} = \frac{\partial\mathcal{E}}{\partial P}. \qquad (37)$$

Dynamical Hamiltonian equations of type (37) naturally arise in the theory of the soliton of the continuous nonlinear Schrödinger equation [1] and in the theory of magnetic solitons [3, 4].

One of the remarkable applications of the equations of motion of solitons in external fields is the description and calculation of Bloch oscillations of the soliton of the discrete nonlinear Schrödinger equation in a uniform external field [8].

To obtain a quasi-classical description of Bloch oscillations, it suffices to use the obvious solution of (33)

$$k = -\eta t \qquad (38)$$

(we assume that $k = 0$ at $t = 0$) and substitute (38) into the equation for soliton velocity, Eq. (22):

$$V = -\frac{1}{N}\sinh\frac{N}{2}\sin\eta t, \quad N = \text{const.} \qquad (39)$$

This is precisely the periodic time dependence of soliton velocity in a uniform external field [8, 10] that determines Bloch oscillations at an $\omega_B = |\eta|$ frequency.

In accordance with (36) and (37), we can introduce force F acting on the soliton,

$$F = -\frac{\partial U}{\partial X} = -\eta N.$$

This makes it clear that, at a given (fixed) force, the $\omega_B = |F|/N$ Bloch frequency is inversely proportional to the soliton power (N).

Bloch oscillations are sometimes related to so-called dynamic localization of a particle moving in an external uniform field with a periodic dependence of the velocity of the particle on its quasi-momentum. We would rather call attention to another aspect of the phenomenon.

Quasi-classical oscillations with one frequency should correspond to some discrete equidistant energy spectrum of a quantum problem. Indeed, such a spectrum in the problem with Eq. (28) does exist and manifests itself by arising of the “Wannier–Stark ladder” (see Appendix).

APPENDIX

Let us return to Eq. (28). The solution to (28) depends on the ω parameter in a very special way: namely, this solution is a function of the $z = n - \omega/\eta$ variable. It follows that the solution is the same at different n and ω pairs satisfying the requirement $z =$ const. This requirement can only be met if

$$\omega = m\eta, \quad m = 0, \pm1, \pm2, \ldots, \qquad (A.1)$$

that is, if set m comprises integer numbers.

It follows that, among the solutions to (13) and (28), there exists a system of oscillating stationary solitons. This is precisely the series of solutions that corresponds to the Wannier–Stark ladder (A.1). Such solutions can be written in the form

$$\Psi_n^m = \Psi_{n-m}\exp[ik(n-m) - i(\omega_0 + m\eta)t]. \qquad (A.2)$$

Solitons of this series with various numbers m have identical profiles with centers displaced by m nodes.

ACKNOWLEDGMENTS

I wish to thank V.A. Marchenko, member of the Russian Academy of Sciences, for discussions on some mathematical problems, and M.M. Bogdan for valuable comments. I am grateful to the Dresden Max-Plank-Institut für Physik Komplexer Systeme, where this work was completed, for hospitality.

This work was financially supported by INTAS (grant no. 167, 1999).

REFERENCES

1. S. P. Novikov, S. V. Manakov, L. P. Pitaevskii, and V. E. Zakharov, *Theory of Solitons: the Inverse Scattering Method* (Nauka, Moscow, 1980; Consultants Bureau, New York, 1984).
2. A. M. Kosevich, Physica D (Amsterdam) **41**, 253 (1990).
3. A. M. Kosevich, B. A. Ivanov, and A. S. Kovalev, Sov. Sci. Rev., Sect. A **6**, 161 (1985); A. M. Kosevich, B. A. Ivanov, and A. S. Kovalev, *Nonlinear Magnetization Waves. Dynamic and Topologic Solitons* (Naukova Dumka, Kiev, 1983).
4. A. M. Kosevich, Physica D (Amsterdam) **119**, 134 (1998); A. M. Kosevich, V. V. Gann, F. I. Zhukov, and V. P. Voronov, Zh. Éksp. Teor. Fiz. **114**, 735 (1998) [JETP **87**, 401 (1998)].
5. A. Hasegawa, *Optical Solitons in Fibers* (Springer-Verlag, Berlin, 1989).
6. M. A. Ablowitz and J. F. Ladik, J. Math. Phys. **17**, 1011 (1976).
7. L. D. Faddeev and L. A. Takhtajan, *Hamiltonian Methods in the Theory of Solitons* (Nauka, Moscow, 1986; Springer-Verlag, Berlin, 1987).
8. R. Schart and A. R. Bishop, Phys. Rev. A **43**, 6535 (1991).
9. A. M. Kosevich, *The Crystal Lattice: Phonons, Solitons, Dislocations* (Wiley, Berlin, 1999).
10. D. Cai, A. R. Bishop, and N. Crönbech-Jensen, Phys. Rev. Lett. **74**, 1186 (1995).

Translated by V. Sipachev

Journal of Experimental and Theoretical Physics, Vol. 92, No. 5, 2001, pp. 871–878.
Translated from Zhurnal Éksperimental'noĭ i Teoreticheskoĭ Fiziki, Vol. 119, No. 5, 2001, pp. 1001–1010.
Original Russian Text Copyright © 2001 by Molotkov, Nazin.

MISCELLANEOUS

A Simple Proof of Unconditional Security of Relativistic Quantum Cryptography

S. N. Molotkov* and S. S. Nazin
Institute of Solid State Physics, Russian Academy of Sciences, p/o Chernogolovka, Moscow oblast, 142432 Russia
**e-mail: molotkov@issp.ac.ru*

Received June 27, 2000

Abstract—A simple proof of the unconditional security of a relativistic quantum cryptosystem based on orthogonal states is given. Limitations imposed by the special relativity theory allow the proof to be markedly simplified as compared to the case of nonrelativistic cryptosystems based on nonorthogonal states. An important point in the proposed protocol is a space-time structure of the quantum states, which is ignored in the nonrelativistic protocols using only the properties of the space of states of the information carriers. As a consequence, the simplification is related to the inefficacy of using the collective measurements against an eavesdropper, the allowance for which is an especially difficult task in the nonrelativistic case. *© 2001 MAIK "Nauka/Interperiodica".*

1. INTRODUCTION

Nonrelativistic quantum cryptography, in contrast to classical cryptography based on the laws of classical physics, is based on the fundamental laws of nonrelativistic quantum mechanics [1, 2]. Security of classical cryptography is based on the unproven complexity of calculating certain functions such as a discrete logarithm. It is implied that the calculation of such functions, as well as the inverse functions, are performed using a physical device operating according to the laws of classical physics. In addition, it is implicitly assumed that the information transmission between legal parties is provided by classical objects. Since the laws of classical physics do not prohibit simultaneous nonperturbing monitoring of any dynamic variables of a classical system, it is impossible to provide for guaranteed detection of eavesdropper intervention in the course of information transfer between legal parties. For this reason, the security of classical cryptosystems is based on the exponentially growing complexity of calculating the key distribution, rather than on detecting an eavesdropper attack during the key transmission.

The laws of classical physics provide only an approximate description of reality. A more rigorous description is provided by nonrelativistic quantum mechanics. Using quantum mechanics, it is possible, in principle, to realize a computational device (quantum computer) possessing a greater computational power in solving certain tasks as compared to classical computational facilities. The factorization problem encountered in the key decoding by an eavesdropper, which is exponentially complex (intolerable) for a classical computer, is only polynomially complex (tolerable) for a quantum computer [3]. Thus, the laws of nonrelativistic quantum mechanics also do not guarantee the unconditionally secure information exchange using well-known classical algorithms. By unconditional security we imply the secrecy based on prohibitions inherent in the fundamental laws of nature, rather than on the technical (computational) complexities.

While prohibiting unconditionally secure classical cryptography (in the aforementioned sense), quantum mechanics offers possibilities for quantum cryptography. Quantum cryptography is based on the possibility of detecting attempts at eavesdropping. This possibility is guaranteed by the laws of quantum mechanics in cases when the information is transferred by quantum systems.

Nonrelativistic quantum cryptography is based on two circumstances dictated by postulates of nonrelativistic quantum mechanics: (i) an unknown quantum state cannot be duplicated (no-cloning theorem) [4]; (ii) it is impossible to obtain information about quantum states belonging to a nonorthogonal basis set without perturbing these states [5].

In nonrelativistic quantum mechanics, the latter prohibition is not valid for orthogonal states. Moreover, there is no prohibition for instantaneous nonperturbation distinguishing between the orthogonal states. For this reason, the use of orthogonal states for nonrelativistic quantum cryptosystems is not even a subject for discussion.

Nonrelativistic quantum cryptosystems make essentially no use of the space-time specificity of quantum states (since both the no-cloning theorem and the statement concerning the impossibility of obtaining information about the quantum states belonging to a nonorthogonal basis set without introducing perturbations are of an absolutely general character). Nonrelativistic quantum cryptography protocols employ only the properties of the Hilbert space of states of the information carriers. The effects of state transmission between remote parties are insignificant and not considered explicitly. Speaking more strictly, attempts at making use of the space-time specificity of quantum states in the absence of a limiting transmission speed apparently cannot bring something essentially new to quantum cryptography.

A strict proof of the unconditional security of a nonrelativistic quantum exchange protocol under conditions when the behavior of both the eavesdropper and the legal parties is restricted only to the laws of quantum mechanics presents an extremely complicated task. To date, several proofs of various degrees of complexity were proposed based on various initial assumptions. However, in view of the problem complexity, no commonly accepted opinion has yet been formed [6–9].

Nonrelativistic quantum mechanics, as well as classical physics, presents an approximate description of the nature. A more adequate description, taking into account both the space-time structure of quantum states and restrictions imposed by the special relativity, is provided by relativistic quantum theory. Since no rational interpretation of relativistic quantum mechanics is available, this theory arises as the quantum field theory (QFT).

The QFT does not close the problem of nonrelativistic quantum cryptography, because the quantum-field system states are described (as well as in nonrelativistic quantum mechanics) by rays in the physical Hilbert space [10]. Since nonrelativistic quantum cryptography protocols use only the properties of states in the Hilbert space, these protocols survive in the QFT. The QFT can ensure a principally new approach to cryptography only provided that the space-time specificity of states are explicitly taken into account in the protocols. In other words, we must take into account that the sates, albeit still described (as in nonrelativistic quantum mechanics) by rays in the Hilbert space, are generated by the field operators (more precisely, by the generalized functions with operator values) bearing information about the space-time structure. The field operators obey the commutation relationships reflecting the microcausality principle. This principle is a consequence of limitations imposed by the relativity, implying the absence of causal relationships for points separated by a spacelike interval in Minkowskian spacetime. In addition, the QFT allows the effects of state transmission in Minkowskian space-time to be explicitly taken into account and used in constructing the cryptographic protocols.

Limitations imposed by the QFT and special relativity lead to a significant difference in some features of the quantum information theory (for detail see [11, 12]) as compared to the nonrelativistic case. Limitations imposed by the special relativity upon quantum measurements were originally considered as long ago as in 1931 by Landau and Peierls [13]. The qualitative considerations formulated in that paper based on the uncertainty relationship, together with the restriction of ultimate speed, led to a conclusion that no precise determination of, for example, momentum within any finite time interval is possible in the relativistic (in contrast to the nonrelativistic) case.

Below we describe a simple example of an unconditionally secure relativistic quantum cryptosystem in a noisy communication channel. The cryptosystem makes use of the quantum field states (photons) as information carriers. The more restrictive character of the laws of relativistic QFT significantly simplifies the proof of the unconditional security of the protocol as compared to the nonrelativistic case. In addition, the proposed scheme can be rather simply implemented in experiment, in contrast to the unconditionally secure exchange protocols in the nonrelativistic case, where an essential role in the proof of security is played by collective measurements that are not provided with a clear scheme of experimental realization. The proposed protocol explicitly employs the causal effects and makes use only of the individual measurements.

The considerations presented below were inspired by the paper by Goldenberg and Vaidman [14]. In our opinion, the ideas formulated in that work were not appreciated [15]. Moreover, subsequent developments [16] reduced the approach essentially to a nonrelativistic cryptosystem based on nonorthogonal states, thus virtually rejecting the initial idea.

The main idea consists in that the “internal” degrees of freedom of a quantum field (photon spirality) are used for encoding the transmitter information, while the spatial degrees of freedom are employed for detecting eavesdropper intervention. This is an essentially new circumstance as compared to the nonrelativistic case, which allows eavesdropper attacks to be detected (with an allowance for the special relativity requirements) by measuring the time delay of the state transmitted and ensures that the eavesdropper would obtain zero information. The fact that the transmitted information represents the quantum field states is also essential for the protocol.

The QFT allows even orthogonal states to be used in the cryptosystems. Since the system states in the relativistic (as well as in the nonrelativistic) case are described by rays in the Hilbert space of states, there are still valid prohibitions concerning unknown state cloning and the nonperturbing reliable differentiation of nonorthogonal states (these theorems are proven using only properties of the space of states).

Important for the following, there are two circumstances dictated by the QFT (for detail, see [17, 18]).

1. For reliably distinguishing between two orthogonal states of the free quantum field, it is necessary that the entire Minkowskian space-time region would be accessible where the state carrier is nonzero. The orthogonal states of the free quantum field can be formally reliably distinguished without introducing errors

only during an infinite time because of their principal unlocalizability related to the impossibility of constructing the field states with a compact carrier in the coordinate space, which would be generated in the four-dimensional space of momentum by the carriers preset on a mass surface.

2. The theory permits the existence of free quantum fields arbitrarily strongly localized in the space-time (i.e., with any degree of localization and the decay rate arbitrarily close to exponential). The principal unlocalizability is dictated by the local character of the QFT.

The latter circumstance is essential for cryptography by admitting the formation of arbitrarily localized states possessing preset arbitrarily small and arbitrarily steep (close to exponential) tails outside the space-time region controlled by the legal parties. The probability of distinguishing between two orthogonal states in the quantum field may vary from 1/2 (indistinguishable states) to 1 (reliably distinguishable states) due to the effects of field transmission from the controlled Minkowskian space-time region to a region accessible for the measurements. More precisely, the probabilities of obtaining a result during a finite time (due to the formation of strongly localized states) may differ from 1/2 or 1 by a preset arbitrarily small value. This parameter can be selected as the smallest in the problem.

The existence of a limiting transmission speed for both the quantum field and classical objects (including measuring ones), the access to the whole region of the field comprising two arbitrarily strongly localized but spatially separated "halves" of the state is principally possible only during a finite time. Therefore, the probability of reliably distinguishing the two states varies from 1/2 to 1 also within a finite time. A strong localization of the two "halves" spaced by τ_d allows the protocol to be written so as to provide that the probability is $P(\tau) = 1/2$ for $0 \le \tau < \tau_d$ and increases in a jumplike manner up to $P(\tau) = 1$ for $\tau = \tau_d$ (within the scale $\Delta\tau \ll \tau_d$ of the state localization). The jump smearing, which is controlled by localizing each half of the state, can be made arbitrarily exponentially small.

Since relativistic quantum cryptography explicitly employs the space-time structure of states, the proof of security cannot be conducted without considering a particular system geometry. This geometry must be explicitly taken into account in contrast to the nonrelativistic case using only the structure of the space of states.

2. MEASUREMENTS INVOLVED IN THE PROTOCOL

Now we will describe the measurements used in the protocol. Since it is necessary to take into account a particular geometry, we will consider a simple one-dimensional model reflecting all features stipulated by the QFT. Let us consider the particles (field quanta) possessing a given spectrum and moving at the speed of light over a one-dimensional mass surface (or the front part of a one-dimensional light cone in the momentum representation, $k^2 - k_0^2 = 0$). The two legal parties (A and B) control the vicinity of points x_A and x_B, respectively (see the figure). The size of controlled regions in the vicinity of these points is determined by the localization of states and can be rendered arbitrarily small (on the order of the state localization). In this geometry, it is sufficient to consider only states transmitted from x_A to x_B with a momentum $k > 0$. All the sates are determined on a single branch of the light cone $\tau = x - t$ ($c = 1$). The Hilbert space of carrier states is $\mathcal{H}_k \otimes \mathbf{C}^2$, where $\mathcal{H}_k$ refers to the spatial and $\mathbf{C}^2$, to the internal (polarization) degrees of freedom.

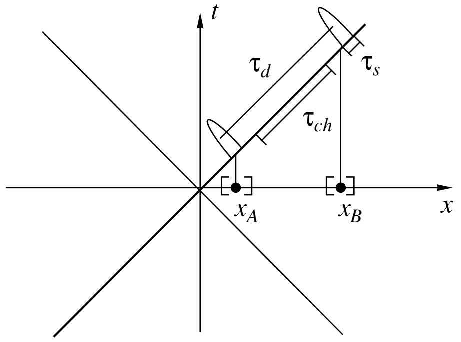

Let us consider a pair of orthogonal states

$$|\psi_{0,1}\rangle = \frac{1}{\sqrt{2}}\int_0^\infty f(k)|k\rangle \otimes (|+\rangle \pm |-\rangle)dk, \qquad (1)$$

where $|\pm\rangle \in \mathbf{C}^2$ are the orthogonal basis states and

$$\langle k|k'\rangle = \delta(k-k'), \quad k, k' > 0, \quad \int_0^\infty |f(k)|^2 dk = 1.$$

In the coordinate representation, the states on the branch of a one-dimensional light cone can be written as

$$|\psi_{0,1}\rangle = \frac{1}{\sqrt{2}}\int_{-\infty}^{\infty} f(\tau)|\tau\rangle \otimes (|+\rangle \pm |-\rangle)d\tau,$$

$$\tau = x - t, \qquad (2)$$

$$|\tau\rangle = \int_0^\infty e^{-ik\tau}|k\rangle dk, \quad f(\tau) = \int_0^\infty e^{ik\tau} f(k)dk.$$

The basis set $\{|\tau\rangle\}$ is nonorthogonal to:

$$\langle\tau|\tau'\rangle = \delta_+(\tau - \tau') \ne \delta(\tau - \tau').$$

A measurement capable of reliably distinguishing the given pair of orthogonal states is represented by the expansion of unity in $\mathcal{H}_k \otimes \mathbf{C}^2$ (and, by the same token, in $\mathcal{H}_\tau \otimes \mathbf{C}^2$, where $\mathcal{H}_\tau$ is the space isomorphous to $\mathcal{H}_k$ and spun on the basis set $\{|\tau\rangle\}$.

The measurement is represented as

$$\begin{gathered}\mathcal{M}_0 + \mathcal{M}_1 = I_k \otimes I_{\mathbf{C}^2},\\ \mathcal{M}_{0,1} = I_k \otimes \mathcal{P}_{0,1} = I_\tau \otimes \mathcal{P}_{0,1},\\ \mathcal{P}_0 = |0\rangle\langle 0|, \quad \mathcal{P}_1 = |1\rangle\langle 1|,\\ |0\rangle = \frac{1}{\sqrt{2}}(|+\rangle + |-\rangle), \quad |1\rangle = \frac{1}{\sqrt{2}}(|+\rangle - |-\rangle),\end{gathered} \tag{3}$$

$$\begin{gathered}I_k = \int_0^\infty |k\rangle\langle k| dk = I_\tau = \int_{-\infty}^{\infty} |\tau\rangle\langle\tau| d\tau = \int_{-\infty}^{\infty} \mathcal{M}(d\tau),\\ \mathcal{M}(d\tau) = \left(\int_0^\infty e^{-ik\tau}|k\rangle dk\right)\left(\int_0^\infty e^{ik'\tau}\langle k'| dk'\right)d\tau.\end{gathered} \tag{4}$$

Note that measurement (4) is nonlocal on the light cone.

The carrier of state $f(\tau)$ on the light cone can be selected arbitrarily strongly localized in the limit as $|f(\tau)|^2 \longrightarrow \delta(\tau)$. Strictly speaking, according to the QFT, the states preset on a mass surface cannot possess a compact carrier in Minkowskian space-time. However, it is possible to construct an arbitrarily strongly localized state with the tails arbitrarily close to exponential [18]. The latter circumstance implies that we may select a time "window" $\Delta\tau$ such that the probability of detecting the state in this time interval would be arbitrarily close to unity. Let us assume that the state (in fact, the norm of the $f(\tau)$ packet) and the interval are selected so that the probability of detection outside the time window $\Delta\tau$ (due to the tails of the state not accommodated within $\Delta\tau$) can be made arbitrarily (exponentially) close to zero. This parameter will be considered as the smallest in the problem. More precisely, the probability of the results of measurements of the input states $|\psi_{0,1}\rangle$ within the time window $\Delta\tau$ in channel 0 (corresponding to $\mathcal{P}_0$) and channel 1 (corresponding to $\mathcal{P}_1$) has the form (see formula (4)):

$$\begin{gathered}\Pr\{\Delta\tau, |\psi_{0,1}|\}\\ = \mathrm{Tr}\left\{\left(\left(\int_{-\Delta\tau}^{\Delta\tau}\mathcal{M}(d\tau)\right)\otimes\mathcal{P}_{0,1}\right)|\psi_{0,1}\rangle\langle\psi_{0,1}|\right\}\\ = \int_{-\Delta\tau}^{\Delta\tau}|f(\tau)|^2 d\tau = 1 - \delta,\end{gathered}$$

where the parameter δ is related to the tail of the state as

$$\int_{|\tau| > \Delta\tau} |f(\tau)|^2 d\tau = \delta \longrightarrow 0.$$

In other words, the problem has two independent parameters: the window $\Delta\tau$ characterizing localization of the state (this interval is selected so as to provide that the integral of the squared amplitude of the state $f(\tau)$ would be arbitrarily close to unity) and the spacing τ_d characterizing the separation of two "halves" of the state (this quantity must be selected such that the tails of the two "halves" would not touch one another to within a preset accuracy, $\Delta\tau \ll \tau_d$). For convenience, below we will consider the state carrier as compact (with an allowance for the above restrictions) because this assumption will not affect the final results.

It is necessary to point out the following. The measurement under consideration cannot be considered as a measurement lasting for the time $\Delta\tau$. For every event, the result of a measurement (i.e., the reading of a classical instrument such as a photodetector with a sufficiently small (formally infinitesimal) time constant operating in a standby mode) appears at a random time instant within $(\tau, \tau + d\tau)$ at a probability density of

$$\begin{gathered}\Pr\{d\tau, |\psi_{0,1}\rangle\}\\ = \mathrm{Tr}\{((\mathcal{M}(d\tau))\otimes\mathcal{P}_{0,1})|\psi_{0,1}\rangle\langle\psi_{0,1}|\} = |f(\tau)|^2 d\tau.\end{gathered}$$

This interpretation is natural and agrees with the classical limit, whereby a classical signal is measured with a time shape of $f(\tau)$.

Let the state $|\psi_0\rangle$ (or $|\psi_1\rangle$) be prepared by the time instant τ_i (with an accuracy of $\Delta\tau$, for which purpose it is necessary to control a space-time region with a size of $\Delta\tau$):

$$|\psi_{0,1}\rangle = \frac{1}{\sqrt{2}}\int_{-\infty}^{\infty}(f(\tau - \tau_i)|\tau\rangle \otimes (|+\rangle \pm |-\rangle))d\tau. \tag{5}$$

This is followed by the unitary transformation independent of the state:

$$\begin{gathered}|\psi_{0,1}(\tau_d)\rangle = U|\psi_{0,1}\rangle\\ = \frac{1}{\sqrt{2}}\int_{-\infty}^{\infty}(f(\tau - \tau_i - \tau_d)|\tau\rangle \otimes |+\rangle\\ \pm f(\tau - \tau_i)|\tau\rangle \otimes |-\rangle)d\tau.\end{gathered} \tag{6}$$

The accuracy of the moment of preparation is determined by the width of the state carrier $f(\tau)$.

The matrix elements of the unitary operator are as follows:

$$\begin{gathered}\langle +|\langle\tau'|U|\tau\rangle|+\rangle = \delta_+(\tau - \tau' - \tau_d)\\ = \int_0^\infty \exp\{ik(\tau - \tau' - \tau_d)\},\\ \langle -|\langle\tau'|U|\tau\rangle|-\rangle = \delta_+(\tau - \tau'), \quad \langle\pm|\langle\tau'|U|\tau\rangle|\mp\rangle = 0.\end{gathered} \tag{7}$$

This unitary transformation is nonlocal on the light cone $\tau = x - t$ (for $\tau_d \neq 0$); the latter condition implies that realization of this transformation requires access to a region with the size τ_d (to within an accuracy of $\Delta\tau$) on the light cone. The physical meaning of this unitary transformation corresponds to a time shift (delay) of a "half" of the state with a polarization component $|-\rangle$. The transformation realized for a fixed x (i.e., locally in the space of coordinates), requires a time $\Delta t = \tau_d$ (because $\tau = x - t$); the transformation performed at a time instant (but nonlocally in space) requires a coordinate space region $\Delta x = c\tau_d$ ($c = 1$).

Note that the space-time interval τ_d on the light cone branch is independent of the reference frame because the light cone is invariant with respect to the Lorentz transformation. For this reason, an eavesdropper cannot make use of the twin paradox [17].

The stretched sates $|\psi_0(\tau_d)\rangle$ and $|\psi_1(\tau_d)\rangle$ are orthogonal. However, the property of being orthogonal is nonlocal, which means that the verification of orthogonality requires access to a space-time region (interval) $\geq \tau_d$ with an accuracy of $\Delta\tau \longrightarrow 0$. In other words, the orthogonality is a nonlocal property in the Hilbert space $\mathcal{H}_\tau$, meaning that all the states $|\tau\rangle$ on which $\mathcal{H}_\tau$ is spun (or the space-time region $\tau \geq \tau_d$) must be accessible.

All the nonrelativistic quantum cryptography protocols imply that the Hilbert spaces of states are always accessible to both legal parties and an eavesdropper. In the relativistic case, the access can be controlled using the effects of state transmission from the regions monitored by legal parties to the region accessible to the eavesdropper. The "extension" of states and the limitation of ultimate transmission speed for both classical and quantum states allows the protocol to be written so as to provide that the whole state is never accessible to the eavesdropper. More strictly speaking, reaching the whole state requires that the entire interval in which the state is present would be accessible. However, attempts at accessing a finite space-time region will result in an unavoidable delay in the state detection by a legal party because of the finiteness of the speed of light. This circumstance makes insignificant the collective measurements, which are effective in the nonrelativistic case (where the entire space of states is accessible for all parties involved in the protocol) and are so difficult to consider in the proof of unconditional security. Thus, we may consider only the individual measurements in every transmission, since any attempt at eavesdropping is recognized by a delay in each message detection by the legal party.

If a $2T$-wide interval T_0 centered at τ_0, such that $T_0 = (-T + \tau_0, \tau_0 + T)$ and $2T < \tau_d + \Delta\tau$, is accessible, then no one measurement on the states $|\psi_0(\tau_d)\rangle$ and $|\psi_1(\tau_d)\rangle$ will distinguish these states (which therefore appear as the same state). This is formally manifested by restriction of the density matrix to a subspace $\mathcal{H}_{T_0}$ spun on the $|\tau\rangle$ states with the carrier belonging to the T_0 interval. The density matrix is

$$\rho_T = \mathrm{Tr}\left\{\left(\left(\int\limits_{T_0} \mathcal{M}(d\tau)\right) \otimes I_{C^2}\right)|\psi_{0,1}(\tau_d)\rangle\langle\psi_{0,1}(\tau_d)|\right\}$$

$$= \frac{1}{2}\int\limits_{T_0} |f(\tau)|^2 d\tau \otimes |+\rangle\langle+| \tag{8}$$

$$+ \frac{1}{2}\int\limits_{T_0} |f(\tau - \tau_d)|^2 d\tau \otimes |-\rangle\langle-|.$$

If the interval $T_0 < \tau_d + \Delta\tau$ does not simultaneously cover the carriers of states with various polarizations (see figure), then only one of the functions $f(\tau)$ or $f(\tau - \tau_d)$ is nonzero. Thus, the measurements in the space-time region (in the interval $T_0 < \tau_d + \Delta\tau$) are incapable of distinguishing the orthogonal states. Therefore, the probability of distinguishing these states is 1/2 (simple coin tossing). The limitation of the ultimate transmission speed implies that the time of access to any interval τ_d cannot be smaller than the magnitude of this interval.

3. DESCRIPTION OF PROTOCOL

Legal parties A and B (henceforth "Alice" and "Bob") can monitor the vicinity of points x_A and x_B ($x_A < x_B$), respectively (see figure). The clocks of Alice and Bob are assumed to be synchronized. The size of the monitored regions must be $\Delta x_{A,B} \sim \Delta\tau$. The known width of the state carrier ($\Delta\tau \longrightarrow 0$) is the smallest parameter in the problem. The channel length ($x_B - x_A = \tau_{ch}$) is also known (although the absolute accuracy is not required).

1. Alice prepares a message corresponding to states 0 or 1 at a random time instant τ_i (to within $\Delta\tau$):

$$|\psi_{0,1}\rangle = \frac{1}{\sqrt{2}}\int\limits_{-\infty}^{\infty} f(\tau - \tau_i - \tau_A)|\tau\rangle \otimes (|+\rangle \pm |-\rangle)d\tau, \qquad \tau_A = x_A. \tag{9}$$

The integration with respect to $d\tau$ in (9) is formally performed over the entire branch of the light cone, but actually the state is formed with the participation of only the basis set vectors $|\tau\rangle$ from the interval $\Delta\tau$.

2. A half of the state (component $|+\rangle$) is submitted to the channel, while another half (component $|-\rangle$) is kept as described by the unitary transformation $U_A(\tau_d)$ (this interpretation of the unitary transformation is quite natural because $U_A(\tau_d)$ has matrix elements with a shift

along the light cone only for components with the polarization $|+\rangle$):

$$|\psi_{0,1}(\tau_d)\rangle = U_A(\tau_d)|\psi_{0,1}\rangle$$

$$= \frac{1}{\sqrt{2}}\int_{-\infty}^{\infty}(f(\tau-\tau_i-\tau_A-\tau_d)|+\rangle \tag{10}$$

$$\pm f(\tau-\tau_i-\tau_A)|-\rangle)\otimes|\tau\rangle d\tau.$$

This transformation is nonlocal and its realization in the vicinity of x_A requires the time τ_d irrespective of the state (0 or 1).

3. Transmission of the state message from Alice to Bob is formally described by the unitary translation $U(\tau_{ch})$ along the branch of the light cone for a time interval τ_{ch} ($\tau_{ch} = x_B - x_A$):

$$|\psi_{0,1}(\tau_{ch})\rangle = U(\tau_{ch})|\psi_{0,1}(\tau_d)\rangle$$

$$= \frac{1}{\sqrt{2}}\int_{-\infty}^{\infty}(f(\tau-\tau_i-\tau_A-\tau_d-\tau_{ch})|+\rangle \tag{11}$$

$$\pm f(\tau-\tau_i-\tau_A-\tau_{ch})|-\rangle)\otimes|\tau\rangle d\tau.$$

4. Bob performs the unitary transformation $U_B(-\tau_d)$, which is independent of the input state and combines the two "halves" together (a back shift of the $|+\rangle$ component toward $|-\rangle$ can be implemented using beam splitters, mirrors, and delay lines):

$$U_B(-\tau_d)|\psi_{0,1}(\tau_{ch})\rangle$$

$$= \frac{1}{\sqrt{2}}\int_{-\infty}^{\infty} f(\tau-\tau_i-\tau_A-\tau_{ch})(|+\rangle \pm |-\rangle)\otimes|\tau\rangle d\tau. \tag{12}$$

The form of matrix elements of the operator $U_B(-\tau_d)$ is analogous to that for the operator $U_A(\tau_d)$ with the substitution$\tau_d \longrightarrow -\tau_d$:

$$\langle +|\langle\tau'|U_B(-\tau_d)|\tau\rangle|+\rangle = \delta_+(\tau-\tau'-\tau_d),$$

$$\langle -|\langle\tau'|U_B(-\tau_d)|\tau\rangle|-\rangle = \delta_+(\tau-\tau'),$$

$$\langle \pm|\langle\tau'|U_B(-\tau_d)|\tau\rangle|\mp\rangle = 0.$$

5. Upon accomplishing the transformation $U_B(-\tau_d)$, Bob performs the measurement realizing the unit expansion according to (3) and (4). The space of the measurement results represents the set $\Theta = \{i, \tau : i = 0, 1;\ \tau \in (-\infty, \infty)\}$ (where index $i = 0,1$ describes the events in channels 0 or 1, respectively):

$$\int_{-\infty}^{\infty}\mathcal{M}(d\tau)\otimes(\mathcal{P}_0+\mathcal{P}_1) = I_\tau \otimes I_{\mathbf{C}^2}. \tag{13}$$

The measurement describes the probability of obtaining the result within the interval $\Delta\tau$ in the channel 0 or 1, which is given by the following expression:

$$\Pr\{(\Delta\tau)\} = \int_{\Delta\tau}|f(\tau-\tau_i-\tau_A-\tau_{ch})|^2 d\tau. \tag{14}$$

The result is nonzero if the interval $\Delta\tau$ covers the state carrier. Since the states are orthogonal, the events in Bob's detection channels uniquely coincides with Alice's messages (noise ignored).

The selection of $\tau_d > \tau_{ch}$ implies that only a part of the state is always available in the channel (only a part of the space of states $\mathcal{H}_\tau$ is accessible). The access to a part of the space of states guarantees that the information about the state in the channel is zero (the probability of distinguishing states is 1/2). Because the ultimate transmission speed is limited, reaching the second "half" of the state requires access to the interval $\tau > \tau_d > \tau_{ch}$, which unavoidably leads to a delay in the moment of message detection at Bob's site

6. Bob communicates to Alice (via a public channel) the moment of detecting the τ_B state (because the $f(\tau)$ carrier width is small, this moment is known to within $\Delta\tau \longrightarrow 0$). If there were no detection at all, the given message is rejected. Upon receiving Bob's message on the detection time, Alice communicates the emission time τ_i. If the detection time at Bob's site is $\tau_B = \tau_i + \tau_d + \tau_{ch}$ (to within $\Delta\tau$), the transmission is accepted. Should a delay in detection be found (exceeding τ_d), the transmission attempt is rejected.

A point of principal importance is that the absence of delay in detection at Bob's site guarantees that an eavesdropper has zero information about the state transmitted by Alice (with a 1/2 probability of distinguishing the states). Deviation of the probability from 1/2 is determined by exponential tails of the state which can be made arbitrarily small by stretching the state "halves" (increasing τ_d) In the absence of delay of a compact state carrier $f(\tau)$, the information gained by the eavesdropper on the transmitted state is definitely zero.

7. An eavesdropper has no information about the remaining messages, but the channel noise (decoherence) results in that the 0 and 1 sequence available to the legal parties is not yet identical. The discrepancy can be brought both by eavesdropping attempts and by natural noise. For example, the eavesdropper may detect the first "half" of the state transmitted by Alice. This registration can be performed within a time $\Delta\tau \longrightarrow 0$ (this allows the eavesdropper to determine i). Then, immediately upon detecting the message, the eavesdropper prepares an arbitrary message with the $f(\tau)$ carrier, which, while not producing any detection delay at Bob's site, will be inconsistent with the state transmitted by Alice and interpreted as the channel noise. According to (8), the probability of determining the moment of message transmission by the eavesdropper is 1/2 (because only half of the state is accessible); note that the fact of signal detection by the eavesdropper provides zero information about the state, the probability of guessing the state being 1/2. The complete

probability of correctly determining the state transmitted via the channel is 1/2 × 1/2 = 1/4. Note that the probability of correctly guessing the state in each message by the eavesdropper doing nothing at all (coin tossing) is also 1/2. At first glance, this is rather unexpected: the eavesdropper has access to the communication channel, but the probability of detecting states is reduced by half as compared to the case of guessing without access to the channel. However, there is nothing surprising in this fact because simple guessing refers to one of the two possible states (0 or 1). In the case of detection, it is necessary to determine additionally the moment i of message preparation (in order to avoid the message being rejected by the legal parties), while the probability of detecting the state half is 1/2. In the case of access to the communication channel, the probability of misinterpretation of the transmitted state (3/4) includes the probability (1/2) of incorrect determination of the very fact of any message preparation within the given time interval. Since the fact of detecting a message provides zero information about the state, the eavesdropper may only guess it, the probability of which is 1/2.

Thus, if the legal parties accept only messages received without delay (more precisely, if a delay does not exceed $\tau_d + \tau_{ch}$), this fact guarantees that the probability of determining the transmitted state by an eavesdropper does not exceed 1/4, which is only half of the probability of correct guessing without intervention into the communication channel.

Thus, there arises a quite curious situation not encountered in the nonrelativistic case. From the standpoint of an eavesdropper, the purpose of which is to obtain maximum information about the key sequence at a minimum probability of being disclosed by legal parties, a correct eavesdropping strategy consists in attempts of simply guessing (which requires no access to the secure channel) of what is sent in each transmission event. Here, it is sufficient to access only the classical (public) channel so as to know the total number of received messages; this channel is accessible to all parties in the quantum cryptography tasks. In this case, the probability of disclosing the eavesdropper is zero because no disturbances at all are introduced into the communication channel. The intervention into the communication channel only has sense when the probability of obtaining the required information (per message accepted by the legal parties) exceeds the probability of coin tossing (1/2).

Thus, the maximum probability that each state transmission attempt undertaken by legal parties is correctly identified by an eavesdropper does not exceed 1/2.

8. Now we have only to solve the problem of key identity at the legal parties. Let us first consider a noiseless communication channel. Upon termination of the data transmission session involving $2N$ messages, Alice and Bob perform a procedure consisting of $m < 2N$ runs of random hashing (parity check with a random bit sequence; for detail see [19]). After each run, the length of the $2N$-bit sequence is reduced by two bits. If the parities coincide in all m hashing runs, the probability that the remaining $2N - 2m$ sequences may differ does not exceed 2^{-m}. This implies that Alice and Bob possess the same key with a probability exponentially approaching unity. According to the above considerations, the probability that an eavesdropper obtained reliable information about the key and remained undisclosed does not exceed $2^{-2(N-m)}$.

Now let the channel be noisy, which is manifested by detection errors at Bob's site, for example, as a result of the polarization rotation. Let the probability of this event (Alice sends 0, Bob detects 1 or vice versa) be $p < 1$. As above, the legal users accept only messages involving no time delay. Upon accomplishing the session involving $4N$ messages accepted, Alice and Bob decode $2N$ messages and evaluate the level of noise in the channel (p value). The knowledge of the probability of error in sending a single bit allows, in principle (provided a sufficiently long sequence is used), selecting an appropriate classical block code [20] that effectively reduces the error of transmitting coded words down to an arbitrarily low level.

For example, Alice communicates to Bob (via the public channel) only the numbers of messages transmitting state 1 (combined in groups of $2k$ messages) and the same for state 0 messages. This yields $2k$-sized blocks (coded 1 and 0). Then, using a majority vote, Bob proves the errors in each group (this coding allows $k - 1$ errors to be corrected), after which the blocks containing k errors are rejected (Bob informs Alice about the numbers of these groups via the public channel). The probability of error in the remaining groups does not exceed $p^k \ll p$. Now the legal parties obtain a sequence of $2\tilde{N}$-sized groups (with new $\tilde{1}$ and $\tilde{0}$). This is followed by a hashing procedure of m runs analogous to that described above, which yields a $2(\tilde{N} - m)$-long sequence. The probability that the remaining sequence with the length $2(\tilde{N} - m)$ is identical for both parties (provided that the parities in these sequences coincide in all m hashing runs) is not less than $1 - 2^{-(\tilde{N} - m)}$.

The block coding is only necessary in order to increase the probability of survival for the sequence retained upon hashing. The hashing procedure can be performed for the initial (rather than block) sequence. However, in this case the probability that hashing will reveal no parity breakdowns in the noisy channel is small. Nevertheless, a sequence that has passed the test is secure and identical (to within the above probabilities). The probability that an eavesdropper obtained reliable information about the key and remained undisclosed is certainly less than $2^{-2(\tilde{N} - m)}$ (it insufficient to know one bit in each code group). The proposed simple coding scheme is apparently not optimum but provides a simple and clear formulation of the relativistic quantum cryptography protocol.

ACKNOWLEDGMENTS

The authors are grateful to V.L. Golo for interest in this study and fruitful discussions.

This work was supported by the Russian Foundation for Basic Research (project no. 99-02-18127) and by the Federal Program "Advanced Technologies and Devices of Micro- and Nanoelectronics" (the "Physical Principles of Quantum Computer" project, no. 02.04.5.2.40.T.50).

REFERENCES

1. S. Wiesner, SIGACT News **15**, 78 (1983).
2. C. H. Bennett and G. Brassard, in *Proceedings of IEEE International Conference on Computers, Systems and Signal Processing, Bangalore, India, 1984*, p. 175.
3. P. W. Shor, in *Proceedings 35th Annual Symposium on Foundations of Computer Science, Santa Fe*, Ed. by S. Goldwasser (IEEE Comput. Society Press, Los Alamitos, 1994), p. 124.
4. W. K. Wootters and W. H. Zurek, Nature **299**, 802 (1982).
5. C. H. Bennett, Phys. Rev. Lett. **68**, 3121 (1992); C. H. Bennett, G. Brassard, and N. D. Mermin, Phys. Rev. Lett. **68**, 557 (1992).
6. D. Mayers, quant-ph/9802025 (1998).
7. H.-K. Lo and H. F. Chau, quant-ph/9803006 (1998).
8. E. Biham, M. Boyer, P. O. Boykin, *et al.*, quant-ph/9912053 (1999).
9. P. W. Shor and J. Preskill, quant-ph/0003004 (2000).
10. N. N. Bogolyubov, A. A. Logunov, A. I. Oksak, and I. T. Todorov, *General Principles of Quantum Field Theory* (Nauka, Moscow, 1987).
11. A. Kent, quant-ph/9810067 (1998); quant-ph/9810068 (1998); Phys. Rev. Lett. **83**, 1447 (1999).
12. S. N. Molotkov and S. S. Nazin, quant-ph/9911055 (1999); quant-ph/9910034 (1999); R. Laiho, S. N. Molotkov, and S. S. Nazin, quant-ph/0005067 (2000); quant-ph/0005068 (2000).
13. L. D. Landau and R. Peierls, Z. Phys. **69**, 56 (1931); L. D. Landau, in *Collection of Works* (Nauka, Moscow, 1969), Vol. 1, p. 56.
14. L. Goldenberg and L. Vaidman, Phys. Rev. Lett. **75**, 1239 (1995); quant-ph/9506030 (1995).
15. A. Peres, quant-ph/9509003 (1995).
16. M. Koashi and N. Imoto, Phys. Rev. Lett. **79**, 2383 (1997).
17. R. Laiho, S. N. Molotkov, and S. S. Nazin, quant-ph/0006010 (2000).
18. I. Bialynicki-Birula, Phys. Rev. Lett. **80**, 5247 (1998).
19. C. H. Bennett, D. P. DiVincenzo, J. A. Smolin, and W. K. Wootters, quant-ph/9604024 (1996).
20. E. J. Mac Williams and N. J. A. Sloane, *The Theory of Error-Correcting Codes* (North-Holland, Amsterdam, 1977).

Translated by P. Pozdeev

Journal of Experimental and Theoretical Physics, Vol. 92, No. 5, 2001, pp. 879–886.
Translated from Zhurnal Éksperimental'noĭ i Teoreticheskoĭ Fiziki, Vol. 119, No. 5, 2001, pp. 1011–1020.
Original Russian Text Copyright © 2001 by Norman, Stegaĭlov.

The Stochastic Properties of a Molecular-Dynamical Lennard-Jones System in Equilibrium and Nonequilibrium States

G. E. Norman* and V. V. Stegaĭlov**
Moscow Physicotechnical Institute, Institutskiĭ proezd 9, Dolgoprudnyi, Moscow oblast, 141700 Russia
**e-mail: henry–n@orc.ru*
***e-mail: vlad–st@yahoo.com*

Received November 30, 2000

Abstract—The K-entropy and the t_m time of dynamical memory (the time of forgetting initial conditions during numerical integration) of a classical system of particles whose interactions are governed by the Lennard-Jones potential were calculated by the method of molecular dynamics. The K value was a characteristic of a system of many particles, and the t_m value proved to increase logarithmically as fluctuations of the total energy of the system decreased; that is, as the accuracy of numerical integration increased. Two different K-entropy values corresponding to the same total energy of the system were found to exist, namely, K_e for the equilibrium and K_n for the nonequilibrium state. The rate of kinetic energy relaxation (t_r^{-1}) was shown to equal K_n, and the K_n value was found to be a more fundamental characteristic than t_r^{-1}. The density dependences of K_e (monotonic) and K_n (nonmonotonic) were calculated. The transition from dynamical (Newtonian) correlations to stochastic for the velocity autocorrelation function was considered. The reasons for the finiteness of dynamical memory in physical processes are discussed. The duration of dynamical correlations in real systems is limited by quantum uncertainty and is of the order of picoseconds. *© 2001 MAIK “Nauka/Interperiodica”.*

1. INTRODUCTION

The arising of irreversibility, stochasticity, and chaos in dynamical systems has been studied in many works (e.g., see [1–20] and the references cited therein). Of great interest is the divergence of trajectories and the K-entropy characterizing this divergence (the Krylov–Kolmogorov entropy and the mean maximum Lyapunov exponent). The K value is also the rate of entropy increase [1, 9, 10], that is, K^{-1} is an important relaxation time.

The $\tau_{\rm pr}$ time of behavior predictability was introduced in [3–5]. This value characterizes the time interval for which the future behavior of a dynamical system can be predicted from the initial conditions by deterministic dynamical equations determining the evolution of the system. Mentioned among the reasons for the finiteness of $\tau_{\rm pr}$ [3–7] were measurement noise, fluctuation forces, and inaccurate knowledge of the differential equations that describe the dynamical system. The value to which $\tau_{\rm pr}$ tends in the limit of negligibly low measurement and ignorance noises was called the predictability horizon, $\tau_{\rm h}$. Both $\tau_{\rm pr}$ and $\tau_{\rm h}$ are proportional to λ_+^{-1}, where λ_+ is the largest positive Lyapunov exponent, and the proportionality factor logarithmically depends on the noise level. It was also assumed that the correlation time of the system is $\tau_c \approx 0.5\lambda_+^{-1}$ [3–5].

Zaslavskiĭ [1] uses the terms “K-entropy” and “correlation splitting time τ.” The K value corresponds to the λ_+ value averaged over the phase space, and τ corresponds to $\tau_{\rm h}$. It was, however, assumed that $\tau = K^{-1}$.

A particular case of dynamical systems is classical many-particle systems. Such systems are numerically studied by the method of molecular dynamics. The idea of the method is very simple: all possible classical systems and media are simulated by a set of N moving atoms and/or molecules, which interact with each other (e.g., see [10, 11, 18, 21–25]). The numerical integration of the corresponding system of Newton equations

$$m_i \frac{d^2\mathbf{r}_i(t)}{dt^2} = \mathbf{F}_i[\mathbf{r}(t)], \tag{1}$$

or

$$m_i \frac{d\mathbf{v}_i(t)}{dt} = \mathbf{F}_i[\mathbf{r}(t)], \tag{2a}$$

$$\frac{d\mathbf{r}_i(t)}{dt} = \mathbf{v}_i(t), \tag{2b}$$

is integrated for each particle to determine the trajectories of all particles. Here, m_i, $\mathbf{v}_i$, $\mathbf{r}_i$, and $\mathbf{F}_i$ are the mass, velocity, and coordinate of the ith particle and the force acting on this particle, respectively ($i = 1, 2, \ldots, N$); the $\mathbf{v}_i$ and $\mathbf{r}_i$ values explicitly depend only on time t; $\mathbf{F}_i$ only depends on the coordinates of particles; $\mathbf{r}(t)$ is the set of the coordinates of all particles, $\mathbf{r}(t) = \{\mathbf{r}_1(t), \mathbf{r}_2(t), \ldots, \mathbf{r}_N(t)\}$; $\mathbf{v}(t)$ is defines similarly; and

$$\mathbf{F}_i = -\frac{\partial}{\partial \mathbf{r}_i} U(\mathbf{r}_1, \mathbf{r}_2, \ldots, \mathbf{r}_N), \tag{3}$$

where U is the potential energy. For instance, for a $\Phi(r)$ pair interparticle interaction potential,

$$U(\mathbf{r}_1, \mathbf{r}_2, \ldots, \mathbf{r}_N) = \sum_{i > j} \Phi(|\mathbf{r}_i - \mathbf{r}_j|). \tag{4}$$

Function U (forces $\mathbf{F}$) are assumed to be given in the method of molecular dynamics. The total energy of the system (E) is the sum of the kinetic T and potential U energies,

$$E = T + U, \tag{5}$$

$$T = \sum_{i=1}^{N} \frac{m v_i^2}{2}. \tag{6}$$

The solution to system (1) or (2) gives the trajectories of particles $\{\mathbf{r}(t), \mathbf{v}(t)\}$.

Set (1) or (2) is exponentially unstable for a system comprising more than two particles (e.g., see [1, 9, 10, 18, 21–24]). The parameter that determines the degree of instability, that is, the rate of divergence of initially close phase trajectories, is the K-entropy. The K-entropy values were calculated by the method of molecular dynamics for system of neutral [10–14, 17–20] and charged particles of two- [26] and one-component [27–29] plasmas. In [30], the notion of dynamical memory time t_{m} (the time of forgetting initial conditions) was introduced. The t_{m} value is determined by the accuracy of the numerical integration scheme [17–19, 26–30]. The t_{m} and t_{h} values [3–5] are similar in nature, their difference is caused by the difference between the noises to which they correspond. The K-entropy values were calculated in [10–14, 17–20, 26–30] for equilibrium systems only. In [1, 3–30], no distinction was drawn between equilibrium and nonequilibrium systems.

In this work, we consider both equilibrium and nonequilibrium two- and three-dimensional systems of particles whose interactions are governed by the Lennard-Jones potential

$$U = 4\varepsilon\left[\left(\frac{r}{\sigma}\right)^{12} - \left(\frac{r}{\sigma}\right)^{6}\right]. \tag{7}$$

We use reduced units in which $m = \varepsilon = \sigma = 1$, and time is measured in $(m\sigma^2/\varepsilon)^{1/2}$ units. For instance, for argon, $\varepsilon = 1.65324 \times 10^{-21}$ J, $\sigma = 3.405 \times 10^{-10}$ m, $m = 6.64 \times 10^{-26}$ kg, and $(m\sigma^2/\varepsilon)^{1/2} = 2.16 \times 10^{-12}$ s. The calculations were performed in the density range $\rho = mn = (0.1\text{–}1.1)m\sigma^{-1/3}$. Periodic boundary conditions were used. The number of particles in the principal cell was varied in the range $N = 16\text{–}216$. In Section 2, the K and t_{m} values for an equilibrium system are calculated and the dependence of the Kt_{m} value on total system energy E fluctuations is determined. In Section 3, the existence of two different K-entropy values for the equilibrium and nonequilibrium states is considered. The rate of kinetic energy relaxation is shown to coincide with the nonequilibrium K-entropy value. In Section 4, we describe the transition of time correlations from dynamical to stochastic as the time interval increases. The physical meaning of the maximum dynamical memory time in real systems is related to low but finite quantum uncertainty noises, which exist in all classical systems. This result is directly related to the Landau hypothesis [2] of the quantum nature of irreversibility.

2. EQUILIBRIUM SYSTEM

2.1. Model and Method of Calculations

For a given U function and particles of the same mass m and for identical initial conditions corresponding to the ith point on an equilibrium molecular-dynamical trajectory, solutions $\{\mathbf{r}(t), \mathbf{v}(t)\}$ to system (2) are found in steps Δt and trajectories $\{\mathbf{r}'(t), \mathbf{v}'(t)\}$ are calculated in steps $\Delta t'$. Averaged differences of the coordinates (velocities) of the first and second trajectories are determined at coinciding time moments,

$$\begin{aligned} \langle \Delta v^2(t) \rangle &= \frac{1}{N}\sum_{j}^{N} (v_j(t) - v'_j(t))^2, \\ \langle \Delta r^2(t) \rangle &= \frac{1}{N}\sum_{j}^{N} (r_j(t) - r'_j(t))^2. \end{aligned} \tag{8}$$

To improve accuracy, averaging over i, $i = 1, 2, \ldots, M$ is also performed. In some time t_l (this value should be considered separately), the differences become exponentially increasing (Fig. 1),

$$\langle \Delta v^2(t) \rangle = A\exp(Kt), \quad \langle \Delta r^2(t) \rangle = B\exp(Kt). \tag{9}$$

The K value is the K-entropy, and the A and B values are determined by the difference of Δt and $\Delta t'$. At

$$t > t'_m \approx \frac{1}{K}\ln\left(\frac{6kT}{m}\frac{1}{A}\right), \tag{10}$$

where T is the temperature, saturation is reached,

$$\begin{aligned} \langle \Delta v^2(t) \rangle &= 2\langle v^2 \rangle = 6kT/m, \\ \langle \Delta r^2(t) \rangle &= 6D(t - t_m) + \langle \Delta r^2(t_m) \rangle, \end{aligned} \tag{11}$$

where $3kT/m$ is the square of thermal velocity v_T and D is the diffusion coefficient. Estimates show that

$\langle \Delta r^2(t_m)\rangle = r_{av}$, where $r_{av} = (\sqrt{2}\,n\sigma)^{-1}$ is the mean path of particles between collisions.

The dynamical memory time is determined by calculating t'_m at the same Δt value and different $\Delta t'$ values of $\Delta t/2$, $\Delta t/5$, $\Delta t/10$, etc. (Fig. 2). The limiting t'_m value when $\Delta t'/\Delta t \longrightarrow 0$ is the dynamical memory time t_m for a given system and the selected numerical integration step Δt. During numerical integration, the system completely "forgets" its initial conditions in time t_m, and the calculated molecular-dynamical trajectory completely ceases to correlate with the initial Newtonian trajectory.

The K-entropy (and t_m) values weakly depend on N [20] starting with $N \sim 10$ (Fig. 3).

2.2. *K*-entropy and Memory Time

The K values are interpreted in the literature [1] as the rate of entropy S changes caused by dynamical mixing of trajectories, and the K^{-1} value is assigned the meaning of the time of correlation decoupling (see also [9, 10]). To consider these statements in the context of molecular dynamics, let us briefly recall the reasoning given in [1, 9, 10].

The entropy S of a subsystem is given by [1]

$$S = k\ln\Delta\Gamma, \tag{12}$$

where $\Delta\Gamma$ is the size of the phase space region where the subsystem resides in equilibrium for almost the whole time. Consider the evolution of some small initially compact $\Delta\Gamma_0$ phase volume element. By virtue of the Liouville theorem,

$$\Delta\Gamma(t) = \Delta\Gamma_0. \tag{13}$$

The structure of the phase volume, however, changes. The trajectories that had close points within t $\Delta\Gamma_0$ as the initial conditions exponentially diverge as time passes. As the volume remains constant, its structure becomes increasingly cut and stretched, and hollows are formed inside. The envelope of this structure bounds increasingly large volume $\Delta\bar{\Gamma}(t)$. From (9), we obtain the estimate

$$\Delta\Gamma(t) = \Delta\Gamma_0 e^{ht}, \tag{14}$$

and if a formula of the $\Delta\Gamma = (4/3)\pi r^3$ type is used, then h coincides with the K entropy within a factor. It follows from (12) and (14) that $h \sim K$ is indeed the rate of entropy changes caused by dynamical mixing of trajectories [1, 9, 10].

It follows from our calculations that time t_m can be interpreted as the time during which phase volume $\Delta\Gamma(t)$ attains its maximum value $\Delta\Gamma_{\max}$, and the entropy reaches the maximum value that corresponds to the equilibrium phase trajectory which is studied in molecular dynamics calculations. In other words, time t_m is

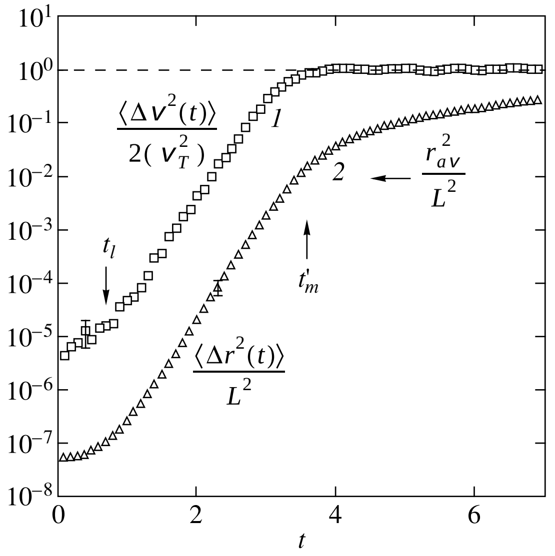

Fig. 1. Normalized averaged differences of (*1*) velocities $\langle\Delta v^2(t)\rangle$ and (*2*) coordinates $\langle\Delta r^2(t)\rangle$ at coinciding time moments along two trajectories calculated for identical initial conditions in steps $\Delta t = 0.001$ and $\Delta t' = 0.0001$; L is the calculation cell edge length, $N = 64$, $\rho = 0.5$, and $T = 0.44$; three-dimensional system ($d = 3$).

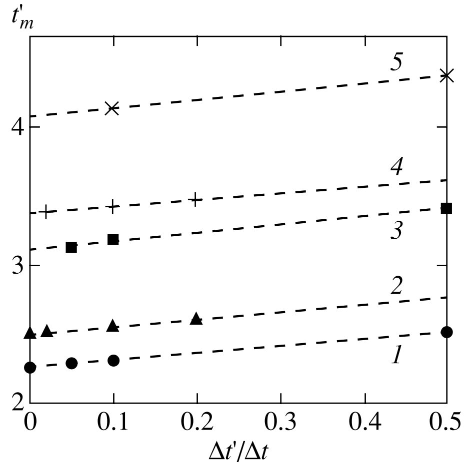

Fig. 2. Dependence of t'_m on $\Delta t'/\Delta t$ for various Δt values: Δt = (*1*) 0.01, (*2*) 0.005, (*3*) 0.001, (*4*) 0.0005, and (*5*) 0.0001 (the leftmost points of lines *1* and *2* correspond to $\Delta t' = 0.00001$); $N = 64$, $\rho = 0.5$, $T = 0.44$, and $d = 3$.

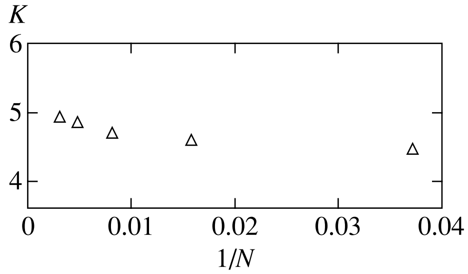

Fig. 3. Dependence of K-entropy on the number of particles N at $\rho = 0.5$, $T = 0.44$, and $d = 3$.

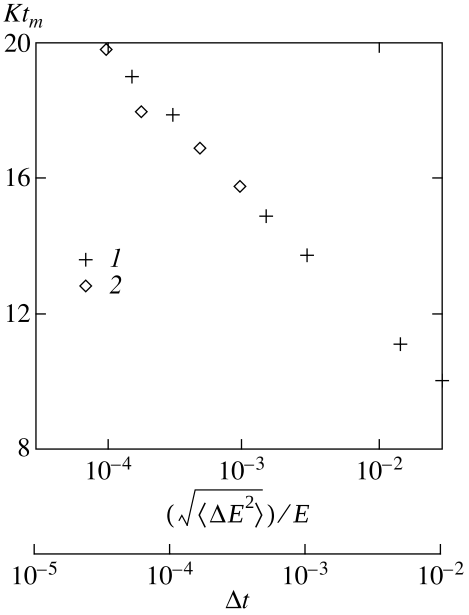

Fig. 4. Dependence of the Kt_m value on the relative system total energy fluctuation $\langle \Delta E^2 \rangle^{1/2}/E$ and integration step Δt: (*1*) Lennard-Jones system with $N = 64$, $\rho = 0.5$, $T = 0.44$, and $d = 3$ and (*2*) nonideal plasma [26] (only the $\sqrt{\langle \Delta E^2 \rangle}/E$ axis corresponds to the plasma).

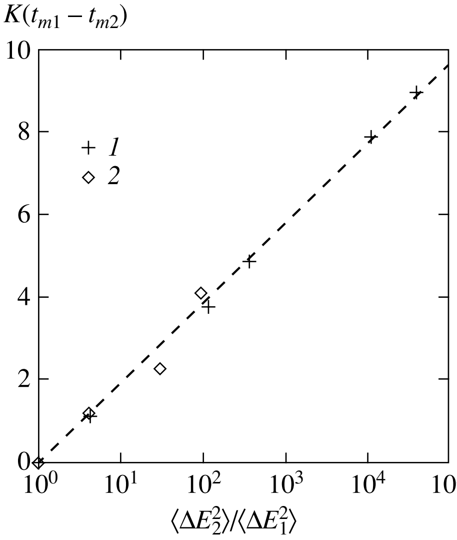

Fig. 5. Dependence of $K(t_{m1} - t_{m2})$ on $\langle \Delta E_2^2 \rangle / \langle \Delta E_1^2 \rangle$: (*1*) Lennard-Jones system with $N = 64$, $\rho = 0.5$, $T = 0.44$, and $d = 3$ and (*2*) nonideal plasma [26].

the time of complete filling of the phase volume in which the subsystem (the molecular-dynamics cell at given temperature T) or, more exactly, the phase point representing this system travels along the molecular-dynamics trajectory. During each subsequent t_m interval of this trajectory, the procedure of complete filling of the $\Delta\Gamma_\mathrm{max}$ phase volume repeats itself.

By the meaning of calculations, t_m is also the time of correlation decoupling (in terms of [1]); that is, $t_\mathrm{m} = \tau$. Clearly, contrary to the $\tau = K^{-1}$ assumption made in [1], the K^{-1} and t_m values may be substantially different. There is not only a qualitative but also a fundamental difference between K^{-1} and t_m. The K value is a characteristic of the many-particle system under study and does not depend on the accuracy and scheme of numerical integration. In contrast, the t_m value depends on the accuracy of numerical integration, which, in this case, plays the role of a coarsening process.

In [1], coarsening parameter ε was introduced which was supposed to decrease to zero in the end of derivations. It was assumed that the result for the time of correlation decoupling was independent of ε and remained finite when $\varepsilon \longrightarrow 0$. In molecular dynamics, the role of ε is played by the accuracy of numerical integration. Clearly, $t_\mathrm{m} \longrightarrow \infty$ as $\varepsilon \longrightarrow 0$. As in [1], the K-entropy is a metric invariant and does not depend on the coarsening procedure when $\varepsilon \longrightarrow 0$.

2.3. The Dependence of Kt_m on Δt and $\langle \Delta E^2 \rangle$

The calculated dependences of Kt_m on Δt and $\langle \Delta E^2 \rangle$ are shown in Fig. 4. The Kt_m value logarithmically increases as the numerical integration step decreases. This result can be obtained from (9)–(11) on the assumption that $A \sim (\Delta t)^n$, where n is determined by the order of accuracy of the numerical integration scheme. Indeed, at time $t = t_m$,

$$6kT/m = 2\langle v^2 \rangle = \langle \Delta v^2(t_m) \rangle = A\exp(Kt_m). \quad (15)$$

Taking the logarithm of (15) yields

$$Kt_m = -n\ln(\Delta t) + \mathrm{const}, \quad (16)$$

or, in another form,

$$K(t_{m1} - t_{m2}) = n\ln(\Delta t_2/\Delta t_1), \quad (17)$$

where t_{m1} and t_{m2} are the memory times for the Δt_1 and Δt_2 values. This result does not depend either on temperature, density, or the special features of the system under study.

Because of the approximate character of numerical integration, energy E [Eq. (5)] is only constant in the mean. The E value fluctuates about the mean value from step to step, and the trajectory obtained in molecular dynamics calculations does not lie on the $E = \mathrm{const}$ surface, in contrast to exact solutions to Newton Eqs. (1) and (2). This trajectory is situated in some layer of thickness $\Delta E > 0$ near the $\Delta E = \mathrm{const}$ surface [18, 19]. The ΔE value depends on the accuracy and the scheme of numerical integration [18, 19, 31–34], and $\langle \Delta E^2 \rangle \sim \Delta t^n$. It follows from (16) and (17) that

$$Kt_m = -\ln(\langle E^2 \rangle) + \mathrm{const}, \quad (18)$$

$$K(t_{m1} - t_{m2}) = \ln\left(\frac{\langle \Delta E_2^2 \rangle}{\langle \Delta E_1^2 \rangle}\right). \tag{19}$$

The results for a Lennard-Jones system and the results obtained in [26] for a nonideal plasma are shown in Figs. 4 and 5. The calculation data well fit Eqs. (18) and (19).

Equation (19) relates the *K*-entropy and the dynamical memory time to the noise level in the dynamical system. This equation corresponds to the concepts developed in [3–7]. Recall that, according to [1], $K(t_{m1} - t_{m2}) = 0$ for the time of correlation decoupling and does not depend on the noise level.

2.4. Selection of the Accuracy of Numerical Integration

The scheme and step of numerical integration should be selected to satisfy the condition

$$\tau_r < t_m < t_0/M, \tag{20}$$

where τ_r is the relaxation time of the dynamical process under study, t_0 is the trajectory length, and $M^{-1/2}$ is the required accuracy of averaging the results. The right-hand side of inequality (20) corresponds to the obvious statistical independence of phase molecular-dynamics trajectory points spaced $t_{\rm m}$ apart. The actual accuracy of averaging may therefore even be expected to exceed $M^{-1/2}$.

3. NONEQUILIBRIUM SYSTEM

3.1. Model and Method of Calculations

In nonequilibrium state calculations, the parameters of the system are the same as with the equilibrium state. The initial conditions are selected as a square or cubic lattice of particles moving at low velocities. Kinetic energy $\langle v^2(t) \rangle$ values and velocity $\langle \Delta v^2(t) \rangle$ and coordinate $\langle \Delta r^2(t) \rangle$ divergences are calculated. We used Eq. (8) for two phase trajectories, the initial conditions for which first differed by a small random value. No averaging over *M* was performed.

3.2. Two K-entropies, Nonequilibrium and Equilibrium

Calculations show that a nonequilibrium system is characterized by the presence of two exponential portions (Fig. 6) of the $\langle \Delta v^2(t) \rangle$ and $\langle \Delta r^2(t) \rangle$ dependences. The first portion corresponds to the evolution of the system up to attaining equilibrium (K_n is the nonequilibrium *K*-entropy value), and the second portion begins after equilibrium is reached (K_e is the equilibrium *K*-entropy value). The *K*-entropy is constant during relaxation at the first stage, although the ratio between the kinetic and potential energies substantially changes as trajectories diverge. We therefore cannot treat the *K*-entropy as a function of temperature. Nor can it be treated as a function of the total energy of the system at a constant density, because the *K* value changes after the attainment of equilibrium; that is, at the same total energy value, there exist two *K*-entropies, equilibrium and nonequilibrium. Nevertheless, the *K*-entropy retains its meaning as the rate at which entropy increases.

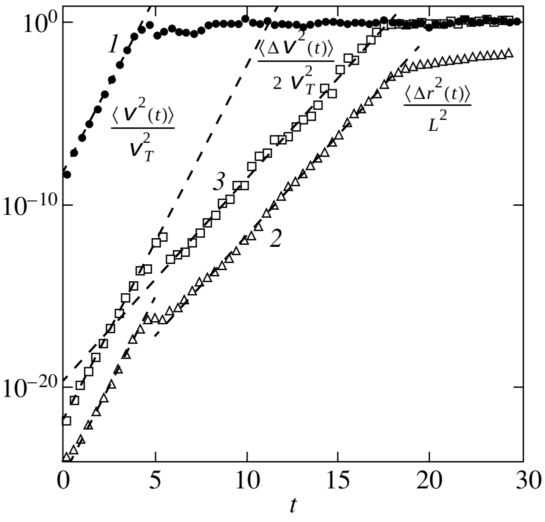

Fig. 6. Normalized time dependences of (*1*) the kinetic energy of the system, (*2*) divergence of coordinates, and (*3*) divergence of velocities in a nonequilibrium system with $N = 64$, $\rho = 0.5$, and $d = 2$.

3.3. Relation between Nonequilibrium K-entropy and the Kinetic Energy Relaxation Time

Slopes (on the logarithmic scale) of the exponential portions of the time dependences of the kinetic energy and divergence of velocities coincide in all numerical experiments within statistical errors (Fig. 6). This coincidence is observed for both two- and three-dimensional systems. It follows that the nonequilibrium *K*-entropy value coincides with τ_r^{-1}, where τ_r^{-1} is the kinetic energy relaxation rate. Time τ_r therefore acquires the meaning of the reciprocal velocity of mixing trajectories.

By analogy with $t_{\rm m}$, we can introduce time t_r at which the kinetic energy of the system attains equilibrium. During kinetic energy *T* relaxation, the $T(t)$ dependence obeys the equation

$$T(t) = T_0 \exp(K_n t), \tag{21}$$

where T_0 is the initial nonequilibrium kinetic energy value. Then,

$$t_r/\tau_r = K_n t_r = \ln(T/T_0), \tag{22}$$

where *T* is the equilibrium kinetic energy value. Precisely t_r rather than τ_r is the kinetic energy relaxation time. Time t_r during which kinetic energy attains equi-

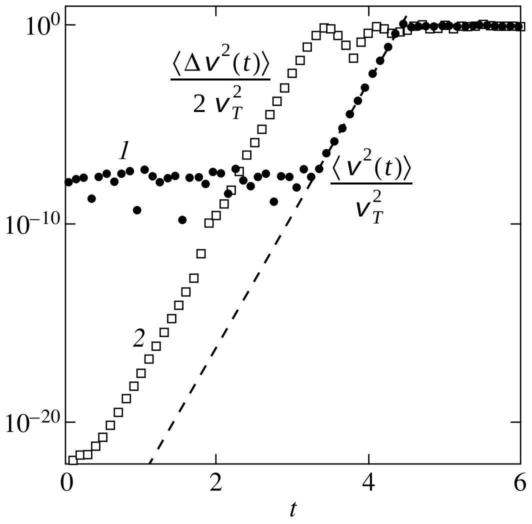

Fig. 7. Normalized time dependences of (*1*) the kinetic energy of the system and (*2*) divergence of coordinates in a nonequilibrium system with $N = 64$, $\rho = 1.1$, and $d = 2$.

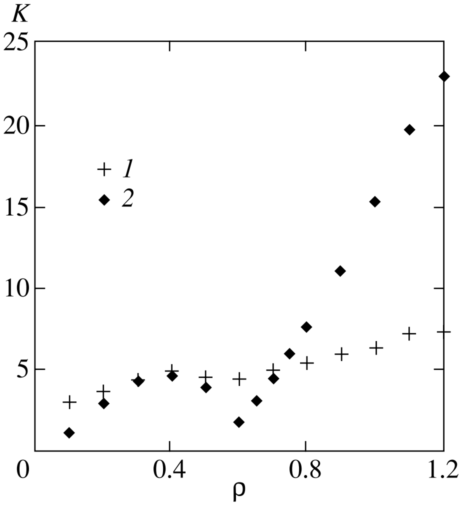

Fig. 8. (*1*) Equilibrium and (*2*) nonequilibrium *K*-entropy as a function of density; $N = 64$ and $d = 3$.

librium is much longer than time τ_r; for instance, $t_r = 20\tau_r$ in Fig. 6.

To determine which of the two values, τ_r or K_n, is of primary importance, calculations for the initially closely packed lattice were performed when the mean kinetic energy of particles for a long time (compared with τ_r) remained unchanged on average (Fig. 7). The lattice remained in a state similar to metastable, and the trajectories exponentially diverged at rate K_n. After some time, the kinetic energy, however, began to increase and relaxed to the equilibrium value, and in this experiment also, the equality $\tau_r^{-1} = K_n$ held. It follows that the K_n and τ_r^{-1} values coincide even when kinetic energy relaxation does not occur simultaneously with the divergence of trajectories. It can therefore be stated that the K_n value determines the rate of kinetic energy increase, and K_n^{-1} is the characteristic relaxation time, which manifests itself both in the divergence of trajectories in a nonequilibrium state and when the kinetic energy attains equilibrium.

The initial (metastable) region in Fig. 7 is outwardly similar to the dependence shown for the equilibrium system at the right of Fig. 6. The *K* value for this state, however, equaled the nonequilibrium K_n rather than the equilibrium K_e value; that is, it equaled the τ_r^{-1} value that appeared later, when the kinetic energy began to relax to equilibrium.

The difference between K_n and K_e was studied in a wide density range (Fig. 8). The calculations showed that the K_n-entropy had a nonmonotonic density dependence. This dependence differed from the monotonic (as in [20]) density dependence of the K_e-entropy of the equilibrium system.

3.4. Selection of Numerical Integration Accuracy

In studying nonequilibrium systems, it suffices to require that t_r be approximately equal to t_0. It is, however, then necessary to perform averaging over the distribution of initial configurations corresponding to the problem to be solved; that is, length t_0 should be calculated for each statistically independent initial configurations. Their number *M* determines the accuracy of averaging $M^{-1/2}$. The selection of the ensemble of initial configurations is a separate problem.

4. THE PHYSICAL MEANING OF DYNAMICAL MEMORY TIME AND THE ROLE IT PLAYS

Compare the dynamical memory time with the characteristic times of the velocity autocorrelation function. The results for this function are shown in Fig. 9. The region where velocity autocorrelation function values exceed 10^{-1} corresponds to times shorter than memory time t_{m}. It follows that correlations in this region are dynamical correlations which follow from the Newton equations. Correlations in the tail of the velocity autocorrelation function occur in the time region where dynamical memory of the initial conditions is not retained; that is, these correlations are of a stochastic rather than dynamical nature.

It would be interesting to study the question whether or not memory time variations caused by increasing the accuracy of numerical integration influence the character of correlations in the region of the transition from dynamical to stochastic correlations. Computationally, this is not a simple problem. It follows from (18)–(19) and Figs. 4 and 5 that t_{m} grows no faster than logarithmically as the accuracy of numerical integration increases. The available computation facilities allow ΔE to be decreased by only 5 orders of magnitude even with the use of refined numerical schemes [32–34]. This would only increase t_m two times. It follows that the region of stochastic correlations would nevertheless remain in the time interval of velocity autocorrelation function calculations [35]. The time of the transition from dynamical to stochastic correlations for various integration schemes depending on temperature, density, and the mass of particles requires additional consideration.

At the same time, the problem of excessively increasing t_m is of no concern for physics. Recall that there exist physical factors that lead to finite dynamical memory times in real systems also [3–7, 15, 16, 36]. The errors of the numerical scheme play the role of negligible (but always finite!) quantum uncertainty characteristics of any system considered classical. In [15, 16, 36], the notion of quasi-classical trajectories was introduced, and the equations of motion in the quasi-classical approximation were obtained; that is, the transition to the classical limit was performed with retaining corrections first-order in the Planck constant h. The resulting equations differed from Newtonian by the appearance of random sources. These sources took into account smearing of wave packets and diffraction in elastic scattering. Attention to the role played by weak inelastic processes was drawn by Gertsenshtein and Kravtsov [7], who studied trajectory perturbations under the action of a thermal electromagnetic field [3] and spontaneous emission of low-frequency photons [6].

The approaches used in [3, 6, 7, 15, 16, 36] were based on the Landau hypothesis that the origin of irreversibility was related to quantum mechanics. Although the Schrödinger equation is symmetrical with respect to time reversal, quantum mechanics in reality contains nonequivalence of two time directions. Deep irreversibility in quantum mechanics is inherent in the measurement process [2], which has a probabilistic character. The use of the measurement procedure allowed quantum noise to be estimated and the quasi-classical equations of motion to be introduced [15, 16, 36].

Quantum noise simulation [15, 16, 36] in molecular dynamics calculations has not been performed as yet. It can, nevertheless, be suggested that, because of the logarithmic dependence of t_m on the noise level, quantum uncertainty should lead to t_m values in the range studied in this work, that is, in the picosecond range. We stress that the aforesaid refers to dynamical memory times of a real dense system of atoms rather than its numerical model.

All of the above allows us to reconsider the traditional views on the problem of reversibility. As has been mentioned, the finite quantum uncertainty value ($\Delta E > 0$) is the reason why the dynamical memory time is always finite in real systems ($t_m < +\infty$). It can be assumed in the quasi-classical approximation that a pencil of trajectories expanding at a K^{-1} rate rather than a single classical trajectory starts at a certain system phase space point. Only the initial divergence conditions, that is, A, B, and t_l [see (9) and Fig. 1], depend on the Planck constant. Applying the standard time reversal procedure at time $t = t^*$ ($\mathbf{v}(t^*) \longrightarrow -\mathbf{v}(t^*)$, $t \longrightarrow -t$) leads to a new pencil of trajectories starting at the $\{\mathbf{r}(t^*), \mathbf{v}(t^*)\}$ point where the system currently occurs. By time t^*, dynamical memory of the initial conditions is partly (or completely) lost, and there is only some probability P_{rev} that the system will return to the initial $\{\mathbf{r}(0), \mathbf{v}(0)\}$ point. Probability P_{rev} exponentially decreases as time t^* increases if $t^* > t_l$. Dynamical memory time t_m is the characteristic time during which this probability reduces virtually to zero; that is, $P_{rev}(t^* = t_m) \approx 0$. It follows that reversibility, that is, the return of the system to the initial conditions, is impossible already at least at times of the order of t_m. It has been noted that, in real systems, t_m lies in the picosecond range, and it can therefore be assumed that the overwhelming majority of molecular processes (such as chemical reactions etc.) are generally irreversible. To summarize, whereas previously, the irreversibility phenomenon was considered unusual, it appears that now, reversible events, if encountered, will require thorough examination.

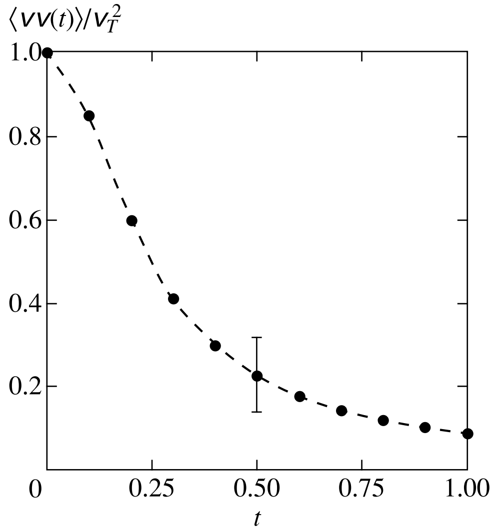

Fig. 9. Velocity autocorrelation function $\langle vv(t)\rangle/v_T^2$ at $N = 64$, $\rho = 0.5$, $T = 0.44$, and $d = 3$.

Estimates of dynamical memory times were obtained in this work for molecular dynamics numerical schemes. The t_m values obtained correspond to the noise level of numerical integration. We, however, established that the dynamical memory time very weakly (logarithmically) depended on the noise level, which allowed us to extend qualitative conclusions to real systems of atoms, in which the finiteness of the dynamical memory time is caused by quantum uncertainty.

ACKNOWLEDGMENTS

The authors thank A.A. Valuev, Yu.A. Kravtsov, and I.V. Morozov for discussions.

This work was financially supported by the Russian Foundation for Basic Research (project no. 00-02-16310).

REFERENCES

1. G. M. Zaslavsky, *Chaos in Dynamical Systems* (Nauka, Moscow, 1984; Harwood, Chur, 1985).
2. L. D. Landau and E. M. Lifshitz, *Course of Theoretical Physics*, Vol. 5: *Statistical Physics* (Nauka, Moscow, 1995; Pergamon, Oxford, 1980), Part 1, Parag. 8; L. D. Landau and E. M. Lifshitz, *Course of Theoretical Physics*, Vol. 3: *Quantum Mechanics: Non-Relativistic Theory* (Nauka, Moscow, 1989, 4th ed.; Pergamon, New York, 1977, 3rd ed.), Parag.7.
3. Yu. A. Kravtsov, Zh. Éksp. Teor. Fiz. **96**, 1661 (1989) [Sov. Phys. JETP **69**, 940 (1989)].
4. Yu. A. Kravtsov, Usp. Fiz. Nauk **158**, 93 (1989) [Sov. Phys. Usp. **32**, 434 (1989)].
5. Yu. A. Kravtsov, in *Limits of Predictability*, Ed. by Yu. A. Kravtsov (Springer-Verlag, Berlin, 1993; TsentrKom, Moscow, 1997), p. 173.
6. M. E. Gertsenshteĭn and Yu. A. Kravtsov, Nauka Tekhnol. Ross., No. 6, 9 (1998).
7. M. E. Gertsenshteĭn and Yu. A. Kravtsov, Zh. Éksp. Teor. Fiz. **118**, 761 (2000) [JETP **91**, 658 (2000)].
8. G. G. Malinetskiĭ, in *Limits of Predictability*, Ed. by Yu. A. Kravtsov (Springer-Verlag, Berlin, 1993; TsentrKom, Moscow, 1997).
9. Yu. L. Klimontovich, *Statistical Theory of Open Systems* (Yanus, Moscow, 1995; Kluwer, Dordrecht, 1995).
10. W. G. Hoover, *Time Reversibility, Computer Simulation and Chaos* (World Scientific, Singapore, 1999).
11. W. G. Hoover, *Computational Statistical Mechanics* (Elsevier, Amsterdam, 1991).
12. W. G. Hoover and H. A. Posch, Phys. Rev. A **38**, 473 (1998).
13. W. G. Hoover and H. A. Posch, Phys. Rev. E **49**, 1913 (1994).
14. K.-H. Kwon and B.-Y. Park, J. Chem. Phys. **107**, 5171 (1997).
15. A. S. Kaklyugin and G. E. Norman, J. Mosc. Phys. Soc. **8**, 283 (1998).
16. A. S. Kaklyugin and G. E. Norman, Ross. Khim. Zh. **44** (3), 7 (2000).
17. A. A. Valuev, G. E. Norman, and V. Yu. Podlipchuk, in *Thermodynamics of Irreversible Processes*, Ed. by A. I. Lopushanskaya (Nauka, Moscow, 1987), p. 11.
18. A. A. Valuev, G. E. Norman, and V. Yu. Podlipchuk, in *Mathematical Simulation. Physicochemical Properties of Matters*, Ed. by A. A. Samarskiĭand N. N. Kalitkin (Nauka, Moscow, 1989), p. 5.
19. G. E. Norman, V. Yu. Podlipchuk, and A. A. Valuev, J. Mosc. Phys. Soc. **2**, 7 (1992).
20. A. A. Valuev, G. E. Norman, and V. Yu. Podlipchuk, Mat. Model. **2** (5), 3 (1990).
21. *Molecular-Dynamics Simulation of Statistical Mechanical Systems: Proceedings of the International School of Physics "Enrico Fermi"*, Ed. by G. Ciccotti and W. G. Hoover (North-Holland, Amsterdam, 1986), Course 97.
22. M. P. Allen and D. J. Tildesley, *Computer Simulation of Liquids* (Clarendon, Oxford, 1987).
23. W. F. van Gunsteren, in *Mathematical Frontiers in Computational Chemical Physics*, Ed. by D. Truhler (Springer-Verlag, New York, 1988), p. 136.
24. *Methods of Molecular Dynamics in Physical Kinetics*, Ed. by Yu. K. Tovbin (Nauka, Moscow, 1996).
25. D. K. Belashchenko, Usp. Fiz. Nauk **169**, 361 (1999).
26. I. V. Morozov, G. E. Norman, and A. A. Valuev, Contrib. Plasma Phys. **39**, 307 (1999); J. Phys. IV **10**, Pr5-251 (2000); Phys. Rev. E **63**, 036405 (2001).
27. Y. Ueshima, K. Nishihara, D. M. Barnett, *et al.*, Phys. Rev. E **55**, 3439 (1997).
28. Y. Ueshima, K. Nishihara, D. M. Barnett, *et al.*, Phys. Rev. Lett. **79**, 2249 (1997).
29. D. M. Barnett, T. Tajima, and Y. Ueshima, Phys. Rev. Lett. **83**, 2677 (1999).
30. G. E. Norman, in *Proceedings of the V All-Union Conference on Structure and Properties of Metal and Slag Solutions*, Part 1: *Theory of Liquid and Amorphous Metals* (Ural. Nauchn. Tsentr Akad. Nauk SSSR, Sverdlovsk, 1983), p. 58.
31. G. E. Norman, V. Yu. Podlipchuk, and A. A. Valuev, Mol. Simul. **9**, 417 (1993).
32. G. J. Rowlands, Comput. Phys. **97**, 235 (1991).
33. M. A. López-Marcos, J. M. Sanz-Serna, and J. C. Díaz, J. Comput. Appl. Math. **67**, 73 (1996).
34. M. A. López-Marcos, J. M. Sanz-Serna, and R. D. Skeel, SIAM J. Sci. Comput. (USA) **18**, 223 (1997).
35. V. Ya. Rudyak, G. V. Kharlamov, and A. A. Belkin, Teplofiz. Vys. Temp. **39** (2), 283 (2001).
36. A. S. Kaklyugin and G. E. Norman, J. Mosc. Phys. Soc. **5**, 223 (1995).

Translated by V. Sipachev